DYNAMIC MODELING AND ENVIRONMENTAL ANALYSIS OF HYDROKINETIC ENERGY EXTRACTION

by

Veronica Miller

B.S. in Mechanical Engineering, University of Idaho, 2004

M.S. in Mechanical Engineering, University of Idaho, 2006

Submitted to the Graduate Faculty of

the Swanson School of Engineering in partial fulfillment

of the requirements for the degree of

Ph.D. in Mechanical Engineering

University of Pittsburgh

2010

UNIVERSITY OF PITTSBURGH

SWANSON SCHOOL OF ENGINEERING

This dissertation was presented

by

Veronica Miller

It was defended on

June 17, 2010

and approved by

Laura A. Schaefer, Ph. D., Professor

Amy E. Landis, Ph. D., Professor

Lisa Weiland, Ph. D., Professor

Sung Kwon Cho, Ph. D., Professor

Dissertation Director: Laura A. Schaefer, Ph. D., Professor

DYNAMIC MODELING AND ENVIRONMENTAL ANALYSIS OF HYDROKINETIC ENERGY EXTRACTION

Veronica Miller, PhD

University of Pittsburgh, 2010

The world is facing an imminent energy supply crisis. Our well-being is linked to the energy supply, and energy is in high demand in both the developed and the developing world. In order to sustain our energy supply, it is necessary to advance renewable technologies. Despite this urgency, however, it is paramount to consider the larger environmental effects associated with using renewable resources.

Hydropower, in the past, has been seen as a viable resource to examine, given that its basics of mechanical to electrical energy conversion seem to have little effect on the environment. Discrete analysis of dams and in-stream diversion set-ups has shown otherwise, though. Modifications to river flows and changes in temperature (from increased and decreased flows) cause adverse effects to fish and other marine life because of changes in their adaptive habitat.

Recent research has focused on kinetic energy extraction in river flows, which may prove to be more sustainable, as this type of extraction does not involve a large reservoir or large flow modification. The field of hydrokinetic energy extraction is immature; little is known about the devices' performance in the river environment, and their risk of impingement, fouling, and suspension of sediments. Governing principles of hydrokinetic energy extraction are presented, along with a two-dimensional computational fluid dynamics (CFD) model of the system. Power extraction methods are compared, and verification and validation of the CFD model through mesh sensitivity and experimental data are presented. A 0.0506 average mesh skew and 0.2m/s velocity convergence was obtained within the mesh sensitivity analysis. In

comparing particle image velocimetry (PIV) data with the CFD model, a 0.0155m offset and 20% error were present. However, including a volume of fluid (VOF) model within the CFD model produced a 5% error improvement and gave a 0.0124m offset. These are improvements over the current state of the art, where visual comparisons are common. Three-dimensional CFD models of a submerged water wheel, Savonius turbine, squirrel cage Darrieus turbine, and Gorlov Darrieus turbine are also presented; however, they are non-VOF CFD models.

Using the results of the CFD models, preliminary predictions could be made of the environmental impact of hydrokinetic turbines with respect to fish swimming patterns. Additionally, a life cycle assessment (LCA) was conducted for hydrokinetic energy extraction (HEE), which gives insight into the total system environmental impact. HEE has been seen as a potentially "benign" form of renewable hydropower. This work provides a benchmark for initial measurement of HEE environmental impacts, since negative outcomes have been present with previously-assumed benign renewable hydropower. A Gorlov system was used to represent a HEE system. LCA was utilized to compare the environmental impacts of HEE with small hydropotential (HPP) power, coal, natural gas and nuclear power. Environmental Protection Agency (EPA) criteria air emissions were quantified and compared over the life cycle of the systems. Life cycle air emissions were used in combination with the TRACI impact assessment tool to compare the systems. The Gorlov system was found to have the lowest life cycle impact with a system lifetime comparison, and compared closely with small HPP.

Finally, various issues connected to the implementation of hydrokinetic power generation were discussed. Policy development and sediment movement were investigated in more detail. Additionally, two applications of this technology were explored: in-situ river health monitoring and remote energy generation.

TABLE OF CONTENTS

LIST OF TABLES

LIST OF FIGURES

PREFACE

I dedicate this dissertation to Kelsey James Miller, my best friend, my husband, and great supporter, for inspiring me to achieve.

The author would like to acknowledge the assistance and support of her fellow graduate student peers for their helpful suggestions and insights. More specifically, the author would like to thank her research lab group, the Energy Systems Lab: Florian Zink, Tony Kerzmann, Jie Bao, and Mike Ikeda. Special thanks to Florian for the extra help in learning relevant software and lengthy conversations in discussing research challenges. The author would also like to thank colleagues who collaborated in research projects, David Torick, David Sanchez, Andrew Trapp, and Emmanuel Ramde, a colleague who provided vital assistance in data collection and synthesis, Andrew Eastman, and an undergraduate researcher, Nick Vukmer, who dedicated himself to learning and improving the research project and put in long hours to do so.

The author would like to acknowledge University of Idaho for her excellent undergraduate and masters' education. Without this strong educational background, this doctoral degree would not be possible. Special thanks to her M.S. advisor, Dr. Steven Penoncello for the direction in completing her M.S. successfully and for believing in her when she did not believe in herself.

Sincere appreciation and thanks to the Mascaro Center for Sustainable Innovation and the Department of Education for educational enrichment and financial support through the "Graduate Assistance in Areas of National Need" fellowship.

The author would also like to acknowledge Dr. Amy Landis, Dr. Lisa Weiland, and Dr. Sung Kwon Cho for reviewing the dissertation and serving on the author's graduate committee. In particular, Dr. Landis's expertise in life cycle assessment methods proved to be invaluable in this work. Special thanks to Dr. Laura Schaefer for serving as major professor and working long hours to make this dissertation possible.

Thanks to the author's husband and family for their love, support, and being instrumental in getting the author to this point in her life. Thank you to Kelsey James Miller for all the encouragement and support to never give up. Thank you to the author's Dad and

Mom, Wallace Meyer and Linda Wells, for the inspiration and encouragement and raising the author to be the woman she is. Thanks to the author's supportive step-parents, Laurie Lutz and Bruce Wells. Thank you to the author's brothers for the laughter and their spouses encouragement. Many thanks to Paul and Laurie Miller and the Miller extended family for their love, support, and prayers.

Finally, appreciation and thanks to the Lord Jesus, the lover of her soul, for blessing the author with this wonderful opportunity to receive this education. Also thanks to His support staff in Pittsburgh, the East End Assembly of God, for providing love, hugs, and prayers.

1.0 INTRODUCTION

1.1 THE NEED FOR RENEWABLE RESOURCES

With energy needs on the rise, and a limited supply of natural resources available, there is currently an increased research interest into alternative energy modes. World energy consumption for 2005 was 100.2 quadrillion Btus, and this is conservatively expected to increase by approximately 1.1 percent each year (1). The total amount of energy resources (i.e. coal, oil, gas, etc.) extracted from the earth in 2005 was 100.49 quads. While it is expected that by 2030 the resources extracted from the earth will still be enough to meet the demand, that expectation assumes that the need for oil will decrease, cleaner processes to utilize coal will be discovered, and our reliance on renewable resources will nearly double (1). Beyond resource depletion, continued use of non-renewable resources also exacts great costs from the environment, since they are traditionally associated with increased air particulates and degradation of natural habitats. Renewable resources have the potential to both alleviate the strain on non-renewable resources and decrease negative environmental effects. Implementation of these technologies must proceed with caution, however, since the utilization of a given renewable resource may also have unforeseen adverse consequences for the environment (2).

Since many urban areas have both a high energy demand and access to rivers, this work focuses upon hydropower as a potentially viable alternative energy resource (3). Traditionally, the most common implementation of hydropower has been in the form of a reservoir or dam that extracts potential energy through a change in height. Dams have also been used for flood control and irrigation, but, despite these benefits, there are also many negative environmental implications, such as loss of land, decreasing migrant fish levels, changes in

flow regimes, temperature change, and destruction of flora and fauna (4–7). A hydropower design that has been proposed to remedy some of these negative effects is an in-stream diversion configuration (sometimes referred to as run-of-river energy conversion), an example of which is shown in Figure 1. This example was implemented in the Middle Mountain Region of Nepal, where agriculture is prominent (8). Many other regions have assessed and incorporated similar designs (9–11). The set-up diverts part of the river in a canal and uses the land's elevation to develop a head pressure for extraction. However minimally invasive this set-up might seem, though, it still has negative effects on the environment, such as a decrease in water downstream (6; 12), variations in temperature on marine fauna (4; 5; 7; 13), ecosystem degradation (14–19), and, more generally, changes to the stream's natural flow (6; 12).

Considering the given negative environmental effects of traditional and other developing hydropower systems, as summarized in Table 1, hydrokinetic energy extraction (HEE) recently has become an area of interest. HEE devices are those that extract kinetic energy rather than potential energy. The advantage of extracting kinetic energy over potential energy in a river is that the kinetic energy method directly extracts flow energy, leaving no need to achieve a high head, either naturally or through artificial means. HEE technologies, like other renewable energy forms, were developed as a result of the 1970s energy crisis, but were left stagnant when the price of oil decreased (20–23). Many of the designs under review are derived from tidal current energy, a ripe topic in the research field (20–22; 24–31), rather than having been developed specifically for river flow profiles. While current designs, described in the following section, address the problem of decreased flow and stagnant effects, little is known about how they will interact in the environment and how they operate in terms of mechanical vibration and the corresponding flows around them. Several studies have linked river ecology activities with flow velocities in the stream, making this a useful tool in hydrokinetic environmental impact studies (14; 16; 32). The goals of the research in HEE are to examine velocity profile mapping and to optimize shapes and device orientation to maximize energy extraction while minimizing environmental impact.

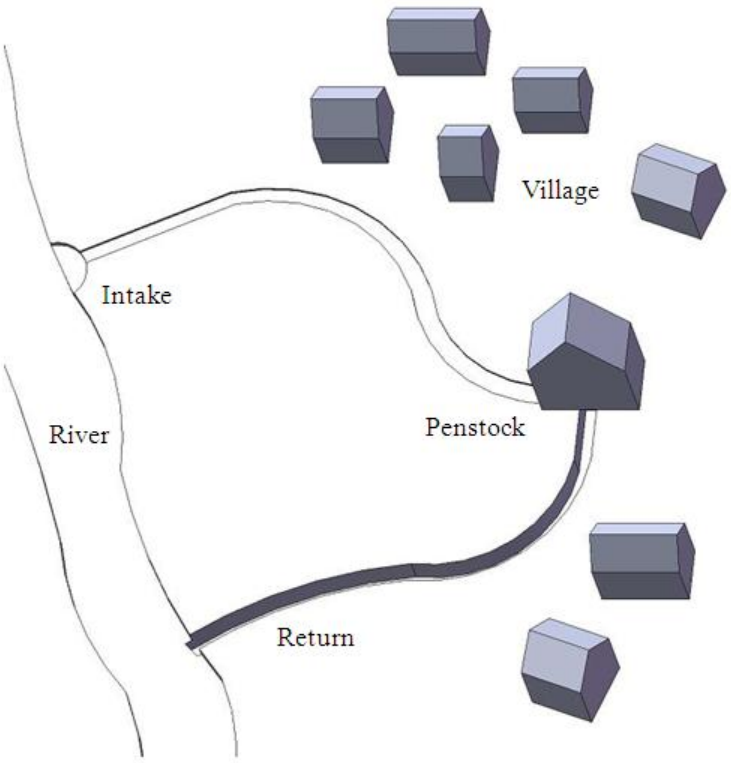

Figure 1: Run-of-River Configuration.

Table 1: Traditional and Other Developing Hydropower Systems and Their Environmental Effects.

Hydropower Systems	Environmental Effects
Reservoir type	Changes of habitat and social impacts due to reservoir
	Modification of river flows
Pumped-storage	Impacts related to elevated storage reservoir
In-stream diversion/	Reduction in flow downstream of diversion
Run-of-river	Limited flooding

1.2 MOTIVATION

The motivation for HEE research lies in the fact that there is a need for more renewable technologies to replace the conventional energy devices that rely on dwindling resources. HEE has the potential to alleviate the energy need while having a minimized environmental impact. The U.S. Department of Energy (DOE) has identified 3400 MW of this type of energy available for exploitation (3). A true optimum for this technology has not been reached, and cannot be achieved without more detailed flow mapping in and around the devices. Furthermore, this type of analysis provides insight into the actual interaction with the environment, which allows for estimation of the potential impact of the technology.

Current technology has focused on traditional approaches to energy development through increasing efficiency and operation optimization. Efficiency, though, can take on many meanings. Typically, for HEE turbines, efficiency derives from a conservation of energy/first law of thermodynamics perspective. This is appropriate for energy extraction, but does not necessarily account for the true efficiency with respect to the environment. Alternatively, exergetic efficiency does account for a turbine's efficiency within its working environment. Exergy is the maximum theoretical work obtainable with reference to the dead state (a state at the temperature and pressure of the surrounding environment). Efficiency can also be a more general term for comparison of an initial product or process to an improvement upon it. An example of this is the definition of being environmentally efficient. A device can be deemed environmentally efficient based on an accepted environmental assessment method, such as that of Life Cycle Assessment (LCA). Operation optimization in this field to date has consisted solely of increasing power output, which relates to energy efficiency. In the literature, this has been accomplished through turbine size, shape, and orientation with consideration of dynamic augmentation. Energy optimization is necessary for HEE, but there are no environmental assessments in the current literature. In this research we address how efficiency appropriately relates to HEE.

Since HEE technology exists to provide clean, renewable energy, it is necessary to assess the system's environmental impact. The U.S. DOE has identified this as a missing area in the research field (33). As history suggests, it is foolish to proceed in these technologies without

this research. Traditional hydropower, which will be referred to as hydropotential power (HPP) throughout this document, was originally considered a renewable technology until fish fatalities and ecosystem degradation were exhibited with these systems. Additionally, in-stream diversion set-ups, or small HPP, have neglected this type of analysis, also leading to ecosystem degradation. Ecosystem degradation encompasses flora and fauna destruction due to temperature changes in the flow regime from overall volume fluctuations. HEE technology addresses this ecosystem degradation since it does not involve changes to the flow volume, but fish impingement is a risk in this system (33; 34). Research in fish swimming patterns shows correlation to eddies, demonstrating that fish prefer less turbulent regions, lending insight into fish passage models (32). Using this information to create a fish passage model with HEE turbine usage is a proactive approach to that of existing fish passage research, which collects fish fatality/harm data (35). Rather than predicting a fatality rate, it is simply measured.

1.3 HYDROKINETIC RESEARCH DEVELOPMENTS

In order to place this research in context, an overview of HEE technologies must be presented. Figure 2 shows a chart of the different types of HEE devices. Some of the devices have been inspired by tidal energy extraction, such as many of the axial flow turbines, while others have been derived from wind energy extraction and applied to tidal energy extraction (29; 31). A main mode of energy extraction within tidal energy is extraction in an estuary where currents are bidirectional. The devices commonly developed for this type of extraction are designed for the lift component within the applied force in order to maximize its extraction in the two-directional environment. One of the base devices closely resembles a standard wind turbine, which is referred to as an axial flow turbine. Extracting the lift component allows the device to turn the same direction no matter which direction the water flows, which is also the case for wind energy extraction. This supposition is the basis for the derivation of all vertical axis turbines.

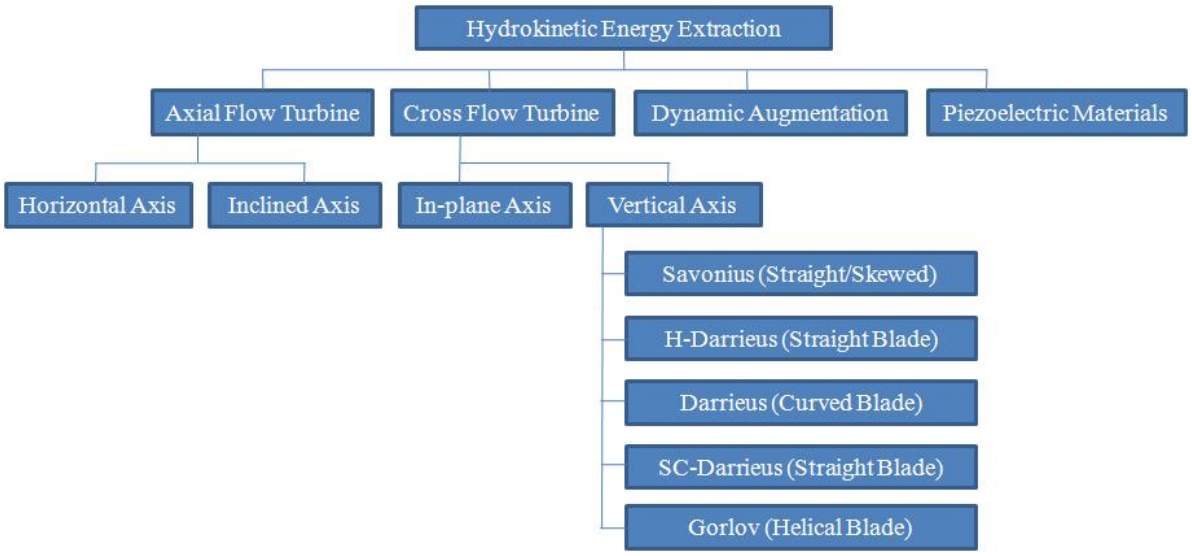

Figure 2: Hydrokinetic Energy Extraction Device Classifications.

Schematics of various HEE turbines are shown in Figure 3. The submerged water wheel, aside from being derived from the historical above or partially-above water wheel, is also inspired from the Savonius turbine. The Savonius wind turbine, like the squirrel cage and Gorlov helical Darrieus turbines, was originally designed for wind, but has also been tested for hydropower extraction, and is oriented vertically in the flow, as shown in the figure (29; 30; 36–38). In development of these devices, it was originally thought that an equivalent amount of wind energy could be extracted for a fraction of the size in water due to the differences in the fluid densities. This also assumes that extracting drag in the river flow field is most effective.

The original Darrieus turbine, shown in Figure 3c, has served as a base model for many HEE devices. The squirrel cage variation utilizes larger end bases for increased structural stability. Developing on this, the Gorlov helical turbine features design modifications inspired from the squirrel cage and egg-beater Darrieus designs, which makes it better suited for energy extraction in the river. The twisted blades are thought to keep the device from pulsating during operation. The Savonius and Gorlov Darrieus turbines have been analyzed experimentally for recent implementation. A test of a scaled Savonius turbine comprised of

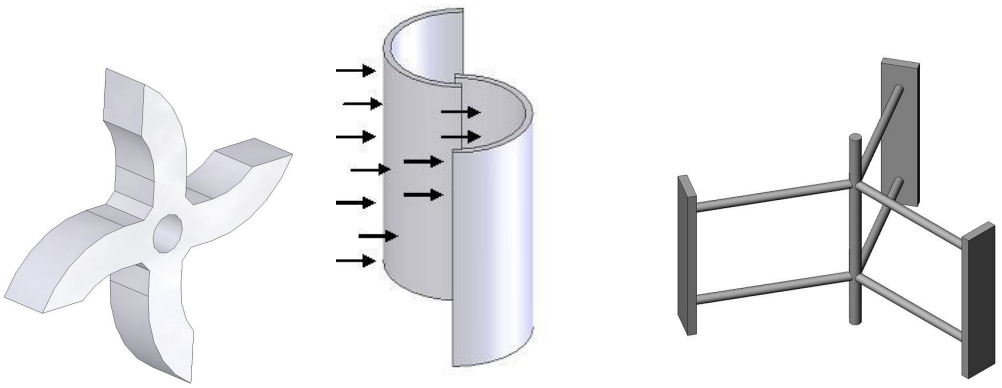

(a) Submerged Water Wheel

(b) Savonius

(c) H-Darrieus

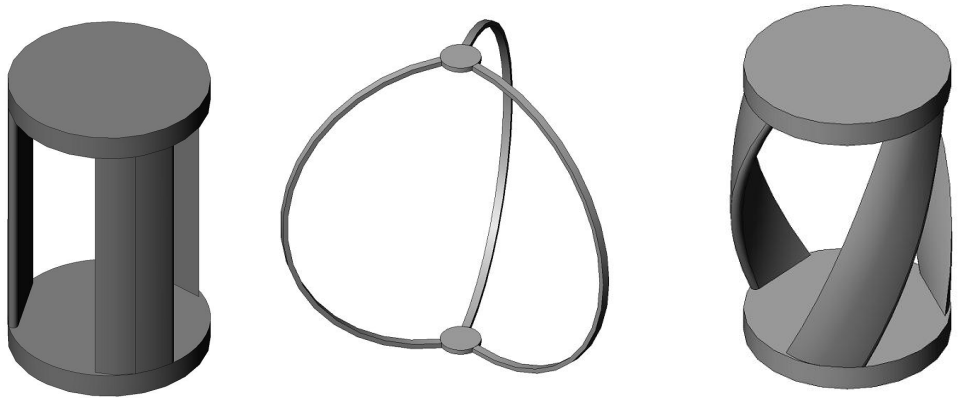

(d) Squirrel Cage Darrieus

(e) Egg-Beater Type Darrieus

(f) Gorlov (Helical) Darrieus

Figure 3: Hydrokinetic Energy Extraction Device Technologies.

two 150 mm diameter blades, oriented horizontally, that drove a 500 W generator in flows of $0.5 - 4$ m/s was described by Leung (38). The goal of the study was primarily to optimize the extraction efficiency for this device. Efficiency was improved from 33 to 62 percent by implementing different casings around it for flow channeling. In South Korea, a 2.2 m, six blade Gorlov helical turbine will be installed, and is expected to extract 210 kW from a 6.17 m/s flow (29). However, in both of these analyses, flow patterns around the device are not fully known and the impact on the aquatic environment has not been determined.

Other methods that exist for HEE are dynamic augmentation and vortex shedding applications. Augmentation devices use principles demonstrated in the Bernoulli equation to increase flow speed and pressure for higher energy extraction due to geometry changes (24; 25). Implementation requirements of this type of device include a minimum river depth of 2 m, and a high river flow rate of at least 5 m/s. A venturi device is a type of augmentation device (shown in Figure 4), and is able to extract approximately 35 kW per unit (25), but minimum operating requirements limit its utilization in many common river conditions. The main types of vortex shedding applications are the use of piezoelectric materials and VIVACE (Vortex Induced Vibration Aquatic Clean Energy). Piezoelectric devices consist of electrode and polymer configurations that harness charge from movement due to pressure fluctuations in a river flow. These piezoelectric materials are shown in Figure 5 and have a power density of 68.1 W/m^3 (whereas wind turbines have a power density of 34 W/m^3 (39)). For their power output to be comparable to traditional hydropower extraction, however, they would require a massive level of material to be placed in the stream bed. In addition to these theoretical estimates being optimistic, the base construction of these piezoelectric materials contain lead, which is not likely to be acceptable for use in aquatic environments. VIVACE is a relatively new project using a rigid structure in flows that utilizes vortex induced shedding for energy extraction (shown in Figure 6), much like the piezoelectric material application. It is projected to extract up to 1000 MW and produce minimal environmental impacts, but there is currently no data to support that projection, and an environmental model has not been created (40). Furthermore, this technology is flow bandwidth limited, meaning it must be properly sized to the stream condition in order for it to function. Since rivers have fluctuations, this could lead to stalling for this particular device.

Figure 4: Rochester Venturi Augmentation HEE Device from HydroVenturi.

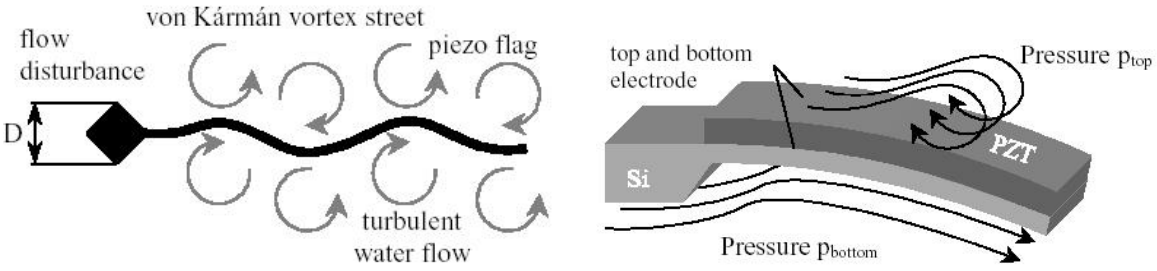

(a) von Krmn's Fluttering Flag

(b) Microstructured Piezo-Bimorph Generator

Figure 5: Piezoelectric Devices.

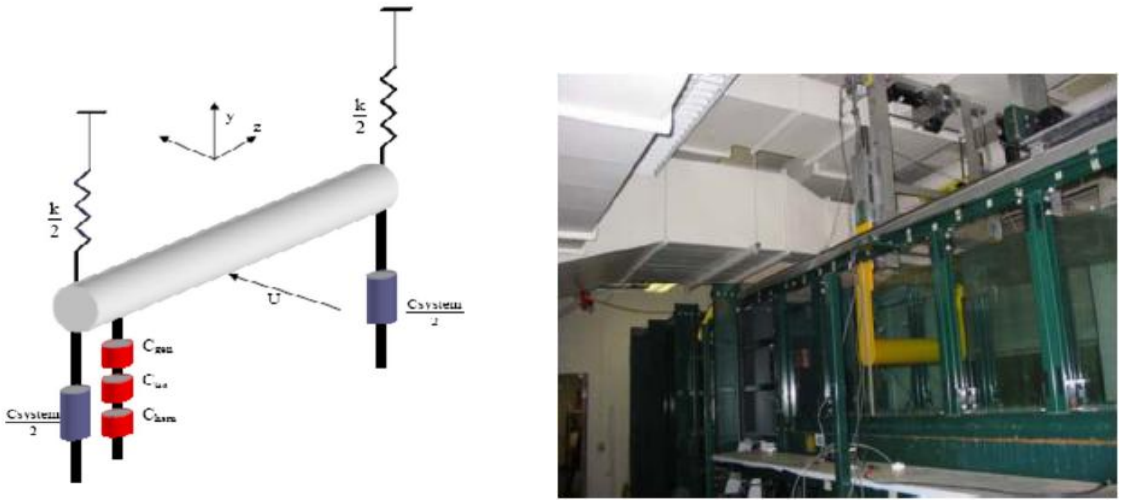

(a) VIVACE Schematic (b) VIVACE Device in Experimental Test Flume

Figure 6: VIVACE.

1.4 RESEARCH DIRECTION

From this literature review, it is clear there is a need for computational fluid dynamic (CFD) models to improve the knowledge base of HEE devices. Specifically, the focus of this research is on turbines, since the other types are in their infancy and more details are known about HEE turbines. The basis for the CFD model is to improve performance and give insight to environmental impact of this type of device. Environmental impact estimates in terms of fish passage can be derived from utilizing the CFD model to make fish passage predictions from fish swimming data. To add another perspective on environmental impact, life cycle assessment (LCA) is conducted for a Gorlov HEE system and the results are compared with a run-of-river small HPP system.

The building of the CFD model will include the review of basic principles of HEE in terms of power extraction, turbine rotation speed, and bulk velocity change. Next, appropriate boundary conditions will be established, and the model will be created within a CFD software package that uses a finite volume approach to solving continuity and Reynolds equations for turbulent motion. The initial model is created with a simple submerged water wheel.

To validate these results, particle image velocimetry (PIV) data is collected and compared with the CFD model. Once validated, the CFD model is extended to three dimensions and includes more complex HEE turbines, such as the squirrel cage and Gorlov (helical) Darrieus turbines.

2.0 PRINCIPLES OF HYDROKINETIC ENERGY EXTRACTION

In order to develop the CFD model, an initial estimate of turbine rotation is necessary. This will be determined from power extraction models based on performance estimation, where the CFD model will be used, iteratively, to determine whether the assumptions are appropriate in the power extraction modeling component. The power extraction models include the ideal power model and comparison to conservation of energy. A simple submerged water wheel turbine was chosen for development of the base model for HEE; however, the model has been designed so that other types of devices may also be modeled within it. It is likely, though, that the focus will be upon vertical axis cross flow turbines as they have already seen promising field implementation, such as that of the Gorlov helical turbine.

2.1 IDEAL POWER

To estimate the power extraction capability of a HEE device, the method commonly used in the field is to use an ideal power calculation (Equation 2.1) developed for wind and tidal energy extraction. This is due to the similar nature of the energy extraction modes. Other researchers have also used this correlation, since both systems involve fluids and either air- or hydro-foils (36; 38; 39). It is important to note, however, that the "ideal" power calculation does not signify a maximum potential power, but rather a simplified, idealized mode for the power calculation.

$$P_{ideal} = 0.5\rho A V_i^3 C_p \tag{2.1}$$

In the ideal power equation, A is the surface area from one HEE turbine arm for the submerged water wheel and any other drag-driven turbine. For lift driven turbines, A is a cross-sectional area. V_i is the inlet velocity to the device, and C_p is a turbine power coefficient, which is defined by Equation 2.2:

$$C_p = \frac{\left(1 + \frac{V_o}{V_i}\right)\left(1 - \frac{V_o}{V_i}^2\right)}{2} \tag{2.2}$$

where V_o is the outlet velocity from the device. Equation 2.1 is derived from the energy equation. It is an approximation of the amount of energy that can be extracted through a wind turbine, but a detailed analysis with blade shape and surface, and the corresponding fluid interactions, would give more accurate results (41). C_p is a simplification of the conservation of mass through a streamtube approach. For an ideal turbine, C_p tends to reach a Betz limit of 0.59. In this power estimate, for a submerged water wheel turbine in a river velocity flow of 0.313 m/s with velocity outlet estimated to be 0.179 m/s, the Betz limit equals 0.53. This is well above published Betz limits for this turbine type (0.2) (37). One reason for this is that the turbine is examined as a complete system rather than simply as a streamtube, therefore allowing for much higher Betz limits. Evaluating a hydrokinetic turbine with the Betz limit alone gives incomplete information, suggesting the need for the complete flow field data available within the CFD model.

In addition to the idealized power calculation, a bulk value that also imparts performance information is the tip speed ratio. It expresses the linear speed of the blade's most outer tip to the downstream velocity (42):

$$\lambda = \frac{r\omega}{V_o} \tag{2.3}$$

In Equation 2.3, r is the arm length of the turbine, and ω is the angular velocity. Figure 7 demonstrates the relationship between the power coefficient and the tip speed ratio for an ideal turbine due to varying inlet velocity. However this does not account for turbine efficiency based on shape and extraction mechanism (lift or drag), and therefore data are needed to improve the device efficiency.

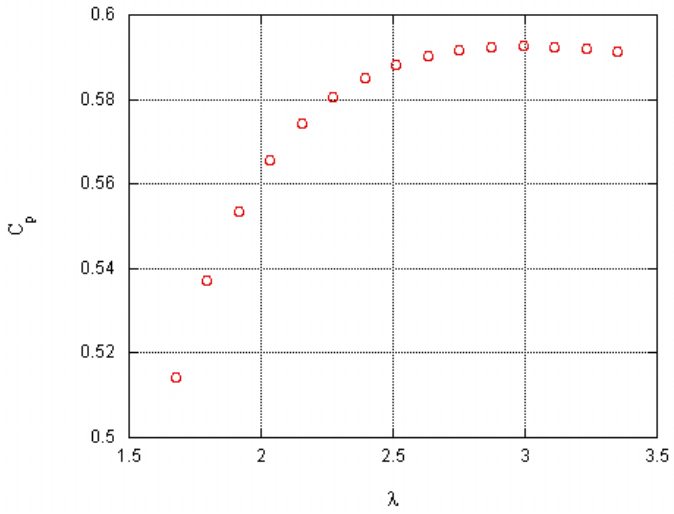

Figure 7: Turbine Efficiency.

2.2 CONSERVATION OF ENERGY

By examining the energy equation, which can be reduced to Equations 2.4 and 2.5 for any rotating turbine, more details of the system are revealed:

$$\dot{W}_s = P = \omega T \tag{2.4}$$

$$-T = \rho Q r \left(V_o - V_i\right) \mathbf{k} \tag{2.5}$$

where ρ is the fluid density, Q is the river's volumetric flow rate, and $\mathbf{k}$ indicates the z-vector component. $\dot{W}$ is the shaft work from the device rotating in the flow, P is the power extracted from the turbine, and T is the torque occurring in the turbine.

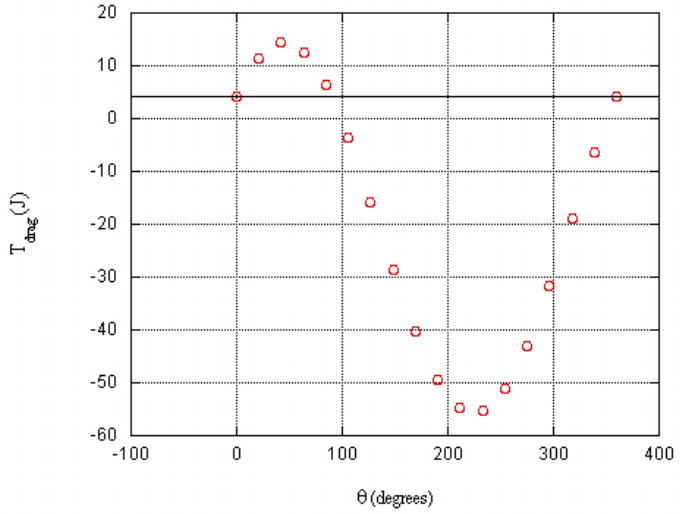

Figure 8: Torque vs. θ.

If friction is to be taken into account, Equation 2.6 should be used in place of T in the energy extraction calculation.

$$-T_{drag}\left(\frac{2}{rA\rho}\right) = [C_{D1}\left(V_i\cos\theta - \omega r\right)^2 - C_{D2}\left(V_i\cos\theta - \omega r\right)^2 + C_{D1}\left(V_i\sin\theta - \omega r\right)^2 - C_{D2}\left(V_i\sin\theta - \omega r\right)^2]\mathbf{k} \tag{2.6}$$

where C_{D1} and C_{D2} are drag coefficients based on the geometry of the turbine.

Clearly, the drag is related to the device rotation angle, θ. This behavior is illustrated in Figure 8. It can be seen that the torque from this particular turbine has a maximum at around 50°. In addition to showing the drag present to the device, this figure also shows the tangential loads on the turbine blades which drive it. Notice in the plot that at 0°, the torque is not 0 J, but rather begins at approximately 5 J (a horizontal line is drawn across to show the complete cycle).

Additionally, θ affects the angle of attack, α, as shown in Figure 9, where the angle of attack is defined in Equation 2.7:

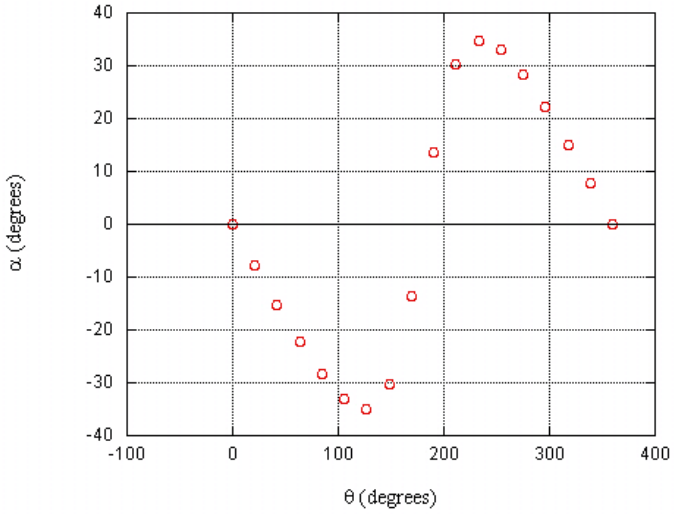

Figure 9: α vs. θ.

$$\alpha = \arctan \frac{-\sin\theta}{\cos\theta + \lambda} \tag{2.7}$$

Both the torque versus θ and α versus θ are currently used in the field for optimization of specific turbine types, shapes, and orientation. More relations can be drawn between lift and drag coefficients and the angle of attack, which, depending on the turbine type, will demonstrate areas where drag or lift should be reduced to increase power extraction. For example, the area for the submerged water wheel turbine should be larger for increased energy extraction, as Figure 8 and Equation 2.6 suggest. Furthermore, small azimuth angles (θ) can lead to stall for lift driven devices. This is not the case for the submerged water wheel turbine chosen in this analysis. However, these parameters coupled with the CFD analysis give a more complete depiction of the true performance.

2.3 COMPARISON

A comparison of these three approaches is shown in Figure 10. These calculations were performed for a submerged water wheel turbine as a basis to develop the theoretical model. P_{ideal} shows the outcome for the idealized power calculation (Equation 2.1), P for the energy equation, neglecting drag effects (Equations 2.4-2.5), and P_{drag} is the energy equation with drag effects (Equations 2.4 and 2.6). Each of these are computed for varying inlet velocities, and the resulting output levels of the power are shown. It is useful to compare the power predictions. It is expected that less power would be extracted when accounting for drag, and the similarity between the ideal and drag models shows that using the true geometry in calculations can change the amount of energy extracted versus the ideal model.

Using the energy equation formulation (Equations 2.4-2.5), preliminary device parameters were chosen for device rotation rate and outlet velocity. Its span is equal to 1.38 m, and the width is 0.305 m perpendicular to the flow. An initial flow velocity is taken from the National Weather Service of 0.313 m/s for the Allegheny River, a typical U.S. river (43). This results in a volumetric flow rate equal to 0.061 m^3/s. The outlet velocity is assumed to be approximately 0.179 m/s (this was chosen as an initial estimate; preliminary analysis from the following flow simulation suggests that this is a reasonable approximation), which results in a torque of 5.661 J and power extraction of 2.56 W per device. The two variables that primarily have an effect in Figure 10 are the blade surface area and the estimated outlet velocity. The blade surface area is a function of the design itself. This can be changed if the power extraction and CFD show it would be favorable, i.e. it would increase power extraction, or offer more displaced eddies from the blade itself, assisting in fish passage. The estimated outlet velocity cannot be directly known from computing the power performance of the turbine, and must therefore be estimated based on some performance metrics from the literature and the comparison to the CFD analysis. Furthermore, the ideal power calculation provides a computational check of the outlet velocity. Within the equation, C_p can be set to 0.59, the Betz limit, where the outlet velocity is calculated to be 0.1201 m/s. This has a small effect on the calculated power output of 5.661 J and indicates the estimated outlet velocity is accurate and conservative.

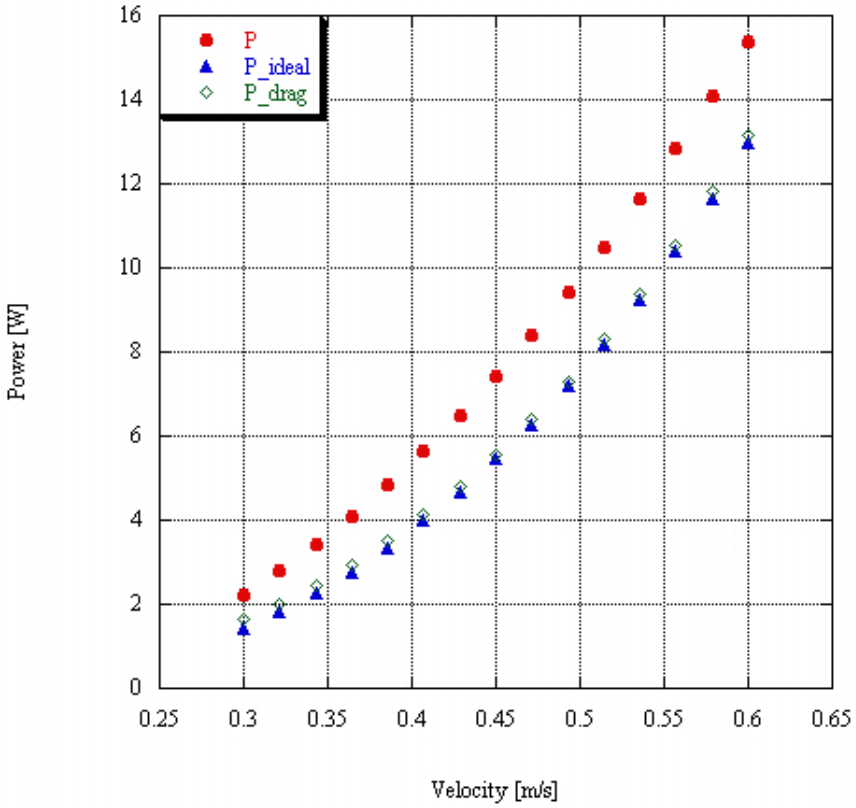

Figure 10: Power Comparison.

The magnitude of the energy extraction levels for the submerged water wheel turbine are quite low, but they are discussed here to give the overall model an initial point of reference. The inherent design of the waterwheel turbine is the reason for this, since it is a drag driven device, and is limited by location and river flow rate. The Darrieus turbines have shown much higher energy extraction levels due to their ability to extract flow energy through the lift component. However, these turbines cannot be accurately modeled using a two-dimensional analysis, and so will be included in the three-dimensional modeling work.

3.0 COMPUTATIONAL FLUID DYNAMICS (CFD) MODEL

The CFD model is created in a CFD software package, FLUENT^{TM}. The model is based on governing equations as discussed in Section 3.1. Then the equations are solved by using a finite volume approach through discretizing the flow field, as explained in Section 3.2. Additionally, Section 3.2 provides more details for the $k-\epsilon$ model used and mesh construction. Section 3.3 discusses how the final mesh density is determined and Section 3.4 shows the two-dimensional CFD model results.

3.1 RIVER MODEL GOVERNING EQUATIONS

River flow is turbulent and, as such, the appropriate model must be chosen for evaluating the mean-flow field. All turbulent flows are characterized by continuity (Equation 3.1) and the Reynolds equations for turbulent motion (Equations 3.2- 3.3) (44):

$$\rho \bigtriangledown \bullet \bar{V} = 0 \tag{3.1}$$

$$\rho \frac{D\bar{V}}{Dt} = \rho g - \bigtriangledown \bar{p} + \bigtriangledown \bullet \tau_{ij} \tag{3.2}$$

$$\tau_{ij} = \mu \left(\frac{\partial \bar{u}_i}{\partial x_j} + \frac{\partial \bar{u}_j}{\partial x_i} \right) - \rho \bar{u_i}' \bar{u_j}' \tag{3.3}$$

Because these are mean-developed equations involving terms for fluctuating velocities, more unknowns are introduced that may also be time dependent. Direct numerical simulation becomes increasingly difficult, requiring additional relations and empirical modeling to

attempt to quantify them. $k-\epsilon$ is one of the more commonly used turbulence models, and is a two equation model introducing two additional variables: k represents turbulent kinetic energy and ϵ is the dissipation rate (Equation 3.4):

$$\begin{aligned} k &:= \frac{1}{2}\left\langle \mid \vec{u_i}\prime \mid \right\rangle, \\ \epsilon &:= \frac{\nu}{2}\left\langle \mid grad\vec{u_i}\prime + grad\vec{u_i}\prime^{T} \mid^{2} \right\rangle \end{aligned} \tag{3.4}$$

This method, however, is somewhat basic among turbulence models, using isotropic turbulence in all directions and requiring different boundary condition models (45; 46). Prescribing the appropriate boundary conditions for the $k-\epsilon$ model involves different variations dependent on the physical scenario to which it is applied. It might seem natural to assign values to k and ϵ at the boundary. This invalidates the model, however, due to low Reynolds numbers and turbulent variations and fluctuations close to the boundary. Instead, wall functions, low-Reynolds-number models, and two-layer models are used. Wall functions describe the flow profile near the wall using approximate calculations and empirical data. Low-Reynolds-number models are used for separating flows in which coefficients of the original $k-\epsilon$ model are adjusted for near wall or boundary layer damping effects. This requires high resolution near the boundary for accurate results. Therefore, two-layer models employ a single-equation model in the viscous layer, while using the $k-\epsilon$ model to describe the bulk flow. In contrast to the $k-\epsilon$ model, the Reynolds stress transport model (RSTM) better quantifies the development of individual turbulent components, but it is limited because of convergence and the realizability condition (45; 46). RSTM is a simplified version of the method that was developed by Launder et al. (47) and better quantifies anisotropic stress components, which are more realistic in nature, as they evolve within the flow (46; 48). This is accomplished by completion of the Navier-Stokes equations, and solving transport equations for Reynolds stresses with an equation for dissipation rate. This method was considered in model development, but the simulation was too complex for convergence to occur. This is due to the turbine rotation within the model where the renormalized group theory (RNG) $k-\epsilon$ model provided an accurate result and better quantified the rotation component of the model.

The RNG $k-\epsilon$ model is similar to the $k-\epsilon$ model, but includes the following improvements (48):

- It has an additional term in the ϵ equation, which improves the accuracy for strained flows.
- The RNG method has enhanced accuracy for swirling flows because the swirl effect on turbulence is included in the model.
- Instead of the user-specified, constant-value turbulent Prandtl numbers implemented within the standard $k-\epsilon$ model, RNG theory provides an analytical formulation for them.

"Renormalized group" is a mathematical technique used in the derivation from the instantaneous Navier-Stokes equations (48) through use of dynamic scaling and invariance together with perturbation methods (49). The derivation results in additional terms and transport equation functions for k and ϵ and different constant values (48). Details for how this changes and fits into the overall turbulence formulation are given in the next section.

3.2 FLOW SIMULATION

3.2.1 Transport Equations

The power extraction correlations from Chapter 2 and the river model have been integrated in FLUENT^{TM}, which uses a finite volume approach to solving the differential form of Equations 3.1-3.3. The finite volume approach refers to integrating the differential form of the governing equations over each volume created when meshing or discretizing the flow field. This is opposed to the finite difference approach or finite element method where other estimates (such as differential equation approximation) are made and the flow field is evaluated at the nodal points rather than the volumes present in the mesh. This means that this CFD approach is Eulerian since the full flow field is evaluated and is specified with pressure, density, velocity, etc. as functions of time (44). A second-order discretization scheme is utilized primarily based on the triangular meshing scheme presented in the next

section. The order of discretization refers to how the solution is calculated. The RNG $k-\epsilon$ model is chosen for the flow simulation based on the geometric complexity and assumptions of standard wall functions at the boundary. Following from continuity, the Reynolds equations for turbulent motion, and the RNG $k-\epsilon$ method, the bases for the simulation within FLUENT^{TM} are (48):

$$\frac{\partial}{\partial t}(\rho k) + \frac{\partial}{\partial x_i}(\rho k u_i) = \frac{\partial}{\partial x_j}\left(\alpha_k \mu_t \frac{\partial k}{\partial x_j}\right) + G_k + G_b - \rho\epsilon - Y_M + S_k \tag{3.5}$$

$$\frac{\partial}{\partial t}(\rho \epsilon) + \frac{\partial}{\partial x_i}(\rho \epsilon u_i) = \frac{\partial}{\partial x_j}\left(\alpha_\epsilon \mu_t \frac{\partial \epsilon}{\partial x_j}\right) + C_{1\epsilon}\frac{\epsilon}{k}(G_k + C_{3\epsilon}G_b) - C_{2\epsilon}\rho\frac{\epsilon^2}{k} - R_\epsilon + S_\epsilon \tag{3.6}$$

3.2.2 Model Inputs

In Equations 3.5-3.6, G_k represents the generation of turbulent kinetic energy due to mean velocity gradients, and is calculated from the exact equation for the transport of k; so that $G_k = -\rho\bar{u_i}\prime\bar{u_j}\prime\frac{\partial u_j}{\partial x_i}$, which is then evaluated using the Boussinesq hypothesis, $G_k = \mu_{eff}S^2$, where S is the modulus of the mean rate-of-strain tensor, $S \equiv \sqrt{2S_{ij}S_{ij}}$ (48).

G_b is the generation of turbulent kinetic energy due to buoyancy (48). Since there is not a non-zero gravity and temperature gradient present within this field, this term is not used to account for turbulent kinetic energy, but does remain in the equation for other simulation scenarios outside of this research.

Y_M accounts for fluctuating dilation in compressible turbulence to the overall dissipation rate (48). This term is primarily to account for compressibility in high Mach number flows, which is not relevant here since the flow is incompressible. Again, the term remains in the overall equation for simulations outside of this research.

There are modifications to this equation to account for low-Reynolds and near-wall regions through turbulent viscosity resulting from the scale elimination procedure in the RNG theory. However, $\mu_t = \rho C_\mu \frac{k^2}{\epsilon}$, with $C_\mu = 0.0845$ (from RNG theory) is used in high-Reynolds number regions. This is close to that used in the standard $k-\epsilon$ model, where it is empirically-determined ($C_\mu = 0.09$) (48).

α_k and α_ϵ are inverse quantities for effective Prandtl numbers for k and ϵ, which are computed by,

$$\left|\frac{\alpha - 1.3929}{\alpha_0 - 1.3929}\right|^{0.6321} \left|\frac{\alpha + 2.3929}{\alpha_0 + 2.3929}\right|^{0.3679} = \frac{\mu_{\text{mol}}}{\mu_{\text{eff}}} \tag{3.7}$$

where $\alpha_0 = 1.0$. However, in high Reynolds number flows $\left(\frac{\mu_{\text{mol}}}{\mu_{\text{eff}}} \ll 1\right)$, which is the case in this simulation, $\alpha_k = \alpha_\epsilon \approx 1.393$ (48).

R_ϵ is an additional term to the standard $k - \epsilon$ model, setting it apart and is derived empirically (48). It is given by:

$$R_\epsilon = \frac{C_\mu \rho \eta^3 \left(1 - \frac{\eta}{\eta_0}\right)}{1 + \beta \eta^3} \frac{\epsilon^3}{k} \tag{3.8}$$

where $\eta \equiv \frac{Sk}{\epsilon}$, $\eta_0 = 4.38$, and $\beta = 0.012$. In order to see the effects of R_ϵ more clearly, Equation 3.6 can be rewritten as:

$$\frac{\partial}{\partial t}(\rho\epsilon) + \frac{\partial}{\partial x_i}(\rho\epsilon u_i) = \frac{\partial}{\partial x_j}\left(\alpha_\epsilon \mu_t \frac{\partial \epsilon}{\partial x_j}\right) + C_{1\epsilon}\frac{\epsilon}{k}(G_k + C_{3\epsilon}G_b) - C^*_{2\epsilon}\rho\frac{\epsilon^2}{k} \tag{3.9}$$

where

$$C^*_{2\epsilon} \equiv C_{2\epsilon} + \frac{C_\mu \eta^3 \left(1 - \frac{\eta}{\eta_0}\right)}{1 + \beta \eta^3} \tag{3.10}$$

The RNG model tends to give similar results to the standard $k - \epsilon$ model when the flows are weakly to moderately strained. This is because where $\eta < \eta_0$, the R term makes a positive contribution, and $C^*_{2\epsilon}$ becomes larger than $C_{2\epsilon}$. For example, when $\eta \approx 3.0$, $C^*_{2\epsilon}$ is ≈ 2.0 in the logarithmic layer, which is close in magnitude to the $C_{2\epsilon}$ value (1.92) in the standard $k - \epsilon$ model (48). Conversely, the R term makes a negative contribution where $\eta > \eta_0$ since this makes $C^*_{2\epsilon}$ less than $C_{2\epsilon}$. The RNG model produces lower turbulent viscosity than the standard $k - \epsilon$ model in rapidly strained flows due to the smaller destruction of ϵ, reducing k, and the effective viscosity (48). Therefore, the RNG model is more responsive to rapid strain effects and streamline curvature than the standard $k - \epsilon$ model, so that the RNG model gives superior performance for this particular flow type.

S_k and S_ϵ are user-defined source terms. $C_{1\epsilon}$ and $C_{2\epsilon}$ are constant values set to 1.42 and 1.68, respectively, based from shear flow air and water experiments conducted by Launder and Spalding (47).

Figure 11: Initial Mesh for a Submerged Water Wheel.

3.2.3 Mesh Construction

For a two-dimensional simulation, an unstructured, triangular mesh, consisting of 135,799 nodes and 268,936 cells, is used for the flow field around a hydrokinetic device and is created in Gambit^{TM}, as shown in Figure 11 (a detailed view of the mesh near the turbine is shown in Figure 12). An average depth for the chosen river (the Allegheny River) is 3 m, and a reasonable length section for observation is 12 m. In this case, the angular rotation for the device would be 0.4536 rad/s, based on the power extraction analysis presented in Chapter 2. However, as will be discussed in Section 3.3, similitude is used to scale the field size for more efficient computation, resulting in dimensions for this field of 0.1524 m (*6 inches*) depth, 0.9144 m (*36 inches*) riverbed length in front of the turbine, and 1.2192 m (*48 inches*) riverbed length after the turbine. After the resize and calculation, the angular rotation is 8.93 rad/s. The scaling is based on similarity to the Allegheny River and could contain small errors due to estimates of the river dimensions. The model could also be re-scaled for other actual rivers, and could also be resized based on other river parameters for turbine utilization.

3.2.4 Boundary Conditions

In this model, the bottom edge is defined as a wall, or no slip condition, and the top edge is defined as a symmetry boundary, while the edge to the left is a velocity inlet, which is set to 0.313 m/s, and the edge to the right is a pressure outlet. The wall boundary condition is a no slip condition, where at $y = 0$, $u = 0$, while the velocity inlet and pressure outlet are required for open-channel flow, meaning that $v = 0.313$ m/s on the inlet plane

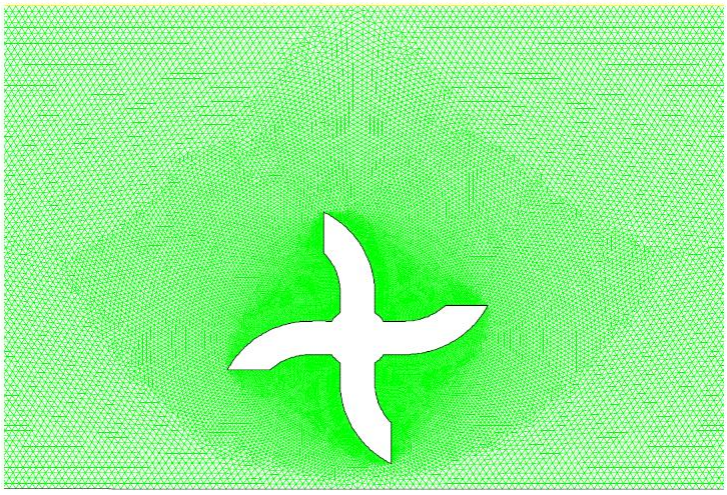

Figure 12: Mesh Detail Around the Turbine.

and p is initially set to atmospheric pressure at the exit plane, but is allowed to fluctuate as the calculation occurs to converge toward a solution. In order to properly account for an interaction between the stream and air in FLUENT^{TM}, a symmetry boundary is used, meaning at $y = h$, $u = 0.313\ m/s$, or $\frac{\partial^2 u}{\partial x^2} = 0$. This is a method commonly used in CFD to impose a no-shear condition. The no-shear condition is needed to ensure a proper open-channel velocity profile. Other defined parameters include gravity set to -9.81m/s in the x-direction, atmospheric pressure, and water density at atmospheric pressure and 20 C.

3.3 MESH SENSITIVITY ANALYSIS

In CFD modeling, it is essential to perform a mesh sensitivity analysis to further verify the results. As previously noted, the model was scaled both to provide a comparison for future experimental tests and to reduce computing load, and therefore allow for more variability in finding valid flow field meshing. Scaling was completed through Buckingham PI theory and was based on the experimental test flume having a 0.1524 m by 0.1524 m (6 inches by 6 inches) flow cross-section. This determined the physical size of the turbine, and then a

sensitivity analysis was used to find the appropriate meshing interval size. The interval size in Gambit^{TM} determines the space between mesh points rather than the mesh point count on a given side or line. A test section length of 2.1336 m (0.9144 m riverbed length in front of the turbine and 1.2192 m riverbed length after the turbine) or 84 inches was used to provide complete flow performance information, i.e. flow disturbance before and after the turbine placement.

To conduct the mesh sensitivity analysis, different mesh interval sizes were defined. Figure 13 shows the mesh construction, which consists of four zones, A-D. Zone A has the smallest interval size in the mesh to enable mesh concentration around the turbine, and zone D has the largest interval size since it is the perimeter of the mesh. Zones B and C are the intermediary sizes in the mesh creating continuity throughout. Mesh size designations are given in Table 2. They were originally chosen arbitrarily; however, to introduce some order, they are spaced evenly, such as in meshes 0, 1, and 2, where the zone A interval sizes are 0.008, 0.004, and 0.002. There is also order established within each mesh. In mesh 0, for example, zone B, 0.016, is twice zone A, 0.008, and zone D, 0.032, is twice zone B. Zone C is the average interval of zones B and D. Note that ratios are assigned with the interval sizes, as shown in Table 2. The ratio for all interval sizes is originally set to 1, meaning mesh points are spaced evenly according to the assigned mesh interval. The zones A, B, and D ratios remain as 1, as indicated in the table. Since zone C is used to connect the turbine with the overall flow field, a last-first ratio, or smoothing ratio, is employed to allow mesh smoothing. Figure 14 shows the interval spacing for a non-uniform ratio, with Equation 3.11 used to calculate the ratios:

$$R = \left(\frac{l_{i+1}}{l_i}\right)^{\frac{1}{1-n}} \tag{3.11}$$

Equation 3.11 reduces to l_n/l_1, resulting in the same last-first ratio for each mesh. There are different ways of computing this within Gambit^{TM}, such as a first-last ratio, which is essentially the opposite of the last-first ratio. The final outcome is still the same, with the goal of smoothing the mesh. However, the last-first ratio was the most straightforward and was therefore chosen to evaluate the mesh for smoothing.

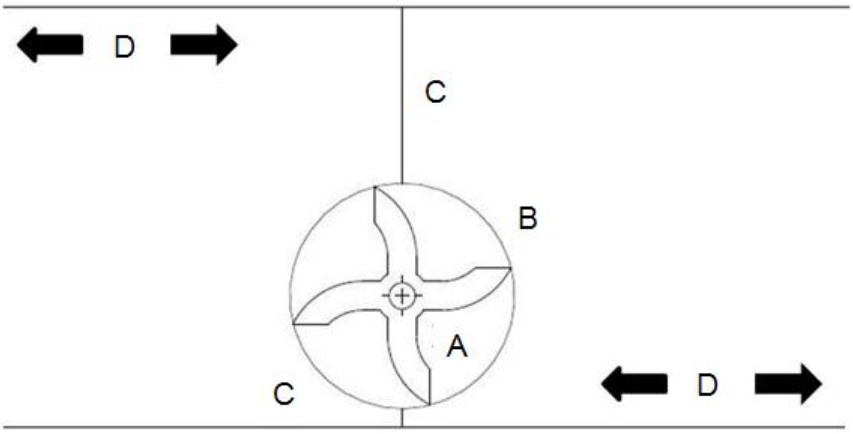

Figure 13: Mesh Diagram.

Table 2: Meshing Intervals and Ratios for a Sensitivity Analysis.

Mesh	Mesh Interval Sizes for Zones A, B, C, and D with Ratios in Parentheses	Number of Elements	Average Skew
0	0.008(1)/0.016(1)/0.024(2)/ 0.032(1)	966	0.07048
1	0.004(1)/0.008(1)/ 0.012(2)/0.016(1)	3490	0.05614
2	0.002(1)/0.004(1)/ 0.006(2)/0.008(1)	13812	0.05229
3	0.001(1)/0.002(1)/ 0.003(2)/0.004(1)	55886	0.051565
4	0.0005(1)/0.001(1)/ 0.0015(2)/0.002(1)	217974	0.05059
5	0.00025(1)/0.0005(1)/0.00075(2)/ 0.001(1)	868788	0.05067

Figure 14: Line Ratios.

To compare the meshes in Table 2, mid-line velocity curves were plotted, as shown in Figure 15a. The mid-line is the velocity line half-way between the top of the turbine and the river surface. It was chosen to show the velocity differences among the various meshes while remaining a constant line of reference between the turbine and river surface boundary conditions. In this plot, mesh 4 is the only mesh that represents a physical behavior that would occur in the flow field, because it shows a velocity decrease where energy extraction occurs. Mesh 5 is excluded from the plot since it showed erratic behavior. This framed the further detailed analysis around mesh 4, as noted in Table 3. The mesh interval sizes were reduced further after several iterations, and the respective velocity curves at the mid-line in meshes where convergence is present are plotted in Figure 15b-c. Physical behavior does not occur until mesh 3.5, however meshes 3.6875, 3.75, and 3.875 do not show physical behavior. This means that it is expected to see a velocity decrease at x=0, where the turbine is located, due to energy extraction in the flow. Physical behavior resumes for meshes 3.9375 through 4.25.

To further analyze this for optimal mesh determination, mid-point velocity and average mesh skew are plotted using mesh element size in Figures 16 and 17. Figure 16 shows x-velocity values taken at a mesh mid-point of $x = 0\ m$ and $y = 0.0728685\ m$ for varying mesh element size. Similar to the mid-line, this is the mid-point on the top line of zone C in Figure 13 and the $x = 0\ m$ point on the mid-line of the mesh. This point was chosen because it is at the midpoint between the top of the turbine and the top river surface, and provides constant reference points among the changing mesh fields. Figure 16 shows velocity mid-points converging with increased element size to approximately $v = 0.2\ m/s$; however, there is some instability around 125,000 to 170,000 mesh elements. There is also instability present from the 250,000 element size and up. This is due to the increase of mesh size with skew, which can be examined in Figure 17. The average mesh skew describes the entire average mesh skewness present in the mesh, or how non-uniform the mesh elements are. Since it is a triangular mesh, the skew amount tells us how many of the elements are not equilateral, and is calculated in Gambit™, the meshing software.

Using mid-line velocity curves, mid-point velocity, and average mesh skew, selection of mesh 4 can give reasonable results due to the physical behavior it gives, convergence among

Table 3: Reduced Meshing Intervals and Ratios for a Sensitivity Analysis.

Mesh	Mesh Interval Sizes for Zones A, B, C, and D with Ratios in Parentheses	Number of Elements
0	0.008(1)/0.016(1)/0.024(2)/0.032(1)	966
1	0.004(1)/0.008(1)/0.012(2)/0.016(1)	3490
2	0.002(1)/0.004(1)/0.006(2)/0.008(1)	13812
3	0.001(1)/0.002(1)/0.003(2)/0.004(1)	55886
3.25	0.000875(1)/0.00175(1)/0.002625(2)/0.0035(1)	71422
3.5	0.00075(1)/0.0015(1)/0.00225(2)/0.003(1)	97224
3.625	0.0006875(1)/0.001375(1)/0.0020625(2)/0.00275(1)	115654
3.6875	0.00065625(1)/0.0013125(1)/0.00196875(2)/0.002625(1)	126774
3.75	0.000625(1)/0.00125(1)/0.001875(2)/0.0025(1)	139618
3.875	0.0005625(1)/0.001125(1)/0.0016875(2)/0.00225(1)	172488
3.9375	0.00053125(1)/0.0010625(1)/0.00159375(2)/0.002125(1)	193048
4	0.0005(1)/0.001(1)/0.0015(2)/0.002(1)	217974
4.125	0.00046875(1)/0.0009375(1)/0.00140625(2)/0.001875(1)	247970
4.25	0.0004375(1)/0.000875(1)/0.0013125(2)/0.00175(1)	285388
4.375	0.00040625(1)/0.0008125(1)/0.00121875(2)/0.001625(1)	330170
4.5	0.000375(1)/0.00075(1),0.001125(2)/0.0015(1)	387934
5	0.00025(1)/0.0005(1)/0.00075(2)/0.001(1)	868788

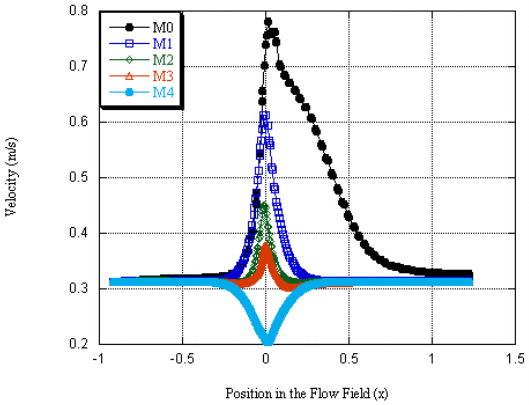

(a) Meshes 0,1,2,3,4

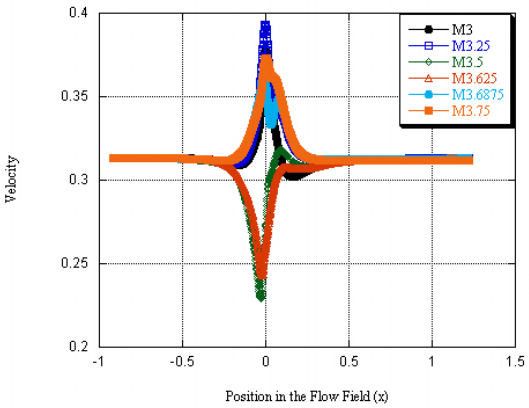

(b) Mesh Refinement 3,3.25,3.5,3.625,3.6875,3.75

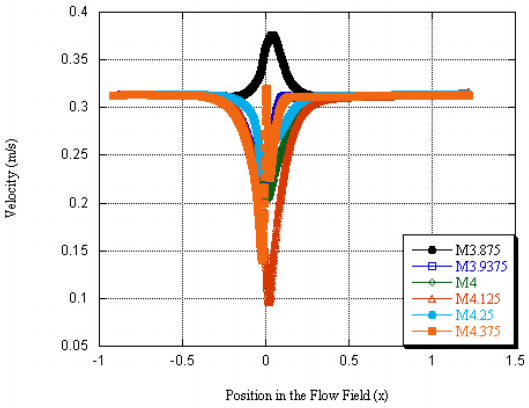

(c) Mesh Refinement 3.875, 3.9375, 4, 4.125, 4.25, 4.375

Figure 15: Mid-line Velocity Comparison.

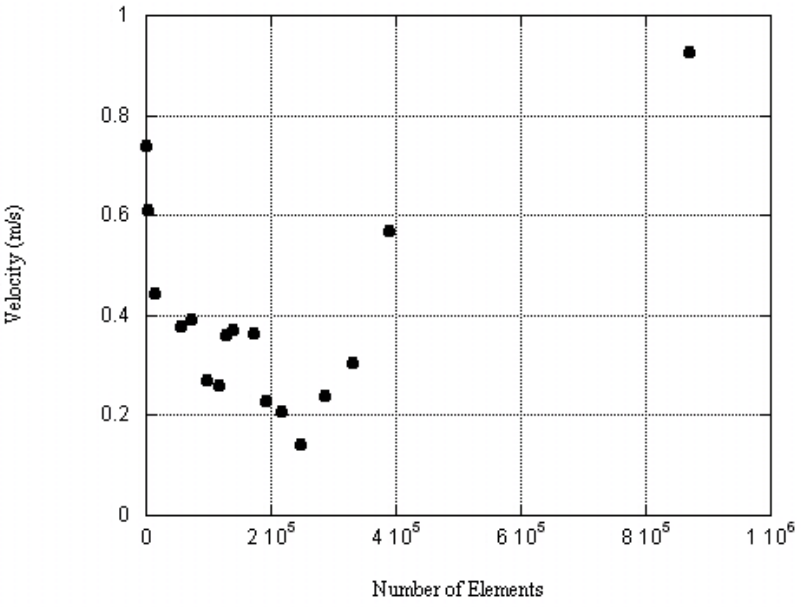

Figure 16: Mid-point Velocity in m/s for Varying Meshing Intervals.

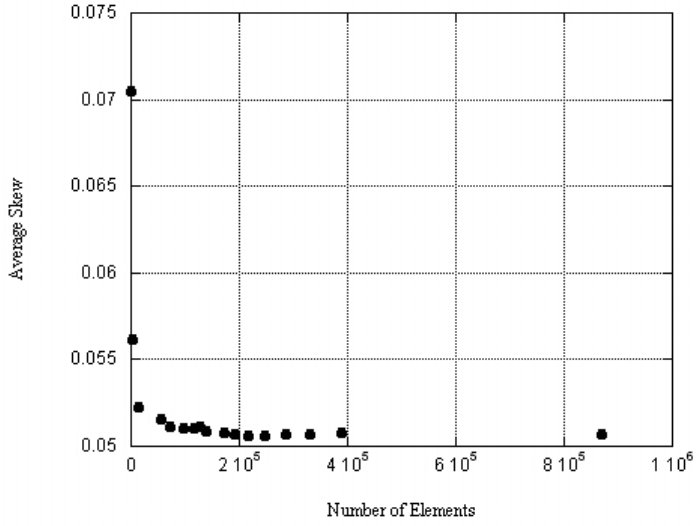

(a) All Meshes

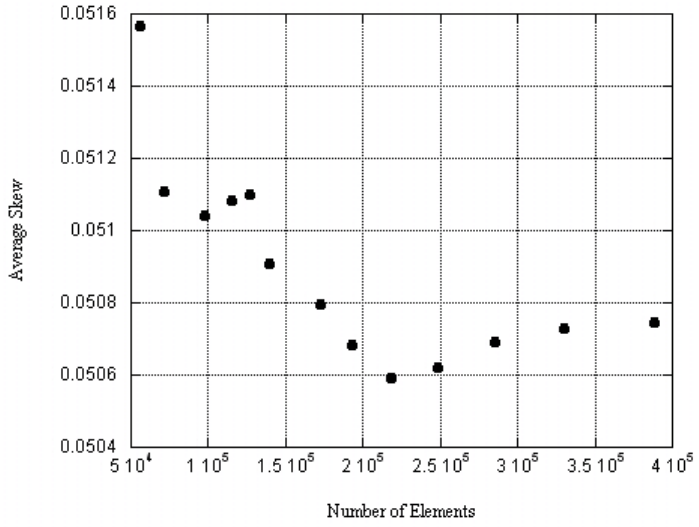

(b) Average Skew Detail

Figure 17: Average Mesh Skew.

compared mid-point velocities, and having the lowest skew. The full results of this mesh were shown in Figures 11 and 12 and then used to develop velocity profiles around the turbine, as discussed below.

3.4 TWO-DIMENSIONAL CFD RESULTS

Combining the system geometry and mesh with the governing equations in FLUENT^{TM}, a flow simulation of a two-dimensional submerged water wheel was created, as shown in Figure 18. This is a plot of velocity magnitude contours with the river flowing from left to right, and the turbine rotating in the clockwise direction. The ordinate is the velocity in m/s and the abscissa is the distance along a river bed in the downstream direction. The velocity profile, upstream of the turbine, is typical of open-channel flow. Peak velocities of $2-5\ m/s$ can be seen at locations near the turbine blades, where high velocity is a result of turbine rotation. Additionally, decreases in the velocity to a low of 0.15 m/s, can be seen after the turbine due to energy extraction in the stream.

The CFD model shows that the initial estimates of velocity decreases from the power extraction model (as discussed in Chapter 2) from the device were reasonable. The power extraction model and CFD model are not independent of one another, however the CFD model gives far more detail about the HEE device operation. In Section 2.3, the outlet velocity was estimated to be 0.179 m/s, which was based on idealized power extraction calculations and this CFD model. The idealized power extraction is influenced by the Betz limit set to the ideal amount of 0.59, giving an outlet velocity closer 0.12 m/s. However, this is not truly attainable because the turbine is reviewed as a complete system rather than a streamtube and published Betz limits for this turbine type are closer to 0.2. So, in constructing the power model, the CFD model was used to give an outlet velocity, while the power model was used to give the rotation velocity in the CFD model. The power models presented in Chapter 2 fall short in comparison to the CFD model in that the idealized power model assumes uniform pressure distribution and the first law uses bulk values where the CFD model gives a detailed flow map of the river in and around the HEE device.

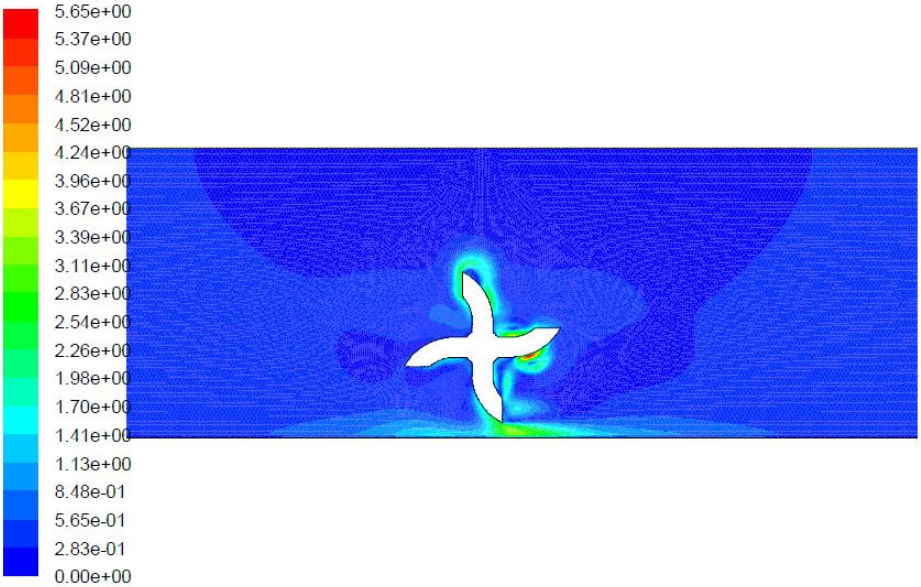

Figure 18: Velocity Magnitude in m/s.

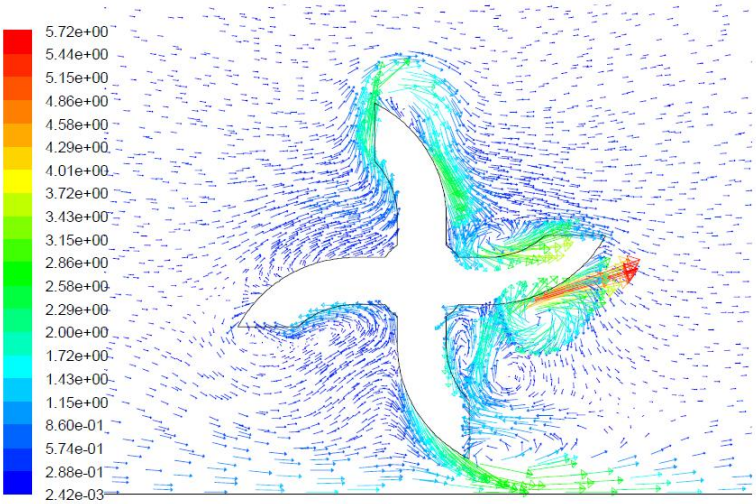

Figure 19: Velocity Magnitude in m/s.

Further details of river movement around this turbine are shown in Figure 19. Some circulatory flows and high velocity regions are seen as a result of the turbine rotation. For example, there is a clear region of circulation evident in the lower right quadrant around the turbine. Further analysis, including extension to the third dimension to study vorticity propagation, is required to quantify the potential impact this might have on fish and other marine organisms. According to Cotel et al. (32), brown trout prefer lower regions of turbulence. In Figure 19, it can be seen that higher turbulent regions form where circulation occurs, and further vorticity analysis can quantify these areas to give a range of turbulence. Additionally, shape changes and/or mooring mechanisms can be applied to remove some of the flow force directed at the bottom of the device as it opposes clockwise rotation.

The top surface river velocity is shown in Figure 20. In the mesh, the turbine is centered at (0,0) and it is shown that the top surface velocity decreases rapidly as the flow approaches the turbine. This is explained by the energy extraction from the turbine, which causes the decrease. The values plotted in this figure further verify the outlet velocity used in the power model.

Finally, Figure 21 shows the dynamic pressure contours for the flow field with the HEE turbine in operation. A pressure increase is present from the velocity increase due to turbine rotation. There are peak pressures as high as $15,200$ to $16,000$ Pa, while the majority of the field is 0.436 Pa.

3.5 SUMMARY

The main outcomes from the work presented in this chapter are:

- A two-dimensional CFD model was constructed to represent a hydrokinetic turbine.
- The CFD model is based on governing equations for a river: continuity and the Navier-Stokes equations, which contain a fluctuating velocity term that is accounted for with the renormalized group $k-\epsilon$ model.
- The flow field with hydrokinetic turbine geometry and mesh were created, and boundary conditions were assigned.

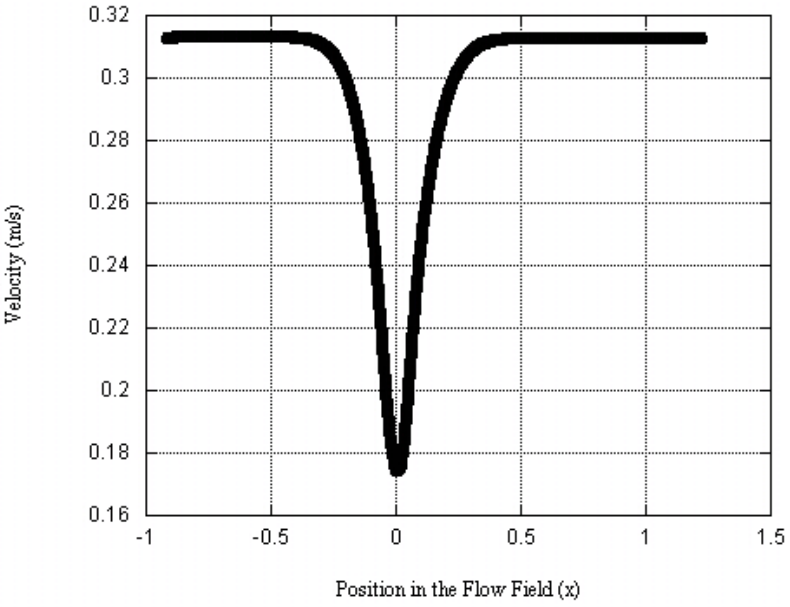

Figure 20: Top Surface River Velocity in m/s.

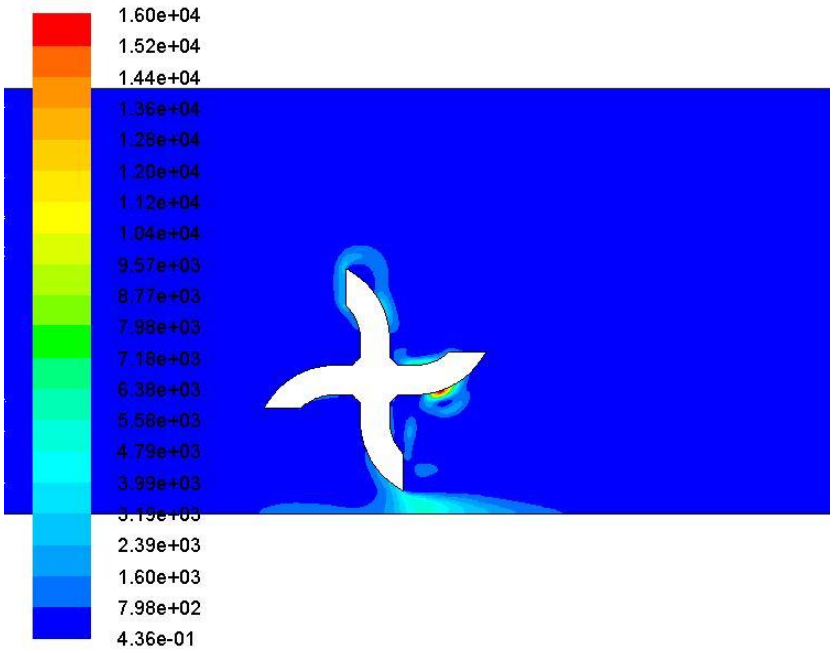

Figure 21: Dynamic Pressure Contours in Pascal.

- A mesh sensitivity analysis was performed to ensure accurate flow field representation, and an appropriate mesh for the flow field was utilized.
- Finally, two-dimensional CFD model results were presented.

4.0 EXPERIMENTAL SET-UP AND PROCEDURE

In order to provide CFD model validation, an experimental set-up was constructed. Careful consideration was given to similarity between the CFD model and experimental set-up.

4.1 EXPERIMENTAL SET-UP

The experimental set-up consists of a recirculating flume and particle image velocimetry (PIV) system. The flume (shown in Figure 22), constructed out of 0.0127 meter (0.5") clear acrylic, was fitted with dual reservoirs at either end of a 2 meter (79") testing channel, and equipped with a fine copper mesh at the input to the channel. A complete drawing package for flume construction is in Appendix A, and Appendix B contains the flume construction procedure. The copper mesh was put in place to facilitate a fully developed flow around the turbine while achieving appropriate flow rates by reducing the randomness of pathlines introduced in the open flow channel. Use of the flume without the copper mesh resulted in an underdeveloped flow which did not simulate the appropriate testing conditions required in this study. The output of the channel was attached to the output reservoir via an acrylic flange sealed with a rubber gasket in order to allow disassembly and reconfiguration of the channel output, as indicated in Figures 23a and 23b. Both ends of the entire flume structure were connected to a one horsepower, electrically driven, centrifugal, cast iron impeller pump. Pump specifications are in Appendix C. Steel axles were also constructed on which the different turbines are put in place using Delrin bushings and steel washers to mitigate frictional forces. The horizontal testing mount is shown in Figure 24a, with a water wheel attached. The squirrel cage and Gorlov turbines are vertically oriented, and were fitted on

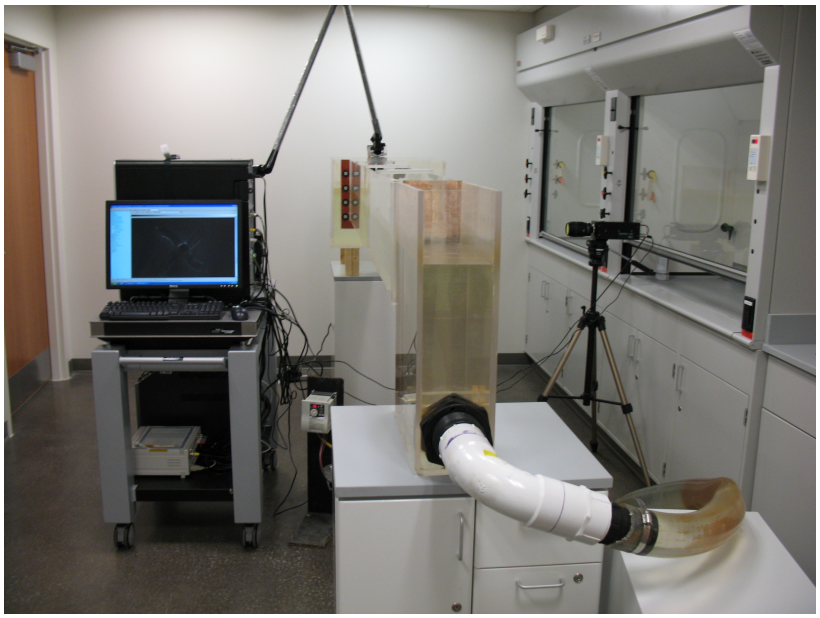

Figure 22: Experimental Set-up

a similar axle. However, the vertical axle required an aluminum mounting frame in order to rest in the testing flume channel, as shown in Figure 24b. Detailed schematics and drawings for both test mounts are in Appendix D. The flume, which holds approximately 55 gallons of tap water, was filled so that the channel contained approximately 0.15 meter (6") of water to represent the same conditions used in the CFD model.

Directly adjacent to the flume channel was an elevated laser table equipped with the necessary testing equipment. This setup (shown in Figure 25) contained the New Wave Research Solo III-15Hz laser, as well as the accompanying New Wave Research liquid refrigerator for the laser (bottom left of Figure 25), TSI LaserPulse Light Arm, TSI LaserPulse synchronizer (bottom right of Figure 25), and the computer system, housing the appropriate data capture and analysis software, Insight 3G^{TM}. This was all secured on a mobile ThorLab laser table for mobility and adequate stability. In order to achieve appropriate illumination of the plane of interest, a small laser arm mounting device was constructed out of acrylic, fastened to the third horizontal support slat of the flume channel, and raised to the appropriate angle, as shown in Figure 24a. The laser emitter was visually set so that the most intense light

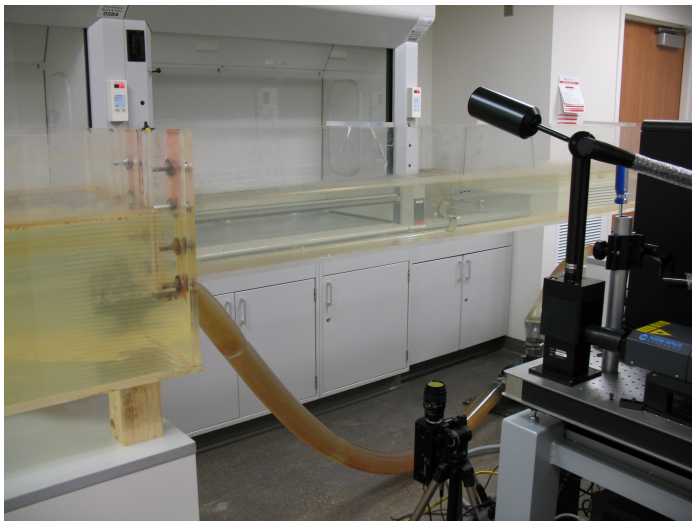

(a) Flume Flange Rear View

(b) Flume Flange Front View

Figure 23: Flume Flange Detail.

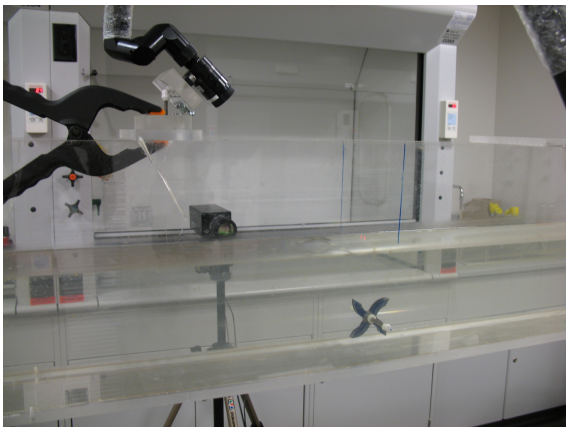

(a) Horizontal Test Mount

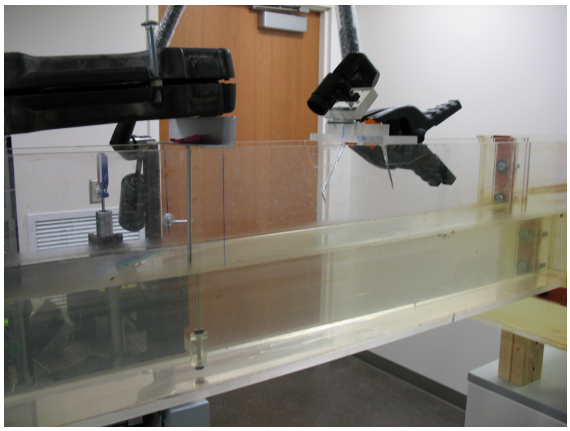

(b) Vertical Test Mount

Figure 24: Turbine Testing Mounts.

from the sheet was positioned in the middle of the plane of interest, propagating from a 25° a 45° angle. The horizontal plane was established by mounting the laser arm on a camera tripod via a 1/4" - 20 bolt and directing it to the appropriate plane. This is best shown in Figure 23a, where the laser is mounted on an arm attached to the mobile laser table rather than a tripod for that particular measurement. Finally, the TSI Powerview 1.4 MP Camera with a 532mm filter was positioned on a similar tripod and oriented so that its field of view was perpendicular to the laser sheet in order to capture the velocity profiles, which is also shown in the respective figures.

4.2 PIV DATA COLLECTION

In order to insure data accuracy, consistency, and upkeep of testing equipment, the procedure remained constant with each new scenario and turbine configuration. No seeding particles were introduced into the system, since tap water, which contains many small contaminants, was coarse enough to be read by the PIV system. Other open channel PIV measurements have been done in unseeded water such as this, corroborating these procedures (50; 51).

Figure 25: PIV System

Before testing began, the pump was disassembled and its volute, axle support, and impeller were sandblasted to remove all of the corroded surfaces which would impede pump operation as well as alter data collection due to particles in the flow. Also, all of the testing surfaces were thoroughly cleaned with glass solvent in order to not impede the camera's view as well as the laser beam. (See Appendix E for a complete list of flume cleaning instructions.)

The objective was to capture velocity profiles from several different planes on and around the different turbines, but with a focus on the submerged water wheel turbine for two-dimensional CFD comparison. The most elementary of these velocity profiles were taken at the vertical and horizontal cross sections of the turbines. Next, the vertical and horizontal planes on the top and on the side of the different turbine configurations were captured. Specifically, the outer planes that were tested differed in their respective coordinates by taking the distance between the edge of the turbine and the nearest wall of the flume perpendicular to the working surface and dividing that by the number of planes desired. The vertical plane space for the water wheel was ultimately divided into five planes (shown in

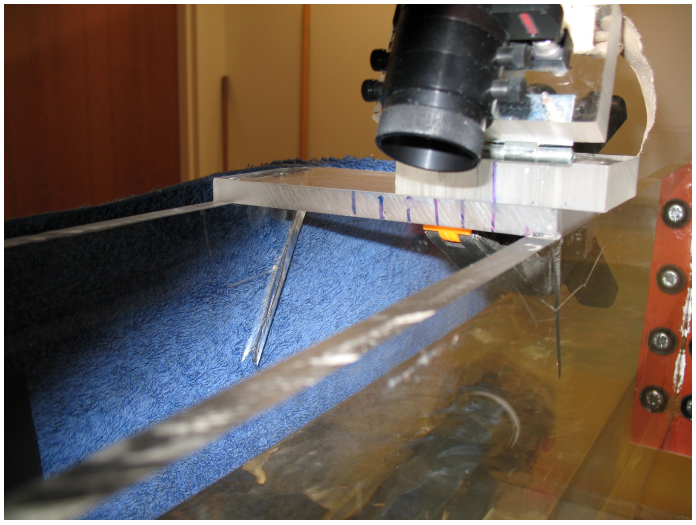

Figure 26: Vertical Plane Markings

Figure 26), while the horizontal plane space was divided into three planes. The fewer number of horizontal planes compared to vertical planes was due to the decreased amount of space. For the horizontal plane space, the measurements could only propagate from the bottom, and the turbine is significantly closer to the bottom than to the side of the flume. The third slat on the testing flume channel (shown in Figure 26), as well as the emitter mount, were marked accordingly so that accurate laser plane placement could be accomplished.

Each turbine was tested individually. Turbines were placed at 1.5 meters (59") down the length of the flume, and the test mount axis was positioned 0.047645 meter (1.875") from the flume bed, while the camera was positioned 1 meter (36") from the flume and 1.168 meter (46") high. Each of the turbines were placed with its designed orientation: the submerged water wheel and Savonius turbines were placed with horizontal axles, while the Gorlov and squirrel cage Darrieus turbines were placed with vertical axles. They were then oriented directly in the center of the flume channel.

The Insight 3G^{TM} software was then configured with the synchronizer, the laser apparatus, and the camera setup to capture velocity profiles. Darkening the testing room was necessary so as to mitigate stray ambient light, which despite the use of the filter on the

camera, would corrupt results. It was found later during data collection that use of flat black painted surfaces surrounding the data collection region would be necessary to reduce laser reflection from various surfaces in the lab. Figures 27a and 27b show laser reflection reduction set-ups for both the horizonal and vertical data collection schemes. Using the features presented in the Insight 3G^{TM} software, the laser was set to full intensity in order to penetrate all of the water and provide accurate results. Also, adjusting the laser to emit light at 532 nm in wavelength corresponded to the camera filter, which was necessary to pick up only reflections presented by the laser and not stray ambient light.

PIV images were created through capturing two frames of illuminated seed particles with the camera. Laser pulse timing was set based on expected vector images and vector quality. The expected vector images were taken from the two-dimensional results presented in Section 3.4. The PIV images based on that data are shown in Figure 28a and 28b. Laser pulse timing is the time between laser pulses and depends on the flow velocity in an experiment. For example, if the flow is fast, a smaller pulse time is desirable, and a larger pulse time is better for slower flows. This is due to the way that the velocity vectors are computed, and is discussed further in the next section.

Figure 28a shows the PIV image without vectors. The image shows illumination on a submerged water wheel turbine. The red circled area indicates where laser illumination was low and the blue circled areas show where the turbine is producing shadows in the PIV image, which reduces accuracy in those specified areas. Figure 28b shows the processed vectors provided from Insight 3G^{TM}. Off or large scale vectors indicate poor data quality. Some of these vectors occur to the upper right of the turbine, but the majority of the vector field shows a uniform velocity distribution prior to the turbine and some circulation directly after, both of which are expected from the CFD vector plots shown previously. The blue circled areas point to the circulation regions, which match well with the CFD vector plots.

There was variability in the flow rate based on how the experimental set-up was constructed, i.e. whether the tube from the pump to the beginning reservoir of the flume (shown in Figure 29) was bent and to what degree, so different velocity measurements for the open-flow channel (without any hydrokinetic turbine) with pump frequency inputs were made with the PIV system. This is shown in Figure 30. The pump was set to a frequency of 50Hz

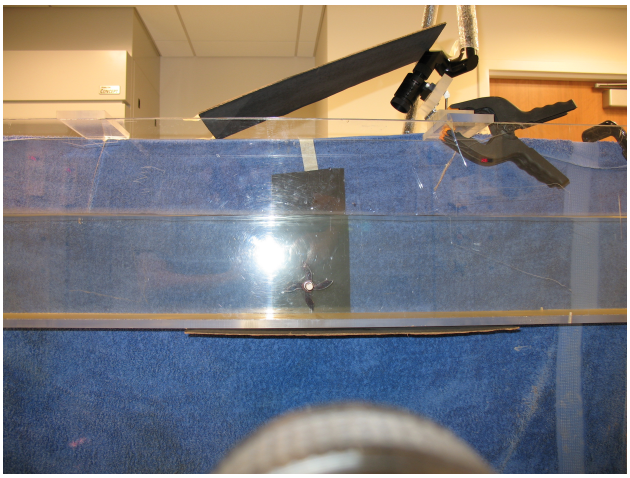

(a) Horizontal Laser Reflection Reduction

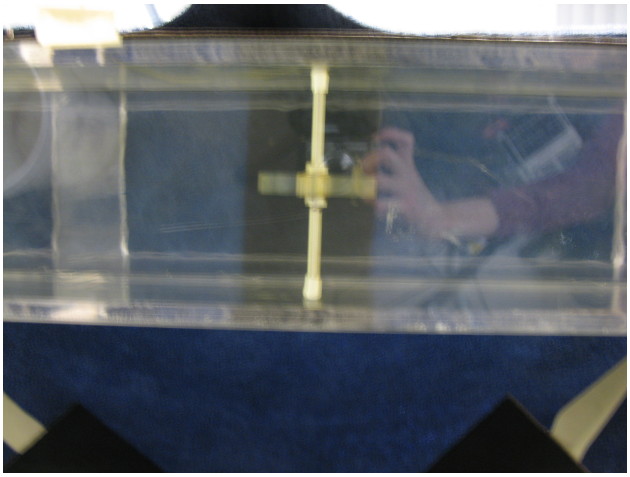

(b) Vertical Laser Reflection Reduction

Figure 27: Laser Reflection Reduction Set-ups.

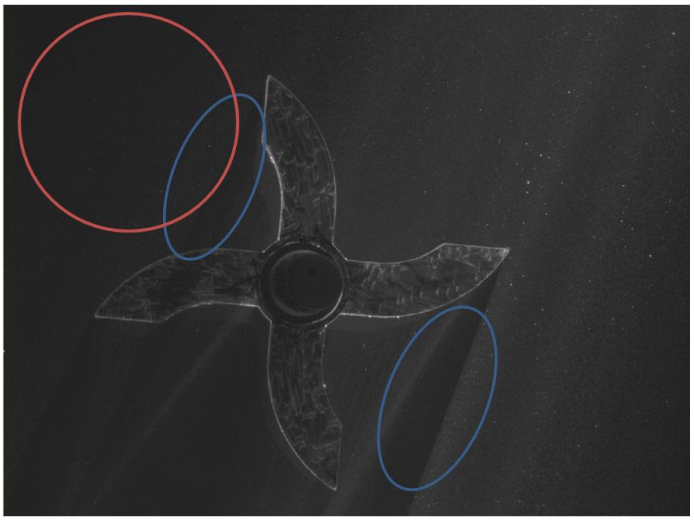

(a) PIV Calibration Image

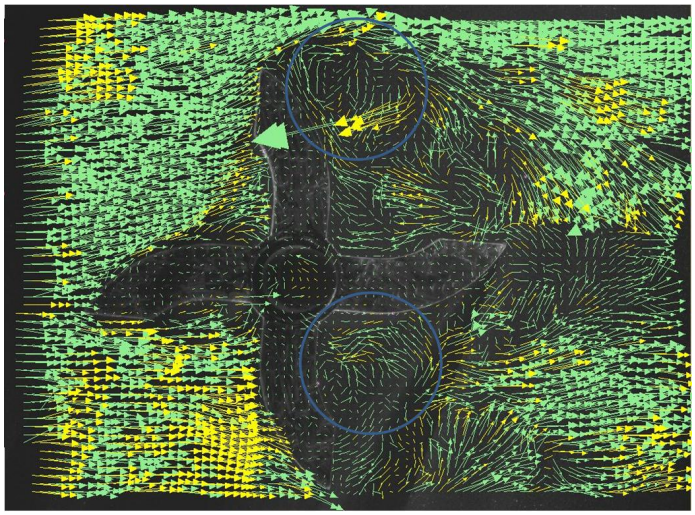

(b) PIV Calibration Image with Vectors

Figure 28: Laser Pulse Timing. The red circled area indicates where laser illumination was low and the blue circled areas show where the turbine is producing shadows in the PIV image.

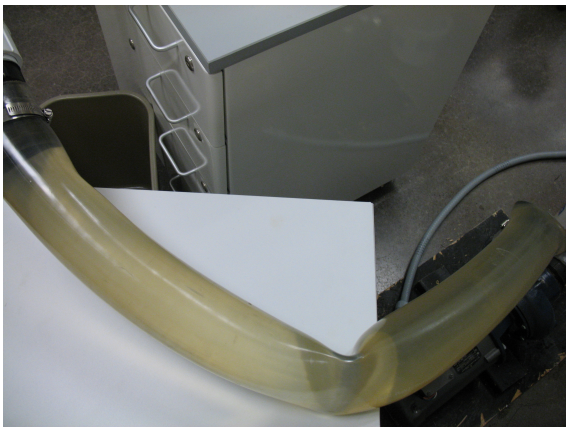

(a) Flume Tube Detail Entering the Flume Reservoir

(b) Flume Tube Detail Close to the Pump

Figure 29: Flume Tube Assembly.

for the final, accurate data collection since it gave the closest inlet velocity value to what was used in the CFD model. (Instructions for operating the flume are given in Appendix F.)

Finally, it was initially unclear how many images were necessary for accurate data. To determine the optimal amount of images a simple test was conducted. Series of 25, 50, 100, 200, 400, 800, and 1000 captures were averaged for a mid-line velocity of an open-flow vertical cross-section. These are plotted in Figure 31. From this plot, it can be seen visually that the data levels-out at around 400 capture images. To provide more detailed information, Table 4 gives an average velocity and standard deviation for each average image capture set. Further image capture amounts of 300, 500, 600, and 700 were averaged to complete the comparison. It can be seen that in testing, averaging 400 image captures is sufficient, because this gives the longest standing velocity average of 0.2966 m/s and a low standard deviation of 0.0012. To verify that the flume is fully developed and has the expected partial parabolic velocity profile shape, velocities were averaged laterally and are plotted in Figure 32. The pump and laser frequency, water level, and software capture settings remained constant throughout each of these tests.

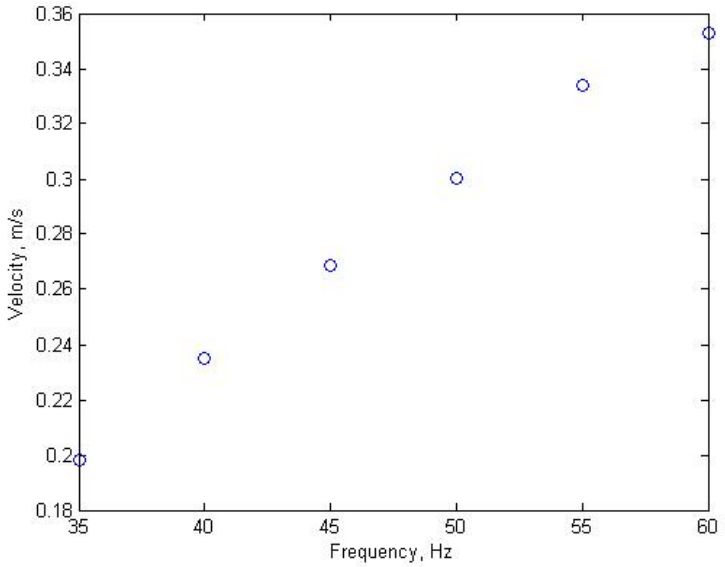

Figure 30: Flume Velocity Rating

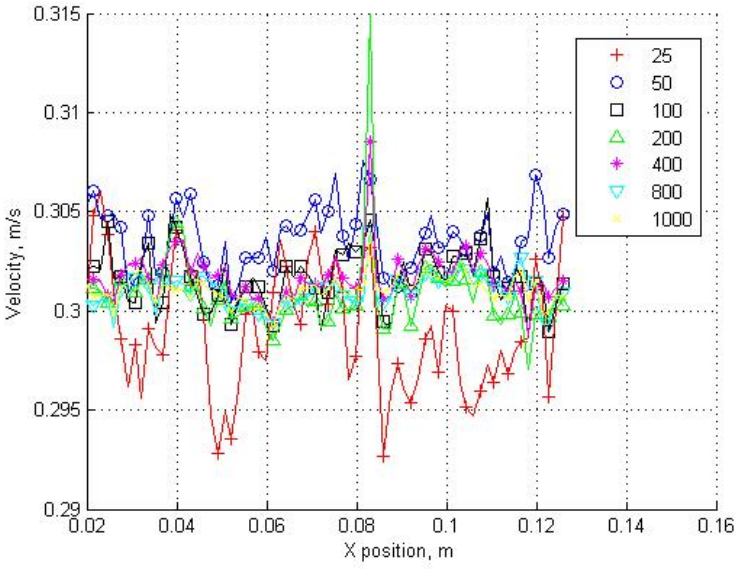

Figure 31: Capture Comparison

Table 4: Meshing Intervals and Ratios for a Sensitivity Analysis.

Captures	V-average (m/s)	Standard Deviation
25	0.2926	0.0062
50	0.2963	0.0037
100	0.2958	0.0021
200	0.2962	0.0014
300	0.2965	0.0014
400	0.2966	0.0012
500	0.2966	0.0013
600	0.2966	0.0012
700	0.2966	0.0013
800	0.2965	0.0013
1000	0.2963	0.0012

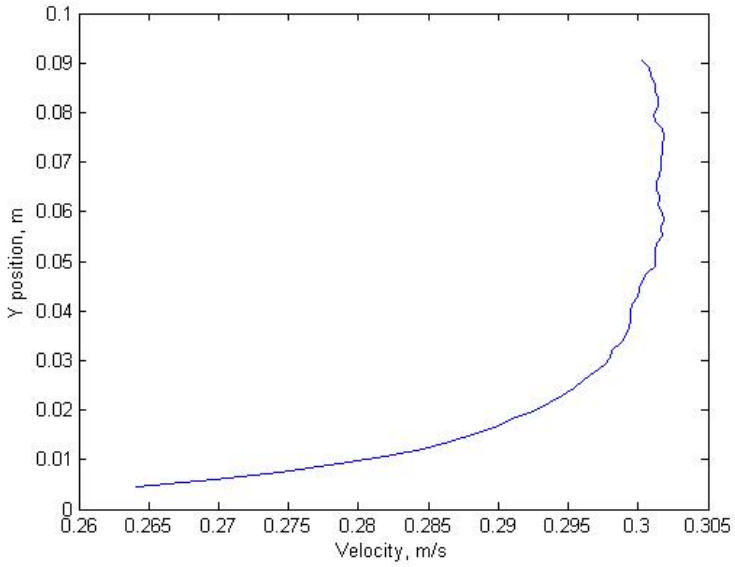

Figure 32: Open Channel Velocity Profile

4.3 IMAGE PROCESSING

In order to produce output data for the vectors of the various observed flow fields, the Insight 3G^{TM} software was used to process the vector images collected after every run. Several processing techniques were employed to determine velocity vectors, remove outliers produced from stray variables, and fill in voids left by others. The primary setting in vector acquisition is the use of the fast fourier transformation (FFT) correlation algorithm, which establishes a correlation between a particular particle in the flow and its neighbors, comparing its movement to all surrounding particles, and thereby determining the most likely path taken. This is accomplished through an interrogation region shown in Figure 33 (52). Because many of the particles look the same, it is increasingly difficult to track them from frame to frame. The entire frame is broken up into a grid of interrogation regions, which contains a group of particles that are fairly unique. Since δx and δy are tracked with the change in interrogation from the first to the second period, and the δt is known, FFT is used to determine particle velocities. As just explained, the PIV system uses a Lagrangian approach to solving the full

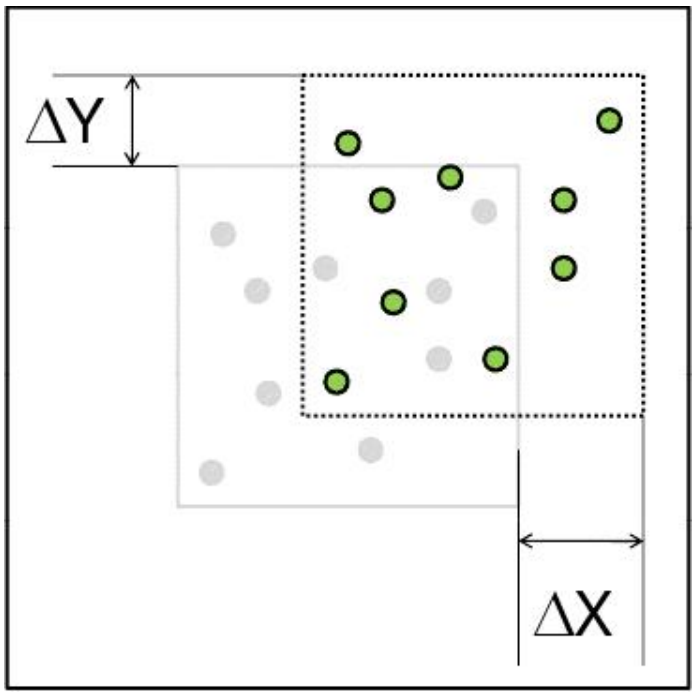

Figure 33: PIV Image Interrogation Region and Displacement Between Frames.

flow field as opposed to the CFD model. The recursive filling technique was used in the processing procedure as well. This fills holes in the data, starting with those with the most valid neighbors. Moving throughout the entire image, it uses the generated vectors to fill in all of the holes initially present. This yields a more complete image for use in later processing and comparisons with the CFD output. During post processing, local vector validation was used. This algorithm analyzes the individual data points and compares them with a mean calculated from the surrounding vectors. If the vector in question is beyond a certain range derived from the calculated mean, then it is discarded. The user gives a tolerance based on model or physical predictions to further define this. For this experiment the default was used, which is set to $dU = 2$.

To complete the post processing, vector conditioning was utilized. Like the recursive filling technique, this fills in holes in the vector field; however, it uses interpolation or local statistics to do so. It performs flow field smoothing or low-pass filtering with a Gaussian convolution kernel. This gives the final full flow field for analysis. Without this step, the flow

field is left with zeroes and extremely high velocity vectors where the image was not fully illuminated, making flow field analysis more complex. These vectors were then exported as both image files with the overlaid vectors, as well as data files with the raw information regarding the vectors' x, y, and total velocities. Completing these image processing steps prepares the PIV data to be compared with the CFD model, covered in the next chapter.

4.4 SUMMARY

The main outcomes from the work presented in this chapter are:

- An experimental recirculating test flume was created to closely resemble the CFD model.
- A PIV system was used to collect velocity data to compare with the CFD model.
- Data collection techniques and tuning of the experiment were included.
- Image processing necessary to produce PIV data sets was discussed.

5.0 CFD MODEL COMPARISON TO PIV DATA

5.1 PARAMETERS FOR COMPARISON

It is important to note that since consistent turbine rotation was not achievable in the flume, each turbine was held stationary in the experiments. The CFD models were then reevaluated without turbine rotation for comparison. This entire chapter involves comparison of a non-rotating CFD model to the non-rotating PIV data. Figure 34 shows how the velocity vectors from the CFD model would differ due to non-rotation in comparison with the rotating CFD velocity vector plot (Figure 19). Once data was collected from the PIV testing apparatus, several methods were used to procure visual representations of the data for ease of analysis. The CFD model was compared to the PIV results using the velocity from both. Velocity was chosen as the main comparative parameter both because of its widespread use in evaluating hydro energy applications, and because of the use of turbulence and vorticity in estimating disruptions to the natural habitat of aquatic flora and fauna. Figure 35a shows the first PIV image for the water wheel from a side cross-section view and Figure 35b shows the same image with velocity vectors after the image had been processed in Insight 3G^{TM}. Initial plotting of the vector fields yielded slight variations between the velocity profiles. To this end, a further analysis was conducted, requiring knowledge of individual velocity vector magnitudes.

After the images were processed, raw vector data had to be sorted in a MatLab program. The base program is included in Appendix G for the open flow analysis and the water wheel comparison. From the open-flow channel analysis, 400 images were required for accurate data. Knowing this allowed the water wheel data to be run as an ensemble in Insight 3G^{TM}, resulting in a single data set, rather than averaging all 400 images in the created exterior

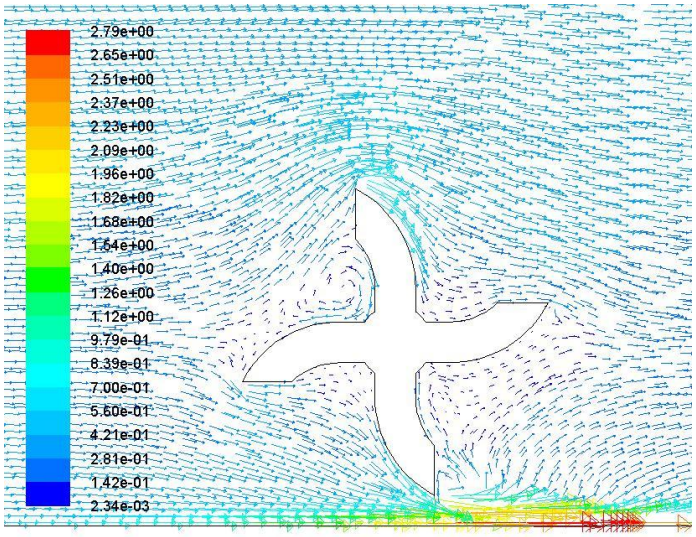

Figure 34: CFD Model Velocity Magnitude in m/s Without Turbine Rotation.

open flow MatLab program given in the appendix. Both PIV data and CFD model velocity pathlines at y=0.0383m above the turbine are plotted in Figure 36. The flume is flowing from left to right, as in the 2-D CFD model. There are many velocity magnitude increases and decreases in both the PIV data and CFD model close to x=0, where the turbine is located. The PIV data does, however, align well with the CFD model before and after the turbine. The CFD model is compared with the PIV data with the contour plots shown in Figure 37. Here velocity magnitude contour plots are shown in m/s. Figure 37b is similar to Figure 19 given in Chapter 3, except that the turbine is not rotating in this plot. Velocity decreases are shown around the turbine with a velocity increase above the turbine due to the lack of rotation.

For further PIV data comparison, the following sets were taken of the water wheel side cross-section: higher illumination, above the turbine, and the turbine wake. Higher illumination refers to the laser giving higher brightness on the turbine due to the adjusted laser angle to the turbine location. Taking data above the turbine and in the turbine wake extends the data collection images, since that is limited to the camera capture frame. These are shown in Figure 38. The data were compared as before, with velocity magnitudes at y=0.0383m, as

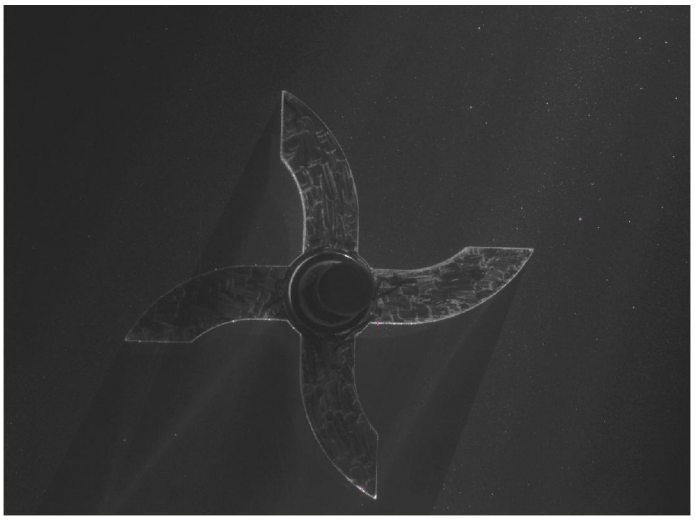

(a) Water Wheel Side Cross-Section PIV Image

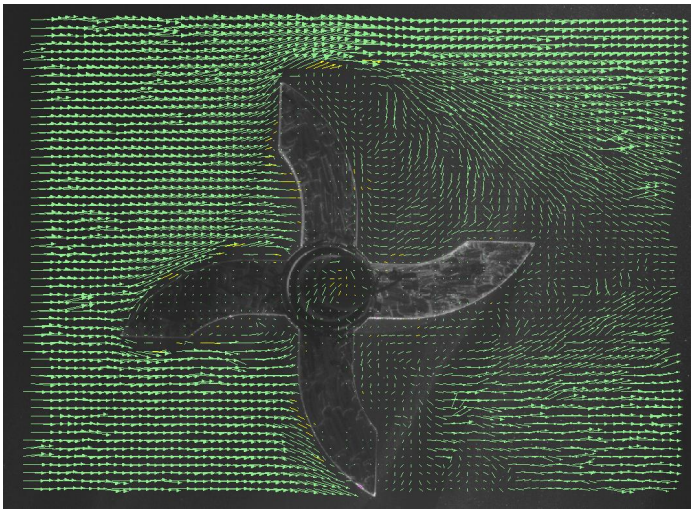

(b) Water Wheel Side Cross-Section PIV Image with Vectors

Figure 35: Water Wheel Side Cross-Section PIV Image (Data Set 1).

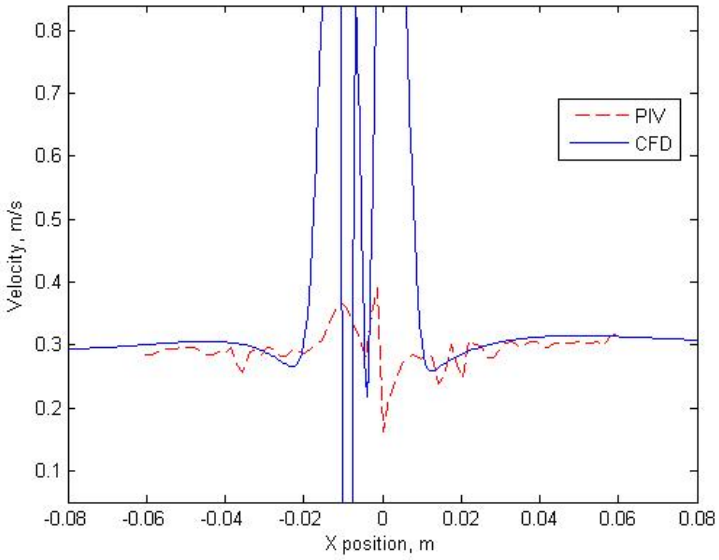

Figure 36: Velocity y=0.0383m Above the Water Wheel Turbine Center.

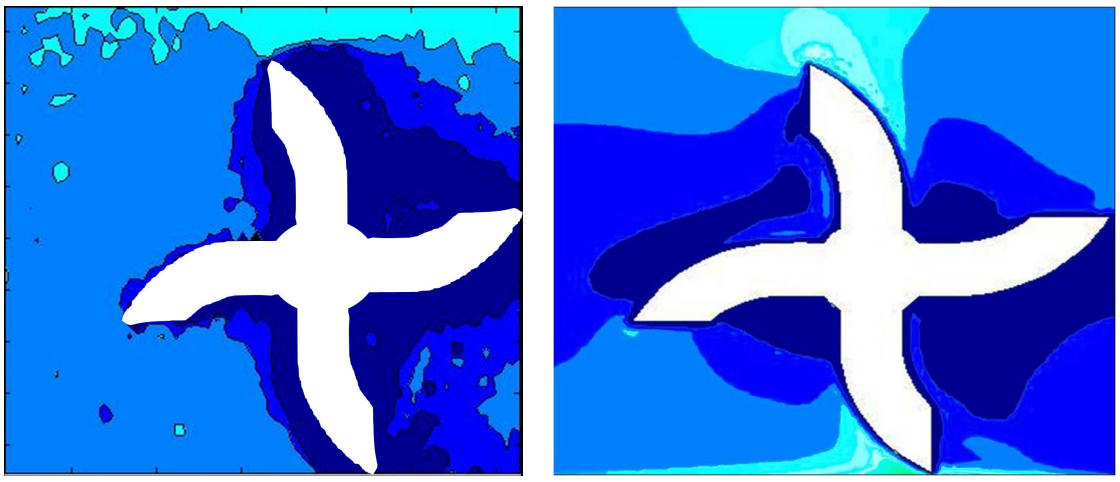

(a) PIV Data Results

(b) CFD Model Results

Figure 37: Velocity Magnitude Contours in m/s.

shown in Figure 39. From these, it can be seen that the PIV data are similar to the first PIV data set, with many velocity magnitude increases and decreases close to the turbine (x=0), and good alignment before and after the turbine. In data sets 2 and 3, the turbine is in a similar location and both data sets give more data points before the turbine and have similar data trends throughout the velocity plot, even close to the turbine. Data set 4 focuses on the turbine wake, and therefore gives more data points after the turbine.

Comparing velocities at a higher location above the turbine gave more information regarding CFD model alignment with the PIV data. In Figure 40, CFD1 and PIV1 are pathlines at y=0.0539m above the water wheel turbine center, and CFD2 and PIV2 are at y=0.0560m above the water wheel turbine center. PIV1 and PIV2 are similar in magnitude and trend, with both containing a velocity increase slightly after the turbine at x=0. The velocity increase is expected since the turbine is not rotating. This creates a decrease in cross-sectional area, causing the velocity to increase according to continuity. CFD1 and CFD2 do not align with the PIV data in this plot, and show a velocity increase (which, again is an expected trend since the turbine is no longer rotating in this model set for comparison to the PIV data) closer to the front of the turbine coupled with a subsequent velocity decrease. Referring back to Figure 39, similar differences can be seen in the area close to the turbine, or close to x=0. There are a few reasons why this occurs. Reviewing Figures 38d and 38f, it can be seen that the circulation regions are further away from the turbine than in the CFD model (Figure 34). This could be due to the wall function in use within the CFD model, use of an incorrect turbulence model in the CFD model, mesh construction around the turbine (i.e. because there is mesh invariance above the turbine, shown in Figure 12, and it is possibly causing an extreme velocity increase at that location), comparing the data to a 2D model instead of a 3D model, or lack of a volume of fluid (VOF) model within the CFD model. The VOF model allows the use of more than one fluid in the model. With the use of this model, the mesh is extended beyond the river surface in the y-direction to allow for an air region, leaving an interaction surface between the air and water at the river top surface. This allows boundary movement, which would be present in nature.

Before investigating the possible model discrepancies, velocity pathlines for both the PIV data and CFD model are plotted in Figure 41. Figure 41a shows all of the pathlines with the

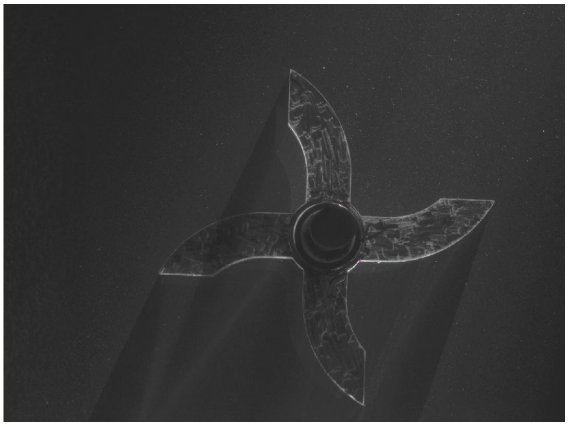

(a) Higher Illumination (Data Set 2)

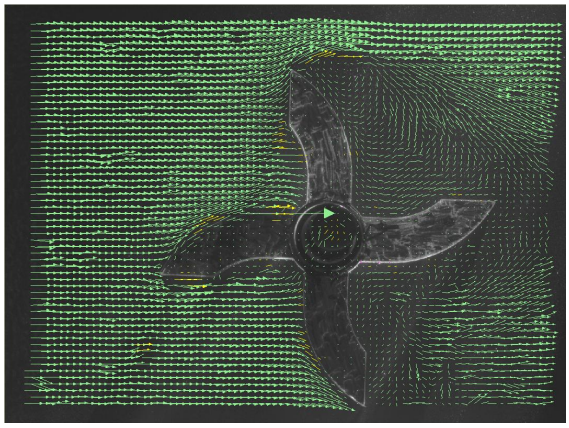

(b) Higher Illumination with Vectors (Data Set 2)

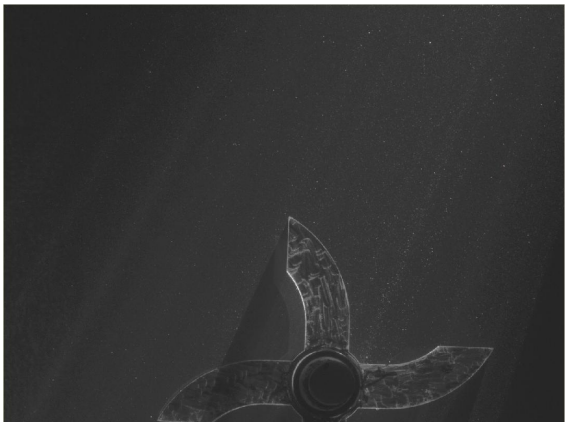

(c) Above Turbine (Data Set 3)

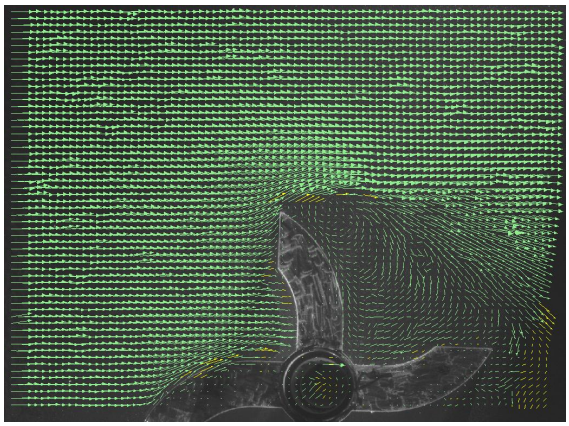

(d) Above Turbine with Vectors (Data Set 3)

(e) Turbine Wake (Data Set 4)

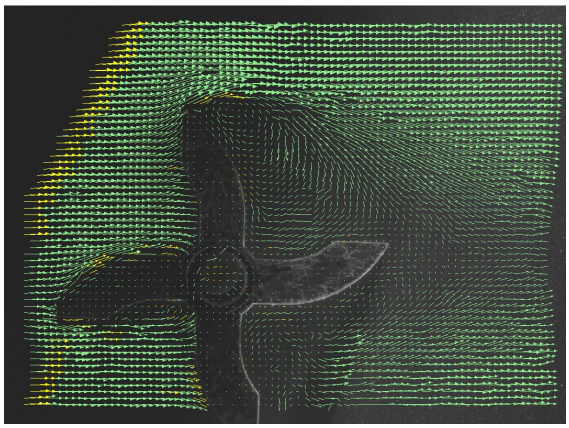

(f) Turbine Wake with Vectors (Data Set 4)

Figure 38: Water Wheel Side Cross-Section Views: 2-4.

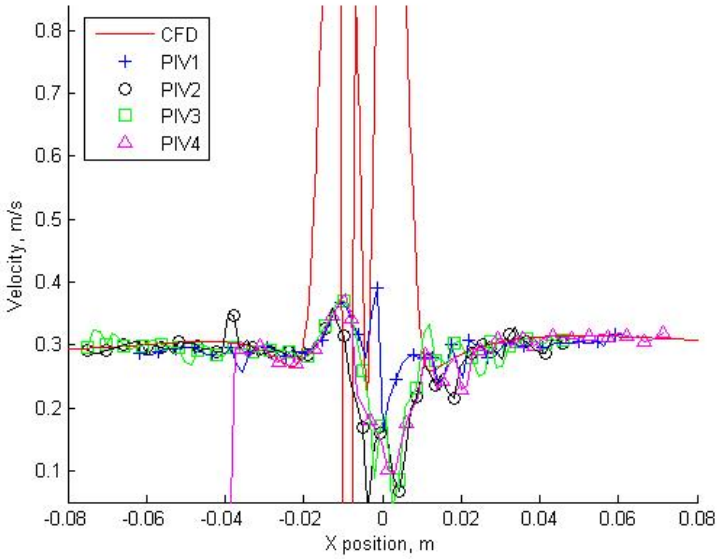

Figure 39: Velocity at y=0.0383m Above the Water Wheel Turbine Center.

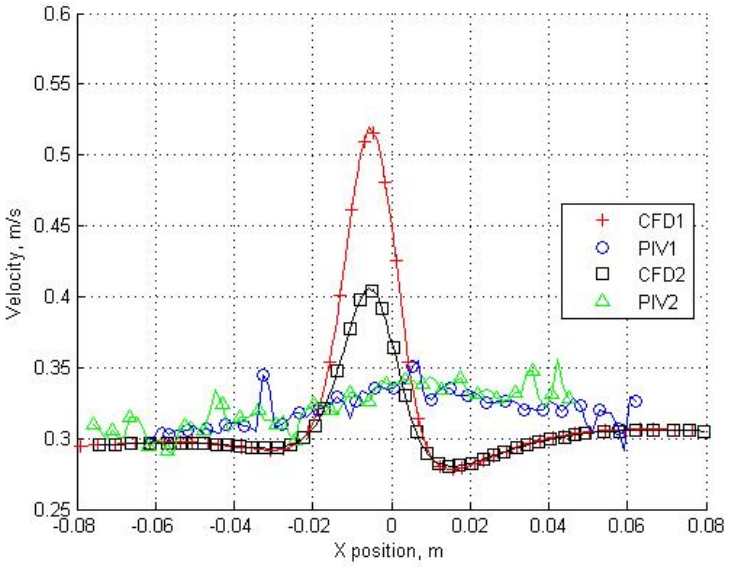

Figure 40: Velocity at y=0.0539m and y=0.0560m Above the Water Wheel Turbine Center.

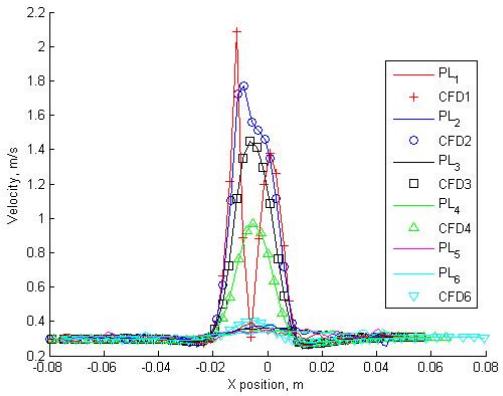

(a) PIV Data Comparison to CFD Model of Velocity Pathlines (PL).

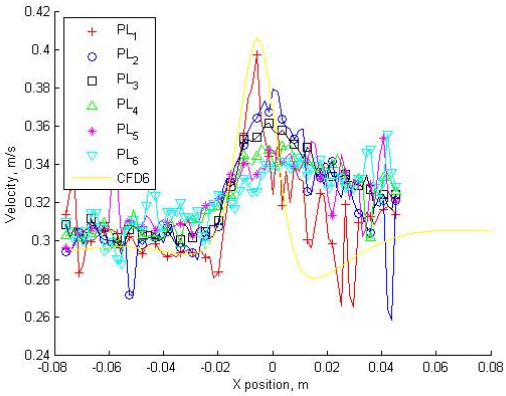

(b) PIV Data Comparison to CFD Model of Velocity Pathlines (PL), Detailed View.

Figure 41: PIV Data Comparison to CFD Model of Velocity Pathlines.

number designation in the name referring to the distance above the turbine: 1 is y=0.0405m, 2 is y=0.0436m, 3 is y=0.0467m, 4 is y=0.0498m, 5 is y=0.0529m, and 6 is y=0.0560m. From Figure 41a, the closer the CFD pathline is to the turbine, the more extreme the velocity increases and decreases become. Figure 41b shows CFD6, where the velocity increases and decreases become less drastic compared with the PIV data. Note that CFD6 aligns well with PL1 of the PIV data. This supports the earlier observation that the circulation region after the turbine is larger in the PIV data. Also, plotting 2D and 3D CFD velocity magnitude results at y=0.0560m gave well-aligned results, as shown in Figure 42. This verifies the validity of comparing the PIV data to 2D CFD, which is useful in this analysis, since the 3D models are much more cumbersome to compute due to their much larger meshes. After these initial analyses, the turbulence model, mesh construction, and VOF model are checked.

5.2 TURBULENCE MODEL CHECK

Through the comparison with the PIV data, it can be demonstrated that the RNG $k-\epsilon$ model (compared with other turbulence models within the CFD model) is indeed a valid

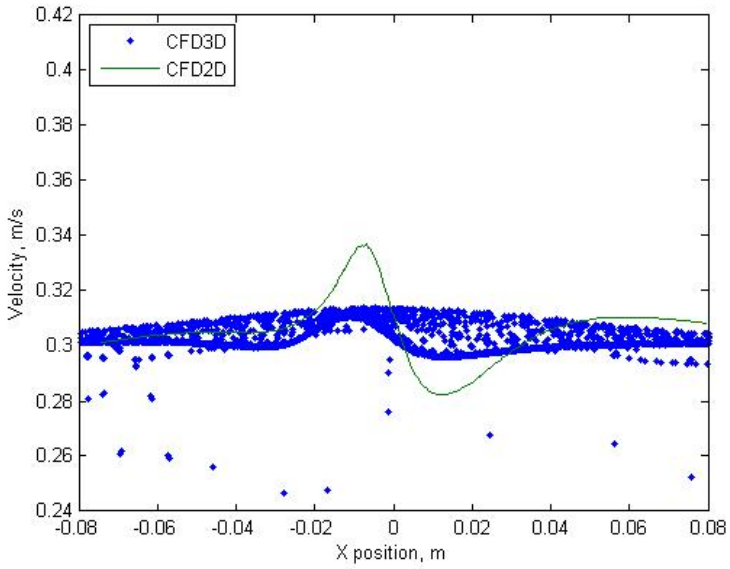

Figure 42: Comparing Velocity at y=0.0560m for 2D CFD Model and 3D CFD Model.

model for this scenario. Figure 43 shows the velocity plot at y=0.0560m for each of the turbulence models and the PIV data. In the figure legend, CFD is the RNG $k-\epsilon$ model, SKE is the standard $k-\epsilon$ model, and RKE is the realizable $k-\epsilon$ model. The realizable $k-\epsilon$ model contains improvements over the SKE in the form of a new turbulent viscosity formulation and a new equation for dissipation rate, ϵ, derived from an exact equation for the mean-square vorticity fluctuation transport (48). It is not advisable, however, to use this model with rotation because it includes mean rotation in the turbulence viscosity definition (48). RSM is the Reynolds stress model discussed in Chapter 3. SKW is the standard $k-\omega$ model, and SSTKW is the shear-stress transport $k-\omega$ model. The standard $k-\omega$ model incorporates modifications for low-Reynolds number effects, compressibility and shear flow spreading, and is based on the Wilcox formulation (48; 53). It is an empirical model based on model transport equations for the turbulence kinetic energy (k) and the specific dissipation rate (ω), which can also be related to the ratio of ω to k (48). The SSTKW model differs from the SKW model in that there is a gradual change from the standard $k-\omega$ model in the inner region of the boundary layer to a high-Reynolds-number version of the $k-\omega$

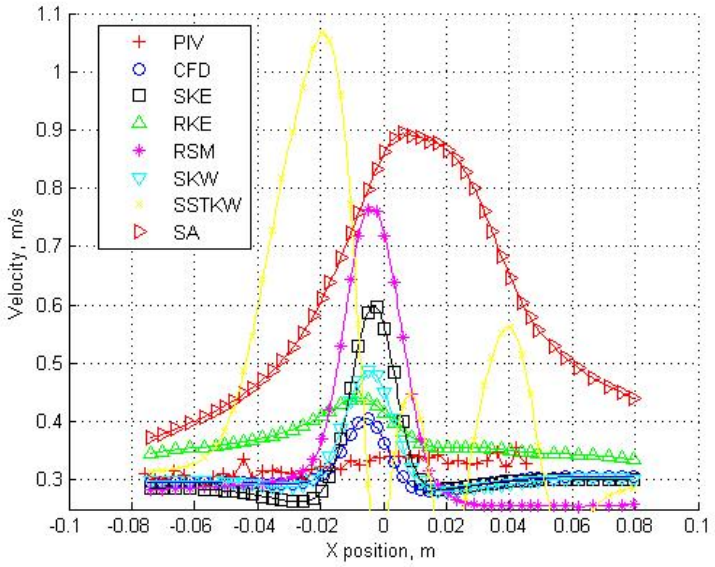

Figure 43: Comparison of Turbulence Model Use within the CFD Model of Velocity at y=0.0560m Above the Water Wheel Turbine Center.

model in the outer part of the boundary layer (48). Also, the SSTKW model modifies the turbulent viscosity formulation to account for the transport effects of the principal turbulent shear stress (48). Finally, SA is the Spalart-Allmaras model, which is a simple, one-equation model that solves a modeled transport equation for kinetic turbulent viscosity (48). It is typically used in aerospace applications where wall-bounded flows are present because of adverse pressure gradients in the near-wall turbulent viscosity (48). While it might not be appropriate to use many of these turbulence methods for modeling a hydrokinetic turbine in an open-channel flow, they are used as a point of comparison. Figure 43 shows that the RNG $k-\epsilon$ model has the closest alignment with the PIV data in terms of velocity magnitude. The RKE model is next with the SSTKW showing the most erratic behavior with much higher velocity gradients around the turbine and even long before and after it. From this plot, it is determined the turbulence model already used in the CFD model is the most valid.

5.3 MESH CONSTRUCTION CHECK

Next, consideration was given to the mesh construction. First, mesh construction, discussed in Chapter 3, was erased from the model, including nodal designations; however, schematic geometry, such as the turbine and flow field dimensions, remained. Three different meshes were constructed and the results are plotted with the PIV and original CFD model results in Figure 44. First, a uniform triangular mesh was constructed at a 0.001 nodal interval size and produced 718,858 elements. This mesh maintained the circular connection around the turbine to the flow field in the schematic geometry, and is denoted as U in the figure. Then the circular region from around the turbine in the schematic geometry was removed and a new uniform triangular mesh (Unr in the figure) was constructed at a 0.002 interval size and produced 182,423 elements. One last mesh modification was moving the attachment geometry of the turbine to the overall flow field to the right of the turbine to see if this had effect on the velocity magnitude peak location. This is called Unrr1 in the plot. Again, a uniform triangular mesh was constructed with a 0.002 interval size was used and this produced 181,459 elements in this mesh. When the velocity at y=0.0560m was plotted for mesh U and compared with the original CFD model, the magnitudes are close to those of the PIV data, as shown in Figure 44. However, this does not remedy the CFD misalignment with the PIV data velocity magnitude. Reviewing velocity at y=0.0560m for mesh Unr did not effect the location of the velocity magnitude peak in Figure 44. Finally, the variation in mesh Unnr1 had no effect on the velocity magnitude peak location when plotting velocity at y=0.0560m in Figure 44. Also the last two meshes produced significantly large velocities above the turbine; however, this is arguably because the mesh density was lower than the previous two meshes. This mesh construction study confirmed the discrepancy between the PIV data and CFD model was not due to the mesh construction presented earlier in this work.

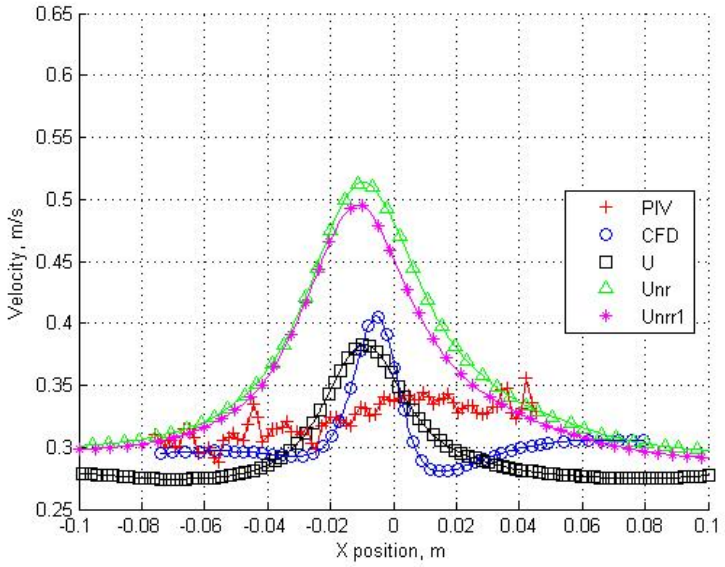

Figure 44: Mesh Construction Comparison of Velocity at y=0.0560m Above the Water Wheel Turbine Center.

5.4 WALL FUNCTION CHECK

Using the PIV data, the wall function in the CFD model was also checked and compared with 1. an enhanced wall function, which includes pressure gradient effects, and 2. a non-equilibrium wall function. These variations are plotted in Figure 45, and are called CFD-EnWallF and CFD-NEqWallF, respectively. The enhanced wall function is a two-layer model approach to distinguish between the viscosity affected region and the fully turbulent region. This is dependent on the distance from the wall and the Reynolds number quantity (48). It has limitations, however, with highly near-wall dense meshes. The non-equilibrium wall function approach also includes pressure gradient effects by using Launder and Spalding's log-law for mean velocity sensitized by these pressure gradient effects (48). In contrast to the near wall function, the two layer approach for this model utilizes turbulence kinetic energy in neighboring wall cells. From the figure, it can be seen that both the enhanced wall function

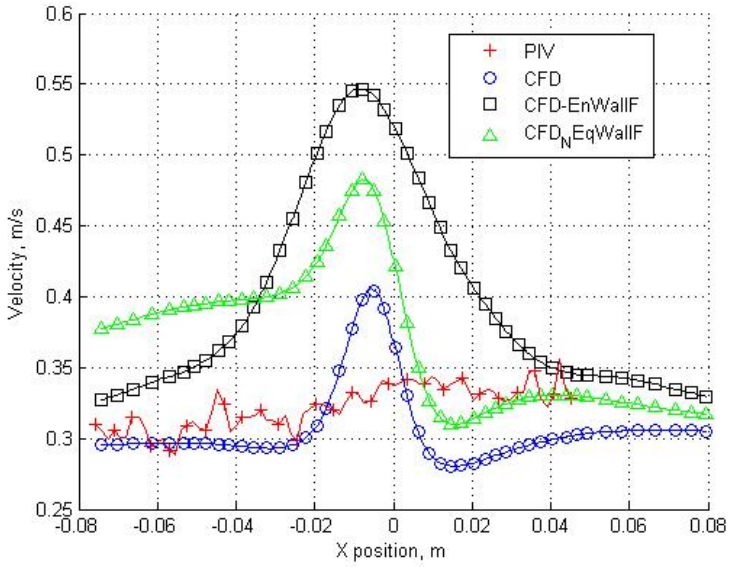

Figure 45: Wall Function Use in the CFD Model Comparison of Velocity at y=0.0560m Above the Water Wheel Turbine Center.

and the non-equilibrium wall function would not improve the model, and, in fact, result in much larger velocity gradients near the turbine.

5.5 VOF MODEL

Finally, use of the VOF model within the CFD model was investigated. In constructing this model, first-order discretization methods were used to calculate the solution. This was found to give a more accurate model and was checked with the initial CFD model. In Figure 46, CFD is the original CFD model, but recalculated using first-order discretization. It can be seen that this results in smaller velocity gradients near the turbine, which aligns better with PIV data. This is a result of the lack of detailed, accurate PIV data close to the turbine, and because any inaccuracies in the mesh are amplified when using higher order discretization methods. The VOF model does, however, produce a more accurate overall

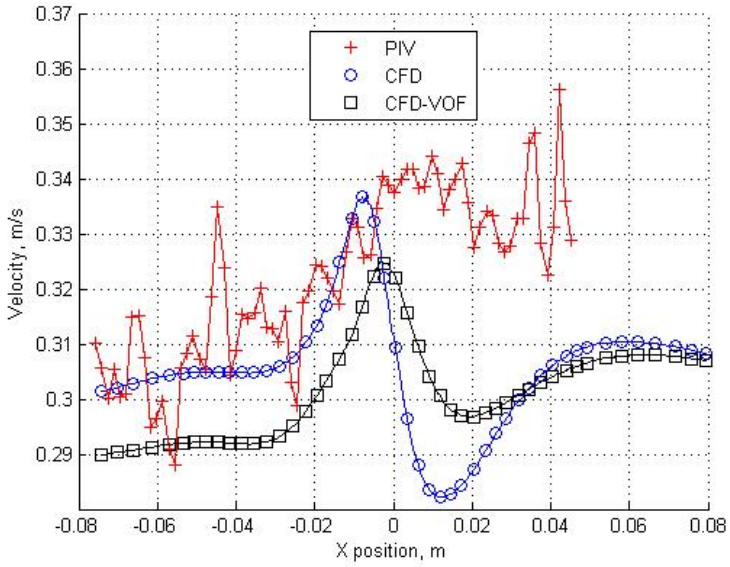

Figure 46: VOF Model Use in the CFD Model Comparison of Velocity at y=0.0560m Above the Water Wheel Turbine Center.

model when compared with the PIV data. An updated velocity pathline plot of the PIV data and the CFD-VOF model is plotted in Figure 47. Instead of CFD6 aligning with PIV1, CFD5 now aligns with PIV1, giving the model an offset in pathline alignment of 0.0124m for a 0.15m system. This offset in pathline alignment also can be seen in Figure 47, where the velocity pathlines from the PIV data can be seen to be offset in their alignment with the CFD model. These results are consistent with a comparison in literature where there was a 0.002m pathline offset in a 0.026m system (54).

The error can be calculated using Equation 5.1, where V_{CFD} is the velocity magnitude from the CFD model and V_{PIV} is the velocity magnitude from the PIV data:

$$\text{Error}, \% = \frac{V_{CFD} - V_{PIV}}{V_{CFD}} * 100\% \tag{5.1}$$

The resulting error plot is shown in Figure 48. As the plot indicates, the CFD-VOF model has a maximum 15% error when compared with the PIV data. The best error obtained with hydrokinetic CFD models is more than 15%, making this model a marked improvement over

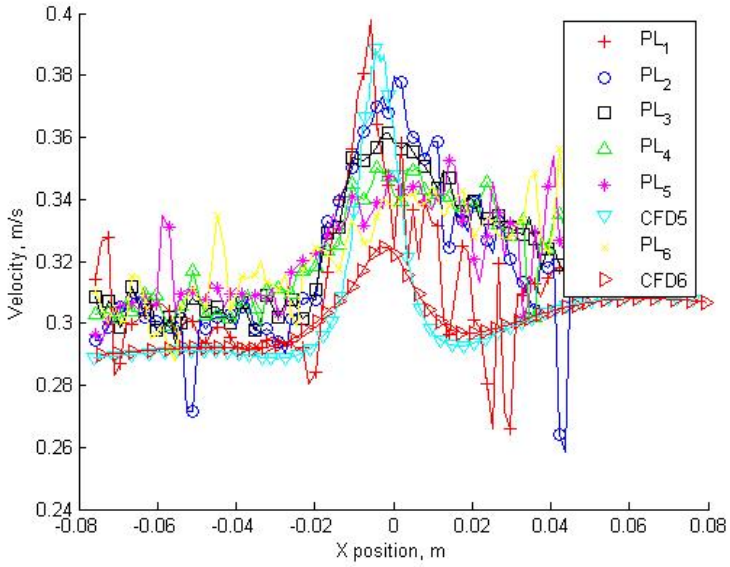

Figure 47: PIV Data Comparison to VOF, CFD Model of Velocity Pathlines.

the current hydrokinetic CFD models (51). When using the non-VOF CFD model, the error maximum is increased to 20%, which is well within other published model accuracy. This comparison of the CFD model to the PIV data is thorough, having a calculated offset, error plot, velocity plots, and visual assessment. Many of the CFD model/PIV data comparisons in literature provide visual comparison (51; 54–56), but few provide further analysis such as velocity plots (55), offset (54), and error(51).

5.6 VERTICAL PLANE COMPARISON

The CFD model was also checked with vertical PIV plane data. The plane designation was discussed in Chapter 4 and is shown in the Figure 26. The planes were spaced evenly for five planes in between the turbine edge and the inside flume edge, equating to 0.013m or 0.52" between each plane. The middle plane (plane 3) is shown in Figure 49. This shows a uniform field approaching the turbine with circulation located on the wake side of the support mount.

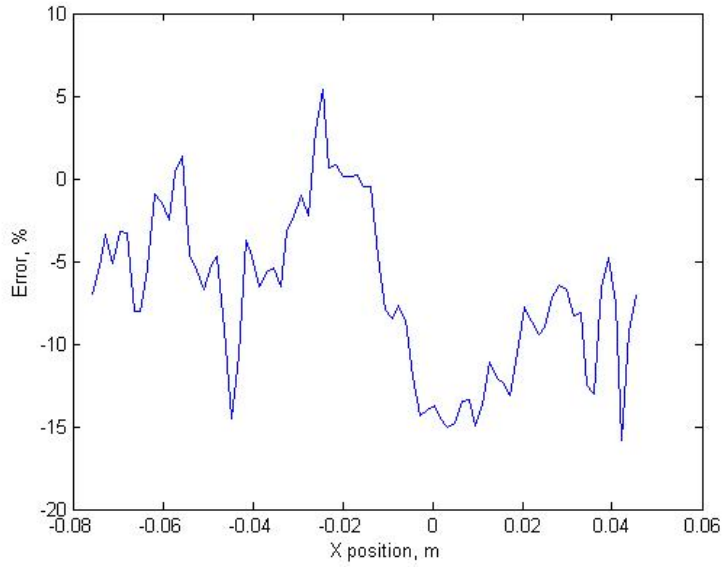

Figure 48: VOF, CFD Model Comparison to PIV Data Error.

PIV data were collected from each plane, and the velocity vectors were averaged, giving a single velocity value for each plane, as shown in Figure 50. The same process was conducted for the CFD model as well. Distance "z" represents the distance away from the turbine edge toward the inside flume edge. As expected, velocity decreases are present near the turbine and flume edges. These plotted values show similar trends; however, as was the case with the pathline comparison, the velocity decrease is much higher near the walls in the CFD model.

5.7 HORIZONTAL PLANE VISUAL COMPARISON

Horizontal PIV images were also captured to complete the experimental analysis of the submerged water wheel for validation of the corresponding CFD model. Figure 51 contains various images captured from this orientation view. Figures 51a-51c detail the horizontal cross-section of the turbine, where the laser sheet is centered at the turbine center. Figure 51a

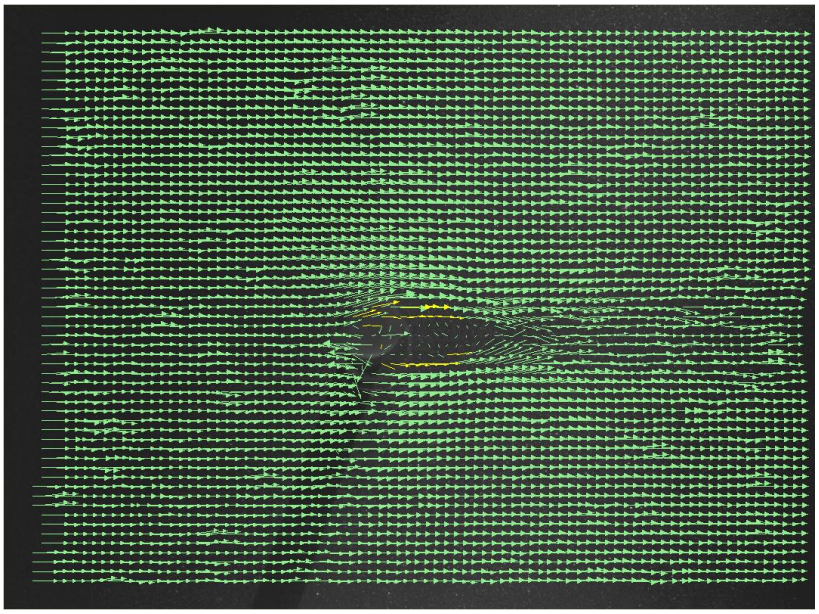

Figure 49: Water Wheel Vertical Cross-Section PIV Image with Vectors, Plane 3 From the Turbine Edge.

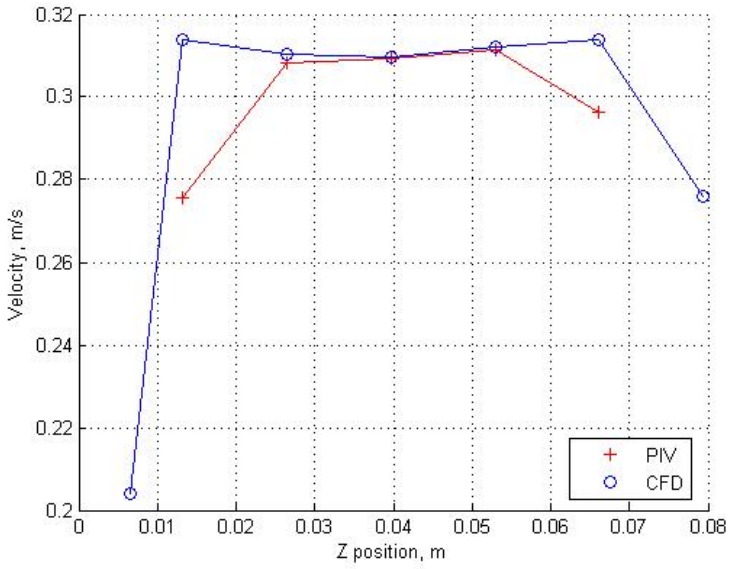

Figure 50: Average Plane Velocity Comparison of the CFD Model to PIV Data.

shows the flow moving toward the turbine leading edge, while Figure 51b shows the turbine wake, and Figure 51c is a centered view of the turbine within the centered horizontal plane. These vector images are compared with the horizontal velocity vector plot of the submerged water wheel 3D CFD model shown in the following chapter. There is agreement in overall vector direction and circulation close to the turbine when compared with the 3D CFD model. Figures 51d-51f illustrate the vector field as the position is moved down the turbine for three planes between the turbine center and flume inside bottom edge. The planes are spaced evenly at 0.012m (0.47"). The vector images show clockwise and counter-clockwise rotations on the top and bottom (according to the visual vector field orientation) wake regions, respectively. These are present in the centered view vector images and in the CFD model presented in the next chapter.

5.8 SUMMARY

The main outcomes from the work presented in this chapter are:

- The CFD model was compared with the PIV data results. The turbine is not rotating in the PIV results since steady rotation could not be established in the experiment. Therefore, the CFD model was recalculated without turbine rotation to be compared with the PIV data results.
- Discrepancies were found with the CFD model comparison to the PIV data results, so this was investigated further.
- Incorporating a VOF component in the CFD model improved alignment with the PIV results.
- The model accuracy when compared with the experimental results is a marked improvement among CFD-PIV comparisons for hydrokinetic turbines, and is well within CFD-PIV comparisons in general.

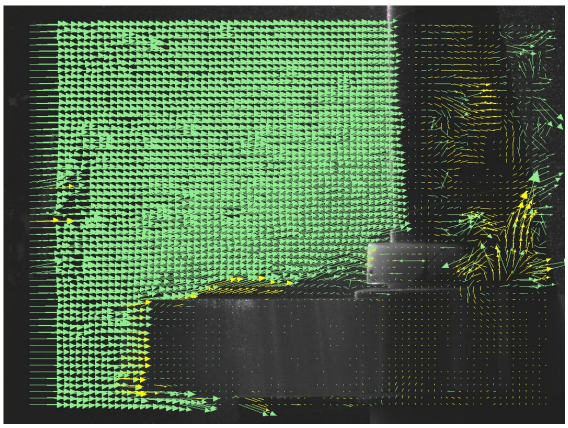

(a) Water Wheel Horizontal Cross-Section PIV Vectors, Turbine Leading Edge

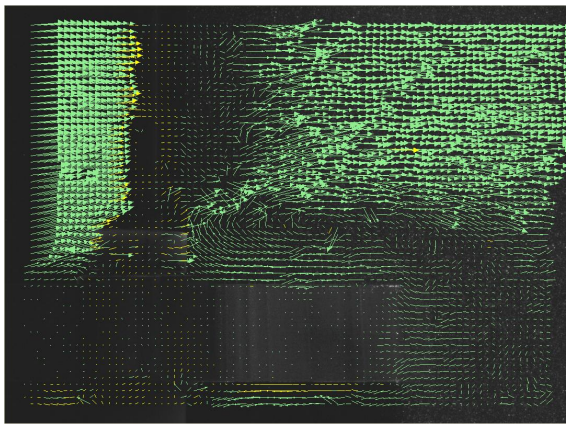

(b) Water Wheel Horizontal Cross-Section PIV Vectors, Turbine Wake

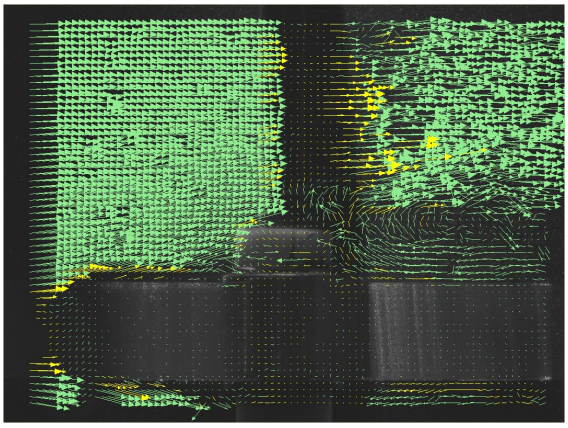

(c) Water Wheel Horizontal Cross-Section PIV Vectors, Plane 0

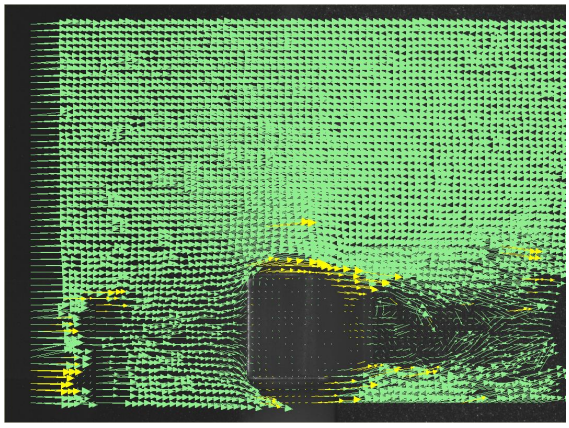

(d) Water Wheel Horizontal Cross-Section PIV Vectors, Plane 1

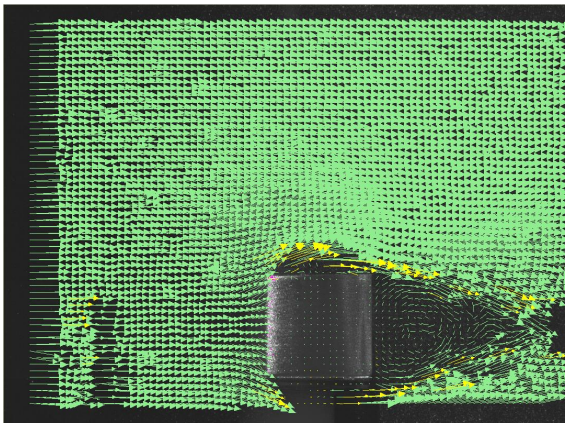

(e) Water Wheel Horizontal Cross-Section PIV Vectors, Plane 2

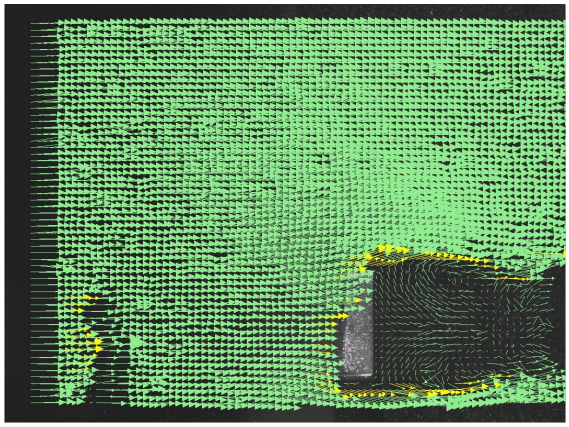

(f) Water Wheel Horizontal Cross-Section PIV Vectors, Plane 3

Figure 51: Water Wheel Horizontal Cross-Section PIV Vectors, Planes 0-3.

6.0 3D CFD MODELS

Once the two-dimensional (2D) submerged water wheel computational model was validated using theoretical performance predictions and PIV experimental data, work could begin on three-dimensional (3D) models. In this chapter, four HEE turbines, shown in Figure 52 (also shown in Appendix H for further dimensional detail), were computationally modeled in three dimensions with rotation. The rotation rates were based on the estimates provided from the power extraction models presented in Chapter 2.

First, 3D geometries and meshes were constructed based from the 2D schematic. For example, for a water wheel turbine, the 3D geometry and mesh are shown in Figure 53. Table 5 provides the mesh interval sizes with ratios according to line location. The surface to the right is the velocity inlet, while the surface to the left is the pressure outlet, the bottom surface is the river bed set as a wall, the surface to the back of the page is the river side (also set as a wall), while the surface to the front of the page is the river/turbine cross-section set as symmetry, and the top surface is the river top surface also set as symmetry. During construction of the geometry, the exact turbine CAD models used in constructing the experimental prototypes were used in the software to create and mesh the 3D schematic to be used in the CFD models (drawings of the turbine prototypes are in Appendix H). The basic constructs of the 2D CFD model were retained in generating the 3D model, in that the RNG $k-\epsilon$ model was used for turbulence with all default settings, and the geometry, meshing approach, and boundary conditions were the same. However, as stated in the previous chapter, first order discretization of the flow field produced results with higher accuracy, so the discretization was reduced to first order. While the CFD-VOF model also produced more accurate results, the 3D models remained non-VOF due to the high cost in

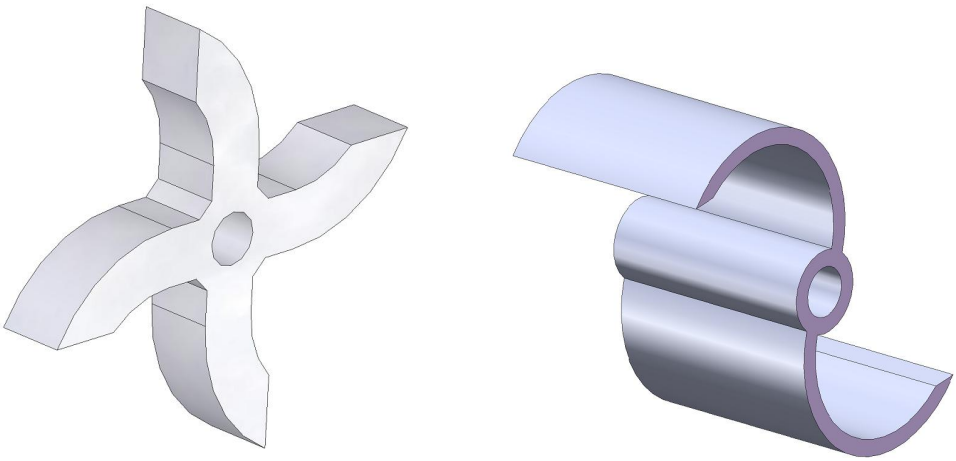

(a) Submerged Water Wheel

(b) Savonius

(c) Squirrel Cage Darrieus

(d) Gorlov (Helical) Darrieus

Figure 52: Hydrokinetic Energy Extraction Turbines for Three-Dimensional CFD Modeling.

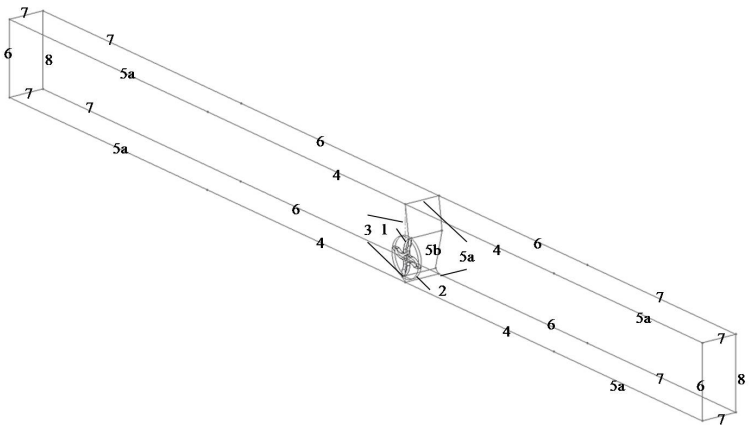

Figure 53: 3D Geometry and Meshing Schematic for a Submerged Water Wheel.

computation time. It was found the non-VOF model produced an additional 5% error to the 15% error reported in the previous chapter.

6.1 SUBMERGED WATER WHEEL TURBINE

A 2D, cross-sectional velocity magnitude contour plot for a 3D CFD model of a submerged water wheel is shown in Figure 54. This plot is similar to the 2D velocity magnitude plot presented in Chapter 3. The color variation corresponds to the velocity in m/s, and the flow is from left to right. Changes to the velocity field can be seen as a result of turbine rotation. The velocity vectors are clearly shown in Figure 55. In this plot, velocity rotation in addition to variation is shown from the turbine rotation. This is also similar to the 2D results shown in Chapter 3. It was demonstrated in Chapter 5 that plotting the velocity at y=0.0560m above the turbine produced well-aligned results between the 2D and 3D submerged water wheel models, as clearly shown in Figure 42. For further detail, Figure 56 shows a horizontal cross-section of the velocity vector plots at y=0, where the turbine center is located. The

Table 5: 3D Meshing Designations.

Line	Mesh Interval Sizes with Ratios in Parentheses
1	0.0005(1)
2	0.001(1)
3	0.0015(2)
4	0.002(1)
5	0.003(2) 0.0025(4)
6	0.004(1)
7	0.006(2)
8	0.008(1)

flow is moving from left to right in this plot, and there is velocity circulation before and after the turbine, as shown in the PIV images.

6.2 SAVONIUS TURBINE

Figure 57 shows a 2D cross-sectional velocity magnitude for a 3D CFD model of a Savonius turbine. Again, the color variation corresponds to velocity in m/s, and the flow is from left to right. This is consistent throughout each turbine plot shown in this section and the following sections. Changes to the velocity field can be seen as a result of turbine rotation. These are further highlighted in Figure 58, which shows the velocity vector plot for the 2D cross-section. In this plot, rotational and variational velocity vectors are shown from the turbine rotation. However, it should be noted that there are higher velocity gradients around the Savonius turbine compared with the submerged water wheel. This is due to the increased

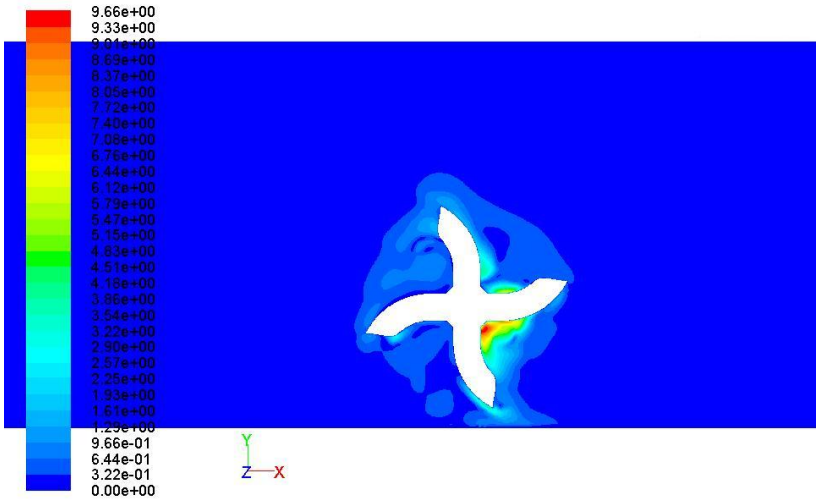

Figure 54: 2D Cross-Section Velocity Magnitude Contour Plot for a 3D Submerged Water Wheel CFD Model.

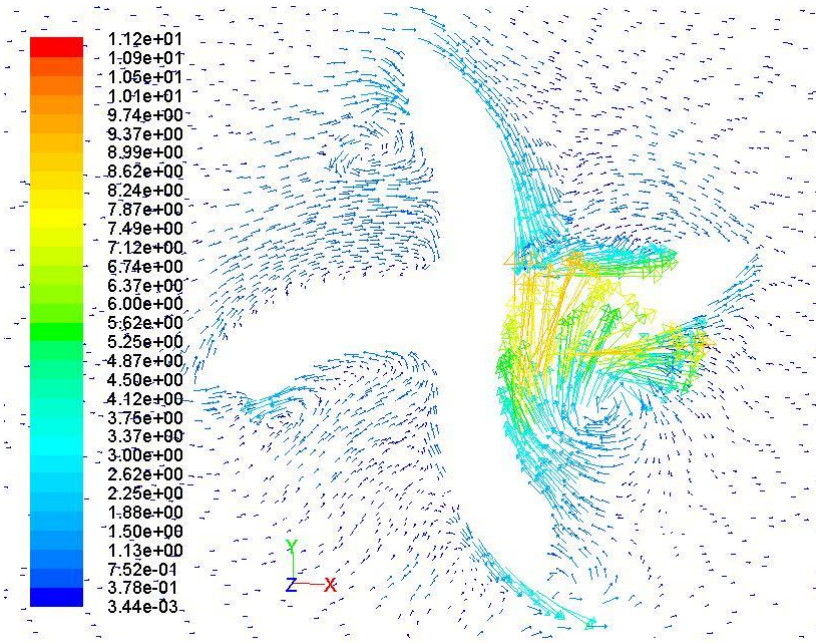

Figure 55: 2D Cross-Section Velocity Vector Plot for a 3D Submerged Water Wheel CFD Model.

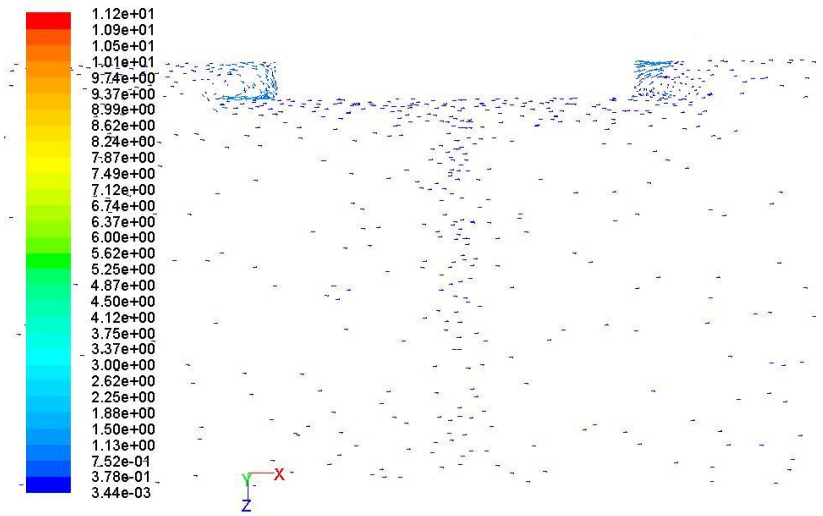

Figure 56: 2D Horizontal Cross-Section Velocity Vector Plot at y=0 for a 3D Submerged Water Wheel CFD Model.

surface area of contact between the turbine blades and the flow, which causes an increased rotation rate. The same effects can be seen in the horizontal plane in Figure 59, which shows large velocity gradients near the turbine when plotting a y=0.0560m plane above the turbine center. Figure 60 shows velocity vector plots for a horizontal cross-section at y=0, where the turbine center is located. The plot shows much larger velocity circulation before and after the turbine than that of the submerged water wheel.

6.3 SQUIRREL CAGE DARRIEUS TURBINE

The 2D cross-sectional velocity magnitude contour plot for a squirrel cage Darrieus turbine is shown in Figure 61. In contrast to the submerged water wheel and Savonius turbine, this plot is a horizontal view, as it is a vertical axis turbine. In the figure, the open-channel side wall is at the bottom, with the river inlet and outlet to the left and right, respectively. The top portion is the river vertical cross-section of symmetry. The detailed velocity variation

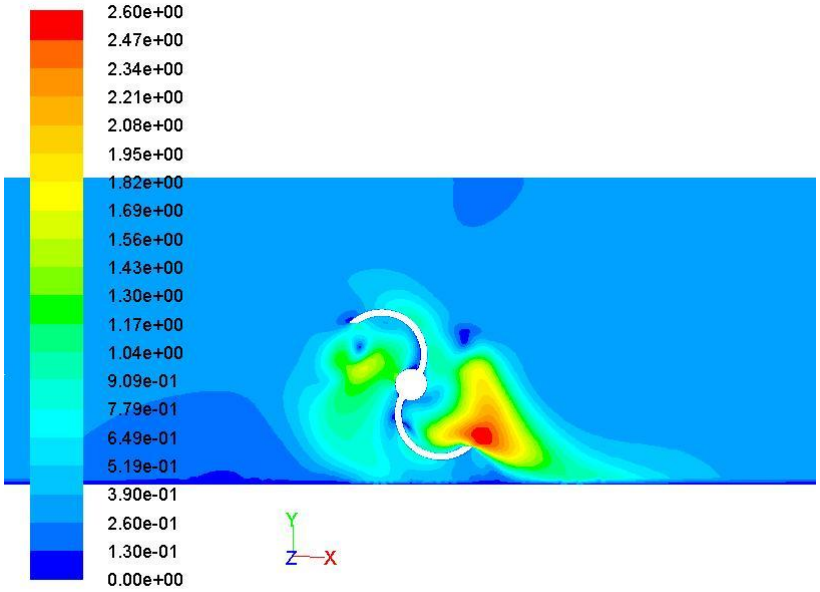

Figure 57: 2D Cross-Section Velocity Magnitude Contour Plot for a 3D Savonius Turbine CFD Model.

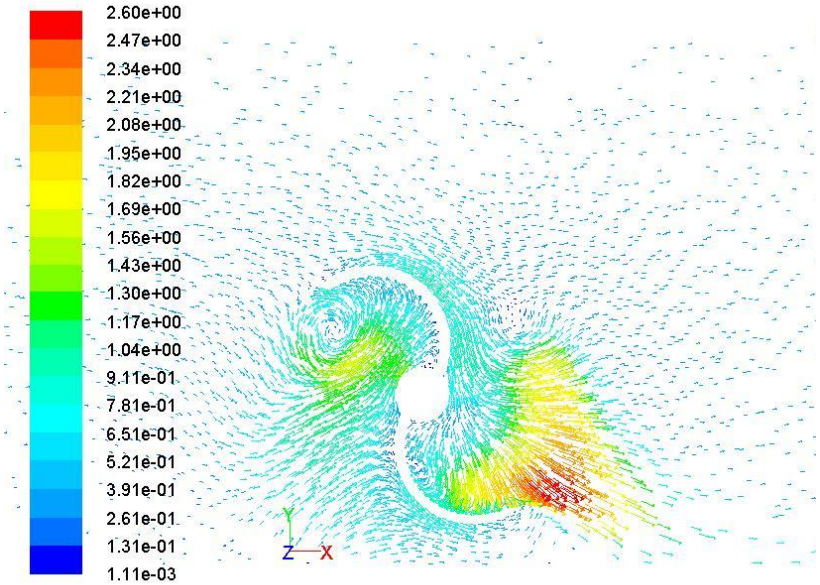

Figure 58: 2D Cross-Section Velocity Vector Plot for a 3D Savonius Turbine CFD Model.

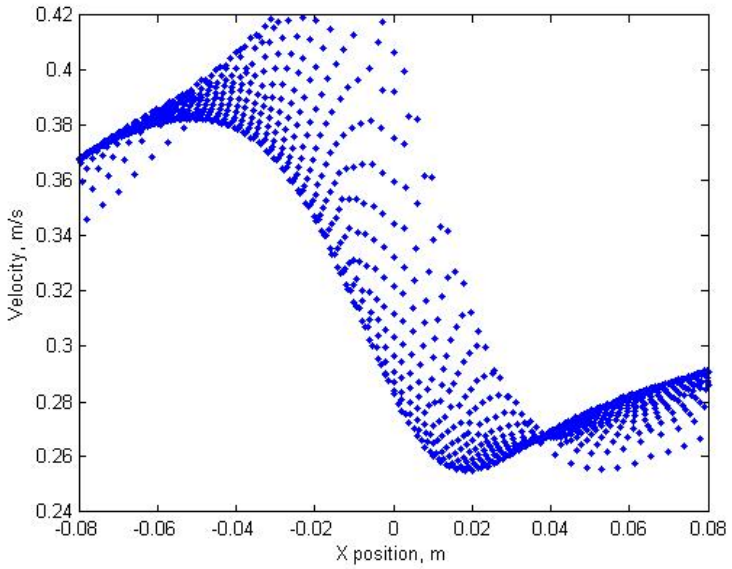

Figure 59: Velocity at y=0.0560m Horizontal Plane for a 3D Savonius Turbine CFD Model.

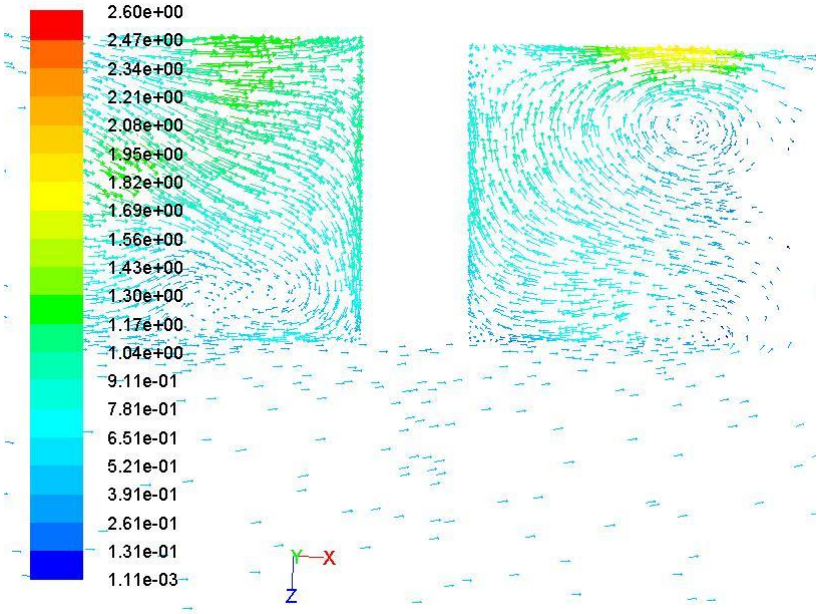

Figure 60: 2D Horizontal Cross-Section Velocity Vector Plot at y=0 for a 3D Savonius Turbine CFD Model.

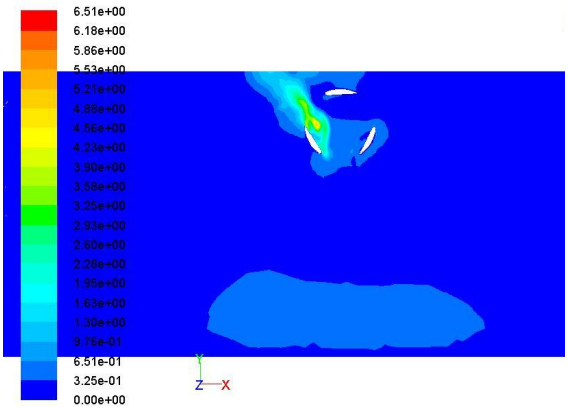

Figure 61: 2D Horizontal Cross-Section Velocity Magnitude Contour Plot for a 3D Squirrel Cage Darrieus Turbine CFD Model.

can be better seen in Figure 62, which shows the velocity vector plot for the 2D cross-section. The turbine is rotating counter-clockwise in this figure, and both the variation and rotation of the velocity vectors are shown as a result of the turbine rotation. From both figures, it can be observed that a higher velocity is present at the inside front of the turbine, and is then dissipated from the turbine's rotation. In plotting velocity for the same horizontal plane, at y=0.0560m (Figure 63), similar trends are present as that of the submerged water wheel. To complete the analysis of the squirrel cage Darrieus turbine, Figure 64 shows the velocity vector plot for the vertical cross-section of this turbine. This shows the flow circulating counter-clockwise toward the turbine top and clockwise toward the turbine bottom. The circulations are a result of the turbine geometry, orientation, and rotation.

6.4 GORLOV (HELICAL) DARRIEUS TURBINE

Figure 65 shows the velocity magnitude contour plot for the Gorlov Darrieus turbine. When compared with the squirrel cage Darrieus turbine (Figure 61), it can be seen that the behavior of the Gorlov turbine is quite similar. However, looking closer at the plots reveals that there

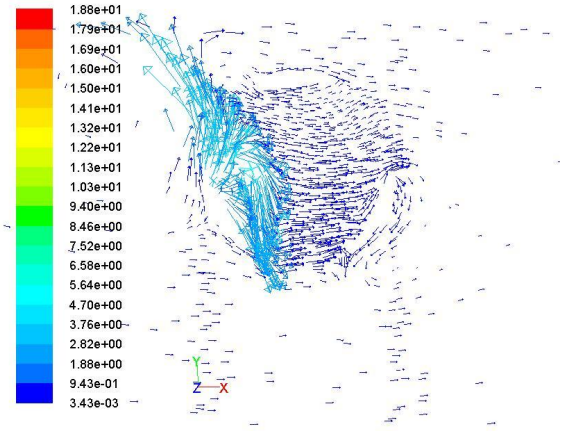

Figure 62: 2D Horizontal Cross-Section Velocity Vector Plot for a 3D Squirrel Cage Darrieus Turbine CFD Model.

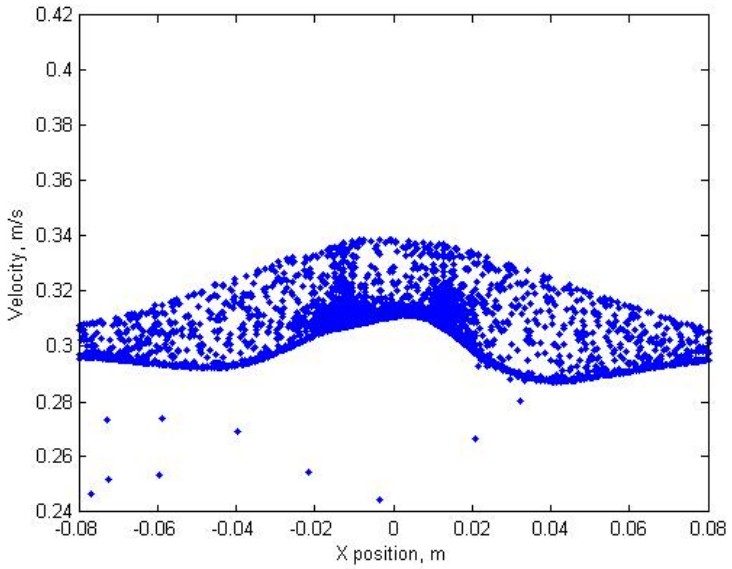

Figure 63: Velocity at y=0.0560m Horizontal Plane for a 3D Squirrel Cage Darrieus Turbine CFD Model.

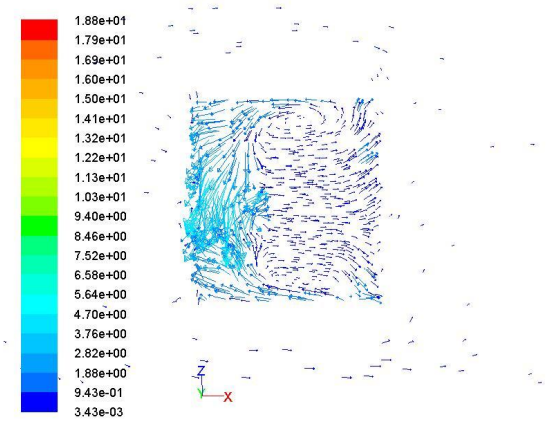

Figure 64: 2D Vertical Cross-Section Velocity Vector Plot at y=0 for a 3D Squirrel Cage Darrieus Turbine CFD Model.

is little to no high velocity region toward the leading edge of the Gorlov turbine compared with the squirrel cage turbine. This is further illustrated in Figure 66, where it is obvious that there is much less internal circulation in the Gorlov turbine (in comparison with Figure 62). This difference in operation can be explained in the blade construction. While the Gorlov turbine has the same overall dimensions as the squirrel cage turbine, the blades are twisted 30° with a slight (an additional 0.0015m or 1/16") outward bend in the middle. Figure 67 also shows less circulation in the longitudinal direction, attributed to the different turbine construction. An important point to note, however, is that due to the higher complexity in Gorlov turbine geometry, fewer mesh nodes were allowed in mesh construction. The squirrel cage turbine was similar to the submerged water wheel in terms of mesh construction, but the mesh component within the Gorlov turbine had to be reduced through an increase of mesh interval size of 0.002. These effects are also carried through in reviewing the velocity at the y=0.0560m plane above the Gorlov turbine, shown in Figure 68. The overall trend is slightly different due to the difference in geometry, and there are high velocity increases directly over the turbine, which are attributed to the lack in mesh refinement at that location. This mesh reduction is also reflected in Figures 66 and 67, with fewer vectors than that of the squirrel cage turbine simulation.

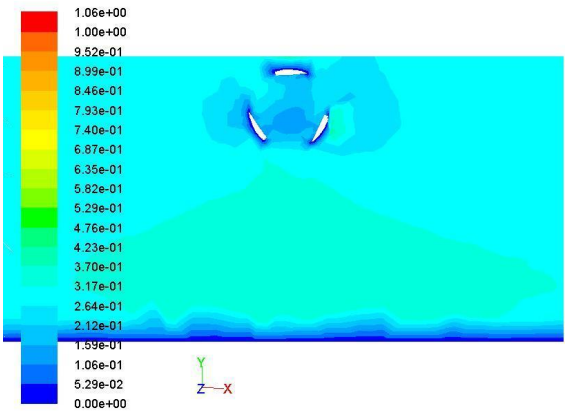

Figure 65: 2D Horizontal Cross-Section Velocity Magnitude Contour Plot for a 3D Gorlov Darrieus Turbine CFD Model.

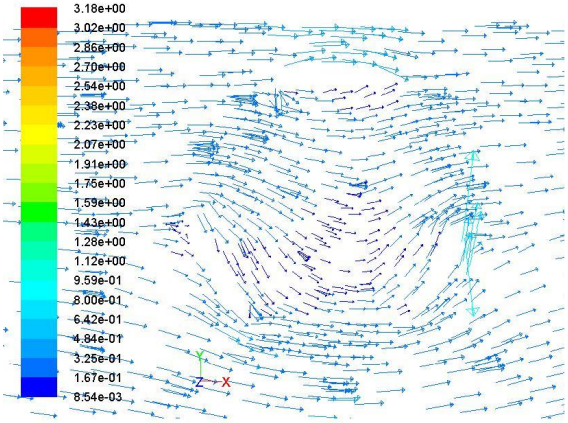

Figure 66: 2D Horizontal Cross-Section Velocity Vector Plot for a 3D Gorlov Darrieus Turbine CFD Model.

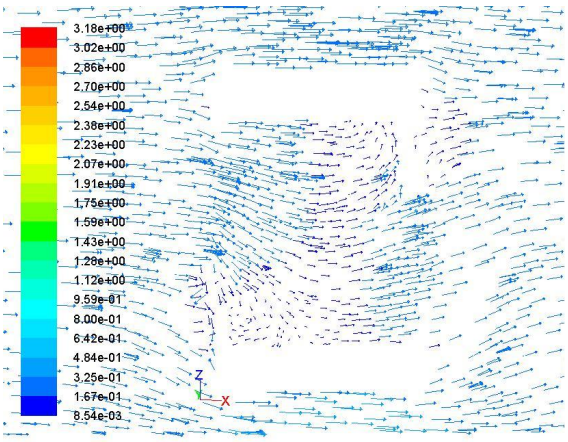

Figure 67: 2D Vertical Cross-Section Velocity Vector Plot at y=0 for a 3D Gorlov Darrieus Turbine CFD Model.

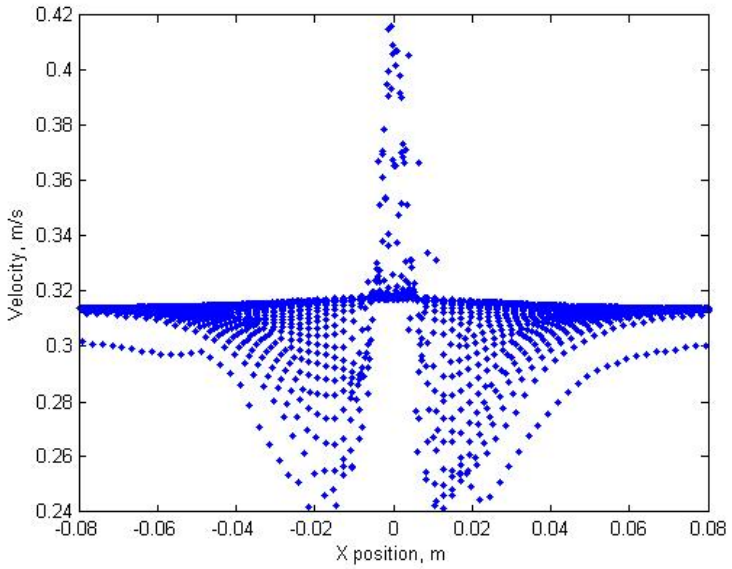

Figure 68: Velocity at y=0.0560m Horizontal Plane for a 3D Gorlov Darrieus Turbine CFD Model.

6.5 HYDROKINETIC TURBINES IN THE ENVIRONMENT

These 3D computational models give far more detailed information about the flow fields around the HEE turbines than the generalized models used in the evaluations given in the existing literature. In addition to fostering optimized design for increased energy extraction through both shape and orientation of hydrokinetic turbines, these models can provide insight into environmental impact modeling. Cotel et al. present plots that show where brown trout are present according to the defined Turbulence Index (TI), as shown in Figure 69 (32):

$$TI = \frac{\sigma}{u_{local}} \tag{6.1}$$

where σ is the standard deviation of instantaneous velocity and u_{local} is the average local current speed (32). From Figure 69, the brown trout prefer lower turbulent regions. This study combined with the CFD models can give an estimate for risk of fish impingement.

Instead of the TI value given in the Cotel et al. study, vorticity can be used to evaluate turbulence. Vorticity is the measure of a fluid element rotation as it moves in the flow field. It can be used as a measure of turbulence and is mathematically defined as the curl of the velocity vector:

$$\zeta = \nabla \times \vec{v} \tag{6.2}$$

FLUENT^{TM} includes this as a model output. Taking the squirrel cage turbine as an example, the vorticity contour plots are shown in Figure 70. When plotting vorticity magnitude, little variation is present across the flow field, indicating that there are minimal turbulence gradients. Figures 70a and 70b show vorticity in x- and y-component form. The x-component of the vorticity shows a higher turbulent region near the leading turbine edge, and the y-component of the vorticity shows a lower turbulent region within the turbine rotation region. Importance can be placed on the x-component of this plot since it is the primary direction of flow and fish swimming. Therefore, considering the vorticity magnitude, it is not clear a brown trout would clear the squirrel cage turbine; however, the x-component vorticity indicates a brown trout would tend to avoid it.

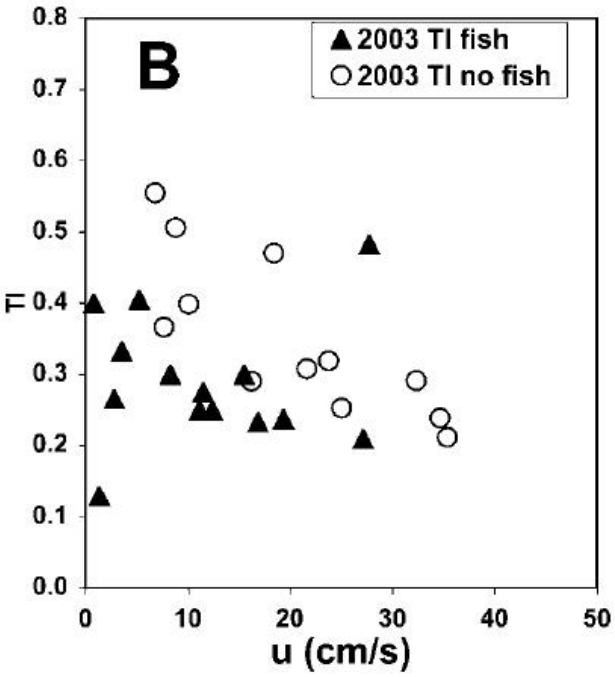

Figure 69: Example of Fish Presence Study From Cotel et al. Showing the Presence of Fish Relating to TI.

(a) Squirrel Cage Darrieus Turbine X-Component Vorticity Contour Plot.

(b) Squirrel Cage Darrieus Turbine Y-Component Vorticity Contour Plot.

Figure 70: Squirrel Cage Darrieus Turbine Vorticity Contour Plots.

This is an initial environmental impacts model for hydrokinetic energy extraction turbines placed in a river. For this initial model, it should be noted that there are limitations in a broader interpretation due to scaling concerns (as discussed in Section 3.2.3) and turbine placement in the stream, which was assigned arbitrarily. Additional results could be found by varying the turbine location. However, these results do provide insight into advancements that could be made to this model.

6.6 SUMMARY

The main outcomes from the work presented in this chapter are:

- Since the 2D CFD model is experimentally validated, 3D CFD models were created for the Savonius, squirrel cage Darrieus, and Gorlov (helical) Darrieus turbines.
- The 3D CFD models were based on the 2D CFD model construction and model verification. The 3D models were created similarly in terms of schematic geometry, mesh construction, boundary conditions, and CFD model definition (turbulence model and calculation parameters). The turbines are rotating in these models based on the power estimate model given in Chapter 2.
- Finally, environmental impact insights were gained from the 3D CFD models. Since risk of fish strike or impingement is present in using hydrokinetic turbines, fishing swimming data is used to give an estimate for this risk. Fish swimming patterns are characterized by a turbulence parameter, and vorticity was used as an estimate for fish strike or impingement with hydrokinetic turbines.

7.0 LIFE CYCLE ASSESSMENT OF HYDROKINETIC ENERGY EXTRACTION

In the same way that CFD can give insight into environmental impact modeling, life cycle assessment (LCA) can provide insight into the specific environmental impacts related to emissions and life cycle energy consumption associated with HEE. By applying LCA to a variety of energy systems, the total emissions related to each type can be clearly seen.

In the literature, some limited work has already been completed in the environmental analysis of traditional hydropower using LCA, with the goal of quantifying emissions produced during construction, operation, and decommissioning. A variety of outcomes were found. In a comparison of a large dam and small dam, the larger dam was found to be favorable based on greenhouse gas (GHG) emissions and payback ratios (57). However, unlike the small dam case in that study, HEE is not expected to have high emissions per material levels, as its inherent design gives a more reasonable material/infrastructure need per power output. For a general energy assessment, hydropotential power (HPP) and run-of-river HPP (which is the type of small HPP with which HEE is compared within this analysis) were found to have excellent performance with respect to the emissions given off for each system (58). This study also pointed to some issues with applying LCA to hydropower, namely that it does not include the benefits of having a reservoir, and its superiority in terms of electricity reliability over other renewable technologies. Furthermore, not all LCAs account for other negative impacts associated with large scale HPP, such as land use, industry disruption, and aesthetics. This study compares hydrokinetics with small HPP, as these devices can be placed in similar locations.

To complete an emissions measurement for hydrokinetic energy extraction, LCA is used. Often when a process or product is examined or optimized, only the direct materials, labor,

and operations costs are considered, and not, for example, emissions and land use. LCA allows the practitioner to evaluate the environmental impacts caused throughout the entire life of the HEE system, from raw materials extraction and construction of the system to its use and maintenance for energy production and, ultimately, decommissioning. The associated guidelines are derived from the American National Standards Institute (ANSI) and the International Organization of Standardization (ISO) 14040 series (59; 60). Within LCA, four stages exist: the goal and scope definition, life cycle inventory (LCI), life cycle impact assessment (LCIA), and interpretation and improvements. There are two types of LCI (process and input/output (61)), but for this case, process LCI will be used. Process LCI involves performing a material balance at each step in the product or process system where the boundaries have been defined by the analyst; the LCI databases are further described in Section 7.3 and listed in Table 6. In comparing different types of energy extraction, it is beneficial to use process LCI because it allows for system breakdown, analysis, and improvement, which is not achievable in input/output LCI.

The third stage of LCA, LCIA, then quantifies the impacts of each LCI. The LCIA is evaluated in this study using the Tool for the Reduction and Assessment of Chemical and other environmental Impacts (TRACI) (62). There are a wide range of impact assessment methods, including Eco-indicator 99, CML, and others (62–64). Eco-indicator 99 and TRACI are the more common impact assessment methods to use based on their categorization of impact types (i.e. aquatic toxicity, ecotoxicity, and human health) and weighting methods. TRACI was chosen as the LCIA method for this study both because the impact categories are appropriate for the systems in this analysis and because they are defined for North America.

7.1 GOALS, OBJECTIVES, AND SCOPE

The general goal for HEE research is to improve its viability and advance the field through improved energy extraction, while also considering its potential environmental footprint.

Specifically, in this study, the goal is to provide a benchmark life cycle air emissions and LCIA for HEE. The objectives to accomplish this are:

- Use LCI to provide an emissions framework associated with HEE. A functional unit of 100 years system lifetime in MJ will be used to compare HEE with small HPP, and coal, gas, and nuclear plants.
- Use TRACI to conduct an LCIA for HEE, small HPP, and coal, gas, and nuclear plants.

The choice of MJ as a system lifetime functional unit is based on the type of energy analysis conducted and the corresponding sizes of the systems. The use of $kW-h$, or kW used on an hourly basis, is more appropriate for energy consumption analyses.

This study highlights air emissions through comparison of HEE use with small HPP or run-of-river power, and coal, gas, and nuclear plants. Air emissions that are of particular interest with energy systems are CO_2, CO, CH_4, NO_x, and SO_x. These are specifically identified by the Environmental Protection Agency as key pollutants given off by the system types reviewed in this analysis. Furthermore, these are pollutants chosen when comparing energy systems in other analyses (65). The system boundary for HEE is described in Section 7.2. System boundaries for small HPP, and coal, natural gas, and nuclear power are set in SimaPro 7.1, the software used to compile the LCI. They include production and preparation, processing, storage, and transportation. Further details for the comparison systems in this analysis are given in the following section.

7.2 SYSTEM BOUNDARIES

Figure 71 describes the HEE system boundaries. The diagram shows "upstream" materials, which is a general term describing the raw materials needed to make the primary 'materials' or components of each system. The "upstream" designation also includes the energy and emissions associated with each raw material. The processes for the comparative energy systems are similar to those of the HEE system, except that transportation, construction and/or assembly, operation, and decommissioning may vary. In the case of construction

of a small HPP plant versus assembly and set-up of the hydrokinetic system, there will likely be more emissions involved with the former since it has a more intricate infrastructure for the development and extraction of energy. The same is true for transportation and decommissioning.

Figure 72 is analogous to Figure 71 and represents the LCA-designated materials and energy requirements of a HEE system. Table 6 provides more detail for the inputs of Figure 72 with the respective data sources and construction and transportation detail specific to the HEE process used in the inventory analysis. The use of 'generator' in Table 6 is a general term that includes power connections, lines, and controls in addition to the system generator.

The LCIs for the comparison systems are available within SimaPro 7.1 (an LCI software package based on process LCI) and are based on energy extraction for Switzerland or Western Europe, from the ETH-ESU 96 library (66). One of the comparison systems is a flow-through hydro system, also referred to as run-of-river set-up, or small HPP. It is a system that uses potential energy from rivers through extracting a small portion and developing head over changes in elevation across land. Little or no storage is needed, and electricity is produced continually (66). The inventory includes the dam structure, tunnel, turbine, generator, plant operation, and dismantling. More traditional generation systems are also used for comparison to a HEE system. The coal energy plant definition includes production of coal products (coke, briquettes, steam coal, lignite) and electricity and thermal energy (industrial and domestic) from coal combustion (66). The inventory consists of coal production and preparation, coal processing, storage and transportation. Similarly, the gas electric plant includes production and delivery of natural gas for industrial and domestic applications. The inventory consists of gas field exploration, natural gas production, gas purification, long distance transportation, and regional distribution. Finally, the nuclear power plant includes uranium extraction and preparation, uranium conversion and enrichment, fuel fabrication, electricity production with a boiling water reactor (BWR) and pressurized water reactor (PWR), reprocessing, and interim and final storage for low intermediate and high level waste.

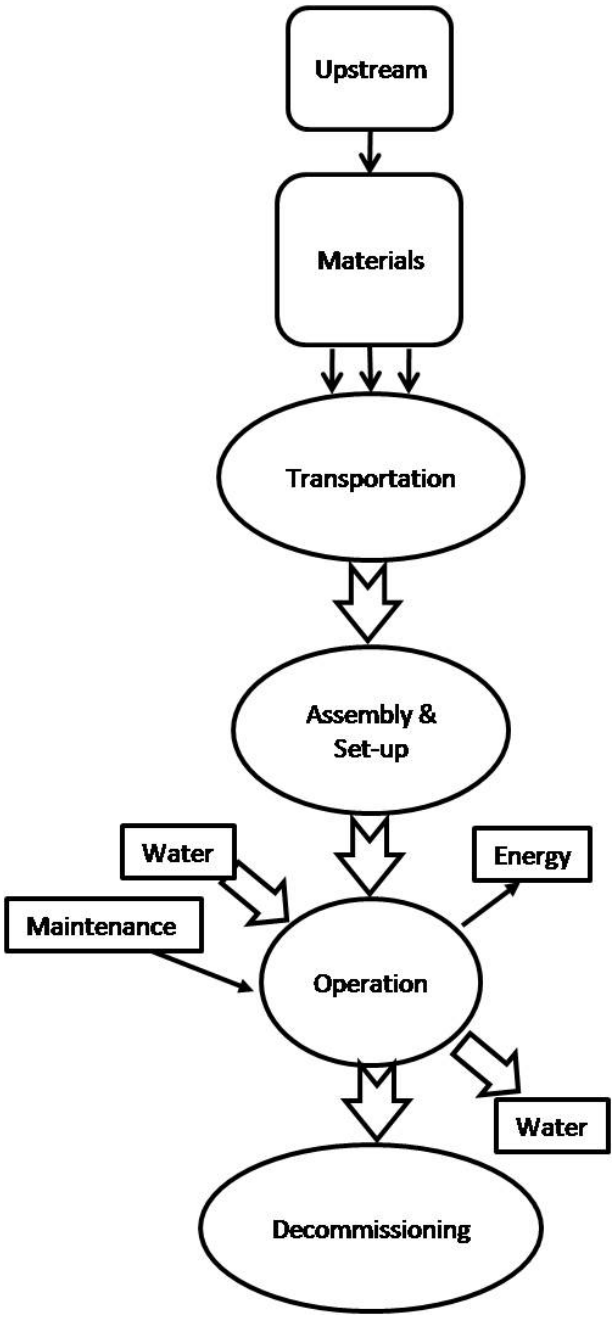

Figure 71: System Boundaries for HEE.

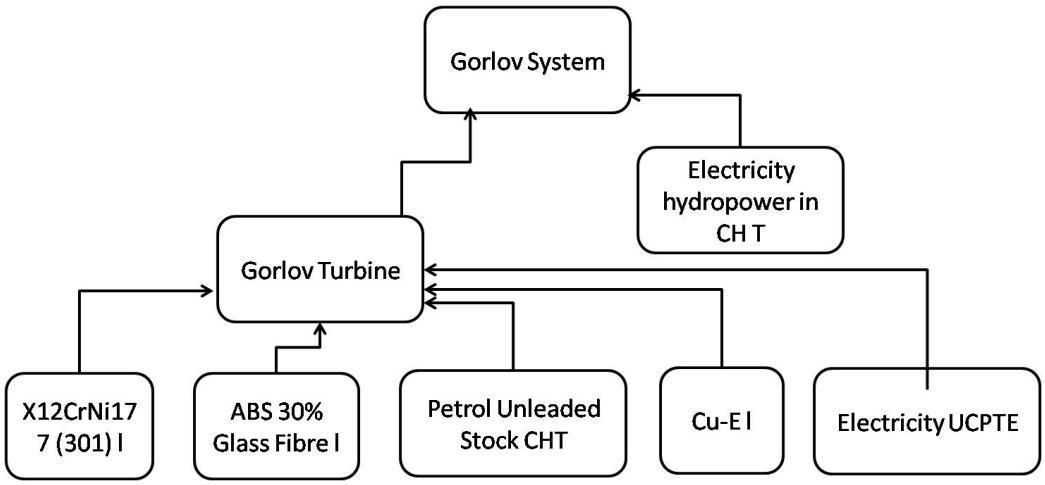

Figure 72: Materials and Energy Requirements Tree Representing a Gorlov HEE System.

7.3 LIFE CYCLE INVENTORY

The LCI provides a complete list of materials and energy going into and coming out of the entire process of each system. Information for the system products come from databases within SimaPro (66), as noted in Table 6. All available databases in this version were used, including the Franklin database (a database containing complete materials, transport, and energy for North America), but IDE MAT 2001 and ETH-ESU 96 are the primary databases in use for this study. Assumptions made in the analysis are the following:

- Since HEE does not currently exist within SimaPro, it was defined as an energy process in SimaPro under the hydro category. It was defined based on estimates of material, transportation, and electricity use in constructing and operating the system. The basis for the inputs into this system derives from available HEE literature (67).
- The functional system lifetime unit was calculated for each of the systems and was recorded in MJ, since that represents energy extracted from each system over the respective lifetimes (100 years).

Inventory for the HEE system was primarily based on an extensive report for a Gorlov turbine system (67). HEE was entered into SimaPro as an energy category, meaning SimaPro

Table 6: Gorlov HEE System Inputs.

Material	Amount	Description	Database
X12CrNi17 7 (301)l	64.2 kg	steel shafts	IDE MAT 2001 (66)
X12CrNi17 7 (301)l	30.84 kg	supports to mooring	IDE MAT 2001 (66)
ABS 30% Glass Fibre	103.98 kg	fiberglass turbine blades	IDE MAT 2001 (66)
Petrol unleaded stock CH S	2 kg	maintenance	ETH-ESU 96 (66)
X12CrNi17 7 (301)l	44.26 kg	generator, steel portion	IDE MAT 2001 (66)
Cu-E l	23.83 kg	generator, copper portion	IDE MAT 2001 (66)
Electricity UCPTE	7 kWh	construction and transport	ETH-ESU 96 (66)

recognizes it as an energy producing system, taking into account available energy from nature (230 GJ in this case). Inputs are illustrated in Figure 72 and given in Table 6. The input tree (Figure 72) shows the main material/process categories that are used to produce a Gorlov turbine. They are X12CrNi17 7 (301)l, ABS 30% glass fibre, petrol unleaded stock CH T, Cu-E l, and electricity UCPTE, all of which are defined in SimaPro. The X12CrNi17 7 (301)l is a material type in SimaPro describing stainless steel, and in the tree it is only one block that contains three separate uses: steel shafts for the turbine, a mooring structure for the turbine, and a portion of the generator (as indicated in the table). ABS 30% fiberglass is the material indicated for the turbine blades according to the report used for this LCA. Since fiberglass is a likely material for turbine blades in the Gorlov system, other material replacements were not investigated further. However, it should be noted that the composition of fiberglass can be highly variable, which would affect the LCA results. It should also be noted, though, that this is a base line analysis, which highlights various points of improvement, so it is not likely this assumption would significantly change the results. Furthermore, SimaPro 7.1 does not contain extensive information on fiberglass types. In addition to these material/process categories, electricity hydropower in CH S is included to account for axillary energy use in the overall Gorlov system. The amounts given in Table 6 were estimated based on information in the report about a single device weight and detail for implementation (67). This was scaled to twelve units for a realistic power extraction scheme. One Gorlov turbine is rated to give 500 W, so twelve units give 6 kW of energy, which converts to 189 GJ annually. Information for the generator portion was estimated based on an LCI for wind turbines (68).

7.4 RESULTS

In this comparison of power systems, it was important to analyze them over their total lifetimes, as different plants will have different emissions ratings for the corresponding lifetimes. Coal, gas, and nuclear were assumed to have 100 years of operation, a reasonable lifetime (57). A more conservative estimate is 50 years for small HPP and the Gorlov system; however, for comparison, two of each system were used (65), meaning two 50 year systems

Table 7: Life Cycle Air Emissions for Energy System Lifetime in kg of Emission/100 years.

Power Type	CO_2 (kg)	CO (kg)	CH_4 (kg)	NO_x (kg)	SO_x (kg)
Gorlov HEE	24848	178	26	102	55
Small Hydro	82808	534	206	326	213
Coal Plant	24428587	6090	97989	25020	26217
Gas Plant	16339490	10923	96814	30647	12404
Nuclear Plant	380836	582	1296	1052	2506

equaling 100 years of small HPP and Gorlov system operation. CO_2, CO, CH_4, SO_x, and NO_x air emissions were highlighted within this study because they are often associated with energy systems. NO_2 could also be included in this list; however, these emissions are generally negligible. Table 7 contains life cycle air emissions of interest for each energy system from the complete LCI for each energy type. In Table 7, Small Hydro is an abbreviation for small HPP. The Gorlov HEE has a lifetime NO_2 emission of 17 kg, which substantiates the assertion that this contribution can be treated as negligible.

As expected, Table 7 shows large life cycle air emissions for coal and gas power plants. Each system emits large amounts of CO_2: 82,808 kg from small HPP, 24,428,587 kg from coal power, 16,339,490 kg from gas power, and 380,836 kg from nuclear power. The Gorlov HEE system emits less of each compound compared with the small HPP system.

TRACI was applied to each entire energy system LCI developed within SimaPro, which includes approximately 1500 inventory compounds in addition to the air emissions highlighted in Table 7. The results were normalized by setting the largest system impact equal to one and calculating the percentage impact in comparison for the rest of the systems shown in Figure 73. In Figure 73, Sm Hydro is the abbreviation for small HPP. The TRACI results show similar trends to the emissions data, in that the coal and gas power plants were found have significant environmental impacts related to global warming, acidification, eutrophi-

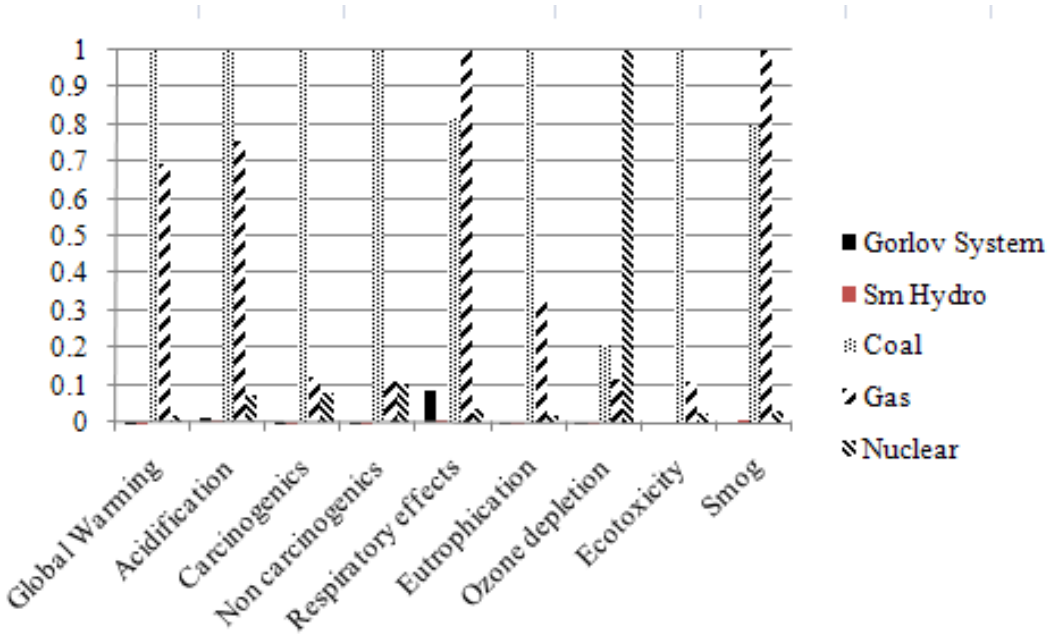

Figure 73: Normalized Impact Assessment using TRACI.

cation, ecotoxicity, and smog formation. Nuclear was found to contribute the highest level ozone depletion among these systems. In fact, Figure 73 shows the Gorlov and small HPP systems have virtually no global warming or ozone depletion impact in comparison to the traditional systems. This is a key point, since a considerable reason for their implementation is to reduce emissions in these specific areas. For further comparison, Figure 74 shows normalized TRACI results for small HPP and the Gorlov HEE system. Small HPP has higher impacts in each category with the exception of acidification and respiratory effects.

To investigate this further, a component impact analysis was performed. Figure 75 shows the contribution of major inventory emissions to the LCIA for acidification impacts. This is a complete list of compounds emitted for these systems, where all compounds were emitted to air; water and soil emissions were insignificant. The largest contributor in the Gorlov system is sulfur dioxide, equaling 22,269 hydrogen moles per 100 years (a unit used to characterize acidification within TRACI). The largest contributors for the small HPP system were nitrogen oxides at 6519 hydrogen moles per 100 years and sulfur oxides at

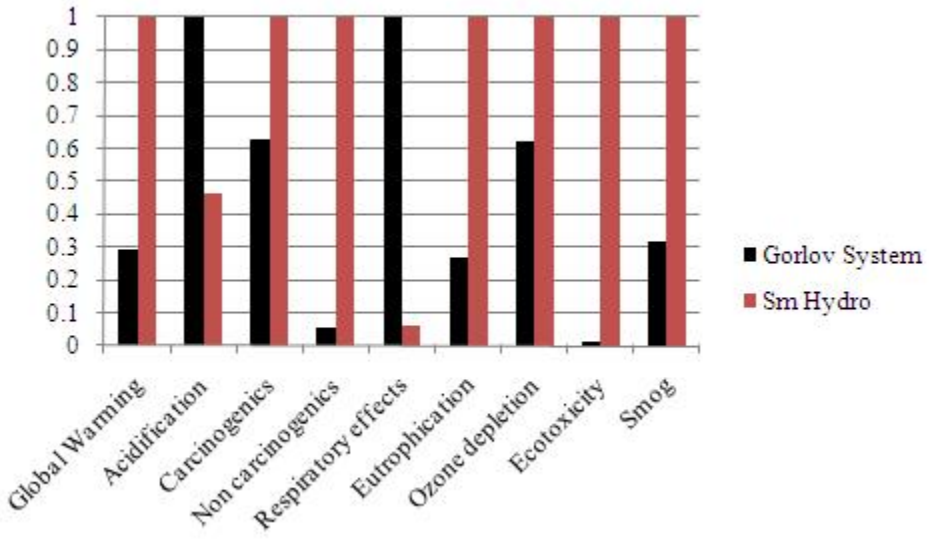

Figure 74: Normalized Impact Assessment for Small HPP and Gorlov HEE Lifetimes using TRACI.

5404 hydrogen moles per 100 years. The respiratory effects component breakdown is shown in Figure 76, and is a complete list of emitted compounds. Again, the major inventory compounds are air emissions, and the largest contributor in the Gorlov system is sulfur dioxide at 106 kg PM2.5 equivalent per 100 years. Figure 77 shows the percentage impact in each category from the Gorlov system materials and processes. It should be noted that in both the acidification and respiratory effects categories, the main contributor is copper from the generator within the system. Copper contributes 85 and 93% to the respective categories. This is from the production of copper; however, new paths for SO_2-free copper production are under investigation (69). Since this component is from the generator and the comparison system, small HPP, should also contain a generator within the overall system, it is speculated that this is missing from the small HPP system definition in the SimaPro database.

Some of the categories where the small HPP system impacts were dominant were also partitioned further. These categories are ecotoxicity, shown in Figure 78, and non-carcinogenics, shown in Figure 79. The contributors to ecotoxicity are more complex than the two previ-

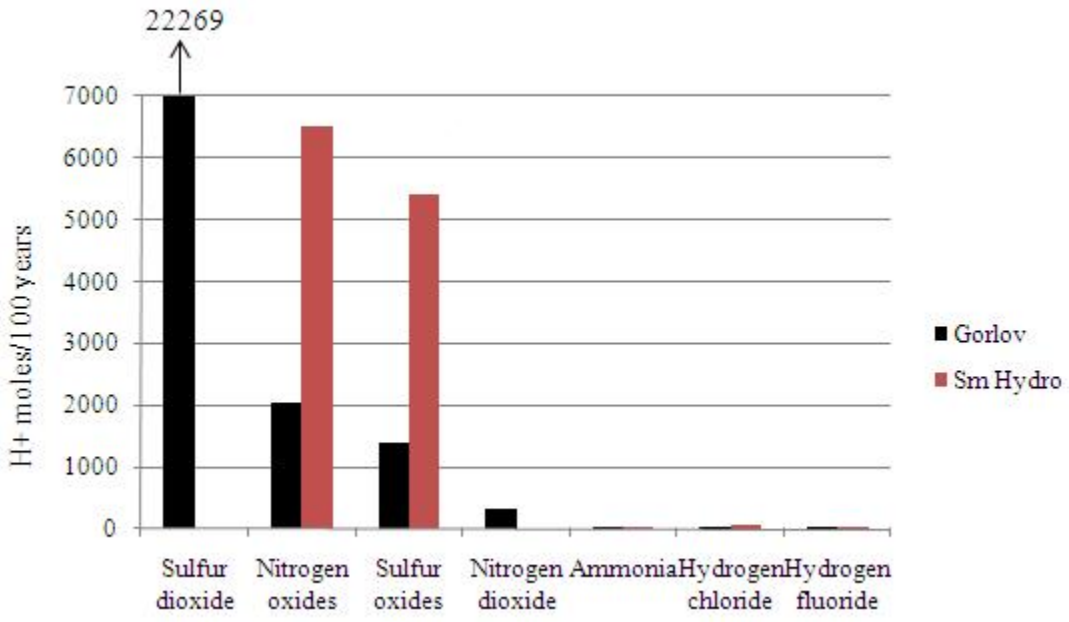

Figure 75: TRACI Acidification Impact Component Breakdown for the Gorlov and Small HPP Systems.

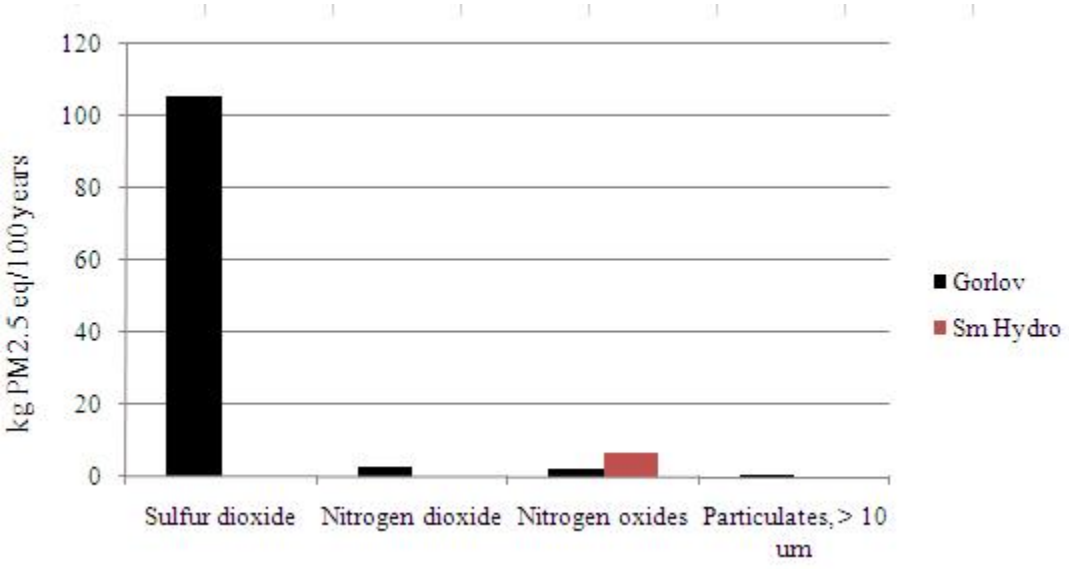

Figure 76: TRACI Respiratory Effects Component Breakdown for the Gorlov and Small HPP Systems.

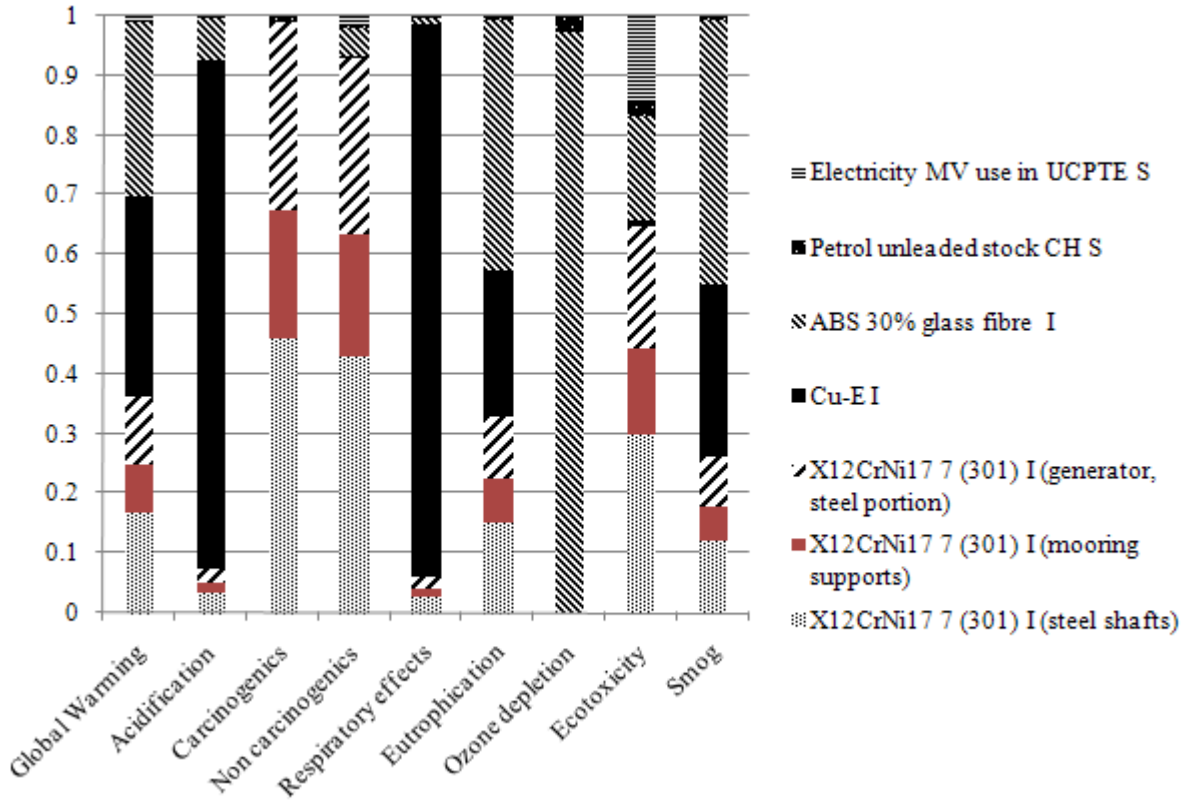

Figure 77: Percentage Impact in Each TRACI Category for the Gorlov System Materials and Processes.

ously mentioned categories. Table 8 is provided to show the breakdown of each component by water, air, and soil, and also by ion versus non ion component, where Figure 78 sums each of these. These results show 95% of compounds emitted. Other compound emission contributors were less than 5%, and can be treated as negligible. The original aluminum ion contribution to water by both systems were reported as significantly high, 36,230 and 327 kg 2,4-D equivalent for the small HPP and Gorlov systems, respectively. The aluminum water contributions were approximately 85% for small HPP and approximately 53% for the Gorlov system. This is a high contribution for aluminum, and it is well known that SimaPro has incomplete or incorrect data for some emissions components. When further investigated, this aluminum level is not supported by the literature, and was therefore removed and the impact was recalculated, as reflected in Table 8 and Figure 78. After the impact recalculation, the dominant inventory emissions for the small HPP system are aluminum in the air and soil contribution equaling 1581 2,4-D equivalent; copper ions in water and copper in air equaling 1888 2,4-D equivalent; zinc in water, air, and soil equaling 1934 2,4-D equivalent; and nickel ions in water and nickel in air equaling 842 2,4-D equivalent. For the non-carcinogenics breakdown (Figure 79), the components are separate and shown in kg toluene equivalent. Emission contributors of less than 5% were neglected. Lead emissions to both water and air are the largest contributors for small HPP within non-carcinogenics, 2,798,220 and 123,685 kg toluene equivalent, respectively. The largest contributor for the Gorlov system in this category is dioxins, measured as 2,3,7,8-tetrachlorodibenzo-*p*-dioxin, equaling 86,133 kg toluene equivalent.

7.5 DISCUSSION

The comparative LCA models a Gorlov system's life cycle impacts and compares them with the emissions from other energy systems: small HPP, and coal, gas, and nuclear power. LCA models of any type have currently not been applied to hydrokinetic energy, and this model therefore provides a base upon which future work can build. From this analysis, it can be seen that Gorlov hydrokinetic energy extraction is favorable when compared with

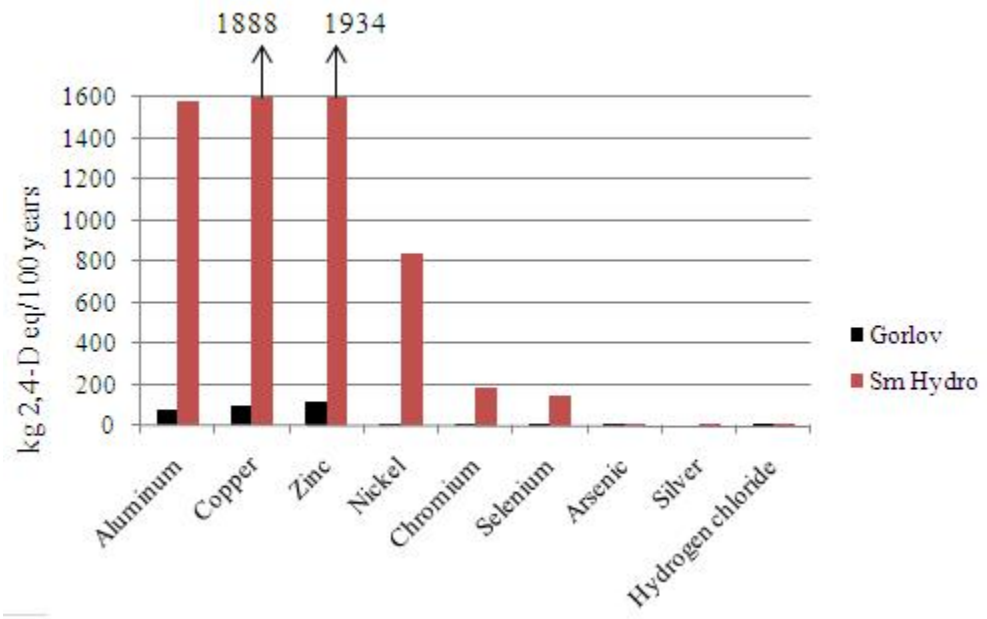

Figure 78: TRACI Ecotoxicity Impacts Component Breakdown for the Gorlov and Small HPP Systems.

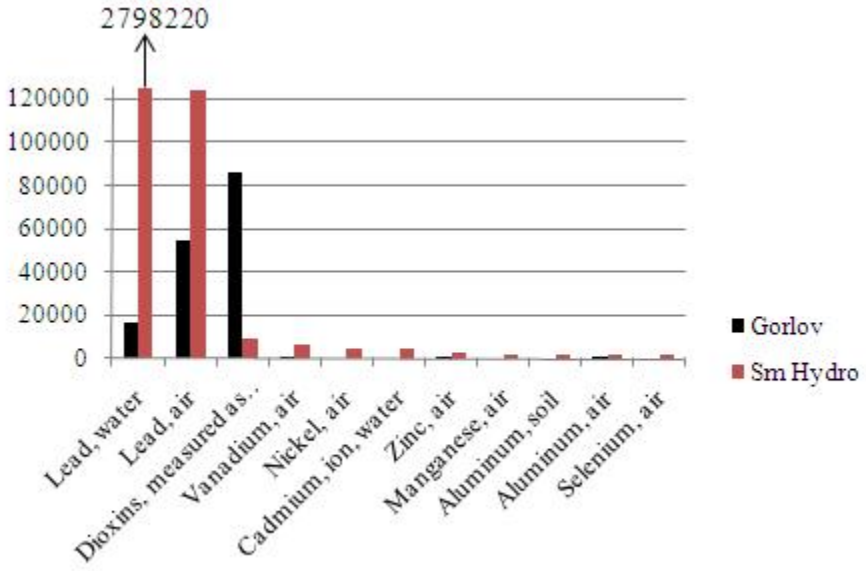

Figure 79: TRACI Non Carcinogenics Impacts Component Breakdown for the Gorlov and Small HPP Systems.

Table 8: TRACI Ecotoxicity Impacts Component Breakdown for the Gorlov and Small HPP Systems in kg Toluene Equivalent.

Small Hydro			
Component	Water	Air	Soil
Aluminum	0	1089	491
Copper	(ion) 1179	709	0
Zinc	(ion) 567	1361	6
Nickel	(ion) 291	551	0
Chromium	(ion) 170	11	0
Selenium	106	35	0
Arsenic	(ion) 10	0	0
Silver	5	0	0
Hydrogen Chloride	0	4	0
Gorlov			
Component	Water	Air	Soil
Aluminum	0	64	9
Copper	(ion) 15	83	0
Zinc	(ion) 10	103	0.12
Nickel	(ion) 2	3	0
Chromium	(ion) 2	0.31	0
Selenium	0.95	0	0
Arsenic	(ion) 0.09	0	0
Silver	0	0	0
Hydrogen Chloride	0	0.39	0

small HPP. Furthermore, it is noteworthy to point out the similarities of the squirrel cage Darrieus turbine (shown in Figure 3d or 52c) to the Gorlov system, indicating the possible use of the Gorlov LCI for the squirrel cage Darrieus system. This is possible because turbine construction is similar and the support system (mooring structure and generator) would be the same. Much of this study is based on estimates derived from HEE literature, and specifically for the Gorlov system. The analysis could be improved with more detailed system construction and installation information, and would be most appropriately performed as a case study or in combination with a specific HEE project for data collection.

Further environmental investigations could also indicate the Gorlov system superiority over small hydropower because of their infrastructure differences. This is based on the negative environmental effects experienced by small hydropower use, such as changes to the overall flow regime (decreased flow and temperature differences) from stream diversion (4; 6; 7; 12). In addition to the work that is already being conducted on fish passage estimation based on swimming preference data and CFD, a new impact metric should be developed to effectively account for system degradation to the local river ecosystem due to energy production.

In the hydrokinetic energy field, LCA has not been previously applied. Often, hydrokinetic energy is viewed as an environmentally benign form of energy, since it is a form of renewable energy and has been designed with the environment in mind. Given today's energy needs and increasing GHG emissions, it may not be entirely appropriate to assign much weight to small amounts of GHG emissions or other slightly harmful effects a potential system may have. However, it is important to have this information, which is proven by the way dams have been approached. Dams were put forth as a means to extract cheap, environmentally benign energy. However, data show this last point to not be true. In addition to flooded lands and decreased downstream flow, these outcomes caused vegetation changes, impacts on fish and bird populations, and destruction of wetlands and local flora and fauna (5; 13–19).

7.6 SUMMARY

The main outcomes from the work presented in this chapter are:

- LCA was used as another environmental impact measurement for HEE.
- Life cycle air emissions were tabulated and a LCIA for the entire LCI was given for HEE, which was used to compare HEE with other energy systems: small HPP, and coal, gas, and nuclear power plants.
- LCA does not account for all environmental impacts specific to hydropower, such as alteration of bottom river habitats. New environmental impact categories specific to this technology are needed. Examples of this are statistical analysis of fish passage, and flow and temperature measurement.

8.0 IMPLEMENTATION ISSUES AND APPLICATIONS

This work focused on computationally modeling hydrokinetic turbines for use in rivers; however, there are practical aspects of this subject that must be explored. First, there must be a need for this technology. As mentioned in the first chapter of this work, the U.S. has identified both the need and the location potential for this technology, dividing it by head and extraction amount (3). However, forecasting for this technology in developing countries, where it would prove useful because of the simplistic design and low maintenance costs, does not exist. In both the U.S. and abroad, there needs to be not only a technology forecast developed, but also the policies to support it. These projects need intelligent infrastructure through precise energy policies to be initiated and successfully executed. Focus must be given to energy policies for hydrokinetic energy extraction in how they are established and promoted and mechanisms for improving current policies.

Additionally, the implementation of the turbines in an actual river environment will unquestionably cause sediment suspension and alteration, and therefore a sediment transport model is needed. Sediment transport is important because some environmental contaminants such as polychlorinated biphenyls (PCBs) tend to adhere to sediment particles rather than dissolving in water, and environmental engineers need to understand sediment transport to predict the spread of these contaminants. High concentrations of suspended sediments can block light and inhibit photosynthesis in phytoplankton and aquatic plants. PCBs, mercury, and other chemical contaminants transported by sediments can biomagnify in the aquatic food web and impact the health of the ecosystem (70; 71). Improved understanding of sediment transport and contaminant movement in the environment contributes to environmental scientists' ability to predict river health.

Both of these extended research areas were investigated further, and are presented in the following sections. In addition, two applications for HEE have been identified, and are also presented.

8.1 POLICY DEVELOPMENT

When composing a policy development plan, small scale HPP can be used as an example. This type of set-up, like hydrokinetic energy extraction, allows for distributed, sustainable energy. Although some hydropower development has caused adverse environmental and ecological effects, this study explores the issues in developing, advancing, and implementing a small scale HPP system that can incorporate and address these issues. Different policies that aid in the effort to start and promote these projects are examined and compared. The study spans from the bureaucratic system to policies that work in cooperation with private industry and mechanisms within the Kyoto Protocol that can also facilitate small scale HPP.

It is often difficult to start a small HPP project in certain regions because of the policies that are in place. An existing procedure used to start a small HPP plant in Greece is shown in Figure 80 (72). The figure shows a very involved process with more than twenty steps, which can take approximately two years to accomplish, in addition to initial procedures to establish a feasible location (72). This time lag, coupled with the pending energy crisis, has resulted in a recent stronger focus on finding policies that support the rapid development of small HPP. A recent analysis of these issues resulted in the development of specific recommendations that can accelerate the use of sustainable energy technologies (73). The recommendations include establishing an energy policy framework, a specific decision-making process, comparison of hydropower project alternatives, improvement of environmental management of hydropower plants, and sharing benefits with local communities. While these are not specific policies, they are recommendations for putting the policies in place; specific policies that are in practice are discussed in the following paragraphs.

One of the largest issues on the front end of a hydropower project is the initial cost. Involvement with private industry is attractive, as it has the economic resources and will

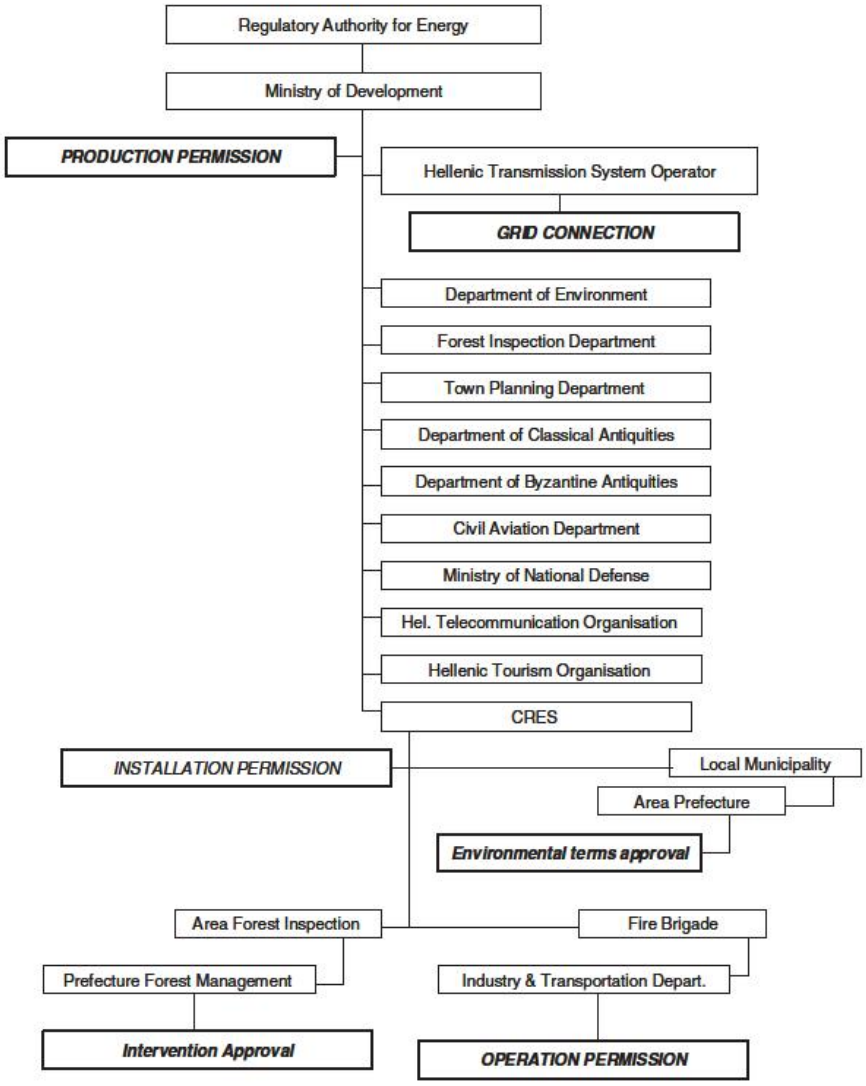

Figure 80: An Example of an Implementation Procedure for a New Small Hydropower Plant in Greece.

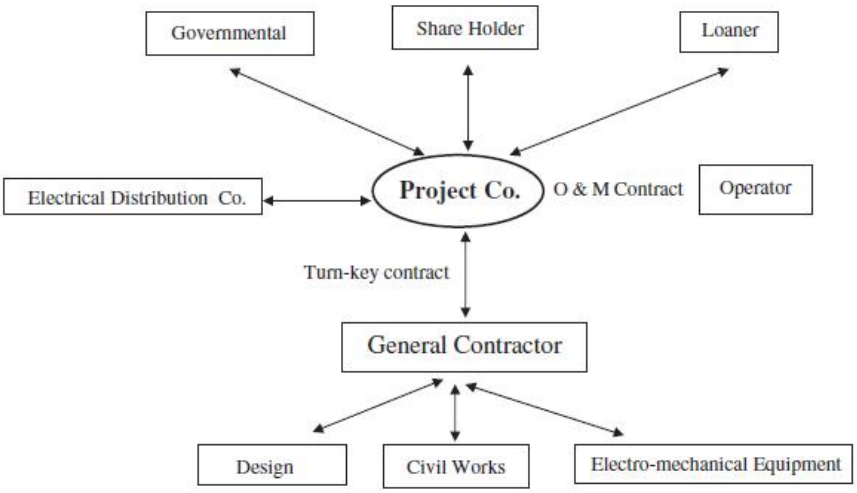

Figure 81: Structure of a BOT contract.

to make a hydropower project happen, and can benefit from its long-term profitability as a result. A method that has been used to encourage private sector participation is the build-operate transfer (BOT) method. A main goal in this method is reducing government interaction within the project infrastructure, which allows for financial risks to be distributed among different sectors. Additionally, because of its integrated, strong structure of having both private industry and the government involved, the interests of the public are protected at the same time (74). After a predetermined initial period of time, the institution is transferred back to the public. This is why this method works so well, as both the private and public sector benefit from the transaction. Within BOT, responsibilities are distributed among different entities in the business agreement. Figure 81 is a schematic that demonstrates this arrangement (74). An analysis in the literature included case studies of BOT, which was complete with various scenarios of different plant sizes and interest rate, and found it to be effective, as opposed to when the projects only consisted of government interaction (74).

Another method that can support and increase small scale HPP is the clean development mechanism (CDM) under the Kyoto protocol (75). The purpose of CDM is to encourage and

enable countries to help other countries in decreasing the overall global emissions. CDM is utilized by developed countries that have strict emissions standards and are having problems meeting them. Instead of decreasing their own emissions, they may assist a developing country to reduce its emissions and receive credit for it. The most challenging issue in implementing CDM is the additionality criterion. Additionality is defined as when the CDM component of a project is additional rather than part of regular business development (76). Many small scale HPP projects may seem that they are part of regular business when, in fact, they can be part of the CDM. In order to address this issue, a baseline was developed which considers both current energy sector performance and future performance, where the CDM is measured from the difference in project performance and the baseline (76). Another analysis found that including an electrification factor decreased the subjectivity under the additionality criterion. The factor decreased subjectivity because it was a measure of the probability of a region obtaining electricity (75). A low factor indicated high additionality, since a low electrification factor meant there was a low probability for the village to get power.

This is a brief overview of the policies to encourage small HPP and hydrokinetic energy development through enhancement of the decision-making processes, comparisons with other related energy projects, improvements to environmental management, and increases in benefit sharing. This technology can help to achieve energy independence from outside sources and improve a society's quality of life. These types of projects are difficult to implement because of the bureaucracy associated in their startup and policy deficiencies in their funding and operation.

8.2 SEDIMENT TRANSPORT

For simplicity, the sediment model is considered as an open-flow channel without the hydrokinetic turbine in place. In many simple open-flow channel analyses, laminar flow conditions are assumed, but in nature, turbulent flow is most common, as was discussed in Chapter 3. The turbulent model is therefore used, and the numerical models of river sediment transport

consist of two major components: a hydraulic flow model and a model of sediment/fluid interaction.

8.2.1 Sediment Modeling in the Literature

Hydraulic Component

Some modelers simplify the hydraulic model of the three-dimensional river system by considering only the downstream and transverse directions. To do this, they either average or integrate the water flow over the depth of the river. One widely used model of this type is Jones and Lick's SEDZLJ (77). Jones and Lick claim that for all practical purposes, a two-dimensional vertically integrated model can capture all of the detail given by a three-dimensional model, particularly in shallow waters which are well-mixed vertically. They argue that in offshore waters where vertical mixing is incomplete, sediment concentrations and transport are lower and model accuracy is less important. For river geometries with complex bottom profiles or in cases where vertical flow velocities are significant, however, three-dimensional simulations can give more appropriate results. Shams et al. cite numerous three-dimensional models of river flow for varying geometries, including meandering channels and islands (46). To model flow near a hydroelectric dam, Sinha et al. (78) developed a three-dimensional model that utilizes approximate factorization techniques for matrix inversion to solve the three-dimensional incompressible Navier-Stokes equations for momentum and continuity.

Sediment Component

Suspended sediments and bottom sediments are treated separately in the models. In some models, transport of the suspended particles is governed by advection and dispersion while the top layer of the sediment bed is transported by rolling and saltation (e.g. (77)). Shams et al. modeled transport of the suspended sediments by considering advection with river flow with a retardation factor to account for drag and gravitational forces (46). In addition, dynamic exchange between the two components is considered in most models, with the bedload eroding to become suspended load and suspended particles depositing into the

bed layer. Erosion rates are frequently computed empirically: in SEDZLJ, the sediment erosion rates are obtained experimentally at discrete values of depth and shear stress in a flume designed to simulate river conditions. Intermediate values between the discrete points measured are interpolated using a linear relationship for erosion vs. stress, and a logarithmic relationship for erosion vs. depth (77). Deposition rates can be modeled using settling velocities based on Stokes' Law coupled with near-bed particle concentrations (77). While the concentration of suspended sediment is low and typically does not exceed several hundred milligrams per liter (79), the suspended particles move much more readily than those at the bottom due to cohesion. For this reason, the suspended load accounts for a majority of the total sediment transport, and thus many models focus on suspended transport only and omit consideration of bottom sediments.

Particle Characteristics

Some models consider variation in particle size. Uneven particle size distributions can impact transport rates by permitting preferential erosion of finer sediments during heavy flow events. This leads to 'bed armoring,' where only coarse, difficult-to-erode sediments remain in high-flow regions such as the middle of a river. In systems that exhibit bed armoring, suspended load transport becomes relatively less important over time as decreased erosion rates result in decreased concentrations of suspended particles.

8.2.2 Suspended Solid Model

In order to provide a basis for future investigation of the environmental consequences of implementing HEE, a suspendied sediment model was created. In contrast to Jones and Lick (77), depth is considered in the two-dimensional model, but consideration of the transverse direction is omitted. The key use of the transverse dimension in their model was to consider the cross-stream distribution of particle sizes. They found that smaller, lighter particles tended to end up near the river banks while the heavier particles were left in the deep channel. This eventually created bed armoring and affected overall erosion rates as discussed above. Because the assumption in this model is that particles are of a uniform size, the transverse direction in this model will not be considered.

This suspended solid model has two components: a CFD model composed in Mathematica™ and a FLUENT™ model. Inputs to both models include a river depth of 3 meters and an average river velocity of 30 cm/s, both based on data for the Allegheny River (43). (This is similar to the CFD model presented in evaluating the hydrokinetic turbines.) This river velocity is representative of those used in other studies (for example (38)). A 12 meter long stretch of river is considered, which was determined to be sufficiently long to avoid numerical inaccuracies due to the grid sizing. The particle diameter is estimated to be 0.134 mm (80) and the particle density is 2.6 g/cm^3 (81). The dynamic viscosity of the river is set to 1.003 $g/m/s$ (48). Atmospheric conditions are used in both analyses. Two models are used to verify the results. The main differences are the method in which the models achieve the results and laminar vs. turbulent calculations. The Mathematica™ model uses the finite difference or finite element approach, while the FLUENT model uses the finite volume approach. The turbulence form of the Navier-Stokes equations were reduced to the laminar formulation for the Mathematica™ model to allow for simplification in creating the model.

8.2.3 Mathematica™ Model

Particle Velocity Model

The Mathematica™ model is based on solving the Navier-Stokes equations for incompressible flow in the river, and then utilizing the resulting fluid velocities in a drag- and gravity-based model for particle motion. A staggered grid of 30 x 120 nodes was created for the analysis. A stretch of river where inlet velocity decreases linearly with depth from a maximum of 0.3 m/s at the free surface to 0 m/s at the sediment interface is also considered. An upwinding factor of γ =0.9 and an over-relaxation factor of ω =1.7 in the iteration loop for solving the Poisson pressure equation are used. The Navier-Stokes model is time-dependent, but the model is allowed to run until steady-state conditions are reached. Because no bottom topography features or pressure changes are incorporated, the flow velocities remain essentially unchanged from the initial conditions (see Figure 82).

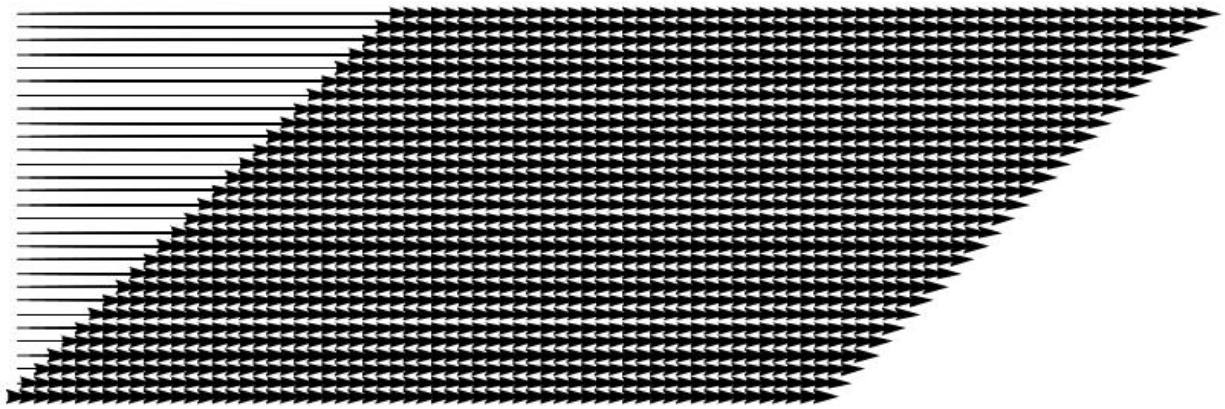

Figure 82: River Velocity Profile, Mathematica™.

For particle motion, a steady-state equation is derived from the work of Shams et al. (46):

$$u_{particle} = u_{fluid} - \frac{d^2 \rho_{particle} g}{18\mu} \tag{8.1}$$

where d is the particle diameter, $\rho_{particle}$ is the relative density of the particle, g is the acceleration due to gravity, 9.8 m/s^2, and μ is the dynamic viscosity of the fluid.

This equation from Shams et al. essentially results in subtracting a constant (0.025 m/s) from the fluid velocity at each point to determine the particle velocity, and thus the result appears similar to the fluid velocity vector plot, as can be seen in Figure 83.

Concentration Model

Additionally, the fluid velocities to predict the sediment concentration throughout the domain using a mass-balance equation from Dietrich et al. can be used (82). Their sediment mass balance equation for steady state is adopted here:

$$u\frac{\partial c}{\partial x} + \frac{c v_{settling}}{depth} = \frac{s}{A} \tag{8.2}$$

On the left hand side of Equation 8.2, u is the fluid velocity, c is the concentration of suspended sediment at distance x downstream of the starting point, and $v_{settling}$ is the particle settling velocity, which is assumed to be constant over the stretch of river under

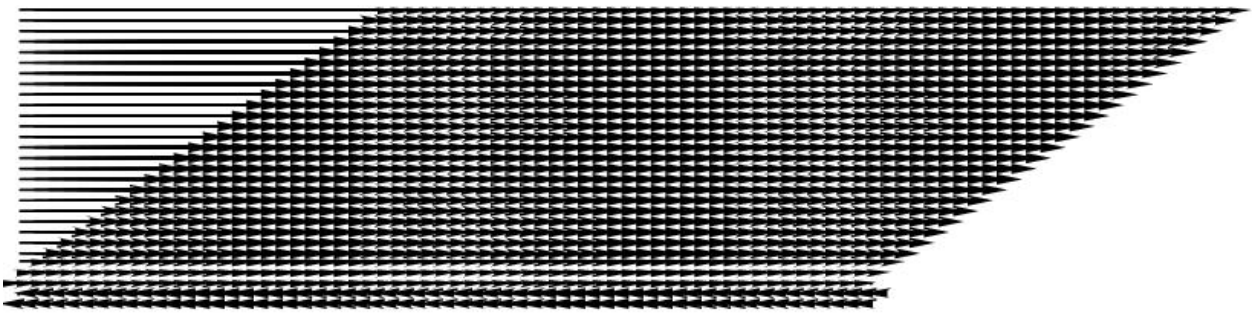

Figure 83: Sediment Velocity Profile, Mathematica™.

consideration for a given particle size. Jones and Lick (77) and Lee et al. (83) each provide slightly different equations for settling velocity based on the particle size and fluid viscosity. Evaluation of both expressions using the particle diameter and density assumed above gives similar results in a value of 1.40 cm/s using Lee et al. and 0.98 cm/s for Jones and Lick.

On the right hand side of the Equation 8.2, A is the cross sectional area of the stream, and s is the source term, encompassing resuspension and bank erosion, and considered to be proportional to (u - $u_{critical}$), where $u_{critical}$ is the critical velocity for particle resuspension. The current model uses a critical resuspension velocity of 4 cm/s based on Jamieson et al. (84). The coefficient of proportionality was selected to be 10 $mg/L/m$ based on calibrations done by Dietrich et al. and based on experimentation with our model (82).

In the current model, like that of Dietrich et al. (82), a depth-averaged sediment concentration using a depth-averaged fluid velocity u is considered. Because the hydrodynamic model results in a stream velocity that is constant with respect to distance downstream, and because $v_{settling}$, depth, and cross-sectional area are held constant in these calculations, variation in concentration comes only from the $\frac{\partial c}{\partial x}$ term, representing the initial concentration gradient.

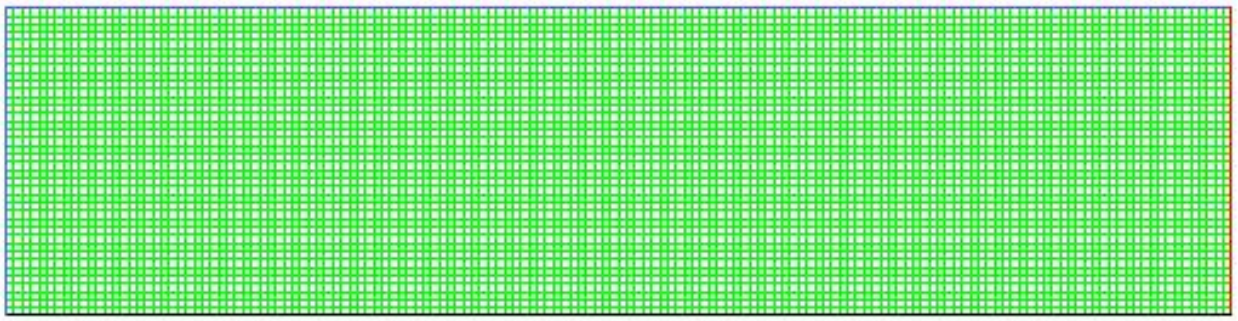

Figure 84: Staggered Grid for the River Model, Gambit^{TM}.

8.2.4 FLUENT^{TM} Model

A multiphase Eulerian model is used to model transport of a dispersed secondary sediment phase in a continuous primary flow field. The Eulerian multiphase model provides a higher accuracy of mixture evaluation because it allows separation of the two phases and then solves continuity and momentum equations with turbulent effects (48). The system under consideration exhibits isotropic turbulent stress, thus we use the $k - \epsilon$ approach to model the viscous component. A staggered grid was created in Gambit^{TM} of 39 x 151 nodes, which was determined based on an interval spacing of 0.08, and is shown in Figure 84. In this model, the bottom edge is defined as a wall and the top edge is defined as a pressure inlet, while the edge to the left is the flow inlet and the edge to the right is an outlet. Other parameters include atmospheric pressure, water density at atmospheric pressure and 20 C, and the inlet velocity of 30 cm/s (43), which was also used in the Mathematica^{TM} analysis. The results from FLUENT^{TM} are shown in Figures 85 and 86. The ordinate is velocity in m/s, and the abscissa is the distance along a river bed in the downstream direction. A typical river velocity profile is shown in Figure 85 with the bulk velocity equal to 0.313 m/s and decreasing toward the river bed. The profile is maintained in Figure 86, but, the bulk flow is slightly slower at 0.279 m/s.

Figure 85: River Velocity, FLUENT™.

Figure 86: Sediment Velocity, FLUENT™.

8.2.5 Results and Discussion

From Figure 82, the fluid velocity is shown to exhibit virtually no change from the inlet condition, with the exception of some decrease due to the drag associated with the bottom surface. This is what is expected for the simplified case, and it is also demonstrated in Figure 85, where the river maintains the inlet velocity for much of the flow, showing velocity decreases at the bottom where drag effects are exhibited. Figure 83 shows the sediment velocity profile is very similar to the river velocity profile, which is expected based on the governing Equation 8.1. This information was used to estimate an inlet velocity for the particles in the FLUENT^{TM} model, which resulted in similar values for the particle velocity, as shown in Figure 86. The consistency between the two models affirms their validity and indicates that they can give valuable information on suspended sediment transport, which can be used for predicting river health and modeling suspended sediment in and around new aquatic technologies.

The concentration model as currently implemented provides satisfactory output for some input assumptions, but needs further refinement to be applicable in the general case. Using the current assumptions ($u_{critical}$=4 cm/s, β=10 $mg/L/m$, and an initial nonlinear concentration gradient with c $\sim$ 200 mg/L decreasing with downstream distance), results that correspond to what would be predicted are achieved (see Figure 87). The ordinate is depth average concentration of suspended sediment in mg/L and the abscissa represents downstream distance.

However, this model is extremely sensitive to the assumptions regarding initial concentration gradient and must be recalibrated for each individual river system. To see why this is necessary, the steady state case with zero initial concentration gradient can be considered, i.e. the suspended sediment concentration c is uniform over the domain. In this simplified case, the governing equation reduces to $c = s{*}depth/(A{*}v_{settling}) = \beta(u{-}u_{critical})/(width{*}v_{settling})$, where β must then be explicitly selected to yield the correct concentration c.

Future work would include enhancements to both the suspended sediment model and incorporation of a hydrokinetic turbine within it. Future versions of the suspended sediment model could incorporate depth into the concentration model by discretizing the domain in

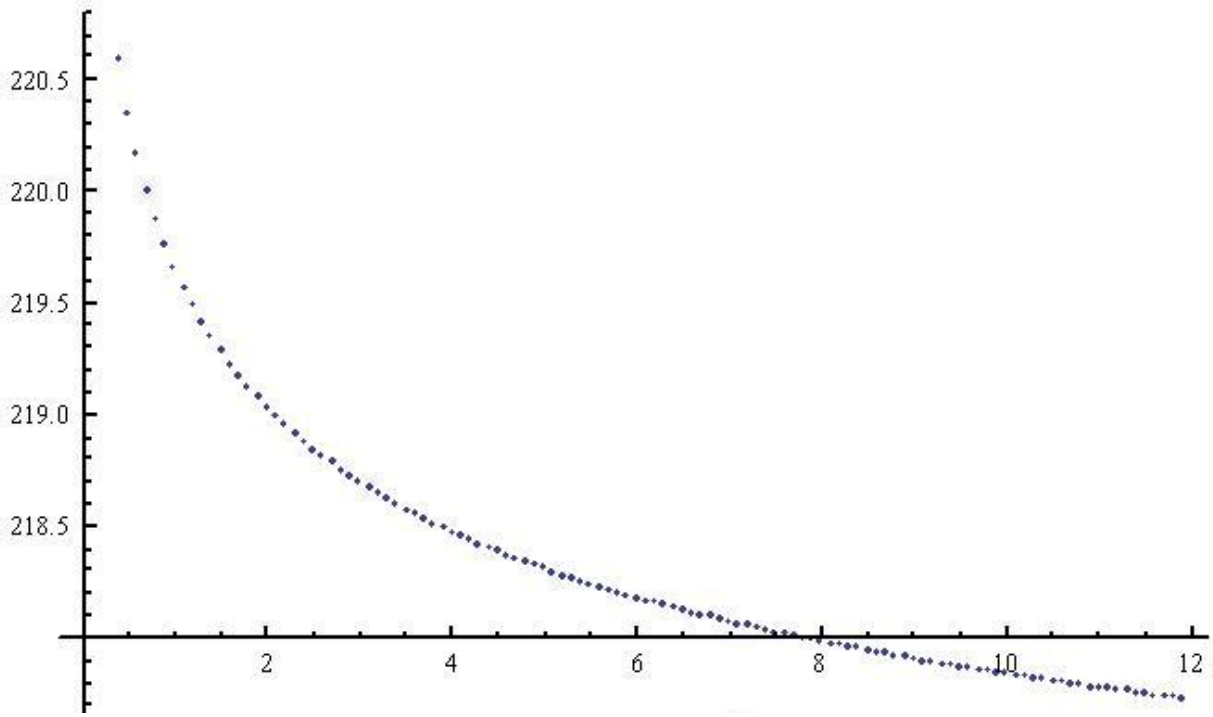

Figure 87: Sediment Concentration Downstream Profile.

the vertical direction and by adding mass flux terms corresponding to settling from cells above and resuspension from cells below. Additional refinements of both the concentration and velocity models could include a nonuniform particle size distribution to account for preferential transport of smaller sediment particles. In each cell, a random number generator would be used in conjunction with a probability distribution function (PDF) for particle diameter to determine the value of d. Sediment particle size distribution data to generate this PDF are available from McNeil and Lick (80). Finally, although the majority of particle transport occurs in suspension, bedload transport, potentially along with more complex river geometries to consider the effects of meanders, could be added to further improve real-world applicability of this model.

8.3 APPLICATIONS

This section discusses two potential applications for hydrokinetic energy extraction: in-situ sensing and remote energy extraction. In-situ sensing uses the technology in an indirect way, as a power supply for another necessary technology, a real-time river health monitoring system. Remote energy extraction is the use of hydrokinetic energy extraction in remote regions of developing countries. These are areas where a river resource is present and there is a need for low cost energy. The following subsections provide more details for the two applications.

8.3.1 In-Situ Sensing

The Columbia, Mississippi, and Yangtze rivers are just three examples of rivers that are impacted by humans daily. Countless other rivers are ecologically impacted and/or impaired, yet state and federal environmental agencies are unable to monitor all of them. The increase in global water demand and hydrologic changes due to global climate change further illustrate the need for advanced environmental sensors. For example, water in the Colorado River has not reached the ocean in the last 5 years due to an over-use by several states.

Global climate change, for some regions, has brought longer droughts and stronger storms (85). As researchers continue to understand the influence of hydrology on ecology and vice versa (86), water resource and environmental engineers need to monitor water quantity and quality in real-time to maximize water use efficiencies for satisfaction of water demands while maintaining the watershed biological integrity.

Current unattended remote automated technologies being used to monitor water quality require intermittent site visits, are expensive, and measure general parameters (i.e. dissolved oxygen, pH, temperature, nitrogen, redox-potential, chlorophyll, blue-green algae, etc.) from which environmental professionals can execute only basic assessments. Additionally, these technologies cannot detect emerging contaminants of concern, let alone at minute concentrations in real time. Since researchers and regulatory bodies rely heavily on water quality data to monitor river health, an inadequacy in the local monitoring device, such as the inability to detect the presence of emerging contaminants of concerns, reduces the quality of the assessments and places public health at risk. These effects on river biological integrity are occurring in ways we have yet to fully understand. Trace contaminants can bioaccumulate in organisms and biomagnify in the ecosystem. The current practice for measuring trace contaminants includes off-site and expensive means that involve sampling directly and lab analysis. Traditionally, these analyses are time- and labor- intensive and are susceptible to error because their concentrations in the environment are minute and constantly changing. Ultimately, to ensure the public health, remote sensors must be developed to monitor various contaminants in real-time in any watershed across the globe. Reliable power sources must be developed for these sensors in order to provide the necessary electrical input for both data collection and transmission.

Development of a hydrokinetic-powered environmental sensor would provide a foundation for understanding bio-electrochemical sensors and hydrokinetic energy extraction while furthering the technological capacity for real-time sustainable comprehensive river water quality assessments. This sensor involves microbial fuel cell technology for the bioelectrical sensor and employs a hydrokinetic turbine for a power source. The bioelectrochemical sensor utilizes the response of a bioelectrode (i.e. an electrode ladened with a biofilm of "stream" bacteria) to assess basic water quality parameters and detect emerging contaminant concen-

trations. Connecting the sensor to a hydrokinetic turbine provides a power source that is renewable and reliable. This method, for the first time, would realize an in-situ biological response (electrical signatures) of an ecological system allowing for an in-depth analysis and a comprehensive understanding of the system. Improving this technology could provide environmental researchers and regulatory commissions (such as the Environmental Protection Agency) with a powerful remote monitoring tool. This application is in the beginning stages; however, preliminary electrical signature data show promising results.

8.3.2 Remote Energy Extraction

Currently, about 54% of households in Ghana have access to electricity, with rural access at only 24.9%, compared to 81% for urban households (87). A review of the Ghanaian topography map and population density map (88; 89), in combination with knowledge of existing Ghanaian electrification, demonstrates that Ghanaian electrification actually neglects over 50% of the overall population (90). (Representative maps are given in Appendix I.) As part of the UN Millennium goals, the national development planning commission of Ghana has outlined energy development as a priority, since it is tied to so many aspects of general well-being, such as health, prosperity, and gender equality (91; 92). Hydrokinetic power (HKP) systems avoid many of the problems encountered with hydropotential power (HPP), such as large population displacement, high infrastructure costs, and large decreases in downstream flow. They utilize a simple design, and can be maintained by local residents for low cost. Furthermore, HKP can be easily installed into a stream and modified with small effort to enhance energy extraction. HKP and small HPP are competing technologies due to their similar power extraction amounts, but the benefits of HKP far outweigh HPP, due to HPP systems' more complicated infrastructure and associated maintenance issues.

Approximately 70 sites, with a total potential of 800 MW, have been identified for small HPP in Ghana; however, none of these sites have been utilized to date (93; 94). A main reason for this is lack of necessary policy backing, while other reasons include minimal small HPP technology knowledge and absence of financial support (94). The lack of policy backing for HPP is largely due to the amount of infrastructure cost (in terms of economics, social

impact, and the environment) compared with the amount of energy available from the system. HKP technology has a lower cost per unit of energy extracted than HPP systems, and is economically comparable with other distributed systems, such as solar, making it a better candidate for policy support. It should be noted that the micro hydropower outlook in Ghana was explicitly developed for small hydropotential, but the projection is that these sites will be more suitable for HKP (95). The stream level can decrease during the dry season, making HKP much more viable in this setting since it involves turbine placement in the stream to extract flow or kinetic energy, and does not require a dam or weir structure to create a reservoir. This results in fewer changes to the downstream locations, such as not completely removing the water source. Additionally, the implementation of a renewable energy law is under review in Ghana to provide support for future renewable energy development and expansion of rural electrification (95). Policies are shifting to give renewable energy technologies, like HKP, further support by creating opportunities for investment in them.

Because of the system's less complex infrastructure, HKP has been identified as a key remote energy technology for developing countries (96). HKP has been a proven technology in certain isolated cases (31; 36; 38; 97; 98). A successful rural application of HKP has been in operation for at least a decade to provide electricity to a health center in central remote Brazil (99; 100). It has already improved quality of life in this region (100). Furthermore, HKP can help improve access to electricity in peri-urban and remote rural areas. Studies have shown that it is cheaper to electrify communities using decentralized systems like hydrokinetic power when they are more than 20 km from the electric grid (101).

Electricity in Ghana

Large scale HPP, in the form of two dams, has been a significant contributor to Ghana's energy sector, providing more than 1100 MW of the total 2200 MW supply in the country (90). However, these types of power plants are not the focus for Ghana's future energy development due to both environmental and social reasons (90). Severe environmental impacts have been exhibited by the two dams in operation. 243,000 hectares of cocoa plantation have been flooded, and two million oil palm plantations have been destroyed. Additionally,

lagoons naturally supplied by the Volta River dried up, allowing aquatic weeds to grow. This has slowed the river, and these weeds have provided a place for disease vectors to form. One result is that the lower part of the river has been declared a schistosomiasis endemic area (95), where the disease rate tripled within a year (102). Further environmental impacts have not been investigated for both large and small HPP in Ghana, but could include decrease in fish populations, flora and fauna destruction from changes to the overall flow regime and temperature, and a decrease in bird populations (6; 7; 33; 103).

The best area in Ghana to implement these technologies is in the northern region for two reasons: 1. it has the highest poverty (104); and 2. it has the poorest electrification (90). The population density (88), in combination with the river/micro hydropotential (95), indicates that the White Volta River is a viable option for HKP implementation. During the dry season, this river does dry up; however, partial electrification is still an improvement, and addresses many of the reasons why this technology is needed, such as residential lighting and vaccine refrigeration. The Ghanaian government shares this perspective: for example, the Bui Dam is scheduled to be operational in February 2013. It will provide around 300 MW after having been constructed for approximately $400 million, but is only expected to operate at 25% capacity due to the dry season.

Regulatory and Policy Framework

In Ghana, the Public Utilities Regulatory Commission (PURC) was established in 1997. PURC is an independent body set up to regulate and oversee the provision of the highest quality of electricity and water services to consumers. The Energy Commission (EC) was also created in 1997, and is required by law to regulate, manage and develop the utilization of energy resources in Ghana, primarily through providing the legal, regulatory and supervisory framework for all providers of energy in the country. More specifically, this is done by the granting of licenses for the transmission, wholesale, supply, distribution and sale of electricity and natural gas, including refining, storage, bulk distribution, marketing and sale of petroleum products and related matters. In order to introduce competition in the power sector, the government has introduced Independent Power Production (IPP) schemes and reforms, such as increasing low electricity tariffs towards international levels. Ghana's

current low tariffs and the delays in establishing a sustainable tariff regime are discouraging many potential power sector investors.

Since the mid-1980s, the Ghanaian government has been financing projects using small levies on petroleum products. The money is paid into an energy fund and used to promote renewable energy and energy efficient projects. A strategic national energy plan was adopted earlier this decade, and covers the period 2006-2020. In this plan, government hopes to achieve 15% penetration of rural electrification through decentralized renewable energy by 2015, expanding to 30% by 2020. The energy plan also sets a target of 10% overall contribution from renewable energy by 2020. Presently, there is no clear policy or regulatory framework to support this renewable energy investment. However, a renewable energy law is being drafted and will soon be passed to parliament for adoption.

Implementation Details

The river velocity will depend on the site in which this technology is placed, and, in turn, the resultant turbine specifications. For an initial HKP system, we will assume 500 W (100 W per turbine) of energy extraction is needed and a 0.3 m/s river velocity is present. With an initial outlet velocity assumption of 0.1 m/s, the HEE turbine would need to have a 10 m swept area.

A potential energy extraction scheme for implementation of the technology using hydrokinetic turbines is shown in Figure 88. It contains a series of turbines connected to a common shaft, which is then connected to a generator and storage system, followed by a possible electrical connection to the local village. It is likely that implementation of a simple storage/charging system (such as batteries) will be appropriate, since the HEE turbines are constantly extracting energy. This is commonly known as a Stand Alone Power System (SAPS). The stored energy can then be collected by local inhabitants for individual use. The turbines can be constructed using common materials such as fiberglass and steel rods for the blades and shaft, respectively. However, if aluminum is more readily available, it would be the blade material of choice, because it is light, less toxic, and easily formable.

It is calculated an average household will need 86.4 kWh annually. Based on a population density of 45 $people/km^2$ and a hydrokinetic energy system able to reach those within a

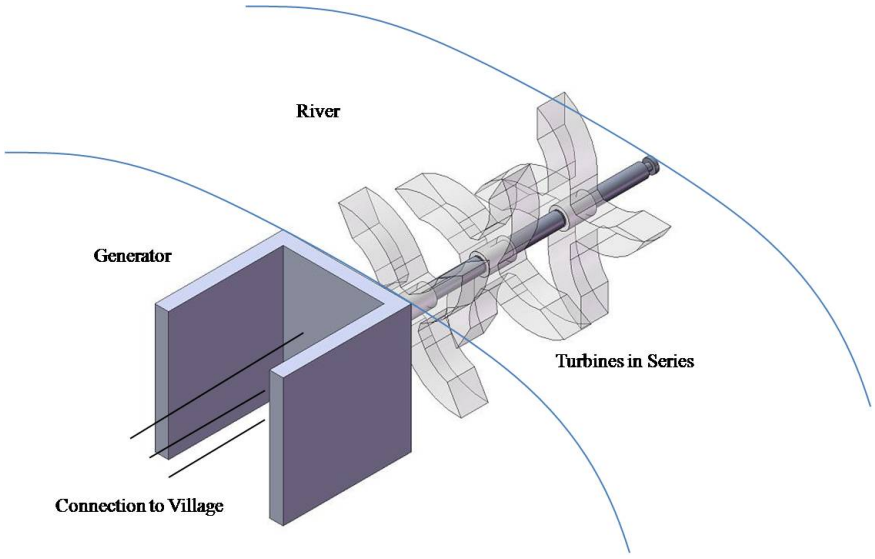

Figure 88: HKP Schematic for an Energy Extraction Site.

5 km radius, the amount of households reached per system is 693, assuming 5 persons to a household. To meet this scenario, 16 turbines that extract 500 W each need to be installed at each site.

From a high level, the cost breakdown of HKP can be disaggregated into material, installation, labor, and maintenance costs. Per turbine, the material cost is estimated at \$360. Installation costs, including site preparation, are expected to be \$4,750 per site, and labor costs per site total \$1,276. The total expected cost per site, calculated with an average of number 16 turbines per site, is therefore \$12,743.90. Maintenance and overhead costs are expected to be 5.5% and 2.5% of annual revenues, respectively. To achieve a reasonable break-even period (since the premise of this energy system is to function at a non-profit level), the cost to users would be \$0.035 per kWh, giving a break-even point of about six years.

Discussion

The implementation of hydrokinetic turbines for energy access in rural Ghana could benefit society in many ways, thus contributing toward a global impact. Energy access can

make everyday tasks simpler and safer. It also has a direct link to a community's health. For example, electrification is important for rural health centers in maintaining vaccine refrigeration. Cheap, widespread electricity directly addresses the UN Millennium goals of eradicating extreme poverty and hunger, promoting gender equality and empowering women, and improving maternal health.

HKP's innovation succeeds where previous methods fell short. The cost of running power from the power producing regions of Ghana to the far reaching rural areas is cost prohibitive. By bringing the power generation facilities closer to the end user, HKP could provide an opportunity for even the poorest of regions to gain access to affordable power. The cost savings is anticipated to be 2.5 cents per kWh, which is a substantial amount. It is anticipated that the government of Ghana would subsidize the poorest of consumers, similar to their current policy for the established utilities, therefore allowing even those with the greatest need access to electrical power (90).

In addition to these important benefits, as stated throughout the dissertation, it is also crucial to ensure environmental sustainability, another of the UN Millennium goals. Preliminary studies show that HKP generation can result in minimal environmental impact. Using one metric, Poff et al. have defined the parameters of any functioning stream as the flowrate, average flowrate over a given time period, amount of time for excessive or recessive flows, flow predictability, and flow stability (6). In reviewing the potential changes to these parameters, HKP will produce an overall smaller effect on the stream, with, for example, less than a 70% flow rate decrease compared with large and small HPP. It is also proactive to implement such an environmentally benign energy type in a developing country, keeping overall global emissions and CO_2 contributions under control. Developing countries that lack a solid energy infrastructure generally contribute less to global climate change, but will be affected most by climate change. They cannot afford to develop an infrastructure that might be controlled or prohibited by future environmental standards.

9.0 CONCLUSIONS AND FUTURE WORK

9.1 CONCLUSIONS

This work summarizes the state of the art in hydrokinetic energy extraction. It presents the governing principles, develops a CFD model with experimental validation to further the understanding of this technology, demonstrates potential environmental impacts, and discusses both implementation issues and applications of the technology. The significance of this work is that it provides a framework for advancing our understanding of and ability to implement hydrokinetic energy extraction technologies. Flow patterns associated with hydrokinetic energy extraction were studied and a model is presented that provides an in-depth flow analysis of these systems. This model more accurately describes flow patterns that result from new, emerging aquatic energy extraction technologies.

The CFD model was checked thoroughly through comparison to model principles, mesh sensitivity verification, and experimental validation. While the comparison to model principles was a qualitative analysis, the mesh sensitivity was advanced to an average skew of 0.0506 and a convergence in the midpoint velocity to 0.2 m/s. The experimental data was gathered through a flume test rig and the use of velocity vector mapping around the turbines with a PIV system. When the PIV data was analyzed, it was found that a CFD-VOF model was more appropriate, and gave an offset of 0.0124 m and 15% error (a marked improvement in hydrokinetic turbine PIV data in comparison to other HEE CFD models).

This validation allowed for presentation of three dimensional models. In addition to more accurately describing more of the flow field, these models allowed for simulation of more complex turbines, such as the squirrel cage Darrieus turbine and the Gorlov Darrieus turbine. The non-VOF model was used in these models due to the high computational

expense of a 3D VOF model. This non-VOF model produced an additional 5% error and gave an offset of 0.0155 m. Even with the additional error, the insights gained from these models is a significant contribution to the literature. Previously, no detailed CFD models have been presented for squirrel cage Darrieus turbines and Gorlov helical Darrieus turbines, especially models that have been rated with offset and error.

The new insights gained from the CFD models can be used to improve the efficiency of HEE devices and to minimize their environmental impact. One measure of this is predicting fish passage with the hydrokinetic turbines in place. Using parameters for brown trout swimming patterns, and their avoidance of high turbulent regions, the flow field with a turbine in place can be reviewed with its relevant turbulence regions. With the x-direction as the dominant flow and fish swimming directions, the x-component of vorticity is examined and reveals a low and high turbulent region at the leading edge of a squirrel cage Darrieus turbine. This would likely indicate a brown trout would avoid it; however, further research is needed for this fish type and to expand the model to include others.

As another measure of the environmental impact of HEE, an LCA was performed. Looking further into the environmental impacts model, GHG emissions have not previously been quantified for any HEE system. This work, through the use of LCA, presents GHG emissions for a Gorlov HEE system. The results are compared with that of small hydropotential power, and coal, gas, and nuclear plants. Small HPP is a comparable system to a Gorlov HEE system, while the other types are viewed as a mix of energy types. Details are presented to provide a benchmark in HEE inventory analysis. Gorlov HEE was found to have similar life cycle impacts to that of small HPP, and overall lower impacts than the other energy types. Furthermore, the choice of fiberglass for turbine blades warrants more research. Fiberglass materials have been found to be rather toxic, thus highlighting the need for a suitable replacement.

The results of both of these studies show that additional environmental metrics are needed. Similar to large-scale hydropower, the issues of fish and local river ecology health still exist for hydrokinetic energy, and so a new LCIA impact category is needed. Using estimated fish passage from HEE CFD and fish swimming data, a statistical metric could be constructed to give values for an impact category associated with aquatic technologies.

These methodologies can be applied to many forthcoming designs, making them useful tools for the field.

In addition to these engineering and environmental analyses of HEE, there are many other areas that must be explored before hydrokinetic power can be successfully implemented. Two of these areas (policy development and sediment transport) were investigated in more detail. In examining renewable energy policies, it was found that these types of projects are often difficult to implement both because of the bureaucracy associated with their startup, and due to policy deficiencies in their funding and operation. Policies to encourage small hydropower development can be instituted through enhancement of the decision-making processes, comparisons with other related energy projects, improvements to environmental management, and increases in benefit sharing.

Quantifying sediment transport is also an important prerequisite for the implementation of HEE. Therefore, a 2-dimensional (non-transverse) model of suspended sediment transport for more general rivers (such as those that might contain a dam or are sites for new aquatic technology) was presented. Many of the current models are only valid for shallow rivers with use-of-depth averaging. The hydrodynamic model for river flow is derived from the Navier-Stokes equations and is combined with the particle equation of motion for suspended particles given by Shams et al. (46). For comparison, the sediment transport in FLUENT^{TM} was also modeled. The models are consistent with one another and give results consistent with expectations. These models can offer valuable information about sediment transport. Additionally, the sediment concentration following Dietrich et al. is modeled (82). The model was found to be sensitive depending on site data, but lends itself to enhancement for future development.

In addition to these implementation issues, two applications for this technology were reviewed: in-situ river health monitoring and remote energy generation. There is a need to develop a better river health sensor, since the current methods are time-consuming, expensive, and not entirely accurate. A sensor that uses microbial fuel cell technology to detect electrical signatures given by contaminants could be powered by a hydrokinetic turbine. This would provide readily accessible, accurate data with a device that is powered by a renewable, reliable source. Hydrokinetic energy extraction can also be used in remote areas of develop-

ing countries where there is access to a river. In Ghana, many sites have been identified for small HPP which could also be used for HKP. In the past, these sites have not been utilized; however, the Ghanaian parliament is setting forth new policies to remedy this. HKP can be implemented easily into rural Ghana, due to its simple mechanical to electrical conversion system and ease of electrical storage. Possible implementation in the White Volta region is discussed and a general HKP scheme for the region is presented. There is a clear need for remote energy extraction in rural Ghana, and HKP is a robust technology that can alleviate this deficiency.

9.2 FUTURE WORK

Hydrokinetic energy extraction is a young field, and there are many fundamental areas of investigation beyond those already discussed in this dissertation that should be developed further.

9.2.1 Structural Issues

In using a new technology in any environment, a material analysis must be considered. In addition to more basic concerns with materials such as strength, elasticity, and low to no chemical interaction or off-gasing, there are also challenges with debris build-up on the turbines, which can be taken into account with material selection. Another structural concern is vibration control, which is more present among the vertical axis cross-flow turbines, such as the squirrel cage and Gorlov (helical) Darrieus turbines. This is present when using hydrokinetic turbines in environments where hydrodynamic forces act on the blades and fluctuate with rotation. The hydrodynamic force changes cause periodic loads on the turbine, resulting in vibration or torque ripple during operation (37). Similar problems have been identified with wind turbine use, where active blade control can be used to control vibration, which can boost turbine efficiency and reduce fatigue (105–112). Finally, with hydrokinetic turbines increasing in use in tidal energy extraction, mooring assessment has become a necessity (in

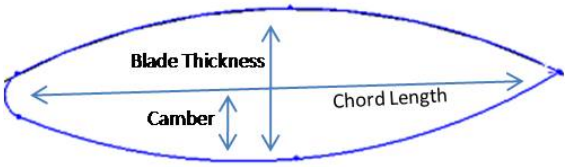

Figure 89: Hydrofoil Design.

terms of the best structure considering internal stresses and overturning moments) to secure a hydrokinetic turbine for operation (113).

9.2.2 Optimization

Additionally, turbine efficiency can improve with blade shape optimization. There are three main specifications that go into a hydrofoil design: chord length, thickness, and camber, as shown in Figure 89. Some analyses compare different airfoils (114; 115), while others select an airfoil (36; 116) for use in hydrodynamic scenarios. There is not a consensus on whether the camber should be altered, and furthermore, there is no ideal hydrofoil shape presented for hydrokinetic turbines. In addition to the blade shape, the use of hydrokinetic turbine augmentation can improve turbine efficiency, and has proven successful (37; 38; 51). (This was also discussed in Chapter 2.)

Furthermore, turbine blade shape optimization could be expanded to better match turbine geometries to the environmental metrics regarding hydrokinetic turbines in the environment. Optimization is based on varying the blade shape through blade thickness and camber, and quantifying the vorticity for each. The squirrel cage Darrieus turbine is a good candidate for this because of the extraction potential combined with the simplistic design and operation principles (36). One example of potential blade thickness and camber variations for five designs is shown in Figure 90, where the camber is slightly adjusted for each design. This also adjusts the blade thickness, since one is not independent of another. To conduct a true optimization, an objective function must be created that balances the magnitude of the

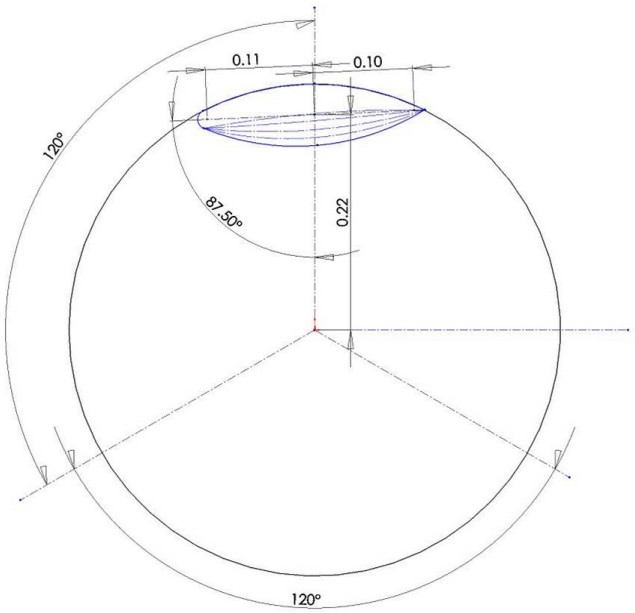

Figure 90: Hydrofoil Variation with Blade Thickness and Camber.

energy extraction with higher vorticity near the turbine blade. The higher vorticity rating is derived from the Cotel et al. study for brown trout (32); however, this parameter can be expanded to other fish types and organisms.

Along with vibration and blade shape optimization, there is an optimal amount of turbines and an optimal turbine arrangement in a full scale hydrokinetic energy extraction system that should be determined. This is somewhat location dependent and is sensitive to array effects. Further analysis is required to determine what these effects are, and how they reduce or enhance each turbine's energy extraction. For example, if there are two turbines located side by side perpendicular to the flow, each turbine may cause increased velocity for the other, increasing their energy output. However, having two turbines one after another perpendicular to the flow is obviously going to decrease the extraction amount for the second from decreased river velocity if it is placed too close to the first.

APPENDIX A

FLUME DRAWING PACKAGE

The following drawings are a complete package to construct the flume. Each part, with the exception of the foam piece and gates, are made from 0.5" thick acrylic sheet. The gates are constructed from stainless steel and the foam is a rubber material.

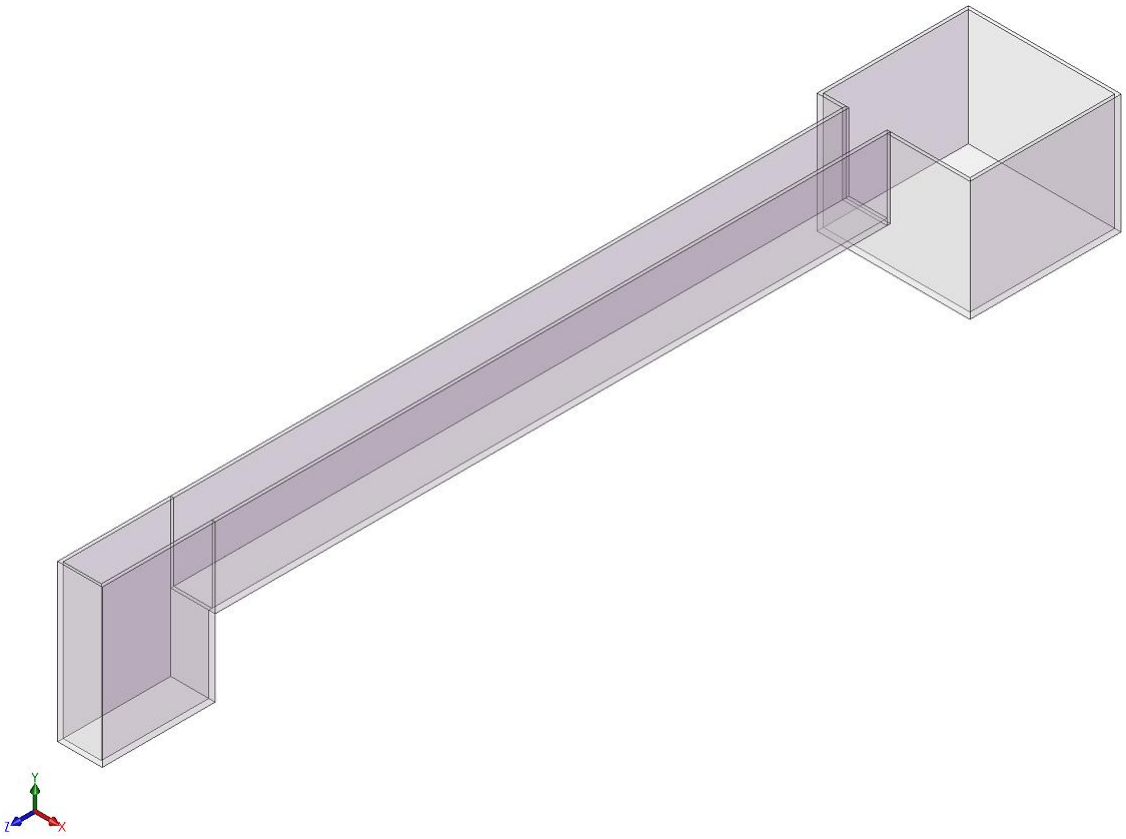

Figure 91: Flume Schematic, Complete with Flume Channel and End Reservoirs.

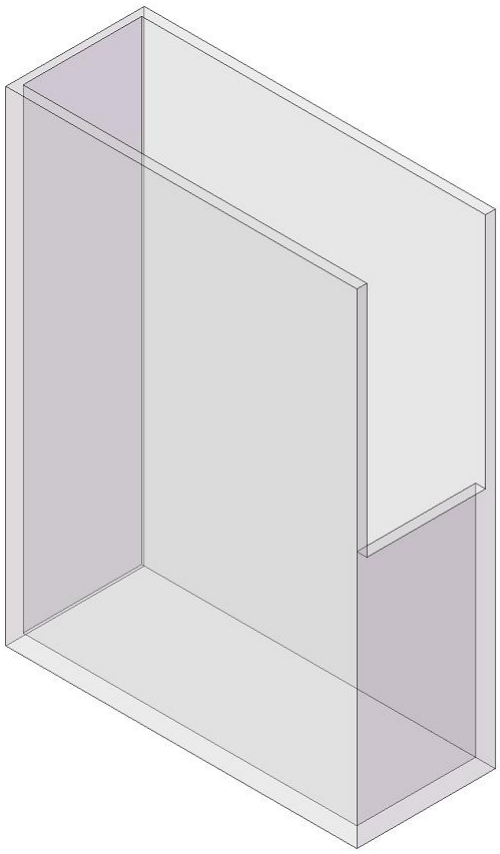

Figure 92: Feed or Overflow Reservoir.

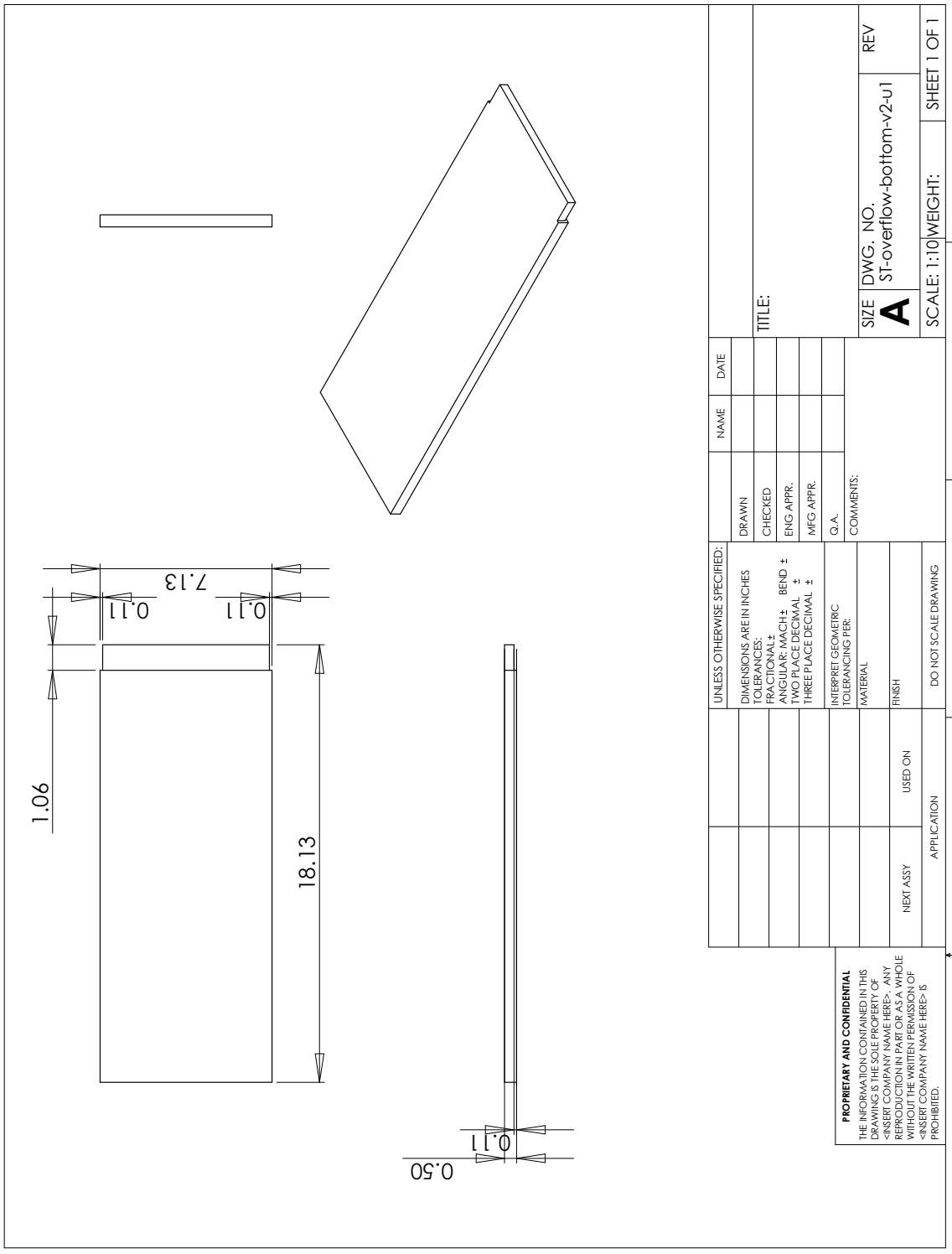

Figure 93: Overflow Reservoir Bottom Part (Version 2, Update 1).

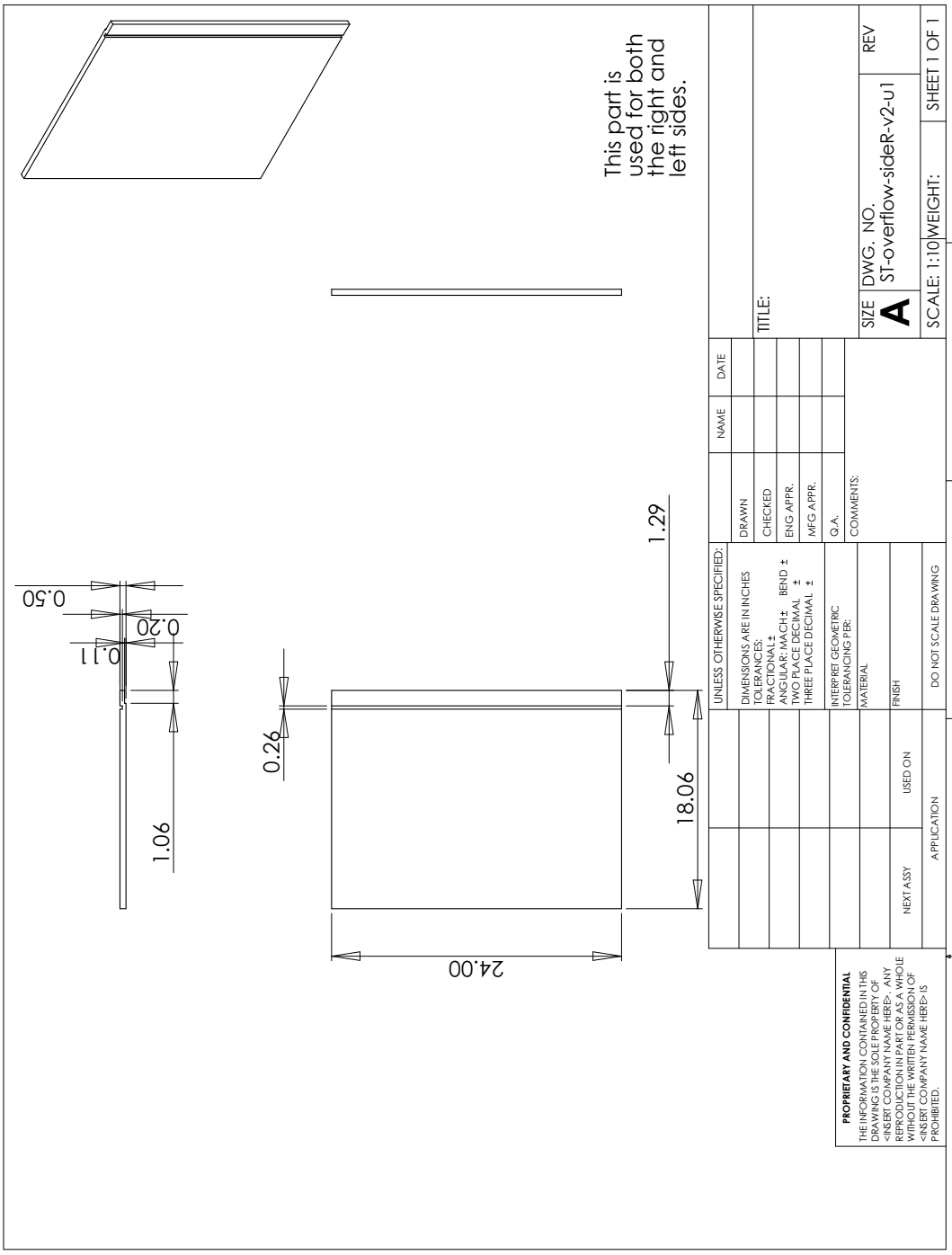

Figure 94: Overflow Reservoir Side Part (Version2, Update1).

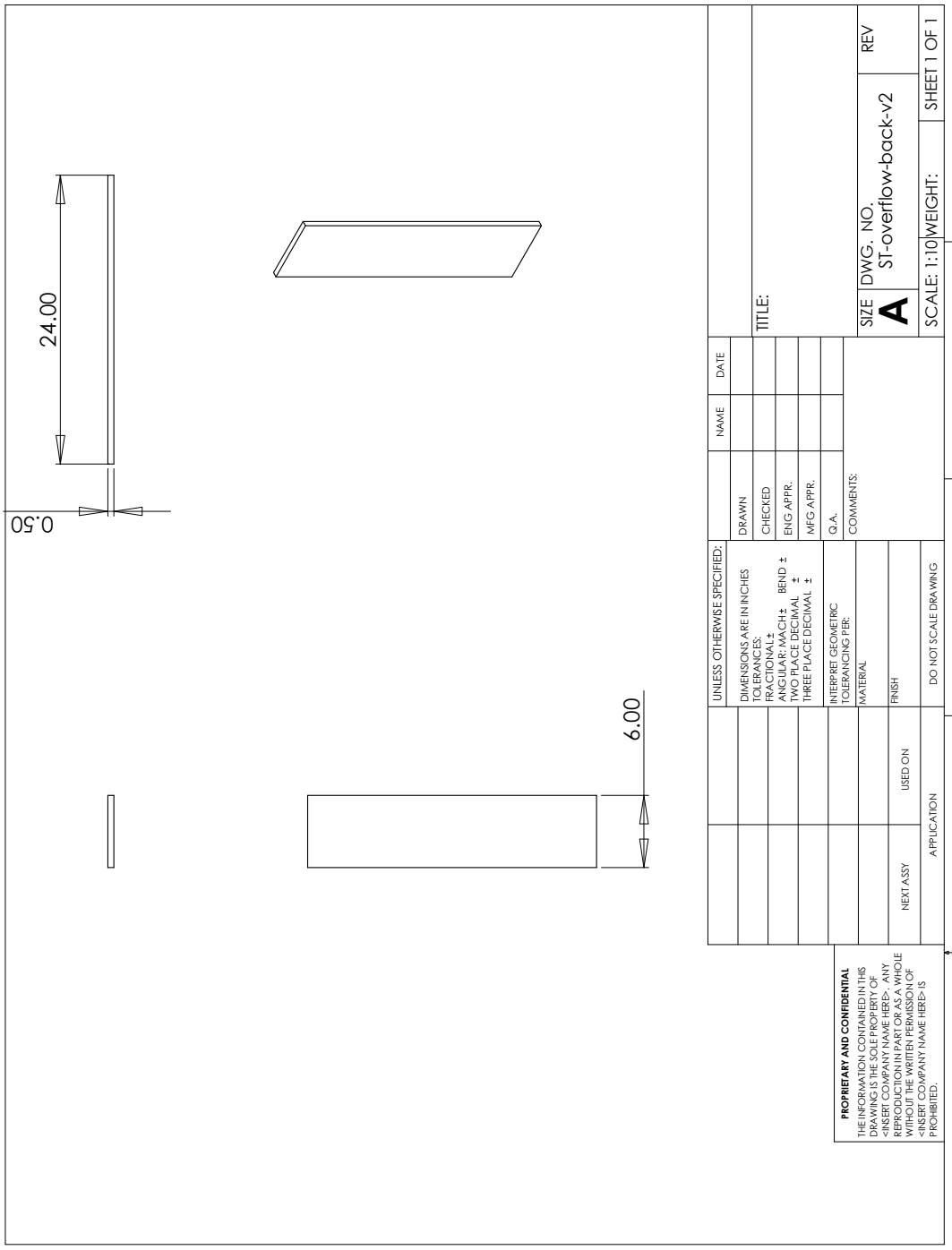

Figure 95: Overflow Reservoir Back Part (Version 2).

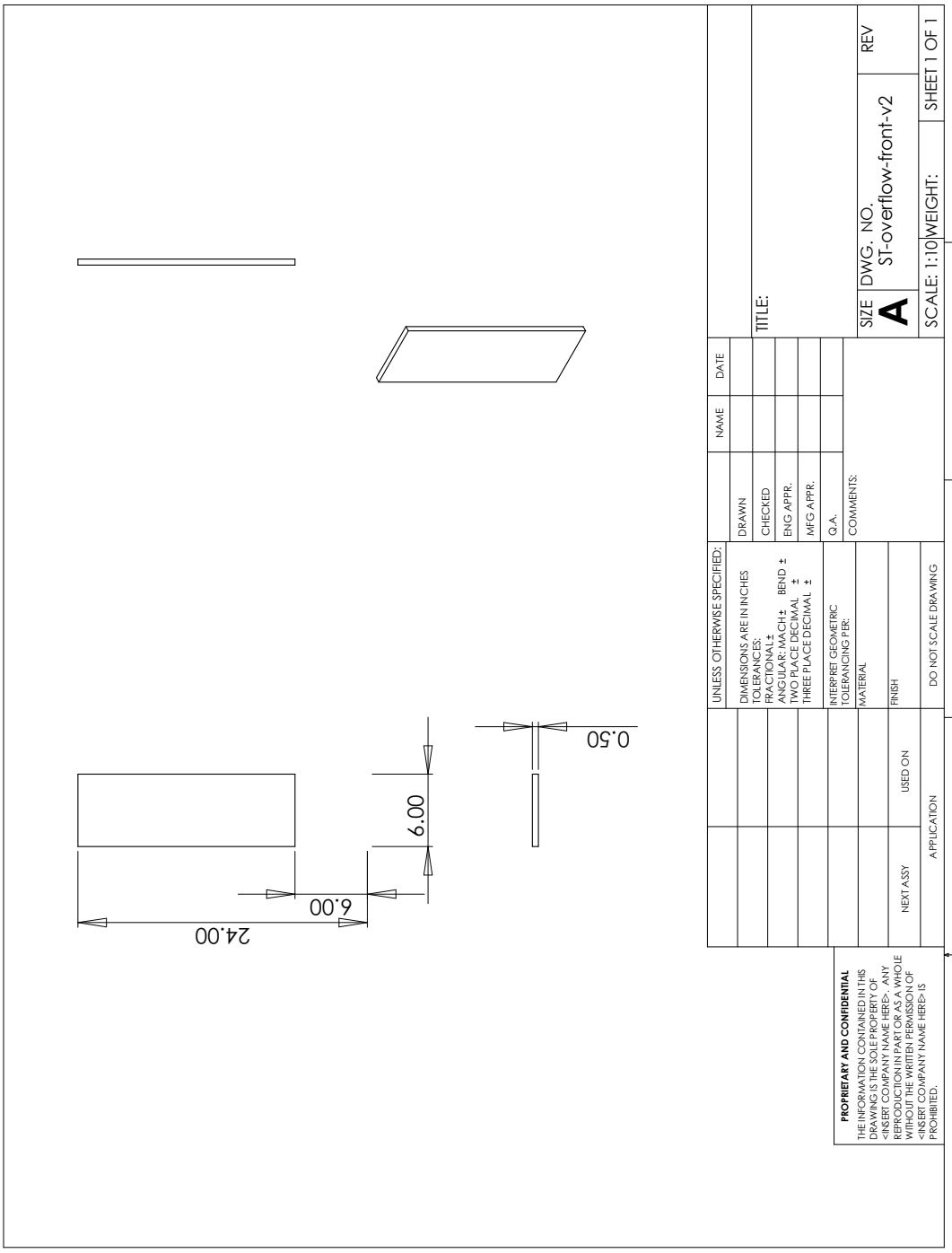

Figure 96: Overflow Reservoir Front Part (Version 2).

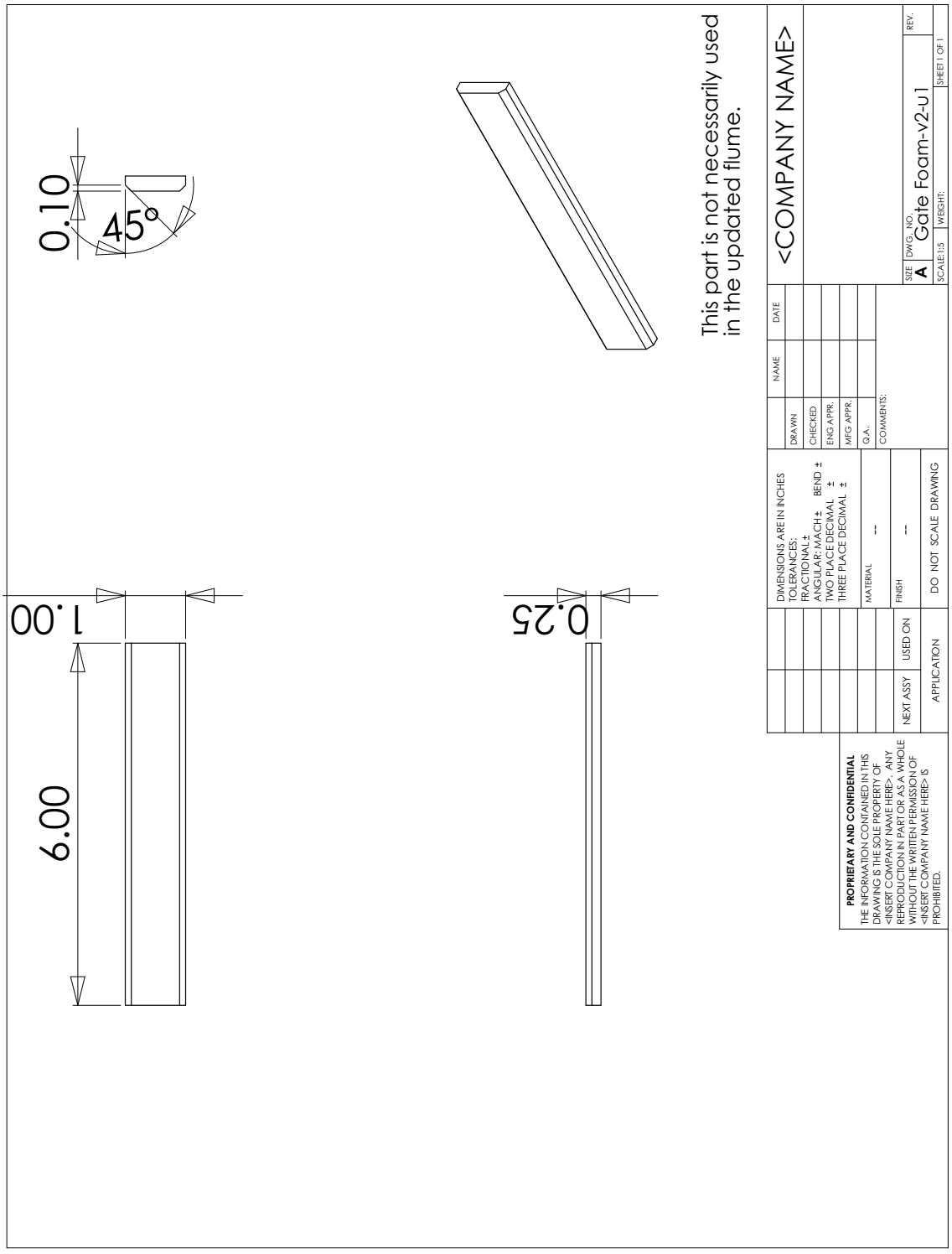

Figure 97: Gate Foam Part (Version2, Update1).

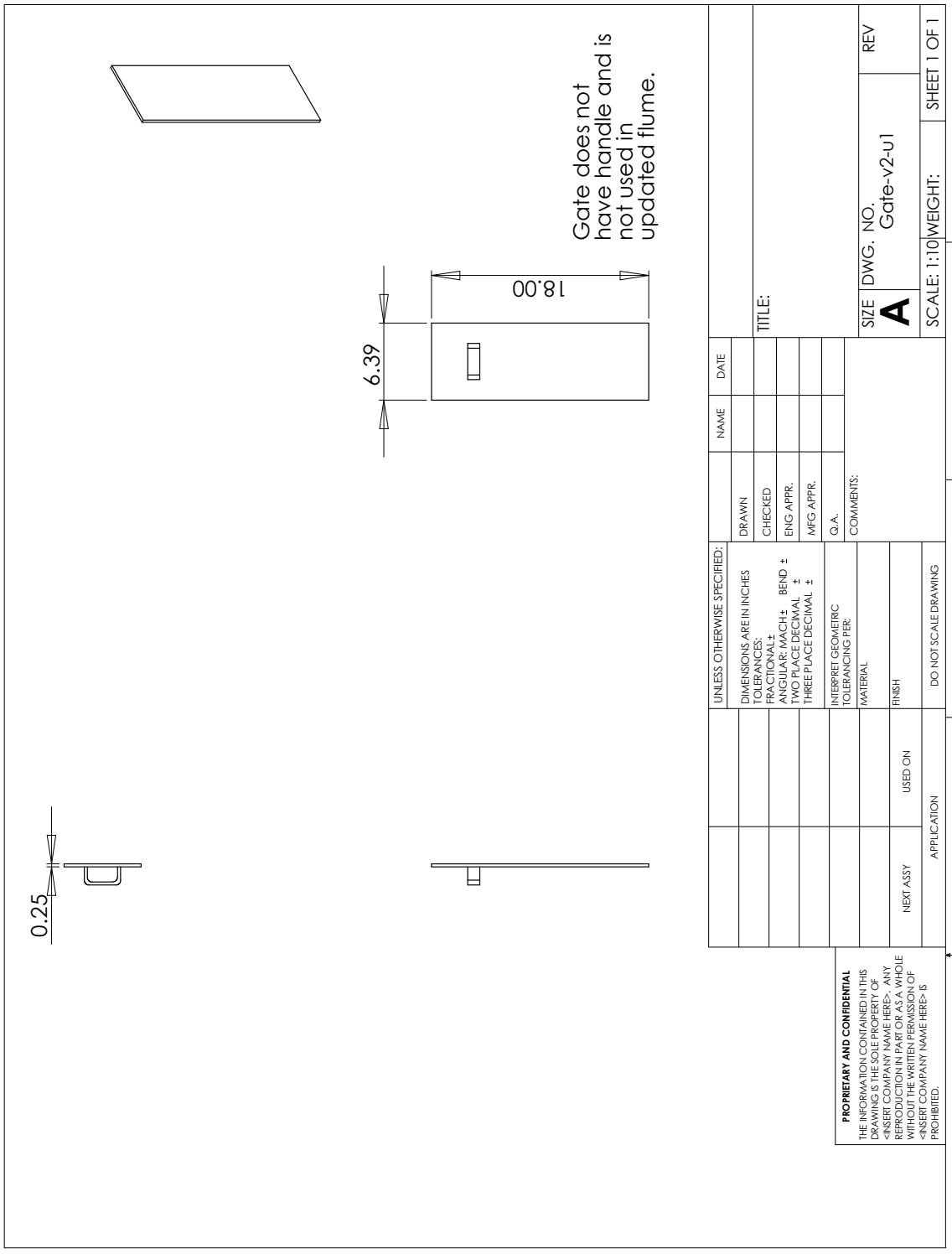

Figure 98: Gate Part (Version2, Update1).

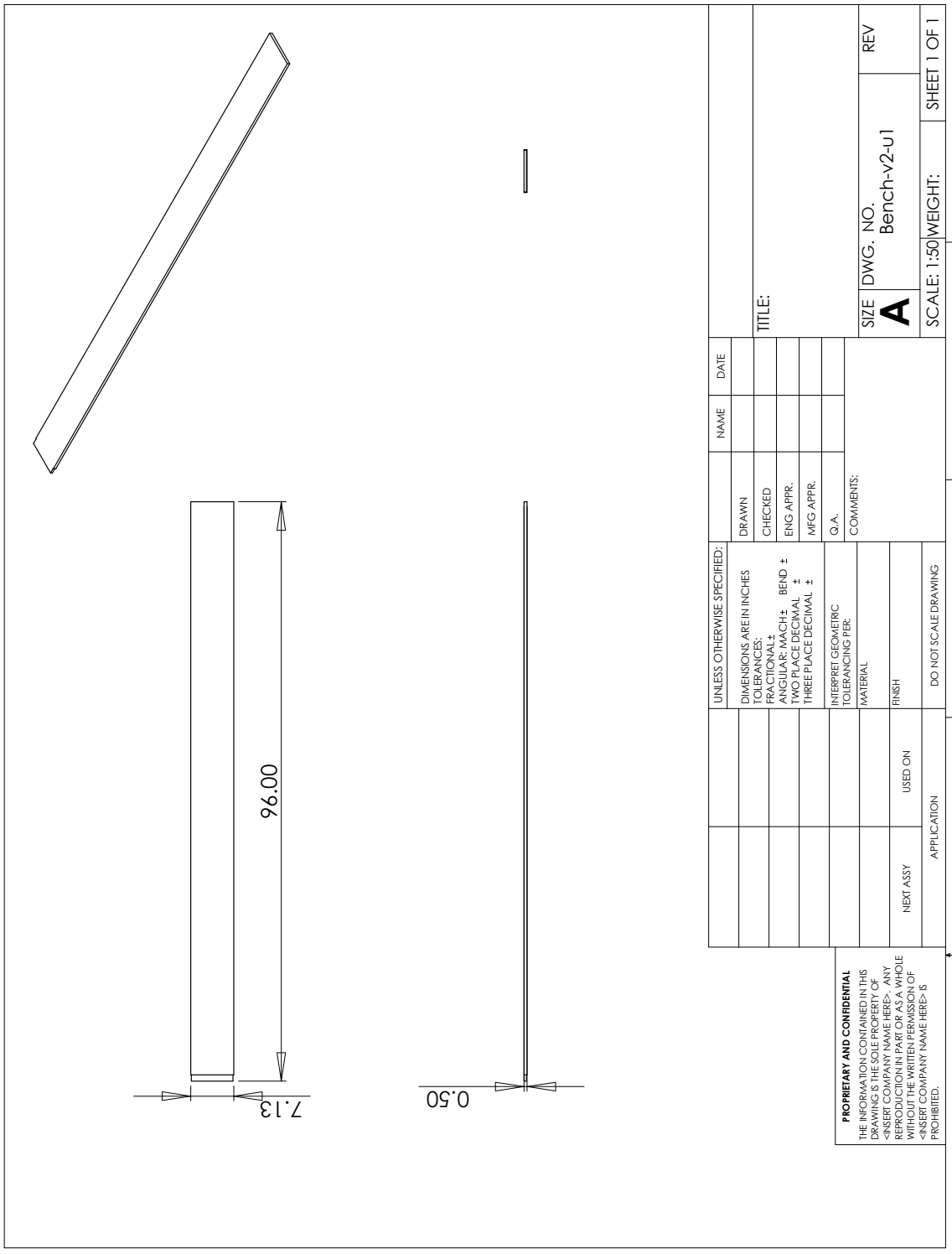

Figure 99: Channel or Bench Bottom Part, (Version2, Update1).

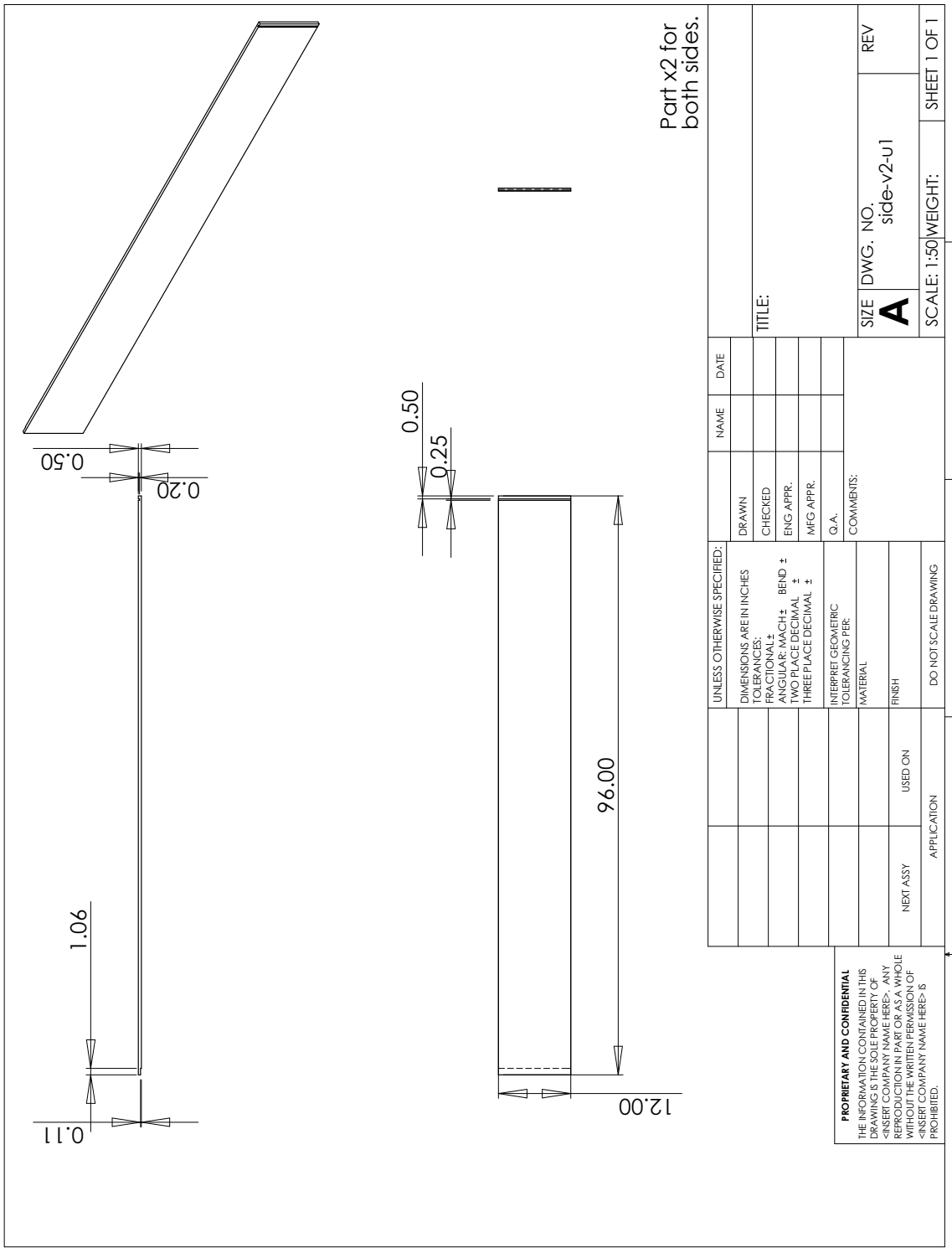

Figure 100: Bench Side Part, (Version2, Update1).

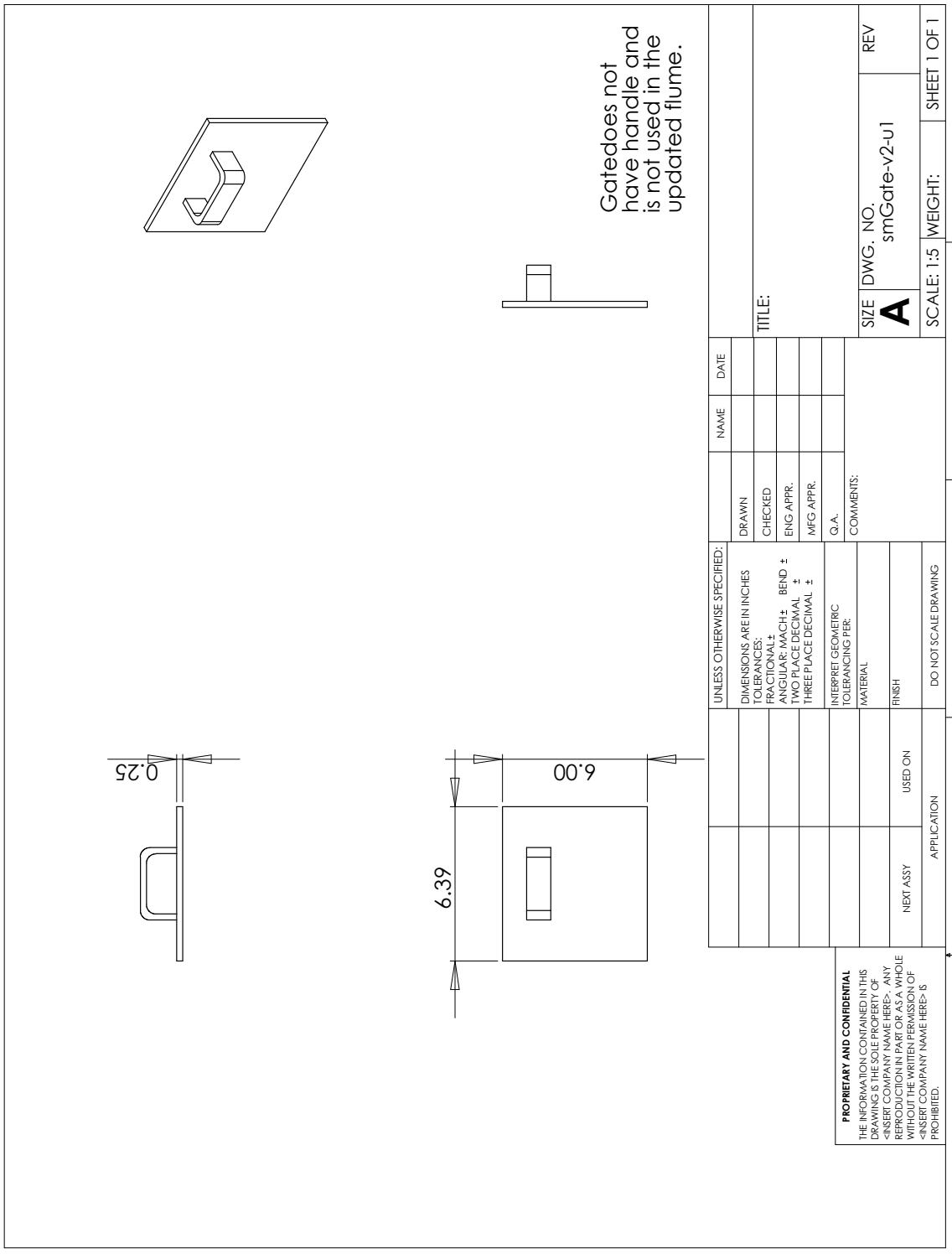

Figure 101: Small Gate Part (Version2, Update1).

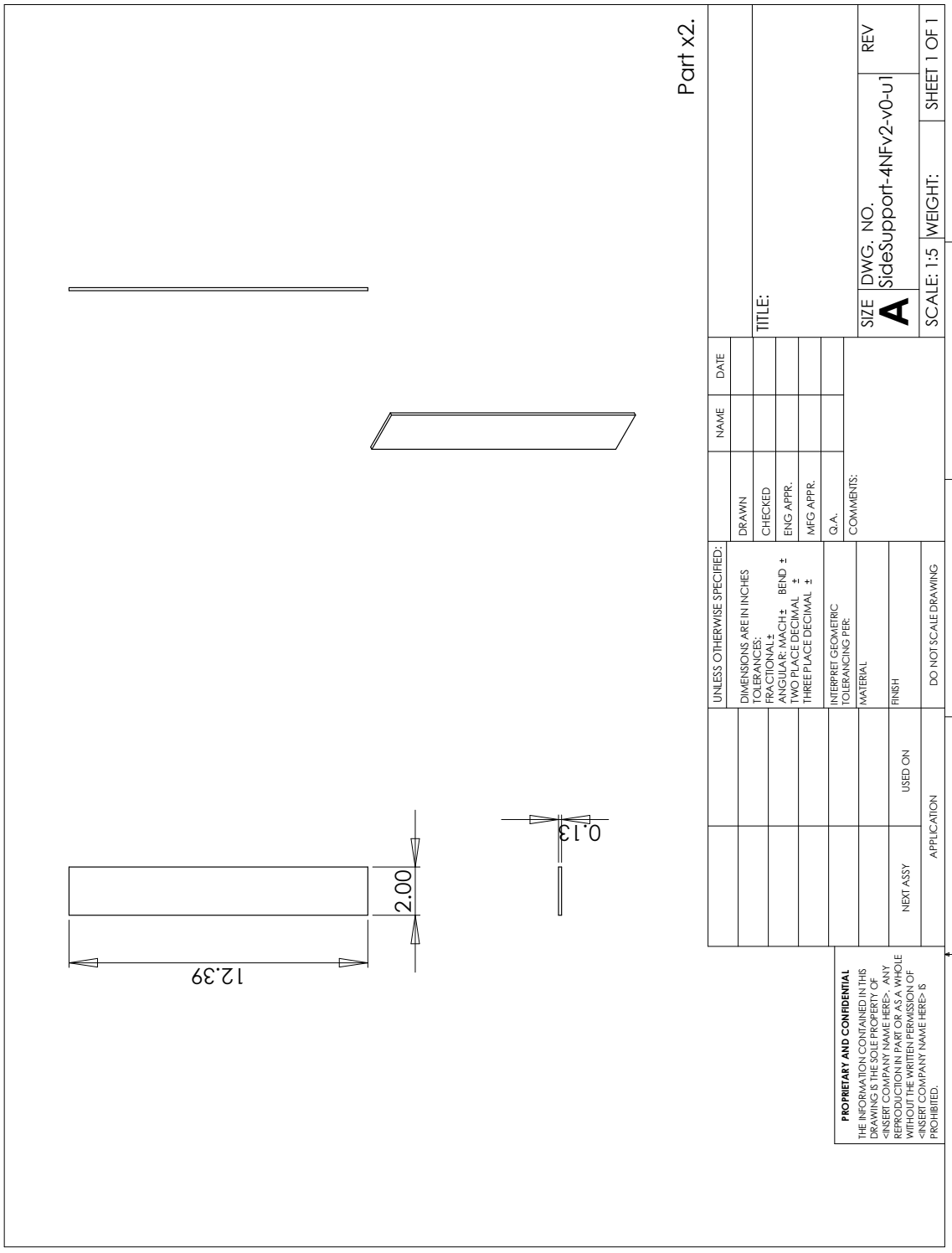

Figure 102: Channel Side Support Part (4NF, Version 2, Version 0, Update1).

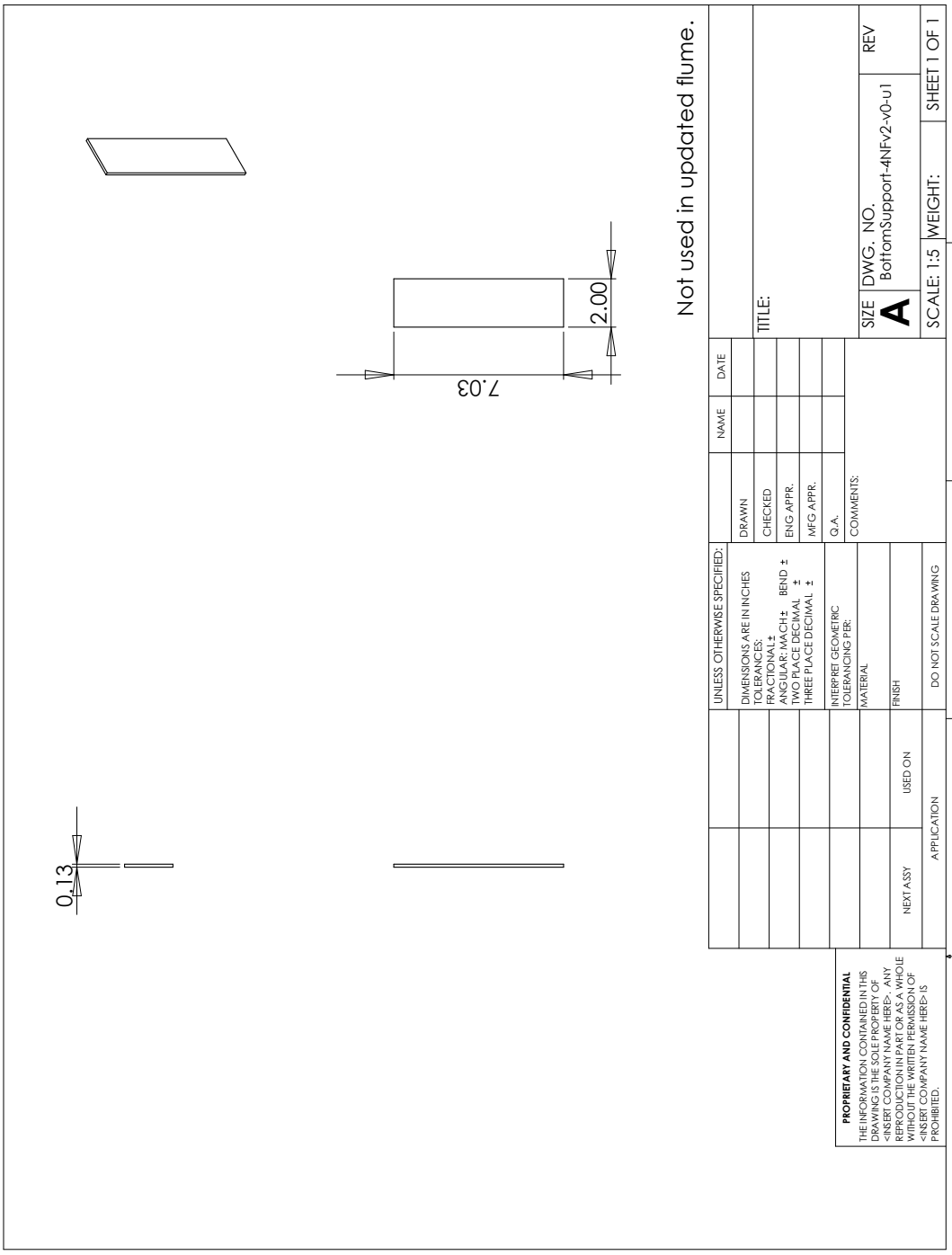

Figure 103: Channel Bottom Support Part (4NF, Version 2, Version 0, Update1).

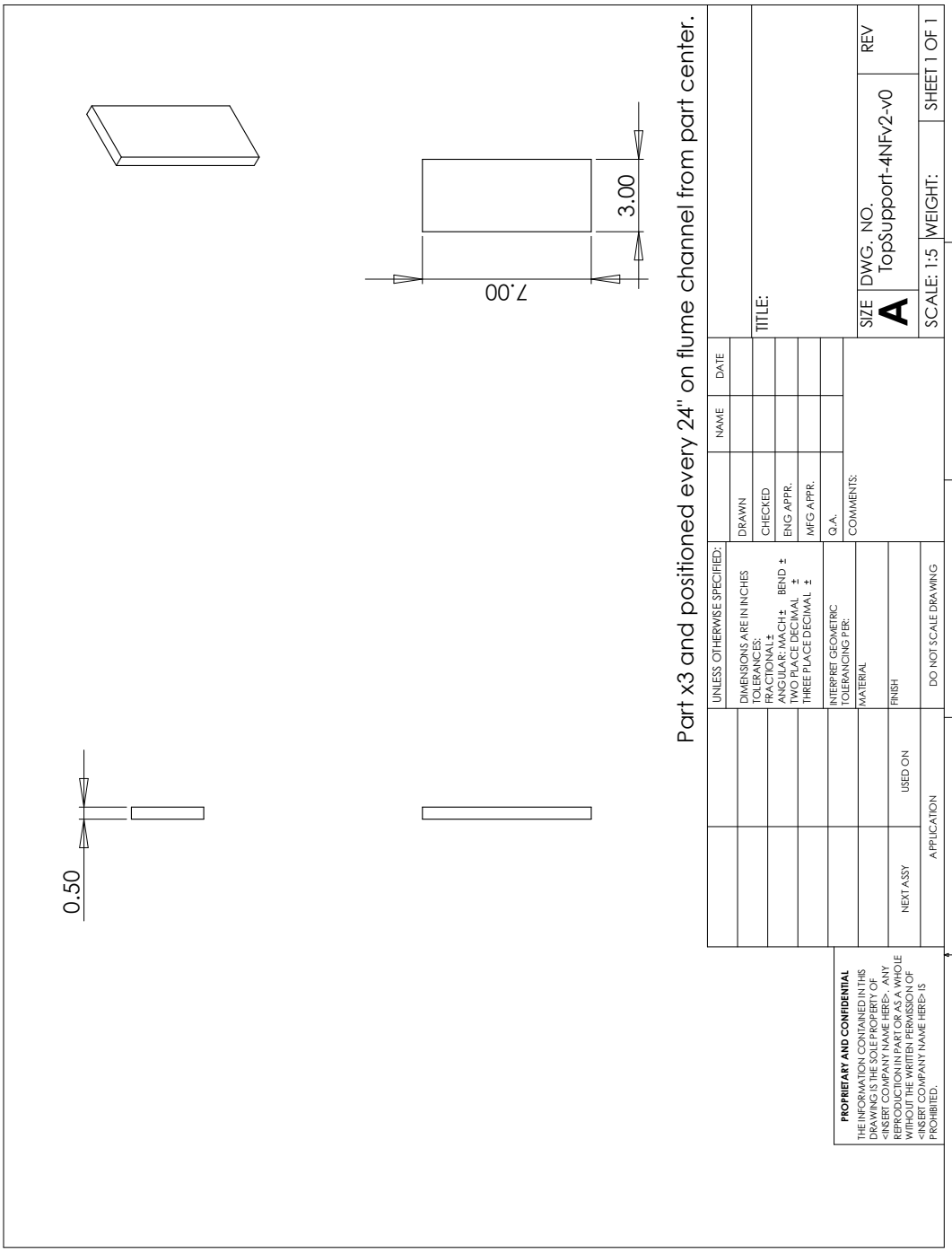

Figure 104: Channel Top Support Part (4NF, Version 2, Version 0).

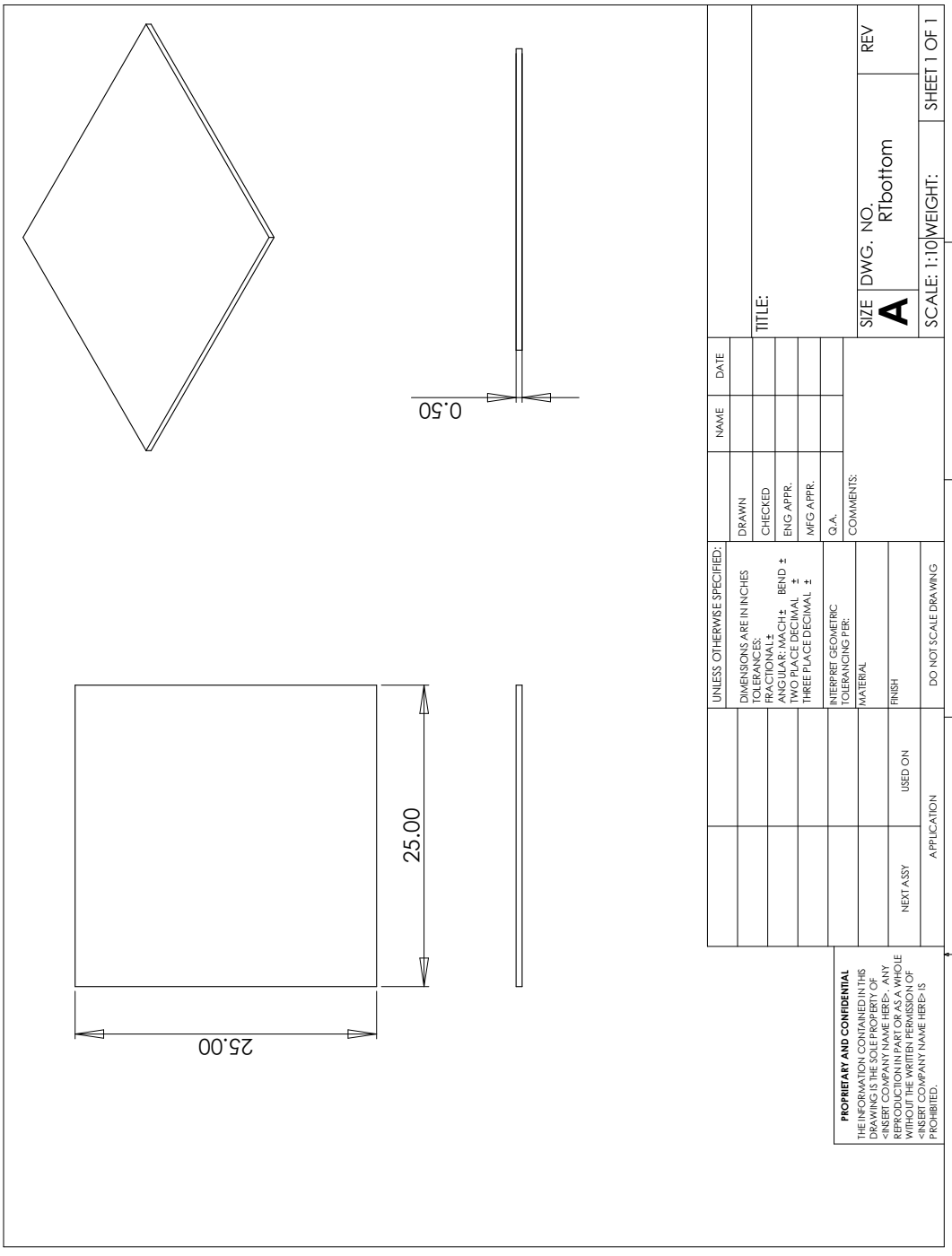

Figure 105: Reservoir Return Tank Bottom Part.

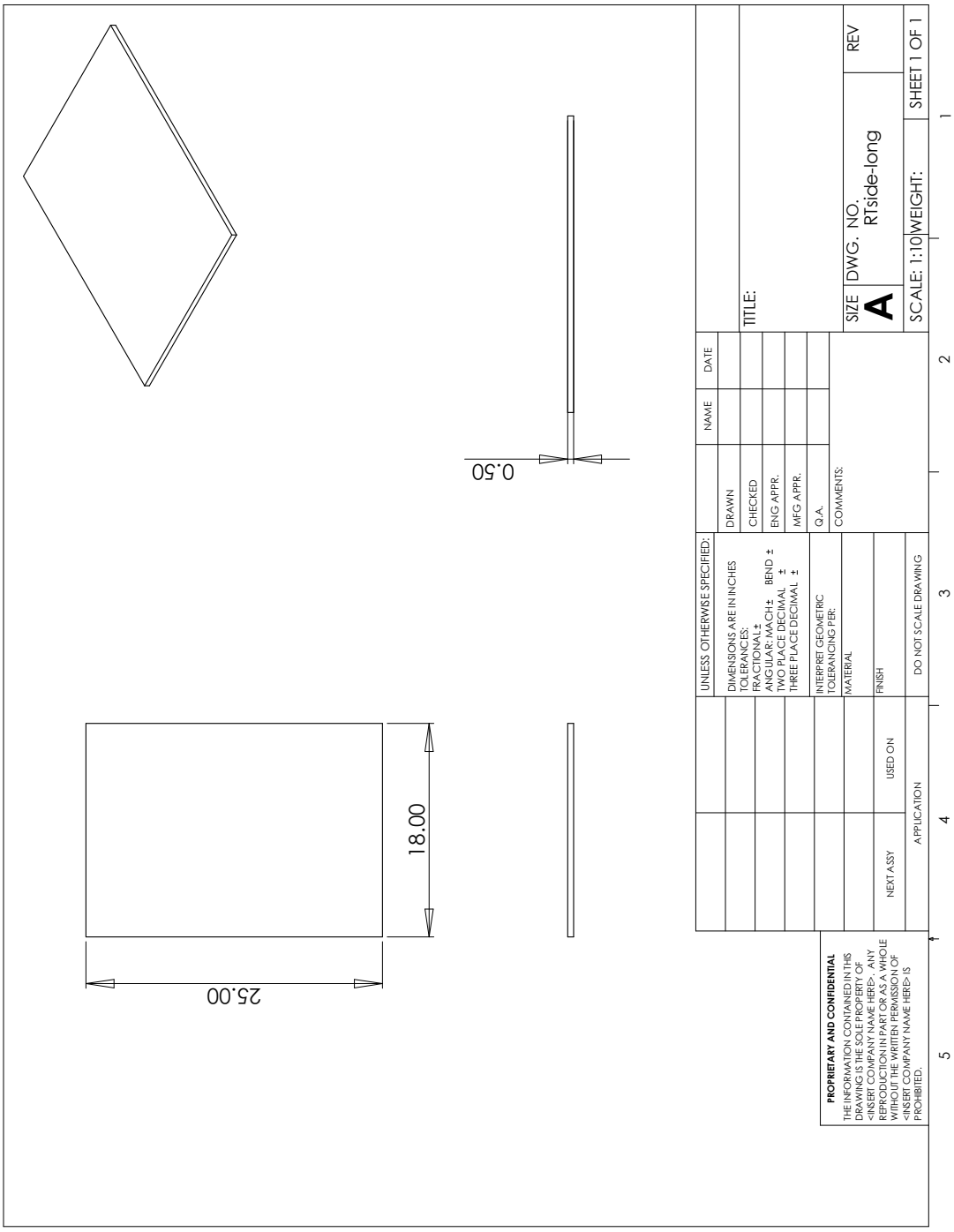

Figure 106: Reservoir Return Tank Long Side Part.

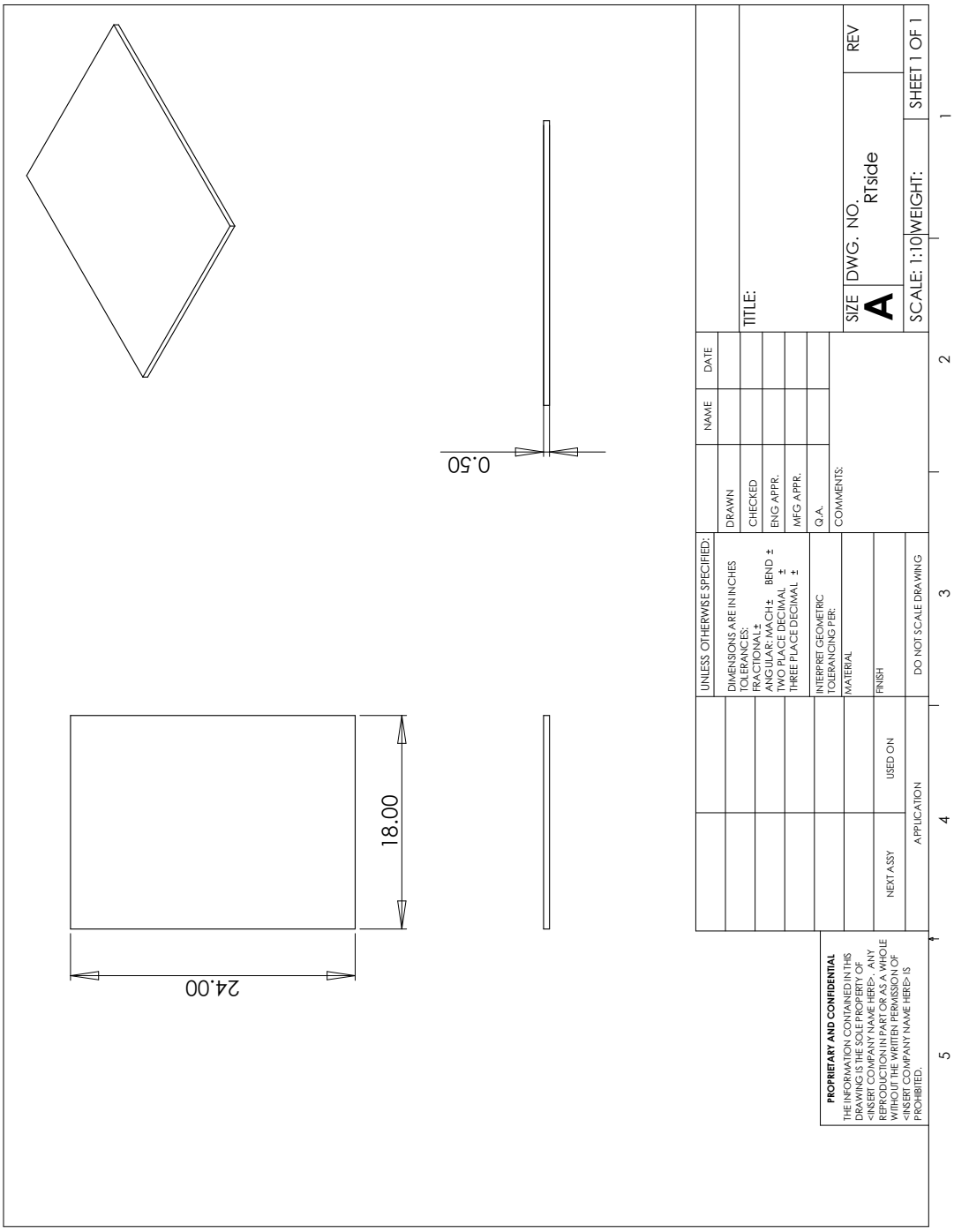

Figure 107: Reservoir Return Tank Short Side Part.

APPENDIX B

FLUME CONSTRUCTION

Each part from the Flume Drawing Package section is machined from the appropriate material, which is acrylic for most, and then the parts are assembled. To assemble the acrylic parts, methylene chloride is used, since it causes a heat reaction with the material, bonding the joints together. Then 3" hose barbs are placed at either end of the flume. The inlet side is fitted with a PVC elbow and then the hoses are attached with steel hose clamps. Upon receiving the pump some assembly was required with appropriately wiring it. Proper connections to the control box and power plug were made. Finally, the pump was fitted with hose barbs and the hoses were attached with steel hose clamps. Further pump details are given in the following appendix.

Originally, the large reservoir was not physically connected to the flume. A later modification includes a flange and bolt connection to physically connect the large reservoir to the flume.

APPENDIX C

PUMP SPECIFICATIONS

The following section contains information for the flume pump specifications.

Pump Data Sheet - Price Pump Company

Company: Pittsburgh Civil Eng. Dept.
Name: David Torick
Date: 9/29/2008

Pump:

Size: RC300
Type: RC
Synch speed: 1800 rpm
Speed: 1750 rpm
Dia: 4.62 in
Curve: 4790045-1
Impeller:
Specific Speeds:
Ns: ---
Nss: ---
Dimensions:
Suction: 3 in
Discharge: 3 in

Pump Limits:

Temperature: 300 °F
Pressure: 75 psi g
Sphere size: 0.31 in
Power: ---
Eye area: ---

Search Criteria:

Flow: 150 US gpm
Head: 13 ft

Fluid:

Water
SG: 1
Viscosity: 1.105 cP
Temperature: 60 °F
Vapor pressure: 0.2563 psi a
Atm pressure: 14.7 psi a
NPSHa: ---

Motor:

Standard: NEMA
Enclosure: Std
Size: 1 hp
Speed: 1800
Frame: --
Sizing criteria: Design Point

---- Data Point ----

Flow:	150 US gpm
Head:	13.5 ft
Eff:	65%
Power:	0.778 hp
NPSHr:	4.66 ft

---- Design Curve ----

Shutoff head:	20.1 ft
Shutoff dP:	8.71 psi
Min flow:	50 US gpm
BEP:	65% @ 125 US gpm
NOL power:	0.784 hp @ 125 US gpm

-- Max Curve --

Max power: 0.784 hp @ 125 US gpm

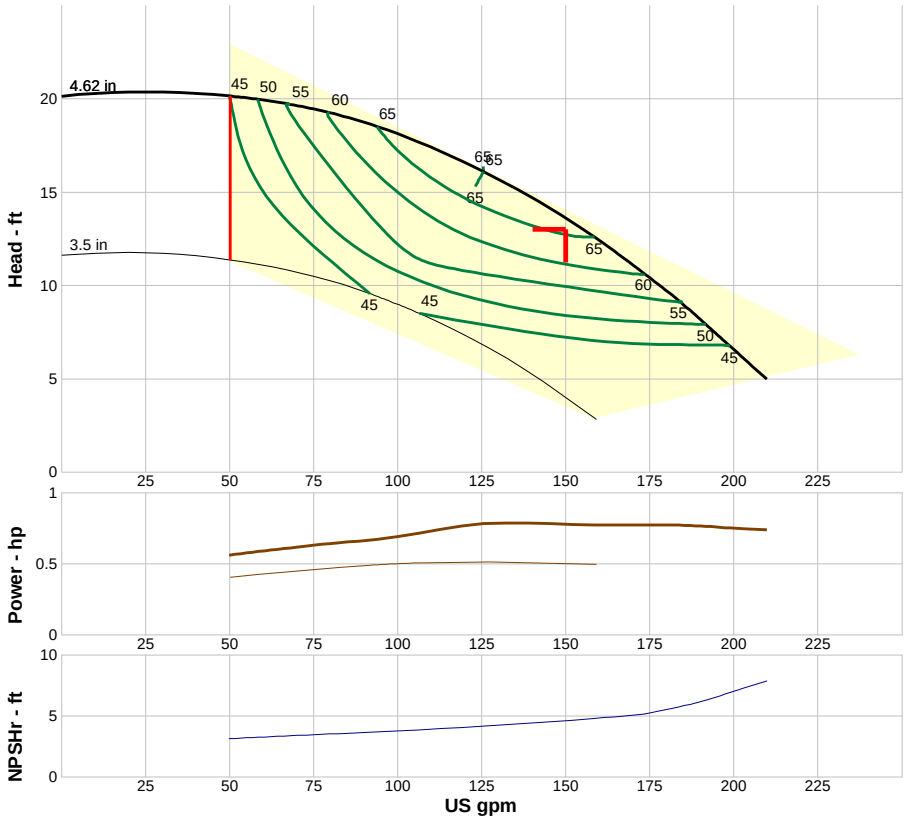

Performance Evaluation:

Flow US gpm	Speed rpm	Head ft	Efficiency %	Power hp	NPSHr ft
180	1750	9.68	56.7	0.775	5.57
150	1750	13.5	65	0.778	4.66
120	1750	16.5	65	0.765	4.1
90	1750	18.7	63.7	0.666	3.67
60	1750	19.9	50.8	0.593	3.29

Selected from catalog: Price Centrifugal Pumps.60 Vers: 1.2

Figure 108: Price Pump Company RC300 Pump Data Sheet.

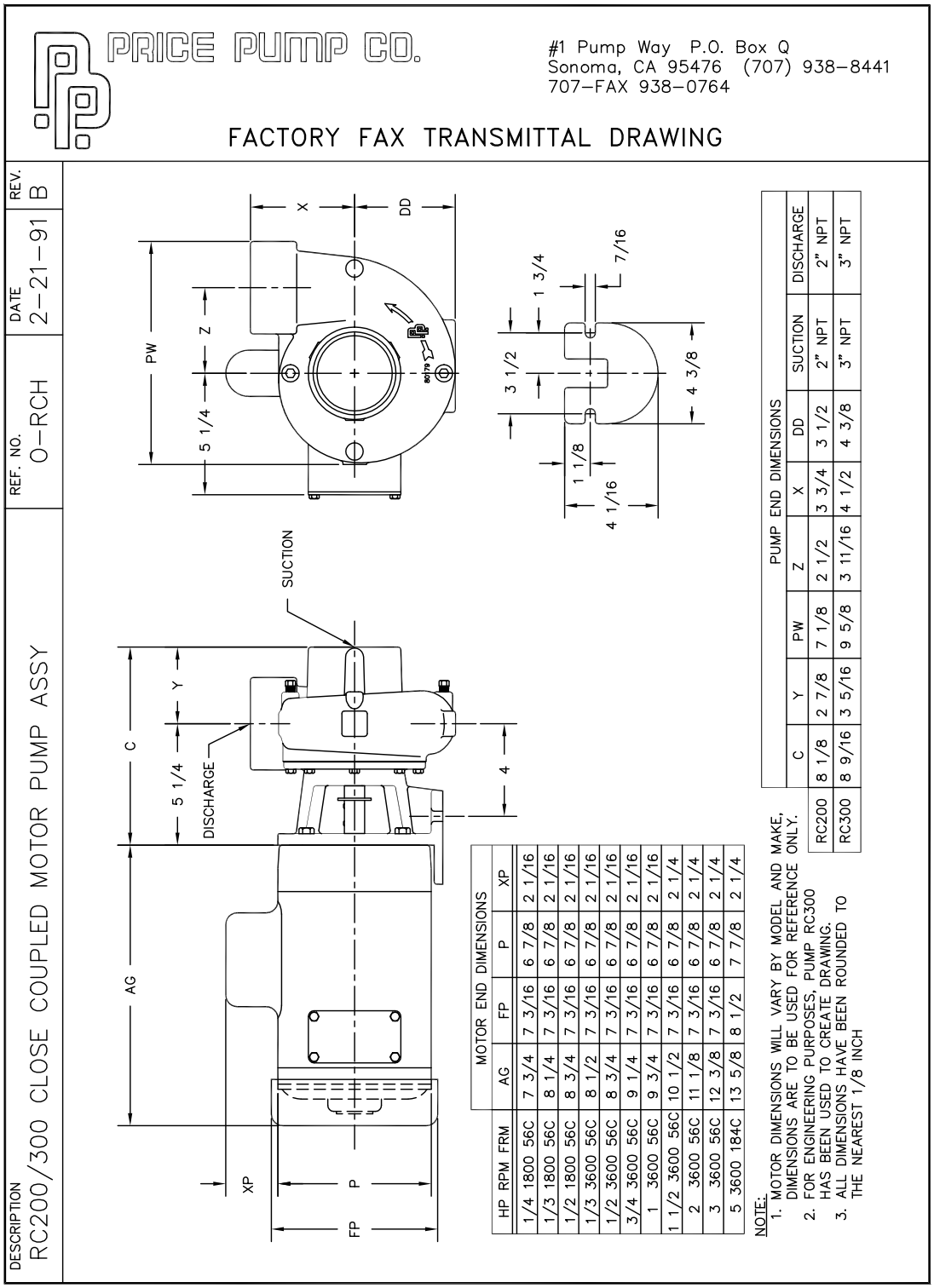

Figure 109: Price Pump Company RC300 Pump Drawing Sheet.

APPENDIX D

TURBINE TEST MOUNTINGS

Turbine mounting schemes were created similarly to the flume construction. The following are drawings and models of the mounts made for both horizontal and vertical axis turbines.

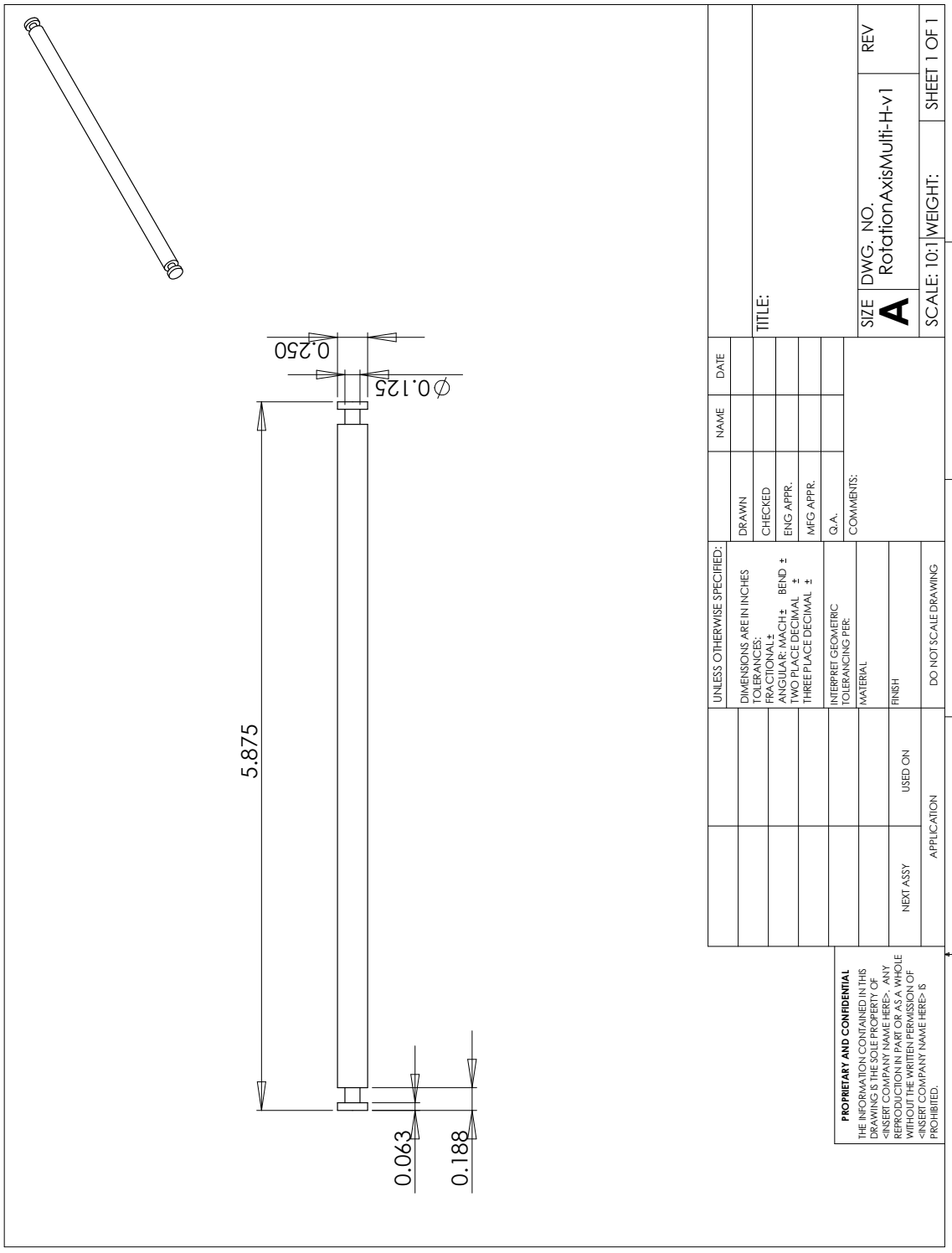

Figure 110: Horizontal Test Mount Part.

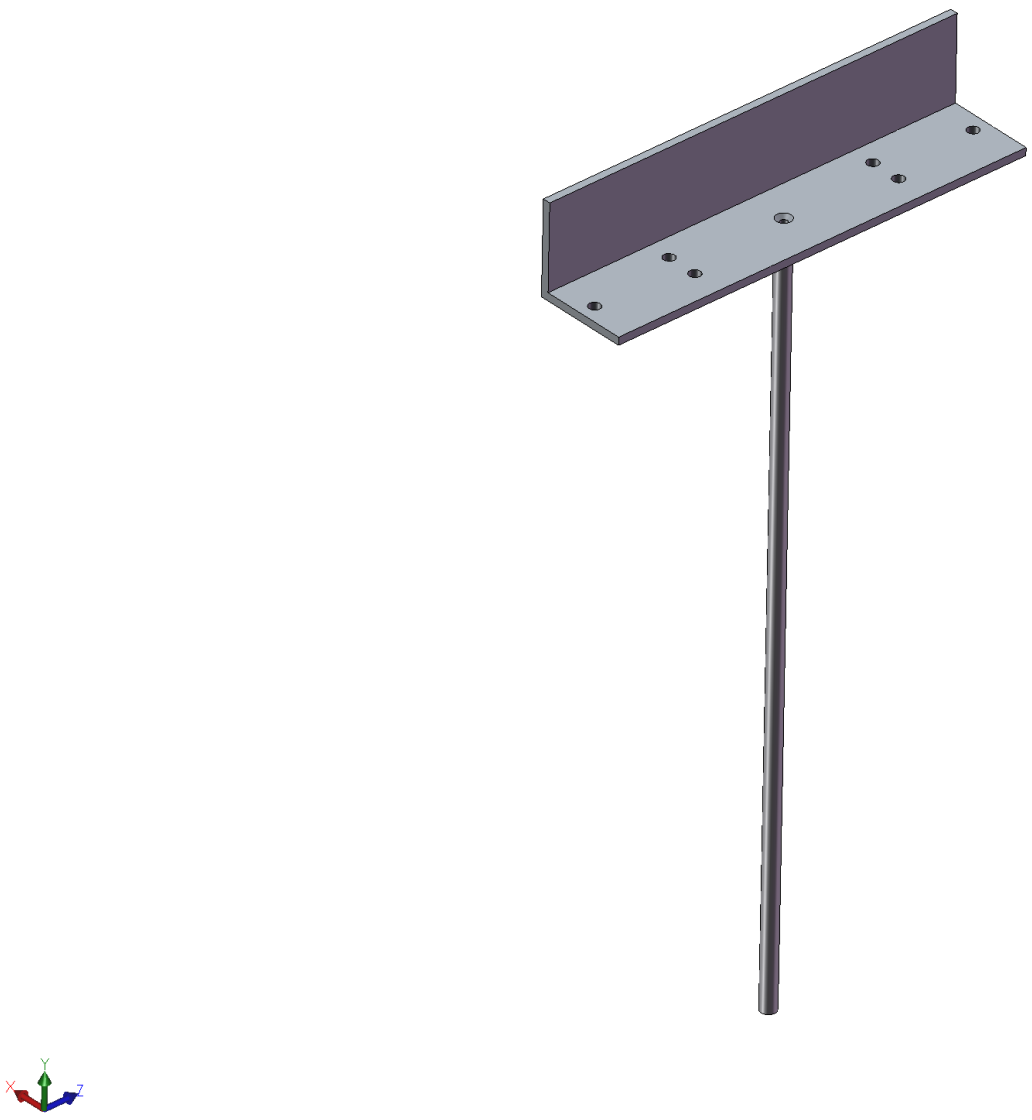

Figure 111: Vertical Test Mount Schematic.

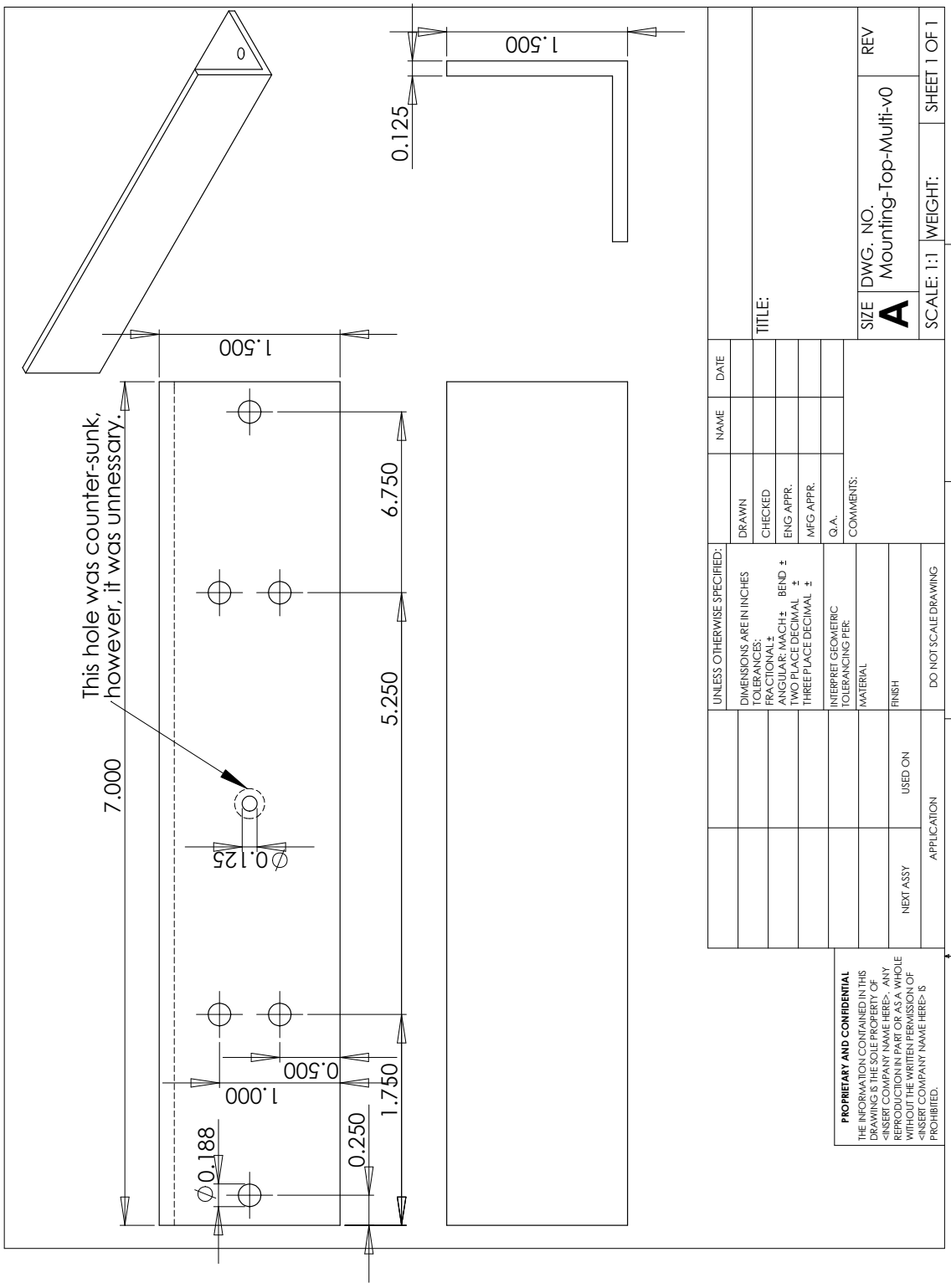

Figure 112: Vertical Test Mount Top Part.

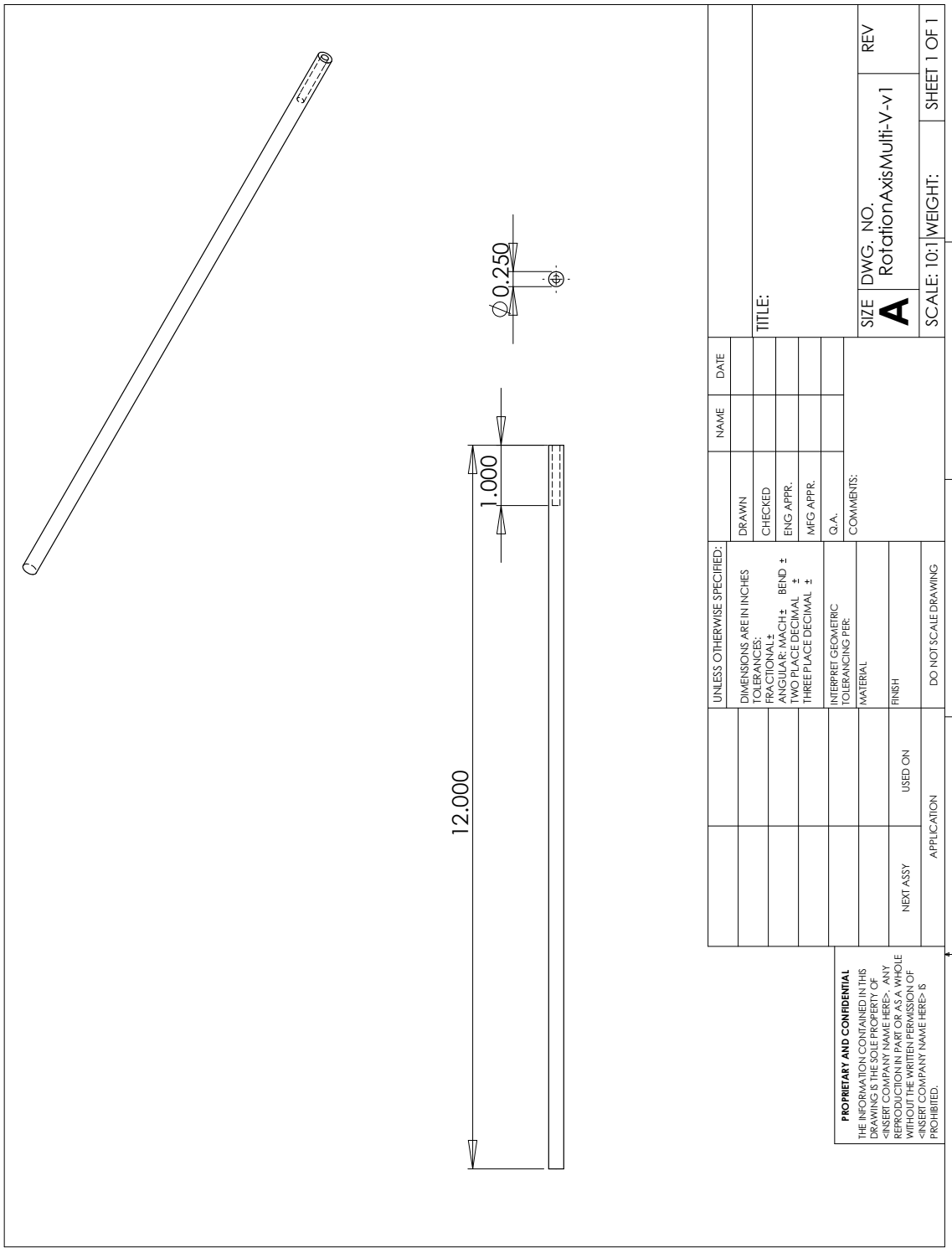

Figure 113: Horizontal Test Mount Axis.

APPENDIX E

FLUME DISASSEMBLY AND CLEANING INSTRUCTIONS

Instructions for disassembly and cleaning of the experimental flume:

1. Empty the reservoirs (starting with the narrow reservoir) by siphoning then soaking up the remaining water with towels or pieces of cloth.
2. Unfasten the pipes on the side connected to the flume, not the pump. Note that at this point, the pipes are full of water.
3. Empty the pipes in a bucket.
4. Clean the flume with a Mr. Clean magic eraser, which removes the grease stains. Acetone works best, but it is not certain if it will dissolve the acrylic, so before using it, it is recommended to test on an area, scrub the grease off, and leave it for a few hours. After removing grease, use sponge, detergent, water and cloth to finish.
5. Disassemble the pump impeller and casing, using a socket wrench.
6. Sand blast the pump casing and impeller, to remove the rust. The process of sand blasting does remove material and it not recommended for a long term solution.
7. Treat the pump casing and impeller with anti rust products Boeshield^{TM}. This should be done under a working fume hood. Before, line the surface with paper towels so it does not become greased. The treated parts should be left drying for about two days. This step is not necessary if the pump casing and impeller are not sand blasted.

8. Clean the pipes that connect the flume to the pump. This can be done with a sponge Luffa, attached to an unfolded hanger or rod. A broomstick or mop handle is useful to push the Luffa sponge.
9. Re-assemble everything.

APPENDIX F

FLUME OPERATION INSTRUCTIONS

Once the flume is assembled and filled, the pump can be operated. To operate the pump:

1. Plug the pump in.
2. Switch the controller to pu by pressing the pu button.
3. Check mode P30 to assure it is set to 1.
4. Adjust to desired frequency.
5. Press run.
6. The frequency may be adjusted during operation by pressing set, then rotating the dial and pressing run.
7. Press stop to stop the flume cycling.
8. Unplug the pump if leaving it for a prolonged (more than 1 hour) duration unattended.

APPENDIX G

DATA SORTING PROGRAM

These programs were created in MatLab for sorting data collected from the PIV experiments. The first is specific to the open-channel flow analysis and includes data file averaging, and the second program shows the calculations involved with many of the submerged water wheel comparisons.

```
%Creation of Data Sorting Program for PIV Measurements of Hydrokinetic
%Energy, V.Miller 10-Feb-10

%Define conversion constants
mpix=0.000096;  %meters per pixel
dt=550;  %time between laser pulses in microseconds
% Change name according to data set
Name = 'OpenFlowOneThousand'; %00000i.T000.D000.P001.H000.L.vec'
numstart = 0;  %Number the counter starts at

for i = 1:400 %this number changes for how many captures to average
    %Initialize all counter variable(s)
    Num = sprintf('%06d', numstart); %06d is places before the decimal

    %Generate the file name
    eval('FileName = [Name num2str(Num) ''.T000.D000.P001.H000.L.vec''];');
    %import the file data and store it in a temporary array
    importdatafile(FileName);

%Velocity matrix construction
pts=data*mpix;
Xvel=pts(:,3)/(dt/1000000);%extracts third column as x-velocity
Yvel=pts(:,4)/(dt/1000000);%extracts fourth column as y-velocity

% This puts the data sets together
Udata(i,:,1) = Xvel;
Vdata(i,:,1) = Yvel;

Uvelocity=Udata';
Vvelocity=Vdata';

% Calculate an averaged velocity field from the data sets
U=mean(Uvelocity, 2);
V=mean(Vvelocity, 2);

%clear unnecessary data and index to the next capture
    clear data
    numstart = numstart + 1;

end

Mag=sqrt(U.*U+V.*V);%calculates velocity magnitude
for m=1:59
    MagY(m,:)=Mag(1+81*(m-1):81*m); %set-up to separate velocity by
    %y-values and takes transpose for set-up of matrix reconstruction
end

% This removes the last column since the data collected there was not good
MagMod=MagY(3:59,2:80);

%Velocity Profile
```

```
Profile=mean(MagMod, 2);

%Flow Field Velocity Average
avg=mean2(MagMod);

%comparison velocity plane, same as water wheel, y=0.073m
VelMag1=MagMod(30,:)';

%comparison velocity plane, open flow mid-plane, y=0.04m
VelMag2=MagMod(15,:)';

%Setting-up position matrix to plot velocity vectors
Y=pts(:,2); %Y values
for m=1:59
    Yposition(m,:)=Y(1+81*(m-1):81*m); %Y values rearranged
end

X=pts(:,1); %X values
for m=1:59
    Xposition(m,:)=X(1+81*(m-1):81*m);
end

%extracting x-position for plotting
Xplot=Xposition(1,2:80)';

%extracting y-position for plotting
Yplot=Yposition(3:59,1);
```

```
%Creation of Data Sorting Program for PIV Measurements of Hydrokinetic
%Energy: Open Flow Velocity Rating, V.Miller 10-Feb-10

%Define conversion constants
mpix=0.000097;  %meters per pixel
dt=550;  %time between laser pulses in microseconds

% Change name according to data set
 Name = 'WaterWheel-SCS-EightHundred'; %000000.T000.D000.P001.H000.L.vec'
 numstart = 0;  %Number used since captures where evaluated as an ensemble

 Num = sprintf('%06d', numstart); %06d is places before the decimal

 % Generate the file name
 eval('FileName = [Name num2str(Num) ''.T000.D000.P001.H000.L.vec''];');

%import the file data and store it in a temporary array
importdatafile(FileName);

%Velocity matrix construction
pts=data*mpix;
U_1=pts(:,3)/(dt/1000000);%extracts third column as x-velocity
V_1=pts(:,4)/(dt/1000000);%extracts fourth column as y-velocity


Mag_1=sqrt(U_1.*U_1+V_1.*V_1);%calculates velocity magnitude
for m=1:59
    MagY_1(m,:)=Mag_1(1+81*(m-1):81*m); %set-up to separate velocity by
    %y-values and takes transpose for set-up of matrix reconstruction
end

% This removes the last column since the data collected there was not
% illuminated
MagMod_1=MagY_1(:,2:80);

avg_1=mean2(MagMod_1);

%comparison velocity plane, for the water wheel, y=0.0859m
VelComp_1=MagMod_1(6,:)';

clear Name
clear FileName
clear data
clear pts


% Data Set 2; Higher Illumination
 Name = 'WW-SCS-EightHundred-Two'; %000000.T000.D000.P001.H000.L.vec'
 eval('FileName = [Name num2str(Num) ''.T000.D000.P001.H000.L.vec''];');

%import the file data and store it in a temporary array
```

```
importdatafile(FileName);

%Velocity matrix construction
pts=data*mpix;
U_2=pts(:,3)/(dt/1000000);%extracts third column as x-velocity
V_2=pts(:,4)/(dt/1000000);%extracts fourth column as y-velocity


Mag_2=sqrt(U_2.*U_2+V_2.*V_2);%calculates velocity magnitude
for m=1:59
    MagY_2(m,:)=Mag_2(1+81*(m-1):81*m); %set-up to separate velocity by
    %y-values and takes transpose for set-up of matrix reconstruction
end

% This removes the last column since the data collected there was not
% illuminated
MagMod_2=MagY_2(:,2:80);

avg_2=mean2(MagMod_2);

%comparison velocity plane, for the water wheel, y=0.0859m
VelComp_2=MagMod_2(6,:)';

clear Name
clear FileName
clear data
clear pts


% Data Set 3; Above Turbine
 Name = 'WW-SCS-EightHundred-Three'; %000000.T000.D000.P001.H000.L.vec'
 eval('FileName = [Name num2str(Num) ''.T000.D000.P001.H000.L.vec''];');

%import the file data and store it in a temporary array
importdatafile(FileName);

%Velocity matrix construction
pts=data*mpix;
U_3=pts(:,3)/(dt/1000000);%extracts third column as x-velocity
V_3=pts(:,4)/(dt/1000000);%extracts fourth column as y-velocity


Mag_3=sqrt(U_3.*U_3+V_3.*V_3);%calculates velocity magnitude
for m=1:59
    MagY_3(m,:)=Mag_3(1+81*(m-1):81*m); %set-up to separate velocity by
    %y-values and takes transpose for set-up of matrix reconstruction
end

% This removes the last column since the data collected there was not
% illuminated
MagMod_3=MagY_3(:,2:80);
```

```
avg_3=mean2(MagMod_3);

%checking the velocity profile
VelProfile_3=mean(MagMod_3,2);

%comparison velocity plane, for the water wheel, to compare with all data
%sets
VelComp_3=MagMod_3(28,:)';

%comparison velocity plane, for the water wheel, y=0.0697m (PIV)
%CFD, y=0.056015m
VelComp_3ex=MagMod_3(17,:)';

clear Name
clear FileName
clear data
clear pts


% Data Set 4; Turbine Wake
 Name = 'WW-SCS-Wake-FourHundred'; %000000.T000.D000.P001.H000.L.vec'
 eval('FileName = [Name num2str(Num) ''.T000.D000.P001.H000.L.vec''];');

%import the file data and store it in a temporary array
importdatafile(FileName);

%Velocity matrix construction
pts=data*mpix;
U_4=pts(:,3)/(dt/1000000);%extracts third column as x-velocity
V_4=pts(:,4)/(dt/1000000);%extracts fourth column as y-velocity


Mag_4=sqrt(U_4.*U_4+V_4.*V_4);%calculates velocity magnitude
for m=1:59
    MagY_4(m,:)=Mag_4(1+81*(m-1):81*m); %set-up to separate velocity by
    %y-values and takes transpose for set-up of matrix reconstruction
end

% This removes the last column since the data collected there was not
% illuminated
MagMod_4=MagY_4(:,2:80);

avg_4=mean2(MagMod_4);

%comparison velocity plane, for the water wheel, set-up to compare same
%mid-line as data sets 1&2
VelComp_4=MagMod_4(12,:)';

clear Name
clear FileName
```

```
clear data
% clear pts

%Setting-up position matrix to plot velocity vectors THESE ARE SPECIFIC TO
%DATA SETS!!! But remain the same since the camera window stays constant.
Y=pts(:,2); %Y values
for m=1:59
    Yposition(m,:)=Y(1+81*(m-1):81*m); %Y values rearranged
end

X=pts(:,1); %X values
for m=1:59
    Xposition(m,:)=X(1+81*(m-1):81*m);
end

%extracting x-position for plotting
Xplot=Xposition(1,2:80)'-0.08193;

%extracting y-position for plotting
Yplot=Yposition(:,1);

clear pts


clear mpix
mpix=0.000099;
% Data Set 3 Check; Above Turbine
 Name = 'WW-SCS-ThreeCk-FourHundred'; %000000.T000.D000.P001.H000.L.vec'
 eval('FileName = [Name num2str(Num) ''.T000.D000.P001.H000.L.vec''];');

%import the file data and store it in a temporary array
importdatafile(FileName);

%Velocity matrix construction
pts=data*mpix;
U_3ck=pts(:,3)/(dt/1000000);%extracts third column as x-velocity
V_3ck=pts(:,4)/(dt/1000000);%extracts fourth column as y-velocity


Mag_3ck=sqrt(U_3ck.*U_3ck+V_3ck.*V_3ck);%calculates velocity magnitude
for m=1:59
    MagY_3ck(m,:)=Mag_3ck(1+81*(m-1):81*m); %set-up to separate velocity by
    %y-values and takes transpose for set-up of matrix reconstruction
end

% This removes the last column since the data collected there was not
% illuminated
MagMod_3ck=MagY_3ck(:,2:80);

avg_3ck=mean2(MagMod_3ck);
```

```
%checking the velocity profile
VelProfile_3ck=mean(MagMod_3ck,2);

%comparison velocity plane, for the water wheel, to compare with all data
%sets
VelComp_3ck=MagMod_3ck(25,:)';

%comparison velocity plane, for the water wheel, y=0.078378m (PIV) THIS WILL
%HAVE TO BE ADJUSTED!!! CFD, y=0.073338m
VelComp_3exck=MagMod_3ck(16,:)';

clear Name
clear FileName
clear data
% clear pts

%Setting-up position matrix to plot velocity vectors THESE ARE SPECIFIC TO
%DATA SETS!!! But remain the same since the camera window stays constant.
Y_ck=pts(:,2); %Y values
for m=1:59
    Yposition_ck(m,:)=Y_ck(1+81*(m-1):81*m); %Y values rearranged
end

X_ck=pts(:,1); %X values
for m=1:59
    Xposition_ck(m,:)=X_ck(1+81*(m-1):81*m);
end

%extracting x-position for plotting
Xplot_ck=Xposition_ck(1,2:80)'-0.0676;

%extracting y-position for plotting
Yplot_ck=Yposition_ck(:,1);

clear pts


% CREATING COMPARISON PLOTS FOR VelComp3 3-20-10
PL_0=VelComp_3;
PL_1=MagMod_3(27,:)';
PL_2=MagMod_3(25,:)';
PL_3=MagMod_3(23,:)';
PL_4=MagMod_3(21,:)';
PL_5=MagMod_3(19,:)';
PL_6=VelComp_3ex;
% plot(Xplot,PL_0,'.',Xplot,PL_1,'x',Xplot,PL_2,'*',Xplot,PL_3,'d',Xplot,PL_4,'+',Xplot,↙
PL_5,'^',Xplot,PL_6,'s')
% plot(Xplot,PL_0,Xplot,PL_1,Xplot,PL_2,Xplot,PL_3,Xplot,PL_4,Xplot,PL_5,Xplot,PL_6)
% legend('PL_0','PL_1','PL_2','PL_3','PL_4','PL_5','PL_6',7)
%Detail
% plot(Xplot,PL_1,Xplot,PL_2,Xplot,PL_3,Xplot,PL_4,Xplot,PL_5,Xplot,PL_6)
```

```
% plot(Xplot,PL_1,'x',Xplot,PL_2,'*',Xplot,PL_3,'d',Xplot,PL_4,'+',Xplot,PL_5,'^',Xplot,↙
PL_6,'s')
% legend('PL_1','PL_2','PL_3','PL_4','PL_5','PL_6',6)
% xlabel('X position, m')
% ylabel('Velocity, m/s')


% IMPORTING CFD RESULTS
% Original Comparison Plot
importfile('midline1');
X_cfd=data(:,1);
CFD=data(:,2);
clear data


importfile('040515');

pts=flipud(data);
Xposition_cfd1=pts(:,1);%extracts first column as x-position
Vel_cfd1=pts(:,2);%extracts second column as velocity magnitude
% modify for PIV comparison
X_cfd1=Xposition_cfd1(858:1093);
CFD1=Vel_cfd1(858:1093);

clear data
clear pts


importfile('043615');

pts=flipud(data);
Xposition_cfd2=pts(:,1);%extracts first column as x-position
Vel_cfd2=pts(:,2);%extracts second column as velocity magnitude
% modify for PIV comparison
X_cfd2=Xposition_cfd2(858:1093);
CFD2=Vel_cfd2(858:1093);

clear data
clear pts


importfile('046715');

pts=flipud(data);
Xposition_cfd3=pts(:,1);%extracts first column as x-position
Vel_cfd3=pts(:,2);%extracts second column as velocity magnitude
% modify for PIV comparison
X_cfd3=Xposition_cfd3(858:1093);
CFD3=Vel_cfd3(858:1093);

clear data
```

```
clear pts


importfile('049815');

pts=flipud(data);
Xposition_cfd4=pts(:,1);%extracts first column as x-position
Vel_cfd4=pts(:,2);%extracts second column as velocity magnitude
% modify for PIV comparison
X_cfd4=Xposition_cfd4(858:1093);
CFD4=Vel_cfd4(858:1093);

clear data
clear pts


% importfile('052915');
%
% pts=flipud(data);
% Xposition_cfd5=pts(:,1);%extracts first column as x-position
% Vel_cfd5=pts(:,2);%extracts second column as velocity magnitude
% % modify for PIV comparison
% X_cfd5=Xposition_cfd5(858:1093);
% CFD5=Vel_cfd5(858:1093);
%
% clear data
% clear pts


importfile('056015midline');

pts=flipud(data);
Xposition_cfd6=pts(:,1);%extracts first column as x-position
Vel_cfd6=pts(:,2);%extracts second column as velocity magnitude
% modify for PIV comparison
X_cfd6=Xposition_cfd6(858:1093);
CFD6=Vel_cfd6(858:1093);

clear data
clear pts

%second comparison with PIV
importfile('053855midline');

pts=flipud(data);
Xposition_cfd6ck=pts(:,1);%extracts first column as x-position
Vel_cfd6ck=pts(:,2);%extracts second column as velocity magnitude
% modify for PIV comparison
X_cfd6ck=Xposition_cfd6ck(858:1093);
CFD6ck=Vel_cfd6ck(858:1093);
```

```
clear data
clear pts


Xplot1=Xposition(1,2:80)'-0.068;
Xplot2_3=Xposition(1,2:80)'-0.08119;
Xplot4=Xposition(1,2:80)'-0.056;


%checking the original comparison
figure
grid on
plot(Xplot1,VelComp_1,'--r',X_cfd,CFD)
legend('PIV','CFD','location', 'best')
axis([-0.08 0.08 0.05 0.84])
xlabel('X position, m')
ylabel('Velocity, m/s')


figure
hold on
% grid on
plot(X_cfd,CFD,'r',...
    Xplot1(1:3:end),VelComp_1(1:3:end),'+b',...
    Xplot2_3(1:3:end),VelComp_2(1:3:end),'ok',...
    Xplot2_3(1:3:end),VelComp_3(1:3:end),'sg',...
    Xplot4(1:3:end),VelComp_4(1:3:end),'^m')
plot(X_cfd,CFD,'r',Xplot1,VelComp_1,'b',Xplot2_3,VelComp_2,'k',Xplot2_3,VelComp_3,'g',↙
Xplot4,VelComp_4,'m')
legend('CFD','PIV1','PIV2','PIV3','PIV4','location', 'best')
axis([-0.08 0.08 0.05 0.84])
xlabel('X position, m')
ylabel('Velocity, m/s')
hold off

figure
hold on
grid on
plot(X_cfd6ck(1:5:end),CFD6ck(1:5:end),'+r',...
    Xplot_ck(1:3:end),VelComp_3exck(1:3:end),'ob',...
    X_cfd6(1:5:end),CFD6(1:5:end),'sk',...
    Xplot(1:3:end),PL_6(1:3:end),'^g')

plot(X_cfd6ck,CFD6ck,'r',Xplot_ck,VelComp_3exck,'b',X_cfd6,CFD6,'k',Xplot,PL_6,'g')
legend('CFD1','PIV1','CFD2','PIV2','location', 'best')
xlabel('X position, m')
ylabel('Velocity, m/s')
hold off

%Plot Comparison
figure
```

```
hold on
plot(Xplot,PL_1,'r',X_cfd1(1:5:end),CFD1(1:5:end),'+r',...
    Xplot,PL_2,'b',X_cfd2(1:5:end),CFD2(1:5:end),'ob',...
    Xplot,PL_3,'k',X_cfd3(1:5:end),CFD3(1:5:end),'sk',...
    Xplot,PL_4,'g',X_cfd4(1:5:end),CFD4(1:5:end),'^g',...
    Xplot,PL_5,'m',...
    Xplot,PL_6,'c',X_cfd6(1:5:end),CFD6(1:5:end),'vc')

plot(Xplot,PL_1,'r',X_cfd1(1:5:end),CFD1(1:5:end),'r',...
    Xplot,PL_2,'b',X_cfd2(1:5:end),CFD2(1:5:end),'b',...
    Xplot,PL_3,'k',X_cfd3(1:5:end),CFD3(1:5:end),'k',...
    Xplot,PL_4,'g',X_cfd4(1:5:end),CFD4(1:5:end),'g',...
    Xplot,PL_5,'m',...
    Xplot,PL_6,'c',X_cfd6(1:5:end),CFD6(1:5:end),'c')
legend↙
('PL_1','CFD1','PL_2','CFD2','PL_3','CFD3','PL_4','CFD4','PL_5','PL_6','CFD6','location'↙
, 'best')
xlabel('X position, m')
ylabel('Velocity, m/s')
hold off

%Detail
figure
hold on
plot(Xplot(1:3:end),PL_1(1:3:end),'+r',...
    Xplot(1:3:end),PL_2(1:3:end),'ob',...
    Xplot(1:3:end),PL_3(1:3:end),'sk',...
    Xplot(1:3:end),PL_4(1:3:end),'^g',...
    Xplot(1:3:end),PL_5(1:3:end),'*m',...
    Xplot,PL_6,'vc',...
    X_cfd6,CFD6,'y')
plot(Xplot,PL_1,'r',Xplot,PL_2,'b',Xplot,PL_3,'k',Xplot,PL_4,'g',Xplot,PL_5,'m',Xplot,↙
PL_6,'c',X_cfd6,CFD6,'y')
%plot(Xplot,PL_1,Xplot,PL_2,Xplot,PL_3,Xplot,PL_4,Xplot,PL_5,Xplot,PL_6,X_cfd6,CFD6)
legend('PL_1','PL_2','PL_3','PL_4','PL_5','PL_6','CFD6','location', 'best')
xlabel('X position, m')
ylabel('Velocity, m/s')
hold off

% Checking 3D CFD results
importfile('056015-3Dmidline');

X_cfd3D=data(:,1);%extracts first column as x-position
CFD_3D=data(:,2);%extracts second column as velocity magnitude
% % modify for PIV comparison NOT NEEDED
% =Xposition_cfd3D(858:1093);
% =Vel_cfd3D(858:1093);

clear data
% %
% % plot(X_cfd3D,CFD_3D,'.')
```

```
% % xlabel('X position, m')
% % ylabel('Velocity, m/s')
% Comparing with data
figure
hold on
plot(X_cfd3D,CFD_3D,'.',Xplot(1:2:end),PL_6(1:2:end),'+r',Xplot(1:2:end),PL_1(1:2:↙
end),'sk')
plot(X_cfd3D,CFD_3D,'.',Xplot,PL_6,'r',Xplot,PL_1,'k')
xlabel('X position, m')
ylabel('Velocity, m/s')
axis([-0.08 0.08 0.24 0.42])
legend('CFD3D','PL_6','PL_1','location', 'best')
hold off

% Checking Wall Functions
importfile('056015midline-EnWallF');

pts=flipud(data);
Xpos_cfd6EnWallF=pts(:,1);%extracts first column as x-position
Vel_cfd6EnWallF=pts(:,2);%extracts second column as velocity magnitude
% modify for PIV comparison
X_cfd6EnWallF=Xpos_cfd6EnWallF(858:1093);
CFD6_EnWallF=Vel_cfd6EnWallF(858:1093);

clear data
clear pts

importfile('056015midline-Non-EqWallF');

pts=flipud(data);
Xpos_cfd6NEqWallF=pts(:,1);%extracts first column as x-position
Vel_cfd6NEqWallF=pts(:,2);%extracts second column as velocity magnitude
% modify for PIV comparison
X_cfd6NEqWallF=Xpos_cfd6NEqWallF(858:1093);
CFD6_NEqWallF=Vel_cfd6NEqWallF(858:1093);

clear data
clear pts

figure
hold on
grid on
plot(Xplot(1:3:end),PL_6(1:3:end),'+r',...
    X_cfd6(1:5:end),CFD6(1:5:end),'ob',...
    X_cfd6EnWallF(1:5:end),CFD6_EnWallF(1:5:end),'sk',...
    X_cfd6NEqWallF(1:5:end),CFD6_NEqWallF(1:5:end),'^g')
plot(Xplot,PL_6,'r',X_cfd6,CFD6,'b',X_cfd6EnWallF,CFD6_EnWallF,'k',X_cfd6NEqWallF,↙
CFD6_NEqWallF,'g')
legend('PIV','CFD','CFD-EnWallF','CFD_NEqWallF','location', 'best')
xlabel('X position, m')
ylabel('Velocity, m/s')
```

```
hold off


% Checking VOF
importfile('056015midlineSKE-VOF-1'); % from original mesh, incorrect river field↙
designation & SKE (std k-ep)
pts=flipud(data);
Xpos_cfd6VOF1=pts(:,1);%extracts first column as x-position
Vel_cfd6VOF1=pts(:,2);%extracts second column as velocity magnitude
% modify for PIV comparison
X_cfd6VOF1=Xpos_cfd6VOF1(858:1093);
CFD6_VOF1=Vel_cfd6VOF1(858:1093);

clear data
clear pts

importfile('056015midlineRNGKE-VOF-2'); % original mesh, RNG model
pts=flipud(data);
Xpos_cfd6VOF2=pts(:,1);%extracts first column as x-position
Vel_cfd6VOF2=pts(:,2);%extracts second column as velocity magnitude
% modify for PIV comparison
X_cfd6VOF2=Xpos_cfd6VOF2(858:1093);
CFD6_VOF2=Vel_cfd6VOF2(858:1093);

clear data
clear pts

importfile('056015midlineRNGKE-VOF-3'); % VOF mesh w/expanded air region, RNG model
pts=flipud(data);
Xpos_cfd6VOF3=pts(:,1);%extracts first column as x-position
Vel_cfd6VOF3=pts(:,2);%extracts second column as velocity magnitude
% modify for PIV comparison
X_cfd6VOF3=Xpos_cfd6VOF3(858:1093);
CFD6_VOF3=Vel_cfd6VOF3(858:1093);

clear data
clear pts

figure
plot(Xplot,PL_1,Xplot,PL_2,Xplot,PL_3,Xplot,PL_4,Xplot,PL_5,Xplot,PL_6,X_cfd6,CFD6,↙
X_cfd6VOF2,CFD6_VOF2,X_cfd6VOF3,CFD6_VOF3)
legend('PL_1','PL_2','PL_3','PL_4','PL_5','PL_6','CFD6','CFD6-VOF2','CFD6-VOF3',9)
xlabel('X position, m')
ylabel('Velocity, m/s')

plot(Xplot,PL_1,Xplot,PL_6,X_cfd6VOF2,CFD6_VOF2,X_cfd6VOF3,CFD6_VOF3)
legend('PL_1','PL_6','CFD6-VOF2','CFD6-VOF3',4)
xlabel('X position, m')
ylabel('Velocity, m/s')
```

APPENDIX H

SCALED TURBINE MODELS FOR PIV EXPERIMENTS CFD MODEL CONSTRUCTION

This appendix contains drawings for the scaled turbine models made for both experiments and CFD model construction.

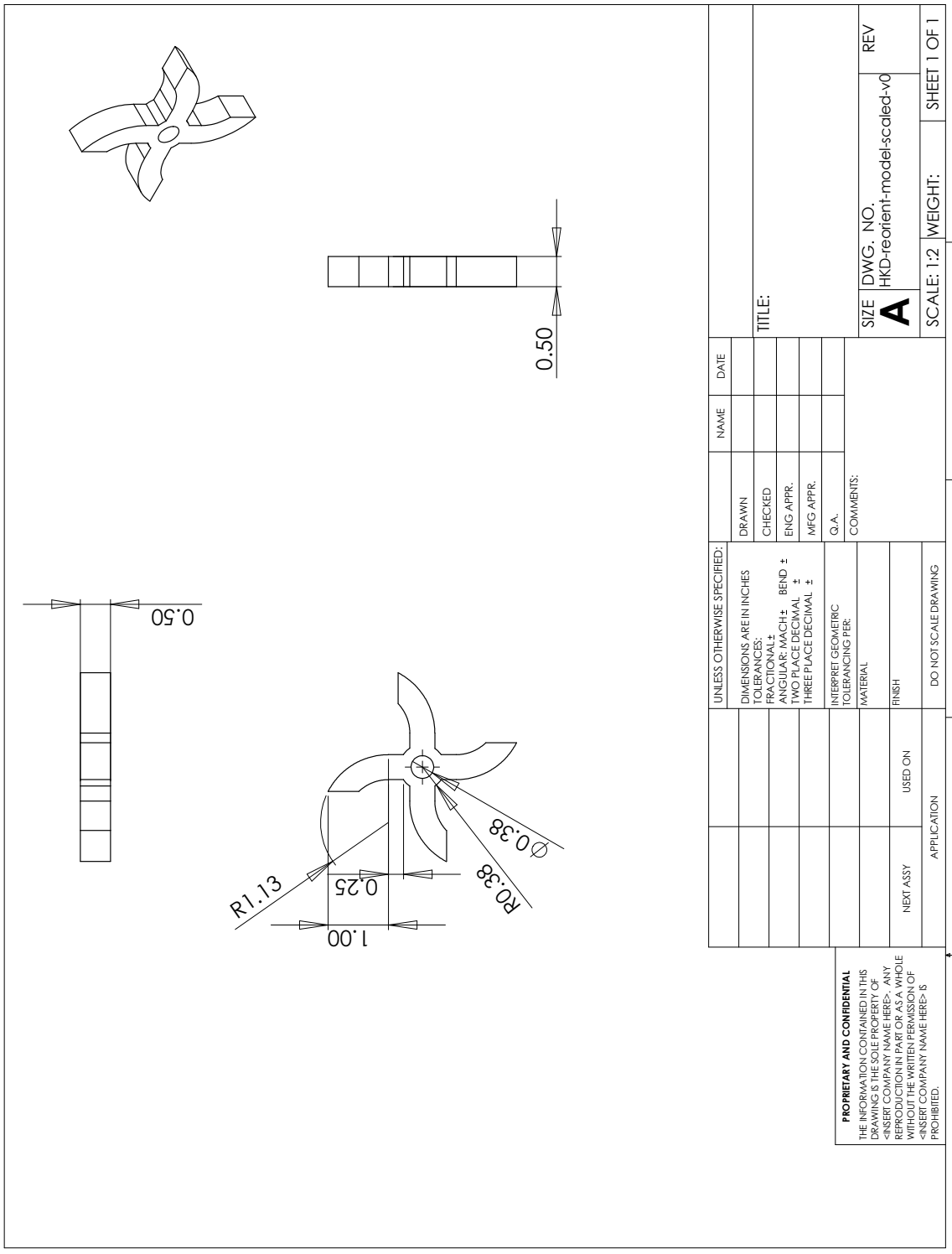

Figure 114: Water Wheel Turbine Part Drawing.

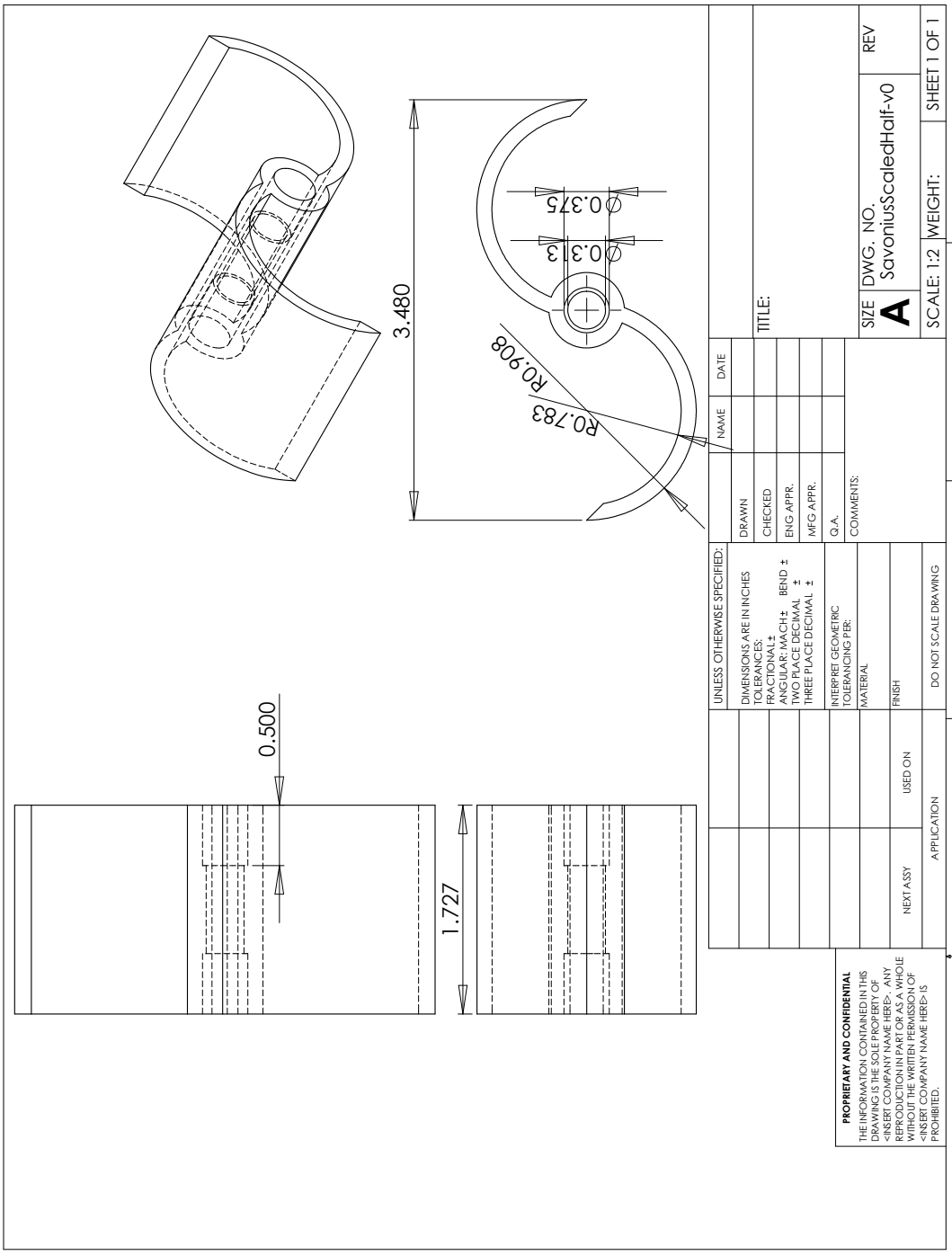

Figure 115: Savonius Turbine Part Drawing.

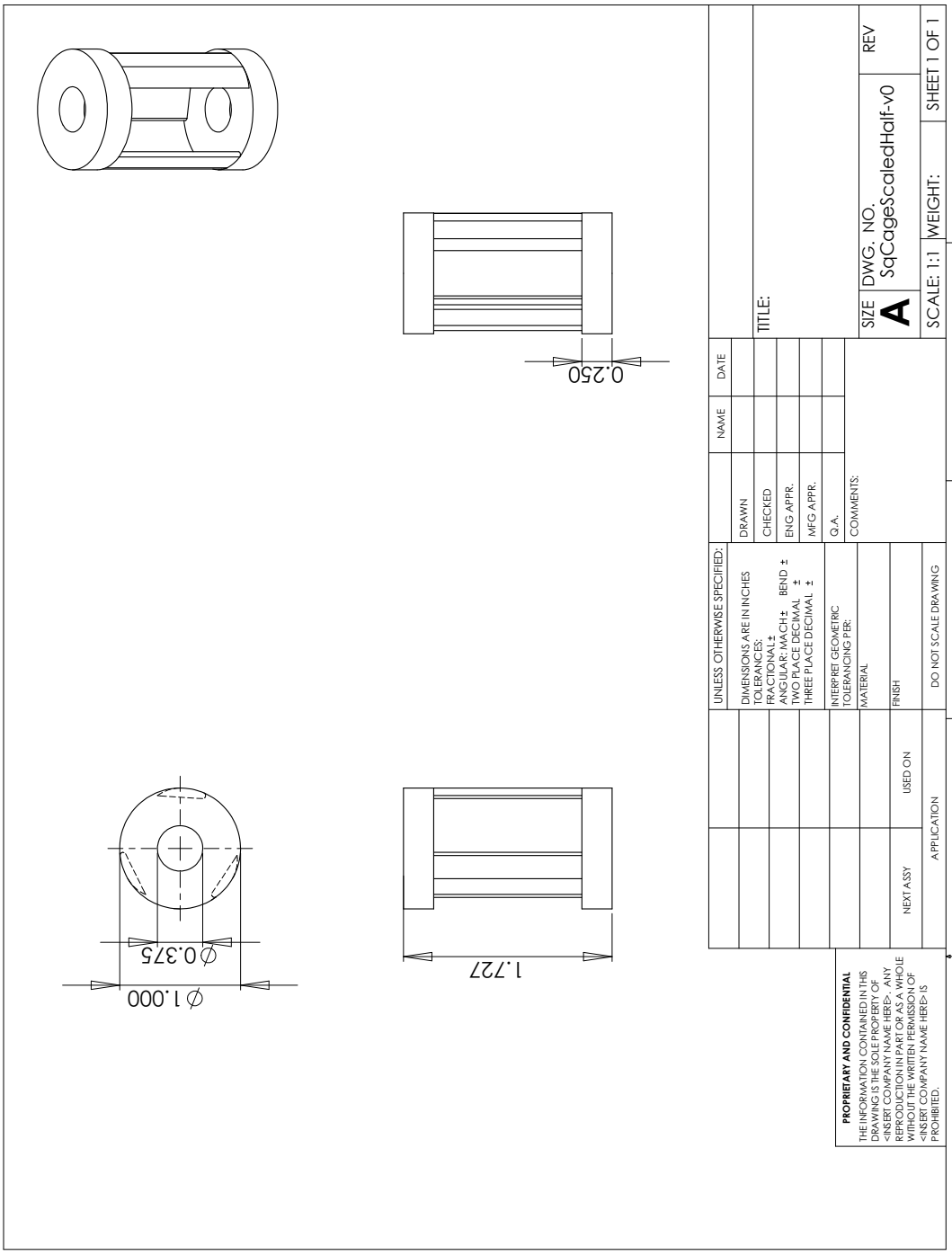

Figure 116: Squirrel Cage Darrieus Turbine Part Drawing.

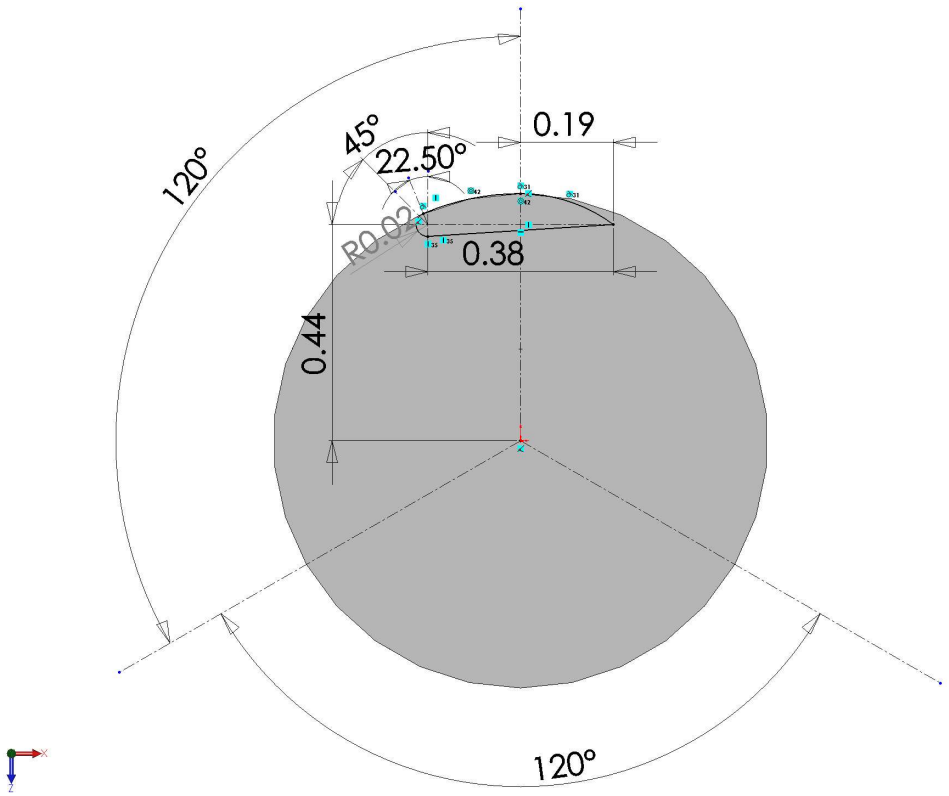

Figure 117: Squirrel Cage Darrieus Turbine Hydrofoil.

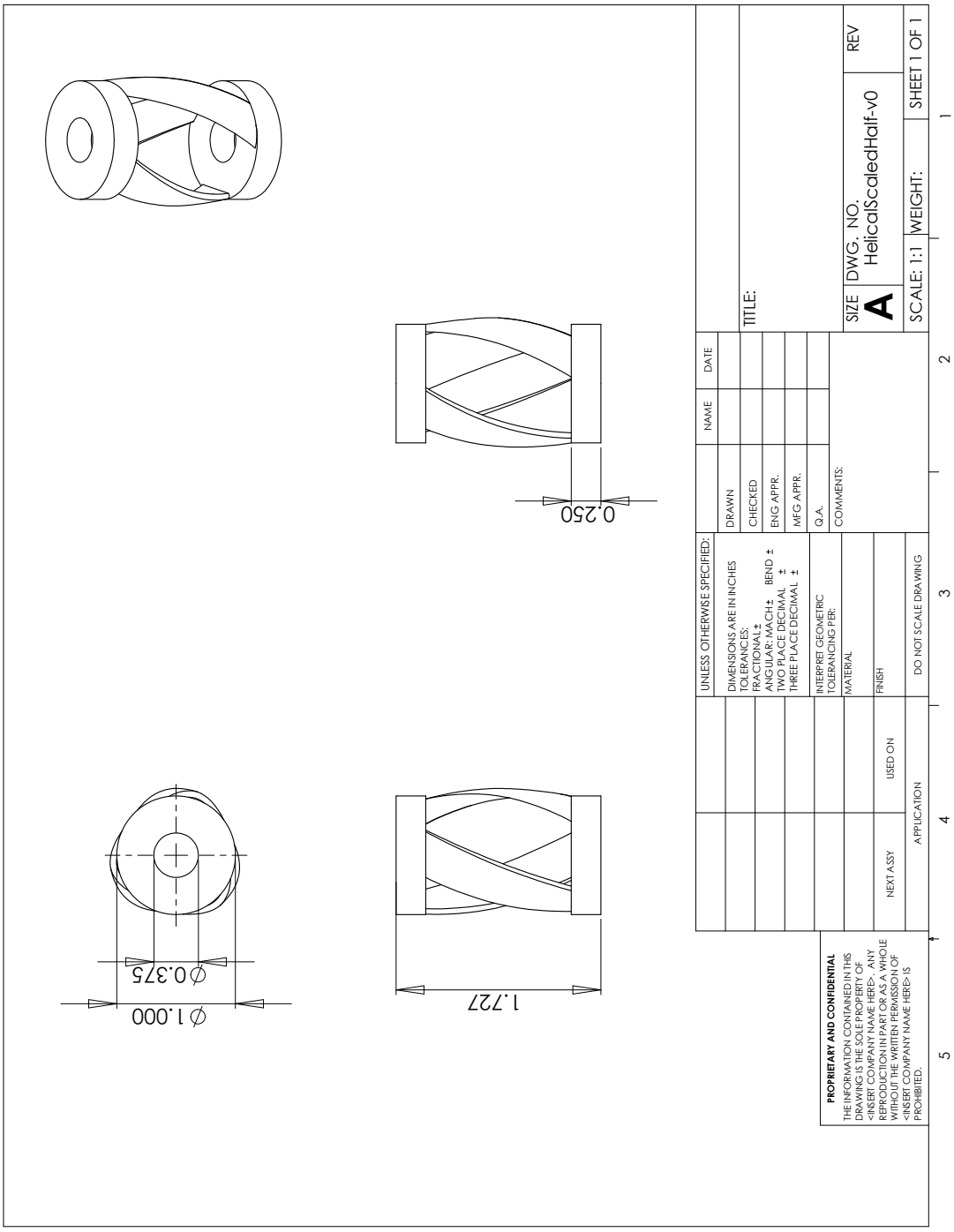

Figure 118: Gorlov Helical Darrieus Turbine Part Drawing.

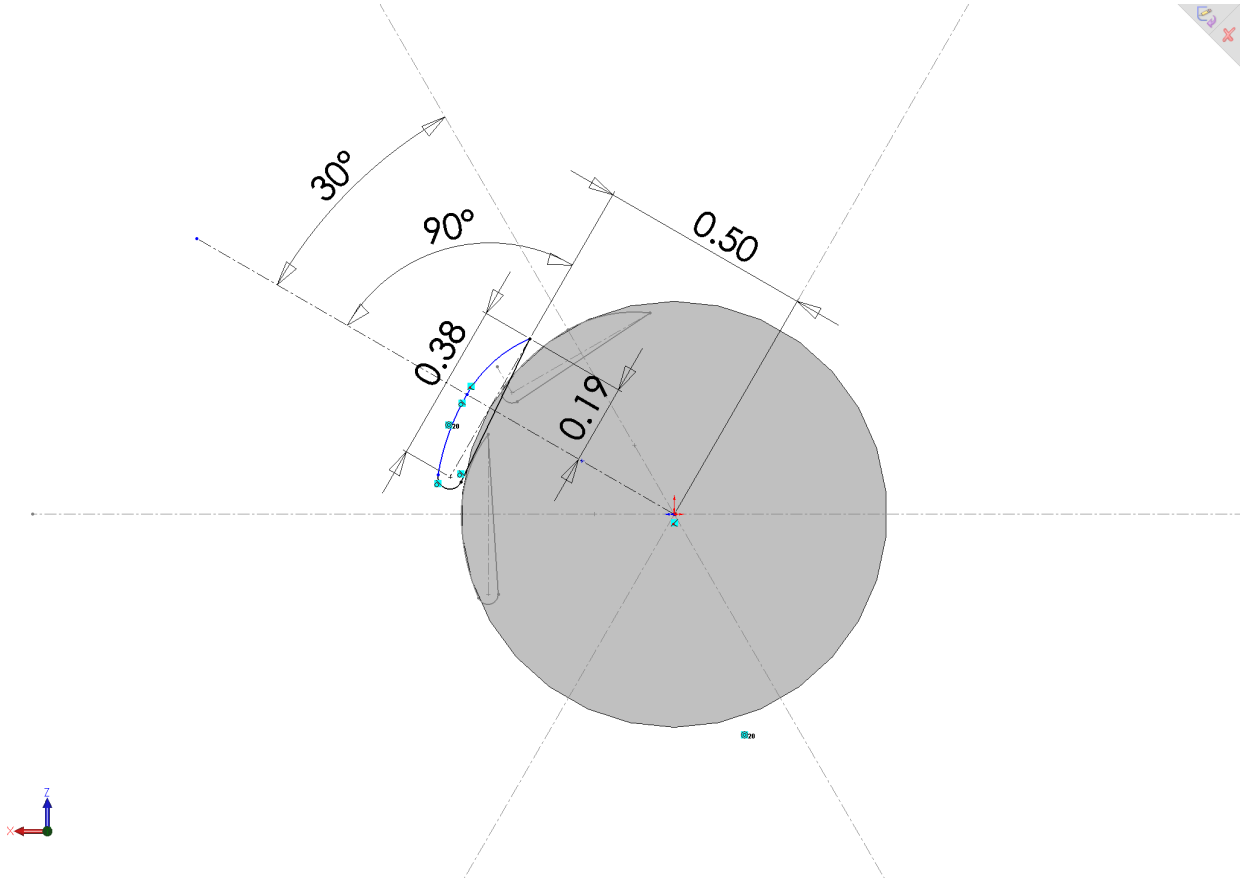

Figure 119: Gorlov Helical Darrieus Turbine Hydrofoil.

APPENDIX I

GHANIAN MAPS

Ghanaian maps that show topography, population density, electricity infrastructure, poverty, hydropower sites, and hydropower sites with population density are in this section (88–90; 95; 104).

Figure 120: Ghana Topography Map.

Figure 121: Ghana Population Density Map.

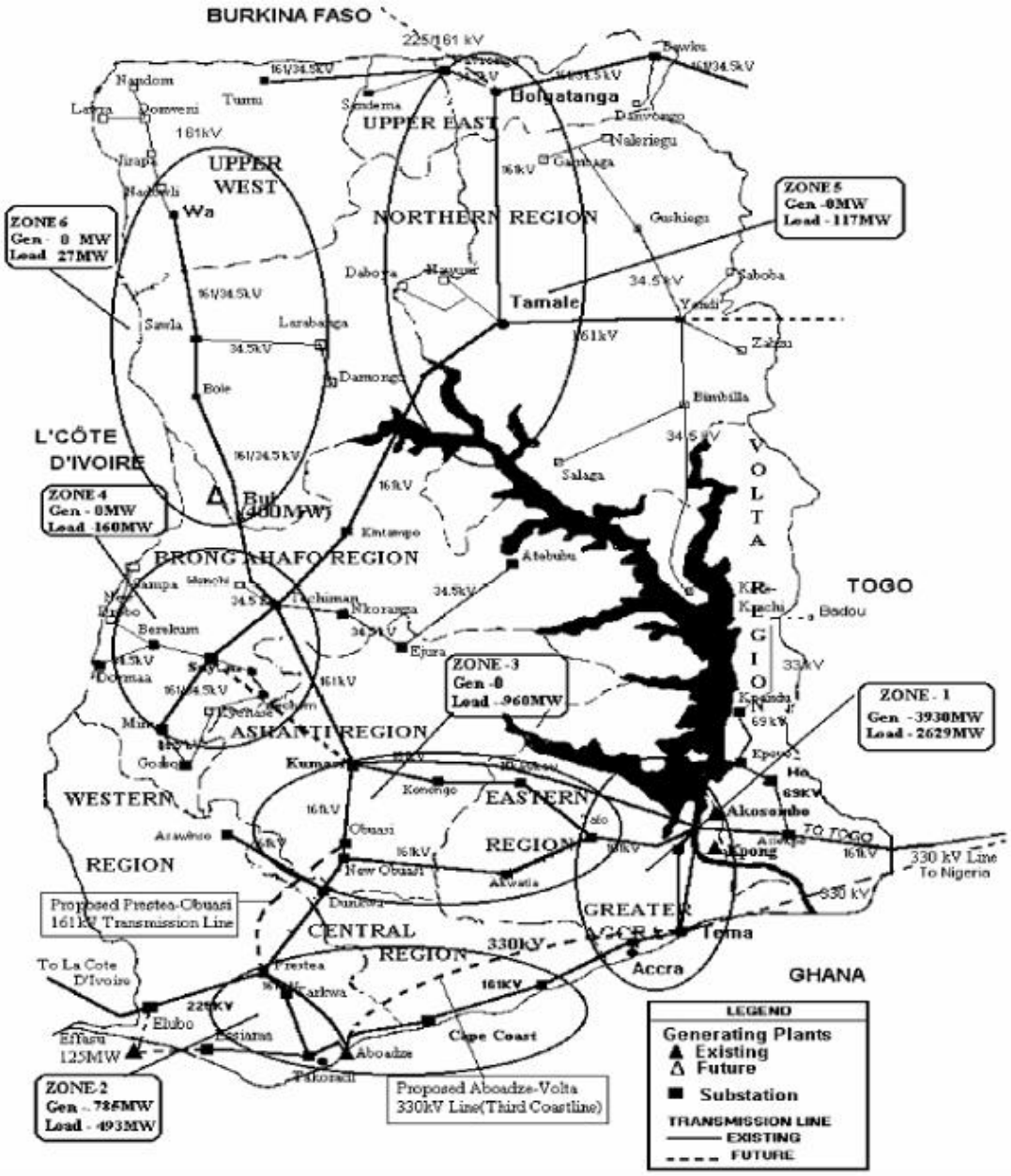

Figure 122: Ghanaian Electricity Infrastructure.

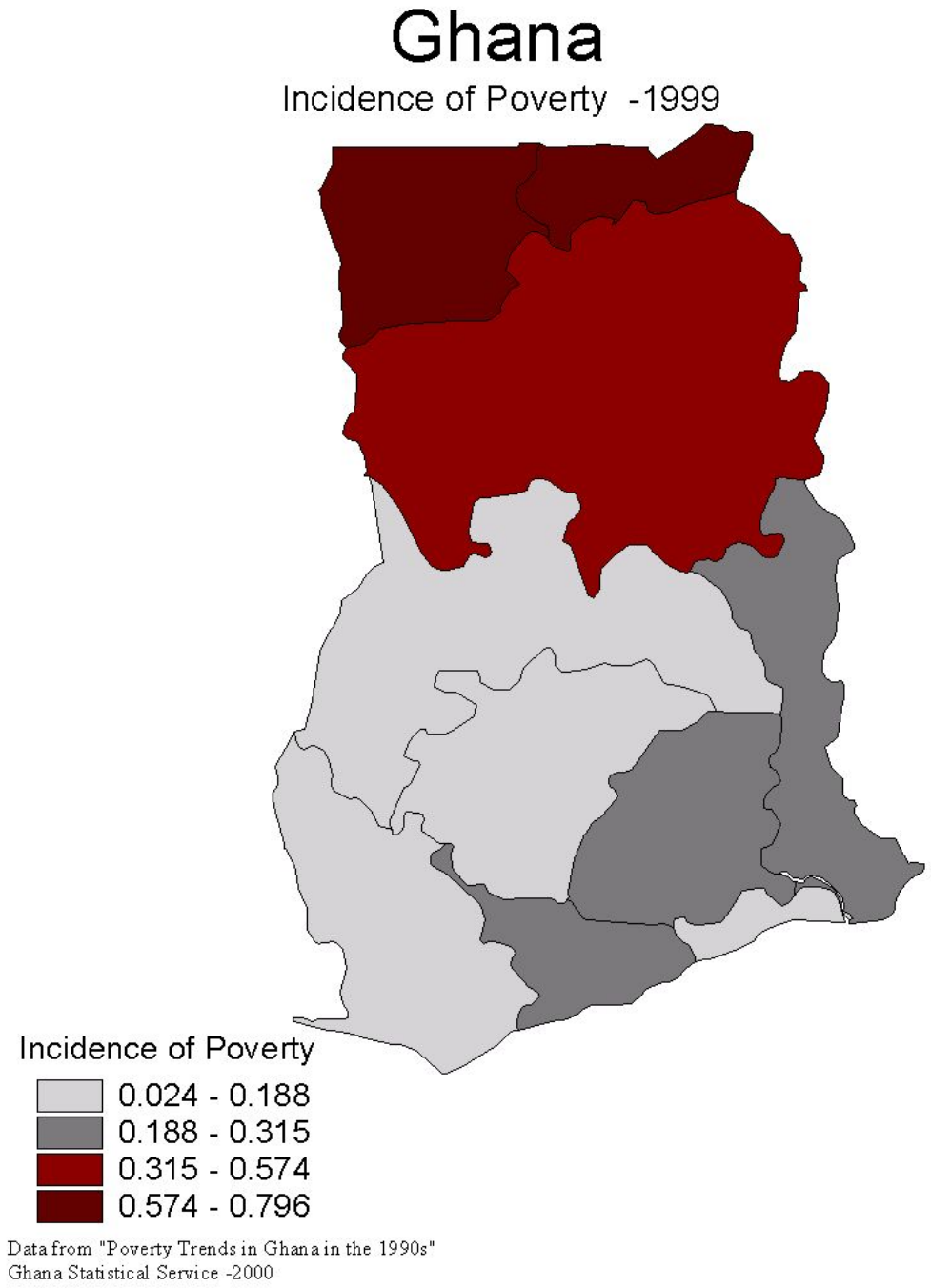

Figure 123: Ghana Poverty Map.

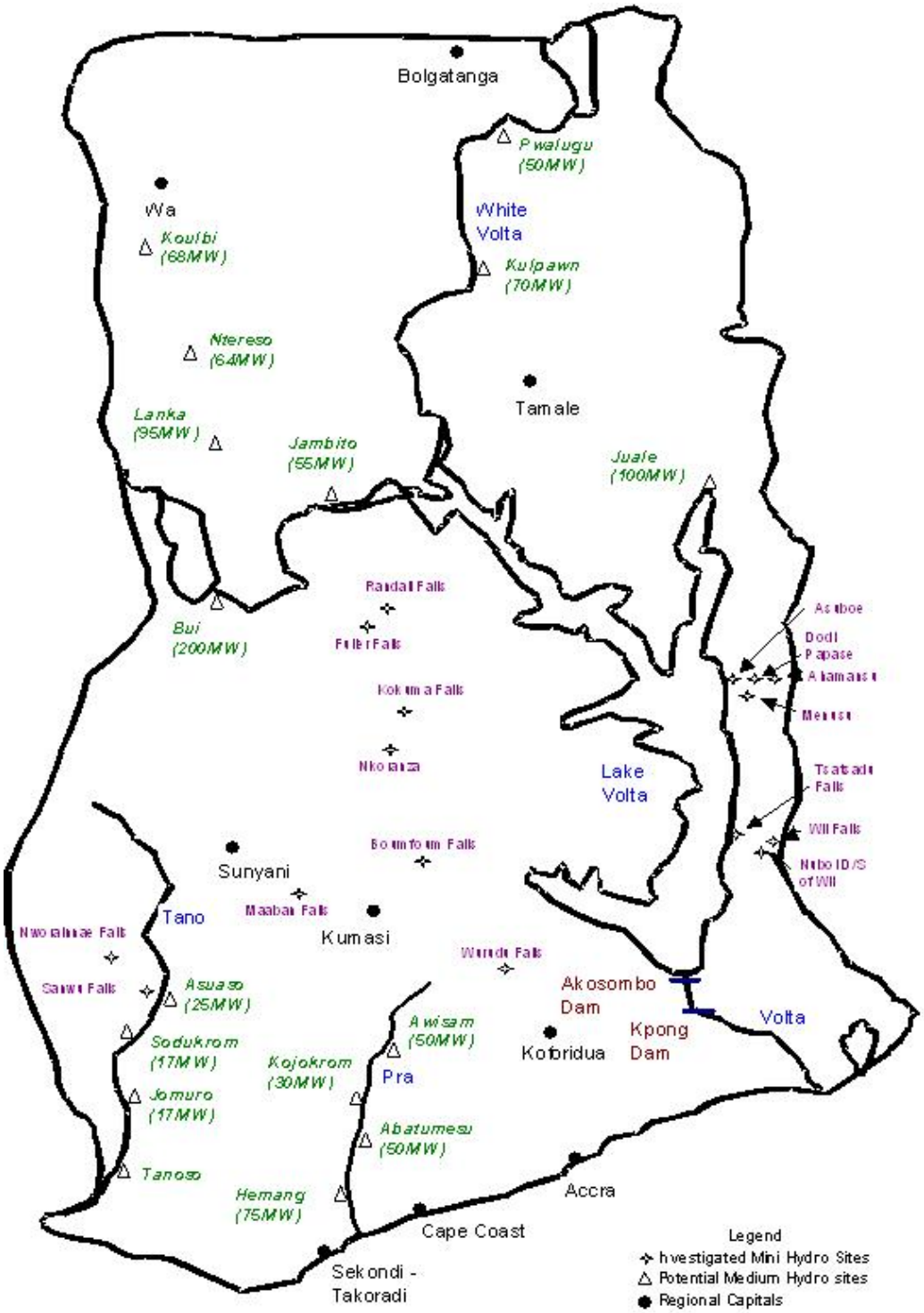

Figure 124: Hydropower Sites of Various Sizes in Ghana.

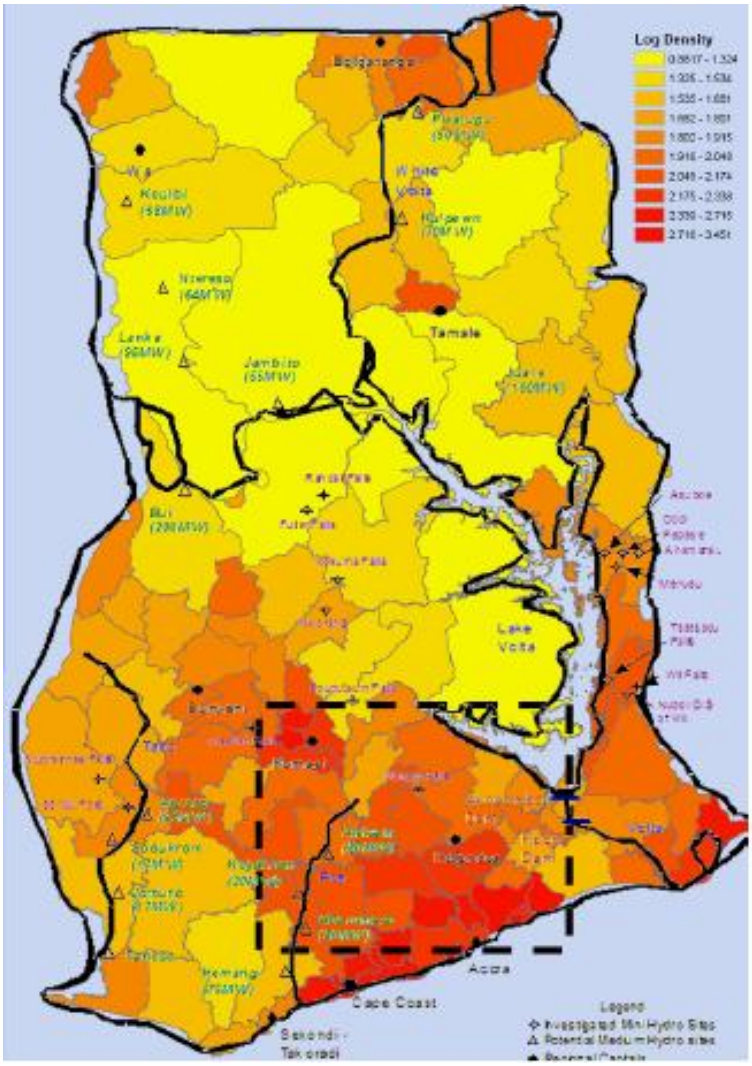

Figure 125: Hydropower Sites of Various Sizes in Ghana with an Underlay of Ghana's Population Density.

BIBLIOGRAPHY

[1] E. I. Administration, *Key World Statistics*, http://www.eia.doe.gov/ (2006).

[2] N. L. Poff, D. D. Hart, *How dams vary and why it matters for the emerging science of dam removal*, BioScience, **Vol. 52 (8)** pp. 659–668 (2002).

[3] D. G. Hall, K. S. Reeves, J. Brizzee, R. D. Lee, G. R. Carroll, G. L. Sommers, *Feasibility Assessment of the Water Energy Resources of the United States for New Low Power and Small Hydro Classes of Hydroelectric Plants*, U.S. Department of Energy, Energy Efficiency and Renewable Energy - Wind and Hydropower Technologies (2006).

[4] D. Altinbilek, *The Role of Dams in Development*, International Journal of Water Resources Development, **Vol. 18 (1)** pp. 9–24 (2002).

[5] L. Ortolano, K. Cushing, *Grand Coulee Dam 70 Years Later: What Can We Learn?*, International Journal of Water Resources Development, **Vol. 18 (3)** pp. 373–390 (2002).

[6] N. Poff, J. Allan, M. Bain, J. Karr, K. Prestegaard, B. Richter, R. Sparks, J. Stromberg, *The natural flow regime. A paradigm for river conservation and restoration*, Bioscience, **Vol. 47 (11)** pp. 769–784 (1997).

[7] E. Anderson, M. Freeman, C. Pringle, *Ecological consequences of hydropower development in Central America: impacts of small dams and water diversion on neotropical stream fish assemblages*, River research and applications(Print), **Vol. 22 (4)** pp. 397–411 (2006).

[8] A. Regmi, *Dyadic design interface between energy and agriculture: the case of Pinthali micro hydro system in Nepal.*, Water Science Technology, **Vol. 47 (6)** pp. 193–200 (2003).

[9] SHP in China, *Hangzhou Regional Center(Asia-Pacific) for Small Hydro Power* pp. 1–27 (2006).

[10] R. Bakis, A. Demirbas, *Sustainable Development of Small Hydropower Plants (SHPs)*, Energy Sources, **Vol. 26 (12)** pp. 1105–1118 (2004).

[11] S. Dudhani, A. Sinha, S. Inamdar, *Assessment of small hydropower potential using remote sensing data for sustainable development in India*, Energy Policy, **Vol. 34 (17)** pp. 3195–3205 (2006).

[12] Gandolfi, Guariso, Togni, *Optimal Flow Allocation in the Zambezi River System*, Water Resources Management, **Vol. 11 (5)** pp. 377–393 (1997).

[13] G. Colonnello, E. Medina, *Vegetation changes induced by dam construction in a tropical estuary: the case of the Mánamo river, Orinoco Delta (Venezuela)*, Plant Ecology, **Vol. 139 (2)** pp. 145–154 (1998).

[14] M. Han, M. Fukushima, S. Kameyama, T. Fukushima, B. Matsushita, *How do dams affect freshwater fish distributions in Japan? Statistical analysis of native and nonnative species with various life histories*, Ecological Research pp. 1–9.

[15] R. Kingsford, R. Thomas, *Destruction of Wetlands and Waterbird Populations by Dams and Irrigation on the Murrumbidgee River in Arid Australia*, Environmental Management, **Vol. 34 (3)** pp. 383–396 (2004).

[16] G. Kondolf, J. Webb, M. Sale, T. Felando, *Basic hydrologic studies for assessing impacts of flow diversions on riparian vegetation: Examples from streams of the eastern Sierra Nevada, California, USA*, Environmental Management, **Vol. 11 (6)** pp. 757–769 (1987).

[17] J. Lovett, J. Hatton, L. Mwasumbi, J. Gerstle, *Assessment of the impact of the Lower Kihansi Hydropower Project on the forests of Kihansi Gorge, Tanzania*, Biodiversity and Conservation, **Vol. 6 (7)** pp. 915–934 (1997).

[18] S. Pearsall, B. McCrodden, P. Townsend, *Adaptive Management of Flows in the Lower Roanoke River, North Carolina, USA*, Environmental Management, **Vol. 35 (4)** pp. 353–367 (2005).

[19] T. Penczak, Ł. Głowacki, W. Galicka, H. Koszaliński, *A long-term study (1985–1995) of fish populations in the impounded Warta River, Poland*, Hydrobiologia, **Vol. 368 (1)** pp. 157–173 (1998).

[20] B. Davis, D. Swan, *Vertical axis turbine economics for river and estuaries in modern power systems*, Montreal: Nova Energy Ltd (1983).

[21] A. Mohamed, *Current turbine for water pumping and electricity generation*, Alternative Energy Sources, **Vol. 6** (1983).

[22] P. Vauthier, *The underwater electric kite East River deployment*, OCEANS'88.'A Partnership of Marine Interests'. Proceedings pp. 1029–1033.

[23] J. Vocadlo, B. Richards, M. King, *Hydraulic Kinetic Energy Conversion(HKEC) Systems*, Journal of Energy Engineering, **Vol. 116 (1)** pp. 17–38 (1990).

[24] U.S. Department of Energy, *Proceedings of the Hydrokinetic and Wave Energy Technologies, Technical and Environmental Issues Workshop*, Energy Efficiency and Renewable Energy - Wind and Hydropower Technologies (2006).

[25] HydroVenturi Renewable Energy Systems, *Rochester Venturi*, http://www.hydroventuri.com (2006).

[26] A. Gorlov, *Hydrogen as an activating fuel for a tidal power plant*, International Journal of Hydrogen Energy, **Vol. 6 (3)** pp. 243–253 (1981).

[27] A. Gorlov, *Helical turbines for the Gulf Stream: Conceptual approach to design of a large-scale floating power farm*, Marine Technology, **Vol. 35 (3)** pp. 175–182 (1998).

[28] A. Gorlov, *The Helical Turbine and its applications for tidal and wave power*, Oceans 2003. Proceedings, **Vol. 4** (2003).

[29] A. Gorlov, *Waving in energy.*, International Water Power and Dam Construction, **Vol. 55 (7)** pp. 26–29 (2003).

[30] A. Gorlov, V. Silantyev, *Limits of the Turbine Efficiency for Free Fluid Flow*, Journal of Energy Resources Technology, **Vol. 123** (2001).

[31] A. Gorlov, R. Zuo, *Some Novel Concepts in Approach to Harnessing Tidal Power*, Ocean Energy Recovery pp. 140–149.

[32] A. Cotel, P. Webb, H. Tritico, *Do Brown Trout Choose Locations with Reduced Turbulence?*, Transactions of the American Fisheries Society, **Vol. 135 (3)** pp. 610–619 (2006).

[33] G. Cada, J. Ahlgrimm, M. Bahleda, T. Bigford, S. Damiani Stavrakas, D. Hall, R. Moursund, M. Sale, *Potential impacts of hydrokinetic and wave energy conversion technologies on aquatic environments*, Fisheries(Bethesda, Md.), **Vol. 32 (4)** pp. 174–181 (2007).

[34] *Report to Congres: Potential Environmental Effects of Marine and Hydrokinetic Energy Technologies*, Tech. rep., U.S. Department of Energy (2008).

[35] J. E. Ehrenberg, *Two Application For a Dual-Beam Transducer in Hydroacoustic Fish Assessment Systems*, IEEE, **Vol. 1** pp. 152–155 (1974).

[36] M. J. Khan, M. T. Iqbal, J. E. Quaicoe, *Design Considerations of a Straight Bladed Darrieus Rotor for River Current Turbines*, Industrial Electronics, 2006 IEEE International Symposium on, **Vol. 3** (2006).

[37] M. Khan, M. Iqbal, J. Quaicoe, *A Technology Review and Simulation Based Performance Analysis of River Current Turbine Systems*, Electrical and Computer Engineering, Canadian Conference on pp. 2288–2293 (2006).

[38] P. Leung, *The development of a novel hydro-electric plant for rivers and oceans*, IMechE Event Publications pp. 51–58 (2004).

[39] S. Pobering, N. Schwesinger, *A novel hydropower harvesting device*, Proceedings - 2004 International Conference on MEMS, NANO and Smart Systems pp. 480–485 (2004).

[40] M. Bernitsas, A. Fellow, K. Raghavan, G. Student, Y. Ben-Simon, E. Garcia, et al., *VIVACE (Vortex Induced Vibration Aquatic Clean Energy): A New Concept in Generation of Clean and Renewable Energy From Fluid Flow*, Journal of Offshore Mechanics and Arctic Engineering, **Vol. 130** p. 041101 (2008).

[41] J. Manwell, J. McCowan, A. Rogers, *Wind Energy Explained: theory, design and application*, Wind Engineering, **Vol. 30 (2)** pp. 169–170 (2006).

[42] M. Patel, *Wind and Solar Power Systems*, CRC Press (1999).

[43] National Weather Service, *Ohio River Forecast Center*, http://www.erh.noaa.gov/er/ohrfc/flows.shtml (2007).

[44] F. White, *Viscous fluid flow*, McGraw-Hill New York (1991).

[45] M. Griebel, T. Dornseifer, T. Neunhoeffer, *Numerical Simulation in Fluid Dynamics: A Practical Introduction*, Society for Industrial Mathematics (1998).

[46] M. Shams, G. Ahmadi, D. Smith, *Computational modeling of flow and sediment transport and deposition in meandering rivers*, Advances in Water Resources, **Vol. 25 (6)** pp. 689–699 (2002).

[47] B. Launder, D. Spalding, *Lectures in Mathematical Models of Turbulence*, Academic Press (1972).

[48] *FLUENT User Guide*, Fluent Incorporated, centerra Resoures Park, 10 Cavendish Court, Lebanon, NH 03766 (1998).

[49] V. Yakhot, S. A. Orszag, *Renormalized Group Analysis of Turbulence. I. Basic Theory*, Journal of Scientific Computing, **Vol. 1** pp. 3–51 (1986).

[50] H. Tritico, A. Cotel, J. Clarke, *Development, testing and demonstration of a portable submersible miniature particle imaging velocimetry device*, Measurement Science and Technology, **Vol. 18 (8)** pp. 2555–2562 (2007).

[51] D. L. F. Gaden, *An Investigation of River Kinetic Turbines: Performance Enhancements, Turbine Modelling Techniques, and An Assessement of Turbulence Models*, Master's thesis, University of Manitoba (2007).

[52] M. Stegmeir, T. Strand, *Part 1: Collecting Good PIV Data, TSI Webinar Training Series*, TSI Incorporated (2010).

[53] D. C. Wilcox, *Turbulence Modeling for CFD*, DCW Industries, Inc. La Canada, California (1998).

[54] J. Oakes, *Flow Field Analysis in an Expanding Healty and Emphysematous Alveolar Model Using Particle Image Velocimetry*, Master's thesis, Rochester Institute of Technology (2008).

[55] M. H. Al-Hajeri, A. Aroussi, K. Simmons, S. J. Pickering, *CFD and PIV Investigation of Flow past a Single Hot Gas Filter*, Chemical Engineering Technology, **Vol. 29** pp. 348–354 (2006).

[56] D. Giordano, S. Giammartini, M. Rufoloni, G. Calchetti, F. Manfredi, E. Giacomazzi, *Comparison Between PIV Measurements and CFD Simulation on a Model of GT Annular Burner*, in *XXV Event of the Italian Section of the Combustion Institute, Rome, Italy* (2002).

[57] Q. Zhang, B. Karney, H. L. MacLean, J. Feng, *Life-cycle inventory of energy use and greenhouse gas emissions for two hydropower projects in China*, Journal of Infrastructure Systems, **Vol. 13 (4)** pp. 271–279 (2007).

[58] L. Gagnon, C. Bélanger, Y. Uchiyama, *Life-cycle assessment of electricity generation options: The status of research in year 2001*, Energy Policy, **Vol. 30 (14)** pp. 1267–1278 (2002).

[59] J. Cascio, G. Woodside, P. Mitchell, *ISO 14000 Guide: The New International Environmental Management Standards*, McGraw-Hill Professional (1996).

[60] J. Guinée, *Handbook on Life Cycle Assessment: Operational Guide to the ISO Standards*, Kluwer Academic Publishers (2002).

[61] M. Bilec, R. Ries, H. Scoff Matthews, A. Sharrard, *Example of a hybrid life-cycle assessment of construction processes*, Journal of infrastructure systems, **Vol. 12 (4)** pp. 207–215 (2006).

[62] J. Bare, T. Gloria, G. Norriss, *Development of the Method and US Normalization Database for Life Cycle Impact Assessment and Sustainability Metrics*, Environ. Sci. Technol, **Vol. 40 (16)** pp. 5108–5115 (2006).

[63] H. Baumann, A. Tillman, *The hitch hiker's guide to LCA: an orientation in life cycle assessment methodology and application*, Studentlitteratur (2004).

[64] P. Consultants, *SimaPro 7.1: Introduction to LCA with SimaPro*, Product Ecology Consultants p. 1 (2007).

[65] X. Di, Z. Nie, B. Yuan, T. Zuo, *Life cycle inventory for electricity generation in China*, The International Journal of Life Cycle Assessment, **Vol. 12 (4)** pp. 217–224 (2007).

[66] P. Consultants, *Simapro 7.1 Multi User*, Pré Consultants. http://www. pre. nl/simapro/simapro_lca_software. htm (2006).

[67] A. Gorlov, *Development of the helical reaction hydraulic turbine*, NASA, **(19990036780)** (1998).

[68] B. Nalukowe, J. Liu, W. Damien, T. Lukawski, *Life cycle assessment of a wind turbine* (2006).

[69] L. Winkel, I. Alxneit, M. Sturzenegger, *New paths for a SO2-free copper production*, Minerals Engineering, **Vol. 20 (12)** pp. 1179–1183 (2007).

[70] J. Mossa, *Sediment dynamics in the lowermost Mississippi River*, Engineering Geology, **Vol. 45 (1-4)** pp. 457–479 (1996).

[71] K. Singh, D. Mohan, V. Singh, A. Malik, *Studies on distribution and fractionation of heavy metals in Gomti river sedimentsa tributary of the Ganges, India*, Journal of Hydrology, **Vol. 312 (1-4)** pp. 14–27 (2005).

[72] J. Kaldellis, *The contribution of small hydro power stations to the electricity generation in Greece: Technical and economic considerations*, Energy Policy, **Vol. 35 (4)** pp. 2187–2196 (2007).

[73] J.-E. Klimpt, C. Rivero, H. Puranen, F. Koch, *Recommendations for sustainable hydroelectric development*, Energy Policy, **Vol. 30** pp. 1305–1312 (2002).

[74] F. Forouzbakhsh, S. Hosseini, M. Vakilian, *An approach to the investment analysis of small and medium hydro-power plants*, Energy Policy, **Vol. 35** pp. 1013–1024 (2007).

[75] N. Tanwar, *Clean development mechanism and off-grid small-scale hydropower projects: Evaluation of additionality*, Energy Policy, **Vol. 35** pp. 714–721 (2007).

[76] H. Winkler, R. Spalding-Fecher, J. Sathaye, L. Price, *Multi-project baselines for potential Clean Developmen Mechanism projects in the electricity sector in South Africa*, Journal of Energy in Southern Africa, **Vol. 12** pp. 449–457 (2001).

[77] C. Jones, W. Lick, *SEDZLJ: A Sediment Transport Model*, U.S. Environmental Protection Agency, Office of Research and Development, National Health and Environmental Effects Research Laboratory, Mid-Continent Ecology Divison-Duluth, Large Lakes and Rivers Forcasting Research Branch, Large Lakes Research Station, Grosse Ile, Michigan pp. 1–116 (2001).

[78] S. Sinha, F. Sotiropoulos, A. Odgaard, *Three-dimensional numerical model for flow through natural rivers*, Journal of Hydraulic Engineering, **Vol. 124 (1)** pp. 13–24 (1998).

[79] J. Ebbert, S. Embrey, J. Kelley, *Concentrations and Loads of Suspended Sediment and Nutrients in Surface Water of the Yakima River Basin, Washington, 1999-2000-*

With an Analysis of Trends in Concentrations, Water Resources Investigations Report. United States Geological Survey, **(4026)** (2003).

[80] J. McNeil, W. Lick, *Erosion rates and bulk properties of sediments from the Kalamazoo River.*, Journal of Great Lakes Research, **Vol. 30 (3)** pp. 407–418 (2004).

[81] D. DiToro, *Sediment flux modeling*, Wiley-Interscience New York (2001).

[82] C. Dietrich, T. Green, A. Jakeman, *An analytical model for stream sediment transport: application to Murray and Murrumbidgee river reaches, Australia*, Hydrological Processes, **Vol. 13 (5)** pp. 763–776 (1999).

[83] C. Lee, D. Schwab, D. Beletsky, J. Stroud, B. Lesht, *Numerical modeling of mixed sediment resuspension, transport, and deposition during the March 1998 episodic events in southern Lake Michigan*, J. Geophys. Res, **Vol. 112** (2007).

[84] R. Jamieson, D. Joy, H. Lee, R. Kostaschuk, R. Gordon, *Resuspension of Sediment-Associated Escherichia coli in a Natural Stream*, Journal of Environmental Quality, **Vol. 34 (2)** p. 581 (2005).

[85] O. Davidson, B. Metz, *Climate Change 2007: Mitigation. Contribution of Working Group III to the Fourth Assessment Report of the Intergovernmental Panel on Climate Change* (2007).

[86] I. Rodriguez-Iturbe, *Ecohydrology: a hydrologic perspective of climate-soil-vegetation dynamics*, Water Resources Research, **Vol. 36 (1)** pp. 3–9 (2000).

[87] G. Y. Obeng, F. Akuffo, I. Braimah, H.-D. Evers, E. Mensah, *Impact of solar photovoltaic lighting on indoor air smoke in off-grid rural Ghana*, Energy for Sustainable Development, **Vol. 12 (1)** pp. 55 – 61, URL http://www.sciencedirect.com/science/article/B94T4-4V9PDFR-6/2/099717434907c0aeca9b23e8d6271748 (2008).

[88] *Population Desity Map of Ghana*, World Trade Press, Best Country Reports, URL http://www.bestcountryreports.com/Population_Map_Ghana.html, access date: 13 Oct 2009 (2008).

[89] *Ghana, topographic map*, UNEP/GRID-Arendal Maps and Graphics Library, URL http://maps.grida.no/go/graphic/ghana_topographic_map, access date: 13 Oct 2009 (1997).

[90] *Guide to Electric Power in Ghana*, Institute of Statistical, Social and Economic Research, of Ghana Legon (2005).

[91] K. Appiah-Kubi, *The GPRS and the Energy Challenge of Ghana. National Development Planning Commission.*

[92] *Developing Energy to Meet Development Needs*, United Nations Industrial Development Organization.

[93] J. P. Painuly, J. V. Penhann, *Implementation of Renewable Energy Technologies - Opportunities and Barriers* (Denmark 2002).

[94] I. Edjekumhene, S. B. Atakora, R. Atta-Konadu, A. Brew-Hammond, *Implementation of Renewable Energy Technologies - Opportunities and Barriers*, Kumasi Institute of Technology and Environment Ghana (KITE) (Denmark 2001).

[95] *School of Engineering Kwame Nkrumah University of Science and Technology: Kumasi Ghana,*, Strategic National Energy Plan - 2000 - 2020 Republic of Ghana (2003).

[96] M. Khan, G. Bhuyan, M. Iqbal, J. Quaicoe, *Hydrokinetic energy conversion systems and assessment of horizontal and vertical axis turbines for river and tidal applications: A technology status review*, Applied Energy, **Vol. 86 (10)** pp. 1823 – 1835, URL http://www.sciencedirect.com/science/article/B6V1T-4VYW6FV-2/2/1f8fb46959079fd5e202a8268dd37ebf (2009).

[97] V. Miller, L. Schaefer, *Dynamic Modeling of Hydrokinetic Energy Extraction*, Proceedings of the 2008 ASME International Mechanical Engineering Congress and Exposition pp. 1–8 (2008).

[98] V. Miller, L. Schaefer, *Computational Fluid Dynamics for Hydrokinetic Turbines*, Proceedings of the 2009 ASME International Mechanical Engineering Congress and Exposition pp. 1–11 (2009).

[99] R. Van Els, C. Campos, A. Henriques, L. Balduino, *Hydrokinetic Propeller Type Turbine for the Electrification of Isolated Households or Community and Social End-Users*, 17th Congress of Mechanical Engineering, S. Paulo, Brazil (2003).

[100] A. C. P. Brasil Junior, L. R. B. Salomon, R. Van Els, W. de Oliveira Ferreira, *A New Conception of Hydrokinetic Turbine for Isolated Communities in Amazon*, 6th National Congress of Mechanical Engineering (2006).

[101] K. Alanne, A. Saari, *Distributed energy generation and sustainable development*, Renewable and Sustainable Energy Reviews, **Vol. 10 (6)** pp. 539 – 558, URL http://www.sciencedirect.com/science/article/B6VMY-4FB91D5-1/2/2e248fd6fddab6a23f6d3d3aa8fb9ad0 (2006).

[102] J. M. Hunter, *Inherited burden of disease: agricultural dams and the persistence of bloody urine (Schistosomiasis hematobium) in the Upper East Region of Ghana, 1959-1997*, Social Science & Medicine, **Vol. 56 (2)** pp. 219 – 234, URL http://www.sciencedirect.com/science/article/B6VBF-450HCK9-4/2/c06480e4264bf36dcaa2ee3077d8db68 (2003).

[103] P. M. Fearnside, *Greenhouse Gas Emissions from a Hydroelectric Reservior (Brazil's Tucurui Dam) and the Energy Policy Implications*, Water, Air, & Soil Pollution, **Vol. 133 (1)** pp. 69–96 (2002).

[104] *Ghana Incidence of Poverty - 1999*, Poverty Trends in Ghana in the 1990s. Ghana Statistical Service, URL http://earthtrends.wri.org/povlinks/map/m_49.php (2000).

[105] P. Bongers, G. van Baars, *Control of wind turbine systems to reduce vibrations and fatigue loading*, Minneapolis, MN, USA, pp. 483 – (1994).

[106] P. M. Bongers, *Experimental robust control of a flexible wind turbine system*, Vol. 3, Baltimore, MD, USA, pp. 3214 – 3218, robust control;Flexible wind turbine systems;Uncertainty bound;Gap metric;Integer arithmetics;Nominal model; (1994).

[107] H. Kondo, *Aeroelastic response and stability of wind turbine generators (behavior of the turbine blade)*, JSME International Journal, Series 3: Vibration, Control Engineering, Engineering for Industry, **Vol. 31 (4)** pp. 719 – 726, isolated Blade;Blade-Element Strip Theory;Aeroelasticity;Lagrange's Equation of motion;Steady-State Response; (1988).

[108] S. Sarkar, H. Biji, *Stall induced vibration and flutter in a symmetric airfoil*, Vol. 9, Vancouver, BC, Canada, pp. 359 – 369, aeroelastic stability analysis;Aeroelastic models;Quasi-harmonic response; (2006).

[109] P. Bongers, *Robust control of a flexible wind turbine based on coprime factorizations*, no. 5, Zurich, Switz, pp. 197 – (1992).

[110] P. M. Bongers, G. E. Baars, S. Dijkstra, *Load reduction in a wind energy conversion system using and H¡sub¿INF¡/sub¿ controller*, Vol. 2, Vancouver, BC, Can, pp. 965 – 970, URL http://dx.doi.org/10.1109/CCA.1993.348206, load reduction;Wind energy conversion system;Variable speed wind turbines; (1993).

[111] T. Ekelund, *Modeling and linear quadratic optimal control of wind turbines*, Doktorsavhandlingar vid Chalmers Tekniska Hogskola, **(1269)** pp. 1 – 146, dynamic load reduction;Variable speed wind power plants;Active yaw regulation; (1997).

[112] P. M. Bongers, S. Dijkstra, *Control of wind turbine systems aimed at load reduction*, Vol. 2, Chicago, IL, USA, pp. 1710 – 1714, fixed speed wind turbine systems;Variable speed wind turbine systems;Integrated dynamic models;Load reduction; (1992).

[113] J. A. Clarke, G. Connor, A. D. Grant, C. M. Johnstone, S. Ordonez-Sanchez, *Contra-rotating Marine Current Turbines: Performance in Field Trials and Power Train Developments*, Proc. 10th World Renewable Energy Congress, Glasgow (19-25, July 2008).

[114] Y. Kinoue, T. Setoguchi, T. Kuroda, K. Kaneko, M. Takao, A. Thakker, *Comparison of Performances of Turbines for Wave Energy Conversion*, Journal of Thermal Science, **Vol. 12** pp. 1–6 (2003).

[115] M. Shiono, K. Suzuki, S. Kiho, *An Experimental Study of the Characteristics of a Darrieus Turbine for Tidal Power Generation*, Electrical Engineering in Japan, **Vol. 132** pp. 781–787 (2000).

[116] S. M. Camporeale, V. Magi, *Streamtube model for analysis of vertical axis variable pitch turbine for marine currents energy conversion*, Energy Conversion and Management, **Vol. 41** pp. 1811–1827 (2000).